Universidad de La Laguna
de La Laguna

UNIVERSIDAD DE LA LAGUNA

INSTITUTO DE ASTROFÍSICA DE CANARIAS

DOCTORAL THESIS

Pioneering the Use of a Plenoptic Adaptive Optics System for Free Space Optical Communications

Author:
Noelia MARTÍNEZ REY

Supervisor:
Dr. Luis Fernando RODRÍGUEZ RAMOS

October 15, 2019

"O idioma é a forza,
que nos xungue e sostén.
Se perdemos a fala,
non seremos ninguén"

Manuel María
A Fala, Obra poética completa I (1950-1979)

Acknowledgements

Como dice una canción de Andrés Suarez, *"tengo demasiado tiempo libre para ser feliz, me estoy volviendo cuerdo"*. Y fue en busca de ese estado de locura, cuando empecé esta tesis en octubre de 2016. . . aunque la idea había germinado un año antes durante una visita de mi director, Luis Fernando, al Observatorio del Teide. Gracias, Luis, por esa idea. Y gracias por todas las demás que vinieron después, por tu constante apoyo y motivación, por enseñarme tanto y guiarme a través de esto que llamamos doctorado, pero que bien podría llamarse "Las aventuras de Indiana Jones y la óptica adaptativa". Gracias por todo el tiempo que has invertido y que, inevitablemente, has quitado de otros aspectos de tu vida; los días, las noches, los desayunos, los almuerzos, las cenas en el observatorio, tus palabras de ánimo cuando todo salía mal, los bocadillos de tortilla y queso a las 5 de la mañana. Por todo, gracias, porque no hubiera podido tener más suerte con mi director de tesis, mi guía, mi mentor.

Gracias a mis padres, mi hermana, mi tía, mi abuela, mi perro Lolo; espero que os sintáis orgullosos de mí, yo me siento muy orgullosa de teneros. Vosotros me habéis acompañado hasta aquí, hasta este punto del camino, y sólo pido que me sigáis acompañando durante mucho tiempo más. No somos una familia grande, somos una gran familia.

Gracias a Fabio, por hacer que me quedase en Tenerife; al final la vida es una sucesión de decisiones, y nunca me arrepentiré de las que he tomado y me han llevado a dónde estoy y a lo que soy ahora, alguien más fuerte.

Y gracias al resto, ya que muchas han sido las personas que me han ayudado a no perderme en la locura: los compañeros y compañeras del IAC que han estado ahí, incansables, para resolverme dudas, para contestar mis emails incluso durante vacaciones, para darme otra perspectiva de los problemas cuando yo ya había perdido la paciencia. . . infinitas gracias a Miguel Núñez, Óscar Tubío, José Marco, Luzma Montoya, Iciar Montilla, Julio Castro, Ángel Alonso, entre muchos otros... supongo que además de aparecer en mis agradecimientos, querréis unas cervezas... Gracias también a mis amigas, que subieron al observatorio un sábado a traerme champú, y en concreto, a mi amiga Gabriela, siempre dispuesta a coger el coche e ir al fin del mundo para que yo me despejase un poco, siempre pendiente, siempre presente, siempre mi persona de marcación rápida.

A special thanks to Zoran Sodnik, from the European Space Agency, for making this research real since the very beginning; to Céline D'Orgeville, from the Australian National University, for hosting me at the Advanced Instrumentation and Technology Centre during four months, and allowing me to participate in the Australian Adaptive Optics Demonstrator, I feel lucky to have lived such a rewarding stay and to have worked hands-on with you all at Stromlo Observatory; to Domenico Bonaccini, from the European Southern Observatory, to count on me for the CANAPY experiment, you have no idea how much I have learned from you, I hope to have the opportunity to keep learning for much longer; also to Mauro Centrone and the INAF-OAR colleagues for making my 10 days in Rome, such a culinary (and professional, of course) experience (*arancio, cacciavite, buco...* I still remember); to Alastair Basden, from Durham University, for answering my emails instantaneously when I was freaking out in the observatory; to Carlos Correia, from Keck Observatory but formerly from Laboratoire d'Astrophysique de Marseille, for all

Todos vosotros estáis en cada una de las palabras escritas en esta tesis.
All of you are present in each of the words written in this thesis.

Contents

List of Figures

List of Tables

xviii

List of Abbreviations

AITC	Advanced Instrumentation and Technology Centre
AO	Adaptive Optics
AOD	Adaptive Optics Demonstrator
AOI	Adaptive Optics for Imaging
AOTP	Adaptive Optics for Tracking and Pushing
BCM	Beam Centering Mirror
BEU	Beam Expander Unit
BPM	Beam Pointing Mirror
BS	Beam Splitter
BTO	Beam Transfer Optics
DARC	Durham Adaptive Optics Real-time Controller
DM	Deformable Mirror
EFM	Elevation Fold Mirror
FOV	Field Of View
FPS	Frames Per Second
FSOC	Free Space Optical Communications
FWHM	Full Width Half Maximum
GEO	Geosynchronous Equatorial Orbit
GSLP	Guide Star Laser Prototype
HP	High Power
HWP	Half Wave Plate
ISS	International Space Station
LEO	Low Earth Orbit
LFM	Laser Fold Mirror
LGS	Laser Guide Star
LGSF	Laser Guide Star Facility
LLT	Laser Launch Telescope
MCAO	Multi Conjugate Adaptive Optics
NCPA	Non Common Path Aberrations
NGS	Natural Guide Star
OGS	Optical Ground Station
OOMAO	Object Oriented Matlab Adaptive Optics
OPD	Optical Path Difference
OPSL	Optically Pumped Semiconductor Laser
ORM	Oservatorio Roque de los Muchachos
OT	Observatorio del Teide
PDF	Power Density Function
PDI	Point Diffraction Interferometer
PE	Piezo Electric
PH	Pin Hole
PS	Phase Screen
PSM	Point Source Microscope
PV	Peak-to-Valley

QE	**Q**uantum **W**fficiency
QWP	**Q**uarter **W**ave **P**late
RC	**R**itchey **C**retien
RF	**R**adio **F**requency
RMS	**R**oot **M**ean **S**quare
RTCS	**R**eal **T**ime **C**ontrol **S**ystem
SCAO	**S**ingle **C**onjugate **A**daptive **O**ptics
SH-WFS	**S**hack **H**artmann **W**ave-Front **S**ensor
SNR	**S**ignal-to-**N**oise **R**atio
SAM	**S**tacked **A**rray **M**irror
TRL	**T**echnology **R**eadiness **L**evel
TT	**T**ip **T**ilt
UWCS	**U**plink **W**avefront **C**orrector **S**ystem
WF	**W**ave-**F**ront
WFS	**W**ave-**F**ront **S**ensor

A mi familia, la que te toca y la que se elige

Chapter 1

Introduction

1.1 Introduction

One of the hottest topics in the field of space communications is the future replacement of the radio-frequency links by the optical technology, which offers many advantages in terms of mass, power, system flexibility and cost to be considered as a good candidate for the space communication race. Koishi et al. (2011) summarises the advantages of optical communications in their article about high data rate optical links, demonstrating the superiority of this technology in comparison with RF (Table 1.1). One of the most remarkable features in the optical links is their capability to carry substantially more information than RF: the typically used Ka-band in radio-frequency (32-38 GHz) allows bandwidths of 500 MHz, whereas for optical systems at 1550 nm wavelength, the bandwidth may be 1000 times larger (Williams, 2007). Among other advantages, it is worth mentioning its high level of security (the light signal coverage is limited to a well defined area), the no interference with any other electronic equipment or network and the non-licensed bandwidth in comparison to RF, whose band is regulated by local and international authorities and sometimes licensed to certain operators.

	Optical communication	RF communication
Satellite	Small and Medium scale satellite	Large scale satellite
Antenna	10cm-30cm Class	2m-5m Class
Data rate	1Gbps-40Gbps	200Mbps-800bps
Spatial Resolution	Very high resolution	High resolution

TABLE 1.1: Comparison of optical links with radio-frequency communications (Koishi et al., 2011)

Free Space Optical Communications (FSOC) Earth-satellite and viceversa are severely influenced by the atmospheric turbulence, which causes several effects on the laser beam. Depending on the origin of the propagation (transmitter placed at the ground or at the satellite), the atmosphere critically impairs the link performance.

Adaptive Optics (AO) systems measure and correct the aberrations caused by the atmosphere and are extensively studied and used in astronomical ground observations. With the aim of fulfilling the AO expected performance, wavefront sensors need a bright enough reference source which is close to the area of interest, in order to measure the turbulence along this line-of-sight and control a deformable mirror which can compensate, to a certain level, the aberrations found. Unfortunately, it is unlikely to find a natural star bright enough to play this role, specially when pointing to the galactic poles, due to the low star density. It is estimated that only a 5% of

the sky regions do have such a reference object (Bahcall and Soneira, 1981); the problem is attenuated by using artificial references, so-called *Laser Guide Stars (LGS)*. The LGSs are laser spots which will be focused at 90km above the Earth surface, where the Sodium layer is located, in case of Sodium Laser Guide Stars; or at around 20km height, when generating a Rayleigh Laser Guide Star. These two are the types of artificial references for AO systems.

In the similar way optical communication lasers suffer from the atmospheric turbulence when travelling from the Earth to the satellite, the Laser Guide Stars are also affected by the same effects on their upwards propagating path; both uplinks will show similar responses and this fact has inspired this thesis research, which focuses on the uplink atmospheric correction.

1.2   Thesis Synopsis

In this thesis, an Adaptive Optics proposal is presented and experimentally verified at both laboratory and telescope, with the objective of compensating the atmospheric aberrations in the uplink beam and, therefore, ameliorate Free Space Optical Communication links performance and the generation of Laser Guide Stars for conventional AO systems.

The research focuses on the active correction of Ground to Space laser beams (optical links and artificial stars), as downlink communications resemble conventional astronomical observations when applying Adaptive Optics techniques: the light is originated in space and it travels downwards through the atmosphere to the receiver (where the AO system would be placed), whereas the uplink needs to be corrected before existing the launching telescope by measuring the atmospheric wavefront with an a-priori unknown reference source. The uplink pre-compensation entails a scientific and technological challenge.

The uplink correction problem was deeply studied by the formulation of all possible solutions, which are properly modelled and simulated with an already existing Adaptive Optics Matlab toolbox, into which new functionalities were coded and integrated (upwards Fresnel propagation, new concept wavefront sensor, etc.). Based on the simulation outcome, the corresponding requirements were formulated for the design of an uplink corrector AO system from the very last element to the control strategy. After the proper hardware acquisition (of both COTS elements and custom-built components), the uplink corrector laboratory scale prototype was built and integrated at IAC laboratory facilities. Finally from January 2019 to May 2019, the Uplink Wavefront Corrector System was integrated at the Optical Ground Station telescope at Teide Observatory, successfully demonstrating the uplink precompensation of the laser beam.

1.2.1   Chapter 2

Chapter 2 presents a summary of all theoretical concepts necessary to fully understand the carried-on research: the basics of the atmospheric turbulence and its effects on optical communication links; the fundamentals of the Adaptive Optics systems and Laser Guide Star generation; as well as an introduction to a novel concept wavefront sensor: the plenoptic camera. The chapter concludes with the proposal of an Adaptive Optics system for the uplink correction.

1.2.2 Chapter 3

Chapter 3 gathers the modelling of the uplink and its pre-compensation by an AO system, together with the simulated outcome of the possible solutions to handle the arisen difficulties (point-ahead angle, tip-tilt retrieval, etc.). This chapter raises the pillar of the proposed, designed and built Uplink Wavefront Corrector System.

1.2.3 Chapter 4

Chapter4 defines the Uplink Wavefront Corrector System design, from initial considerations to final design decisions. The chapter starts with the assessment of the optimal telescope optical configuration as it is a driver for the whole optical design; after that, the chapter is divided into the main subsystems of the Uplink Wavefront Corrector System.

1.2.4 Chapter 5

Chapter 5 describes the simulation test bench for the Uplink Wavefront Corrector System, designed with the purpose of characterising the maximum number of subsystems to the possible extent at laboratory scale.

1.2.5 Chapter 6

Chapter 6 demonstrates on-sky the feasibility of the plenoptic wavefront sensor as a novel concept for atmospheric turbulence sensing, which offers several advantages in comparison to conventional Shack-Hartmann wavefront sensors.

1.2.6 Chapter 7

Chapter 7 presents the on-sky validation of the Uplink Wavefront Corrector System, from its integration at the Optical Ground Station telescope (Teide Observatory) to the validation of the uplink correction in an upwards propagated laser beam in closed-loop operation.

1.2.7 Conclusions

Chapter 8 summarises the conclusions that have been reached during the development of the research presented in this thesis.

1.2.8 Appendix A

Appendix A describes the potential of the plenoptic wavefront sensor for solar Adaptive Optics; a plenoptic camera is installed in the VTT solar telescope at the Teide Observatory and the resultant conclusions are presented. Furthermore, the plenoptic camera is modelled and simulated in a multi-conjugated adaptive optics system for solar atmospheric correction.

1.2.9 Appendix B

Appendix B summarises a collaboration stay at the Advanced Instrumentation and Technology Centre in the Australian National University (Stromlo Observatory, Canberra) for the Assembly, Integration and Verification tasks of the Adaptive Optics Demonstrator, an instrument also involving uplink pre-compensation of a laser beam.

Chapter 2

Theoretical Background

2.1 Introduction

A Free-Space Optical communication system consists of a line-of-sight technology which transmits a modulated laser beam through the medium for broadband communications, performed from satellite to satellite, from satellite to aircraft/drone and vice versa, from ground to ground, or from satellite to ground and vice versa (Raj, Selvi, and Raghavan, 2010). The research described in this thesis will handle the last scenario: satellite-ground and ground-satellite FSO communications, known from now on as downlink and uplink, respectively.

FSO systems used to work near the 850 nm spectral range, although 1550 nm has been selected as a common wavelength for ultra high speed optical links, due to the continuous pursuit of bandwidth increase: optical devices using the 850nm spectral range cannot operate above 2.5Gbps, on account of the power limitations imposed for eye safety, and of the larger influence of the solar background radiation on their performance (Jasmine, Robinson, and Malaisamy, 2015). In case of bi-directional links, it is common to have different wavelengths for downlink and uplink (Kaushal and Kaddoum, 2017).

Optical communications systems use highly coherent modulation schemes because they provide higher sensitivity, longer relay distance, larger communications capacity and better receiver selectivity, in comparison to systems using intensity modulation direct detection. However, coherent modulation is vulnerable to the atmospheric turbulence, since wavefront and amplitude of laser carrier signal are distorted by this turbulence with time in the free space (Cao et al., 2017). While propagating through the atmosphere, the laser beam experiences several effects along its transmission path due to random refractive index fluctuations in the atmosphere itself (consequence of inhomogeneities in the temperature and pressure) causing the deterioration of the received signal quality, which undergoes fluctuations in both intensity and phase, impairing the link performance. Atmospheric propagation effects cause the FSO channel to be highly variable with a rate of change as high as 1 kHz and with power fades greater than 10 dB (Nader M. Namazi, 2006).

This chapter describes all theoretical concepts necessary to understand the proposed solution to improve the FSO links by correcting the atmosphere influence on them.

2.2 Atmospheric Turbulence

The atmosphere is a very dynamic system which is usually divided into a number of layers depending on its mean temperature profile: the lowest layer, the troposphere,

extends from the Earth surface up to 10 or 12 km; in it, the temperature of the non-stable air decreases steadily with altitude causing a turbulent mixing.

The atmospheric turbulence is a consequence of small-scale spatial and temporal variations in air temperature causing fluctuations in the atmospheric refractive index (Eq. 2.1); these fluctuations can be modelled according to Kolmogorov law (Eq. 2.2).

$$n(h) = E[n(h)] + n_1(h) \tag{2.1}$$

Where $E[]$ represents the ensemble averaging, n_1 is the refractive index fluctuation with $E[n_1(h)] = 0$, and $E[n(h)] \approx 1$ for the atmosphere.

$$D_n(h) = E[|n_1(h + h(0)) - n_1(h(0))|^2] = C_N^2 h^{2/3} \tag{2.2}$$

Where $D_n(h)$ is the structure function of the refraction index, and the structure constant C_N^2 represents the turbulence strength, whose typical values are contained within the range from 10^{-17} (weak turbulence) to 10^{-13} (strong turbulence); the relation between the structure function of the refraction index and the turbulence strength is known as the Kolmogorov's energy spectrum function (S. Shaik, 1988).

The effect of the atmospheric turbulence is usually quantified by measuring the wavefront phase, a bi-dimensional map associated to the imaging system pupil and produced while the light propagates through the medium (Tyson, 1991). The wavefront phase results from considering the light propagation like a scalar field depending on spatial and temporal coordinates (Goodman, 1996); it is presented in Eq. 2.3.

$$u(P, t) = A(P) \cos 2\pi v t + \phi(P) \tag{2.3}$$

Where P is the position, v is the frequency, and $A(P)$ and $\phi(P)$ represent the amplitude and phase, respectively, related to this spatial position. It is the phase component the one which mostly determines the light propagation through an optical system (the amplitude component has some implications at much lower orders) and so it is the wavefront phase, the magnitude of interest to extract the atmospheric turbulence from.

2.2.1 Isoplanatic Angle

The isoplanatic angle delimits an angular patch up on the sky within which the degree of correlation between the complex amplitudes of the light travelling through two corresponding angular locations, falls to a suitable threshold value, such as 0.5 (Stewart McKechnie, 2015). Glindemann (2011) defines the isoplanatic angle such that the rms phase difference between two points at ζ and at $\zeta - \theta h$ is 1 rad. Isoplanatic angles are determined mainly by atmospheric turbulence at intermediate and higher altitudes. One considers two well-separated light waves (i.e. binary stars) travelling towards the telescope, those two waves will tend to pass through separated turbulence structures, which will cause a decorrelation between the resulting aberration on both stars and will impose a limit on the isoplanatic angle; however, if the same light waves travelled through lower altitudes, the turbulence structure would be the same and, therefore, aberrations would be basically equal.

The isoplanatic angle, described in detail in Tyson (1991) is defined in Eq. 2.4.

$$\theta_0 = [2.91 k^2 \int_{path}^{L} C_N^2(h) h^{5/3}]^{-3/5} \tag{2.4}$$

Where k is the wavenumber ($k = 2\pi/\lambda$), L is the propagation path length and h is the distance at which each turbulence layer is located.

Andrews and Phillips (2005) defines the special case of the isoplanatic angle for an upwards-propagating Gaussian spherical beam wave (Eq. 2.5).

$$\theta_0 = \frac{cos^{8/5}(\zeta)}{[2.91k^2 \int_{h_0}^{H} C_N^2(h)(h-h_0)^{5/3}dh]^{3/5}} \tag{2.5}$$

Where h_0 is the height above ground level of the uplink transmitter and $H = h_0 + Lcos(\zeta)$ is the satellite altitude at zenith angle ζ.

Following the example of the binary star, the optical communication link travelling from one satellite to one ground station may suffer different turbulence conditions than the one travelling from the same location on Earth to the same satellite due to the point-ahead angle (angular difference between the location at time t when the laser beam is propagated from Earth and the satellite location at time $t + dt$, when the the laser is received by the satellite terminal, see Section 2.3 for further detail). The relationship between the isoplanatic angle on a specific location and the difference between the point angle of the downlink and the uplink, has been studied and simulated in Chapter 3 in order to know whether one link could be corrected with the wavefront measurements on the other one (with the possible use of a predictive controller) or, on the contrary, some additional mechanism would be necessary to quantify and reduce the atmospheric influence, such as a Laser Guide Star launched to the sky location where the uplink will take place.

2.3 Optical Communications in Turbulence Media

The atmosphere can be thought of as a medium into which energy is injected in the form of thermally induced convection or wind shear. The upper scale at which this energy is dissipated is known as the *outer atmospheric scale*, commonly designated as L_0 and representative of the largest size eddies involved in its flow, that upon reaching a critical point, break down to smaller scales by a cascading process until an inner scale size l_0 is reached (Hemmati, 2006).

Considering a laser source placed in the deep space that spreads to hundreds or thousands of kilometres, its beam width exceeds by far the atmospheric characteristic spatial scales, which are in the range of a few tens of meters, therefore all the atmospheric eddies will be smaller and the main effects induced by them on the downlink will be those related to this situation: beam broadening, scintillation and loss of spatial coherence. However, an upward propagating laser, originated from an optical ground station and transmitted to space, will imply a beam width within the inertial range of the atmosphere (the scale size bounded by the outer scale L_0 and the inner scale l_0 is referred to as the inertial scale, and it typically ranges from 10–100 m (L_0) to 0.1–1 cm (l_0)). As a consequence, the uplink will be mostly affected by large angular displacements: beam wander and fluctuations in the angle-of-arrival (Hemmati, 2006). However, in case of using relatively big launching telescopes, scintillation effects will also be detected in the uplink beam (Guo et al., 2010).

2.3.1 Satellite Pointing Angles

The pointing and tracking systems become the keys to success in FSO communication links; as the wavefront sensor to measure the atmospheric turbulence will be

placed on the same axis than the optical links used to perform the communications, the pointing angles (also known as look angles) are the ones of interest.

From the ground station point of view (Figure 2.1), the position of a satellite within its orbit is defined by the look angles: azimuth and elevation; the azimuth is the angle of the direction of a satellite, measured in the horizon plane (a tangent plane to the surface of the Earth at observer's position), from geographical North in clockwise direction (from $0°$ to $360°$); and the elevation is the angle between a satellite and the ground station horizon plane (from $0°$ to $90°$).

A geostationary satellite is characterized by a circular geosynchronous orbit in the plane of the Earth's equator with a radius of approximately 42164km measured from the center of the Earth. With GEO satellites, the look angles to point the emitter (in case of uplink) or the receiver (in case of downlink) of the ground station only need to be adjusted once as the satellite will remain in a given position permanently. However, in order to propagate a laser beam to the spacecraft (uplink), the speed of light needs to be taken into account as well as the time it gets to reach the satellite from the Earth; a laser beam projected from a ground station must point ahead of the object by an angle of $2v/c$. where c is the speed of light and v, the orbital speed (Parenti, 1992).
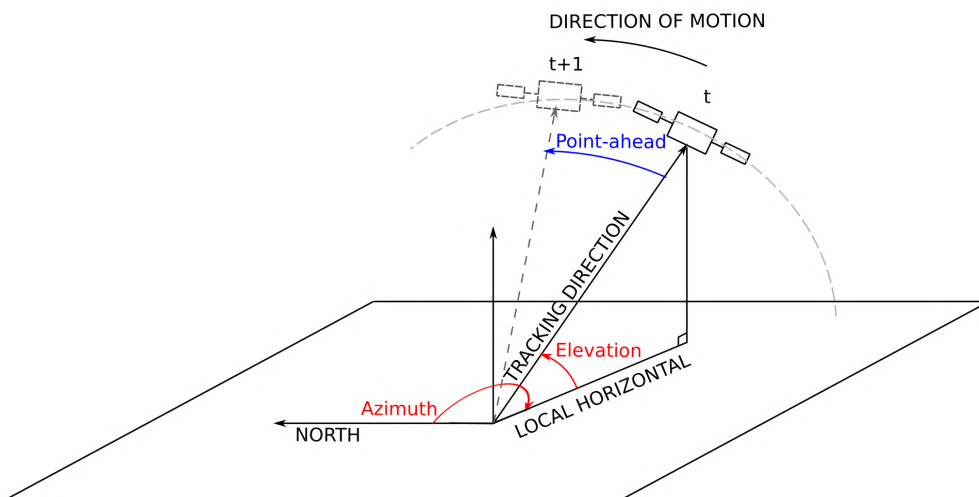
FIGURE 2.1: Engagement geometry for propagating a laser beam to a satellite.

GEO satellites move with an orbital velocity (v) of approximately 3.07 km/s; therefore, its point-ahead angle would be around $20\mu rad$ (4 arcsec), whereas satellites in Low Earth Orbit (LEO) would vary their velocity depending on their altitude: the International Space Station (ISS) is considered the study case at an altitude of around 400 km and orbital speed of 7.668 km/s, implying a point-ahead angle of 10.5 arcsec.

This pointing geometry will have severe implications over the uplink corrector design as it will be critical for the selection of a reference source to measure the wavefront aberrations on the propagation path.

2.4 Adaptive Optics

Adaptive Optics (AO) systems measure the atmospheric wavefront either at the telescope aperture or at certain heights above it, and command one or several deformable mirrors to correct the detected aberrations, with the purpose of improving the quality of the acquired data.

Adaptive Optics was first proposed by Babcock (1953), although it did not become feasible until the advances in computer technology at the end of the eighties (Hardy, 1998).

The typical configuration of a closed-loop adaptive optics imaging system is shown in Figure 2.2, whose main elements are the wavefront sensor (WFS), the deformable mirror (DM) and the control computer which performs real-time calculations. The basic operation of the system is as follows: light from the astronomical object or the satellite is captured by the telescope and its optics; afterwards, it is divided into two paths, one to be sampled by the WFS and the other to the imaging system (a science camera). The control electronics computes and sends the necessary corrections to be carried out by the deformable mirror, which finally corrects the image. The sharper image is sent back to the science instrument.
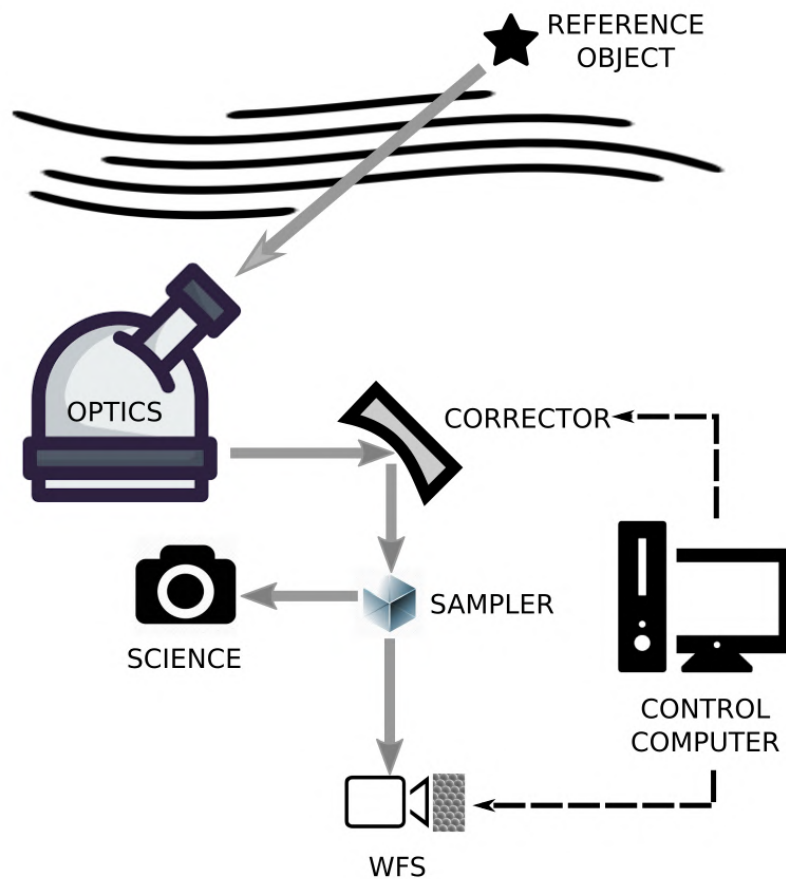
FIGURE 2.2: Typical AO system configuration.

2.4.1 Laser Guide Stars

Laser Guide Stars (LGSs) are artificial references for the adaptive optics systems, which are used to cope with the lack of natural stars up on the area of interest. They are produced by laser beams projected to the atmosphere to create focused spots of light as if they were a natural point-source. There are two common types of LGSs: Rayleigh guide stars which consist of pulsed lasers that take advantage of the Rayleigh backscattering from air molecules produced at altitudes up to around 20km; and Sodium guide stars, tuned lasers which produce an output wavelength of 589nm and a focused beam at altitudes of 90 km by exciting the sodium atoms existing at this layer.

Figure 2.3 shows the Na-LGS launched at Observatorio del Teide (Tenerife) during the ESO-Wendelstein-Laser campaign in March 2015.

FIGURE 2.3: LGS at Observatorio del Teide during ESO-Laser Campaign in March 2015. Copyright: Daniel López (IAC).

As LGSs are projected upwards in the atmosphere and their light travels downwards towards the telescope, the laser is deflected twice through nearly the same path but in different direction. Therefore, tip and tilt compensate almost completely, creating a quasi-stable LGS image in the telescope focal plane (a fast steering mirror is still necessary to correct for the TT fraction induced by the slight difference in the optical path of the upwards and the downwards propagated beam, as launch and receiver aperture have usually different sizes); consequently, the atmospheric TT cannot be retrieved from the Laser Guide Star. Current AO systems use Natural Guide Stars to solve this problem, although this research proposes a novel solution

still in low Technology Readiness Level (TRL), which needs to be further investigated (see Section 3.5).

2.4.2 Wavefront Sensing

Once the necessary reference on the sky has been found, it is essential to have the proper instrumentation to measure and quantify the atmospheric phase at a time instant t. Wavefront sensing is the first step in the atmospheric turbulence correction.

There are two different approaches to sense the atmospheric aberrations; both will try to obtain the Optical Path Difference (OPD) function of the wave, although the direct methodology measures the pupil OPD directly, performing an explicit determination of the phase whose non-desirable components will be corrected by using this information. Some examples of this sensor type are the Point Diffraction Interferometer (PDI) Wavefront Sensor and the Radial Shear Interferometer Wavefront Sensor (Tyson, 1991). Otherwise, the indirect wavefront sensors measure either local slope (dW/dy or dW/dx) or differential wavefront (dW) as a function of pupil coordinates (Tyson, 2000), and instead of using the explicit information of the phase, they translate it into signals which will be used to compensate the wavefront itself. This methodology is the one that rules sensors as the Shack-Hartmann Wavefront Sensor, the Pyramid Wavefront Sensor or the Plenoptic Wavefront Sensor (see next Section 2.5).

2.4.3 Predictive Control in Adaptive Optics

The predictive control consists of levering a dynamic model of the atmosphere to estimate its next state based not only on the wavefront measurement, but also on the model. Since 1997, predictive control has been used in AO to optimize the unavoidable delay between measurement and correction (Hardy, 1998).

One of the most well-known control algorithms, the Linear Quadratic Gaussian Control (with Kalman filter as a predictor) has been successfully tested in laboratory (Petit et al., 2009) and on-sky (Correia et al., 2015) within currently working AO systems.

Predictive control is mostly thought for time-related estimations and not space-related predictions, although its use to compensate for tip/tilt anisoplanatism has also been studied (Flicker and Rigaut, 2002), and it could be also analysed in case of the anisoplanatism between two optical links separated by a point-ahead angle, if there were enough correlation between the atmospheric turbulence on each of the communication directions (downlink and uplink).

2.5 Plenoptic Technology

Plenoptic technology is introduced in this with the aim of gathering all fundamentals to understand the operation of the plenoptic camera and its functionality as wavefront sensor within an Adaptive Optics system for astronomical observations and from now on, also for optical communications.

2.5.1 The Plenoptic Function and the Light Field

The fundamental concepts in the field of plenoptics are the *plenoptic function* and the *light field* which will be reviewed to obtain a global understanding of the whole technology.

The study of the light has been explored for centuries: since Ibn al-Haytham's "Book of Optics", published sometime between 1028 and 1038 back in the 11th century, and the Leonardo da Vinci's notebooks in the 15th century, but it was not before the nineties when a ray-based model of light encompassing all perceivable properties was proposed: the plenoptic function (Adelson and Bergen, 1991).

Consider a pinhole camera. Each sample on the sensor plane is a ray passing through the pinhole propagating in a different direction, but at a fixed position in space. The recorded image is a 2D subset of all light rays in the scene; the full set is a 7D function that models the directional light distribution at all possible positions in a 3D space (Adelson and Bergen, 1991). The seven dimensions of this function, denoted by $P(\theta, \phi, \lambda, t, P_x, P_y, P_z)$ where (θ, ϕ) are the incidence angles of the light ray over the pinhole of coordinates (P_x, P_y, P_z), are simplified without the variables t, time, and λ, wavelength of the incident light. The rays involved in the plenoptic function can be parametrized in different ways. Figure 2.4 shows two of these parametrizations.

(a) By Angular coordinates   (b) By Cartesian coordinates
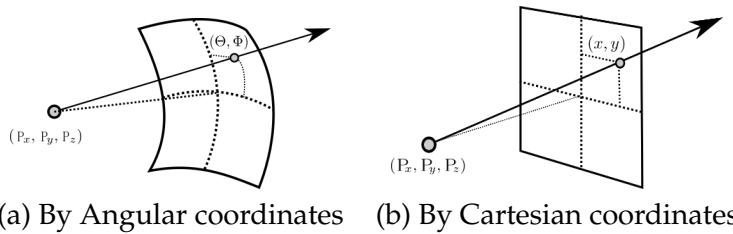
FIGURE 2.4: Parametrizations of the plenoptic function (Lüke, 2014).

As stated by Adelson and Bergen (Adelson and Bergen, 1991), the plenoptic function is an ideal concept and it is not possible to completely specify it for a real scene because the light travelling through all the points in the space, in every direction, in every time instant and within all the spectrum is not measurable. However, the plenoptic function can be seen as the basis for three-dimensional computer vision techniques, as most of passive 3D vision methods employ a subset of the information contained in the plenoptic function data (i.e. stero-vision techniques, depth from focus or depth from video). The plenoptic function is the link between the objects of a scene and their images. Structures in the plenoptic function are related to the geometry of the objects and to the optical properties of their materials. Extracting and identifying these structures in a sampled version of the plenoptic function, allows to extract geometric features of the objects. This idea was also introduced by Adelson and Bergen in their definition of the early vision periodic tables.

The 5D representation of the plenoptic function can be further reduced by assuming that the radiance of light rays does not change along their paths in free space, therefore a 4D slice of the plenoptic function fully describes the spatio-angular light variation in free space. This 4D set of rays is known in computer graphics as the *light field* (Gortler et al., 1996) (Levoy and Hanrahan, 1996), although the term was previously coined by Gershun (1939). It is possible to have information about the position of any point in the space while the structure generating it in the 3D plenoptic space is known and detectable (Berent and Dragotti, 2007). However, the functionality of interest in the plenoptic technology is its capacity of generating aperture images (in an optics system, i.e. a telescope) from different viewpoints, capability that also allows the direct estimation of the wavefront gradients in this area.

2.5.2 Plenoptics Wavefront Sensing

One important application of the plenoptic camera is its use as a wavefront sensor for astronomical measurements; this utilization was first described by Clare and Lane (2005) for the case of point sources and recently it has been analysed by the AO group at Instituto de Astrofísica de Canarias and Universidad de La Laguna (J. M. Rodríguez-Ramos, 2008) (Rodriguez Ramos et al., 2009) (Rodríguez-Ramos et al., 2010) (Montilla et al., 2010) (Rodriguez Ramos et al., 2012), who have also studied the possibility of computing the tomography of the atmospheric turbulence and the height variations of Laser Guide Stars beacons.

In 2015, Rodríguez Ramos (2015) proved the capabilities of the plenoptic camera as wavefront sensor: it was demonstrated its capability to measure the wavefront gradients in the system aperture.

Gradient Wavefront Reconstruction

When placing the plenoptic camera at the telescope focal plane (Figure 2.5), it generates pupil images from as many different viewpoints as microlenses building the array, which can be processed to generate the aperture images associated to each viewpoint direction and by computing their relative displacement, estimate the wavefront slope.
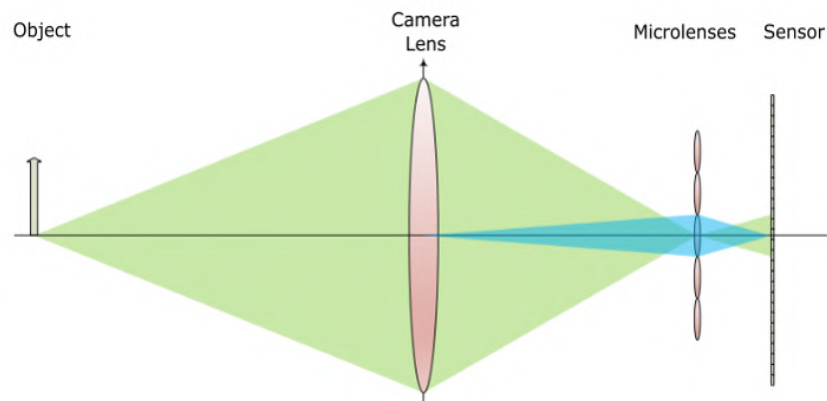
FIGURE 2.5: Optical schematics of the plenoptic camera. The plenoptic WFS gathers both spatial and angular information in the same frame; in green, the object image and in blue, the aperture reimagination by the central microlens as example (Rodríguez Ramos, 2015).

Figure 2.6 shows the image synthesis process: by extracting every pixel at position p inside each of the microlenses and reordering them by considering the position of the microlens where they are coming from, pupil image p is created; likewise, repeating the procedure with all the pixels at position $p + n$, pupil images $p + n$ are generated. Each of these synthesised pupil images corresponds to an equivalent Shack-Hartmann subaperture, fact that allows to make profit of all available techniques for the Shack-Hartmann sensor. Once the subaperture images are extracted, the lateral displacements among them will be used to calculate the local slopes and this information will grant the wavefront extraction after a global integration.
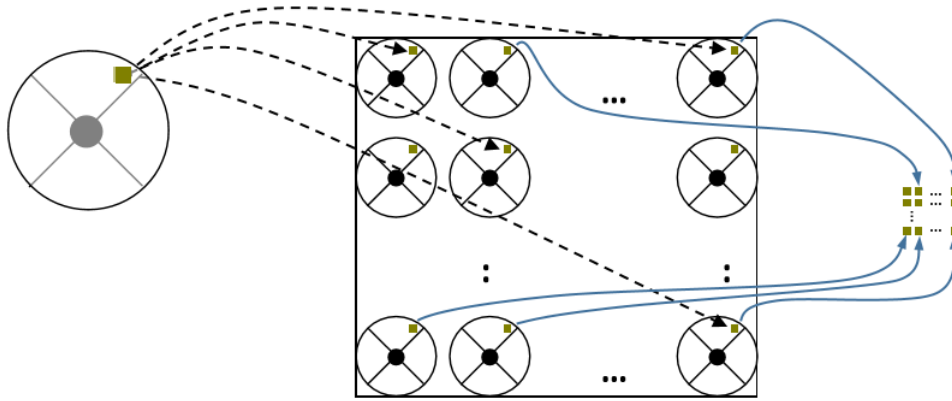
FIGURE 2.6: Subaperture image reconstruction. Left, aperture image of the telescope pupil; centre, plenoptic image on the sensor; right, procedure to synthesise the subaperture image corresponding to green viewpoint (Rodríguez Ramos, 2015).

The wavefront reconstruction from the gradients is performed by following the procedure in (Roddier and Roddier, 1991), which consists of the mathematical development in the Fourier domain of the wavefront (Eq. 2.6).

$$\phi(u_1, u_2) = FFT^{-1}(\alpha_{pq})$$ (2.6)

Where p and q are the vertical and horizontal spatial frequencies, and $\phi(u_1, u_2)$ is the aperture phase. The coefficients to minimise the mean square error are calculated by Eq. 2.7.

$$\alpha_{pq} = \frac{ipFFT[S^x(u_1, u_2)] + iqFFT[S^x(u_1, u_2)]}{p^2 + q^2}$$ (2.7)

Comparison to Conventional Wavefront Sensors

With the purpose of further illustrating the use of the plenoptic camera as wavefront sensor, it needs to be compared to the most conventional sensors in Adaptive Optics systems: the Shack-Hartmann wavefront sensor (SH-WFS) and the Pyramid wavefront sensor (PY-WFS).

Similar to the plenoptic camera, the SH-WFS consists of a detector and a lenslet array located at the pupil plane (instead of at the telescope focus plane in the plenoptic WFS case); this lenslet array re-imagines the telescope pupil image onto the detector, creating as many sub-pupils as microlenses in the array. Due to the atmospheric wavefront, the pupil images move from their nominal position in a regular grid (defined by the array geometry) when the wavefront is plane, to new positions in the two orthogonal directions (x, y). The centroids (x, y) displacements are proportional to the (x, y) wavefront slopes at each subaperture (Figure 2.7). Two of the main limitations of the SH-WFS, with respect to the plenoptic WFS, are caused by its optical design: on one hand, if the reference source suffers from large displacements due to strong turbulence conditions, the centroid will disappear from the subaperture; and on the other hand, if the image in the pupil focal plane is elongated (LGS elongation), it will be clipped by the subaperture and the slopes computation will be affected. In terms of flexibility and simplicity, the SH-WFS does not allow changes in the pupil sampling without changing the microlens array, whereas in the plenoptic camera,
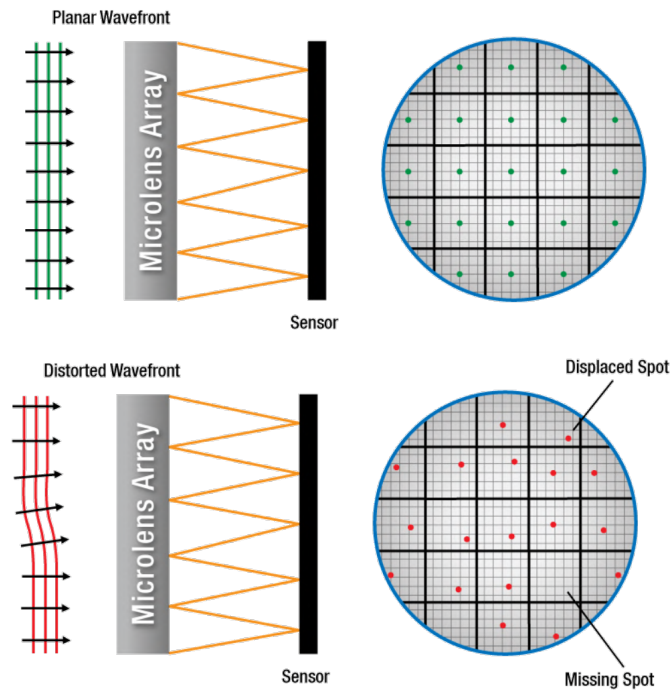
FIGURE 2.7: Shack-Hartamann wavefront sensor working principle.
Images from (*Shack-Hartmann Wavefront Sensors*).

one could perform later pixel recombination with the same lenslets; finally, the optical integration of the Shack-Hartmann in a set-up, implies one additional lens to collimate the incoming beam, while on the contrary, the plenoptic WFS works at the focus plane. Ko and Davis (2017) analyses the performance of a SH-WFS and a plenoptic camera when distributing the light among similar number of pixels at each sensor, achieving sensitivities of $0.293mrad$ in the SH-WFS and $0.297mrad$ in the plenoptic camera; therefore, the sensitivity is similar in both. However, the plenoptic camera is demonstrated to perform better in scenarios of strong turbulence, in which the Shack-Hartmann would present subapertures with multiple focal spots or intensity null (Ko and Davis, 2017). Rodríguez Ramos (2015) tested the simultaneous operation of a SH-WFS and a plenoptic camera on sky, accomplishing high correlation indexes between both wavefront measurements.

Another more and more commonly used sensor is the Pyramid wavefront sensor, which consists of placing a pyramid in the focal plane, which divides the stellar light into four parts, creating four images of the telescope pupil at the detector (Figure 2.8). The normalized intensity differences among the images, are proportional to the wavefront slopes in the two directions. Regarding large displacements and extended sources, the pyramid wavefront sensor gets saturated, when the atmospheric turbulence causes large displacements in the source, and its response becomes nonlinear as the slope in one (or both) of the directions cannot longer be estimated; concerning the elongation, the use of the PY-WFS with extended sources is possible but it has an impact on the wavefront sensor sensitivity as the source image on the pyramid tip will always be bigger than the diffraction limit. Both disadvantages can be solved by introducing certain modulation to make the image rotate over the pyramid in synchronised operation with the camera acquisition, introducing further

complexity in the system. Besides the modulation add-on difficulties, the optical design of the PY-WFS is also more complicated with respect to the plenoptic WFS, as, in addition to the pyramid itself, it also needs a relay lens. No quantitative comparison has been found regarding the plenoptic camera and the pyramid wavefront sensor; therefore, the author remarks the interest of performing simultaneous wavefront measurements with the plenoptic camera and the pyramid, in order to get better knowledge of the advantages and disadvantages of the first one over the last one, as, due to time constraints, it could not be covered within this thesis.
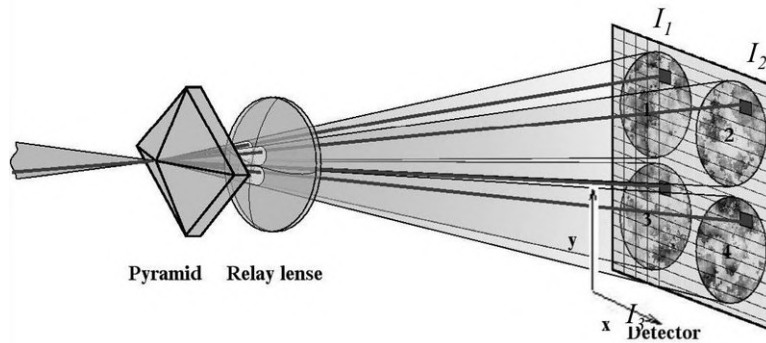
FIGURE 2.8: Pyramid wavefront sensor working principle (Ragazzoni, 1996).

When using point sources as sensing reference, the only drawback of the plenoptic camera (in comparison to both SH-WFS and PY-WFS) is the need of the source to be extended over more than one microlens, otherwise, no slope computation could be performed. This issue is solved by locating the plenoptic camera slightly out-of-focus, defocusing on-purpose the pupil image. This small defocus will be later-on corrected by the deformable mirror.

Table 2.3 gathers the main features comparison of the plenoptic WFS with both Shack-Hartmann and Pyramid WFS.

	Plenoptic WFS	**Shack-Hartmann**	**Pyramid WFS**
Large Displacement	No limitation	Saturation	High Saturation
Extended Objects	No limitation	Anisoplanatism	Modulation
Point Source	Added defocus	No limitation	No limitation
Sampling Flexibility	Later pixel recombination	Array change	Modulation
System simplicity	Microlenses at the telescope focal plane	+1 Lens for aperture image	Pyramid itself +1 Lens

TABLE 2.3: Comparison of the plenoptic camera to conventional wavefront sensors.

2.6   Adaptive Optics for Optical Links and Beam Shaping

By applying AO techniques to the optical communications links, beam wavefront aberrations are suppressed to the possible extent; Wilson et al. (2004) and Hemmati (2006) demonstrated through simulations up to a 6dB improvement in SNR when

using adaptive optics in daytime with high background environment for downlink communications.

There are some references in literature about correcting atmospheric turbulence on optical communication links, although most of them try to minimize its effect by modelling statistically the aberrations in a way that the beam receptor has some predefined information in order to reduce data loss when the fading occurs (Zhu and Kahn, 2002) (Zhu and Kahn, 2003) (Cole and Kiasaleh, 2004) (Toyoshima, Takenaka, and Takayama, 2011). Other studies (Abou-Rjeily and Slim, 2011) focus on reinforcing the communication by placing multiple receptor devices, which could compensate each other in case of link intensity loss, although the non-broadcast nature of the FSO links makes this option not the most suitable one, as one emitter shall be entirely dedicated to send the signal to the relay. Another research group (Luna et al., 2009) proposes the use of hybrid links: optical links operated together with RF.

All previous studies concentrate upon "static" corrections: either they formulate the expected response of the links through the atmosphere or they use a back-up solution in case of fading and data loss (multiple receptors or hybrid link) and thereby, the turbulence influence on the communication is reduced. However, they are not properly measuring atmospheric wavefront and correcting it "on-the-fly"; related to this idea, few examples can be found in bibliography: Raj, Selvi, and Raghavan (2010) presents one system that controls aligning, tracking and position of the laser beam in closed-loop by dividing the beam into two, one for measuring scintillation with a photo-diode and the other one for quantifying the variations in the angle-of-arrival. In the same line of dynamically correcting the atmosphere, Zepp (2013) and Feng, White, and Wilkinson (2013) analyse the possibility of using a holographic wavefront sensor within the FSOC systems.

Finally, Feng, White, and Wilkinson (2014) propose the utilization of a modal zernike wavefront sensor to measure and correct the aberrations in optical communications; the operation consisted of applying a positive and a negative bias to the input signal and by subtracting both outputs, the result was related to the amplitude of the modal content of the incoming wavefront, allowing aberration correction by phase conjugation method.

Additionally, related to laser beam correction (not necessarily FSOC), it is worth to mention the beam shaping techniques, which are not proper AO corrections of the laser, but pursue the optimization of the beam to be launched with static alterations on both amplitude and phase of the laser, the so-called 2-DM concept: two deformable mirrors are introduced in the laser launch path to compensate for the static aberrations the beam could suffer before existing the telescope. The first approach to the 2-DM concept was proposed by Kanev and Lukin (1991) and further study since then by several researchers in the AO community (Guesalaga et al., 2012), (Béchet et al., 2014), (Escarate et al., 2017), (Wu et al., 2018).

2.7   Uplink Wavefront Corrector System. The Proposal

FSO links from ground to space and vice versa use the atmosphere as the communication channel. If this channel were ideal, the transmitted data would reach the receiver at maximum rate; hence, the more the atmosphere looks like to an ideal media, the better the communication performance would be, and this one is the aim of the proposed Adaptive Optics system: characterising the channel as much as possible in order to use this information to extract the atmospheric contribution from the

links and make them propagating through a media as close as possible to the ideal case.

The Uplink Wavefront Corrector System is proposed as a proof-of-concept instrument to demonstrate the advantages of applying Adaptive Optics techniques to Earth-Satellites optical communications, or the so-called upwards propagation path of a laser beam, and furthermore, to the Laser Guide Star generation by creating more focused and hence, brighter spots in the Na layer or in the upper parts of the atmosphere. This goal will be achieved by the uplink atmospheric pre-compensation of the laser beam.

The Uplink Wavefront Corrector System will consist of an Adaptive Optics system which will introduce on-purpose added aberrations onto the laser by creating certain shapes in a deformable mirror; those shapes will depend on the atmospheric turbulence which will have been previously measured by a plenoptic camera. The research in this thesis becomes a novel understanding of the Adaptive Optics systems themselves, opening up a vast field of new applications for AO.

Chapter 3

Computer Simulations

3.1 Introduction

Several types of simulation procedures were developed in order to check three main features which will have crucial implications on the AO system design for the up-link correction. Firstly, some simple simulations were carried out to know whether both communication links (downwards and upwards propagation) would be inside the isoplanatic area (isoplanatic simulation) or not; it was necessary to justify the use of a LGS propagated to the uplink expected location in contrast to the use of the downlink signal itself as a reference source; secondly, a more complex methodology was built to get knowledge of the uplink correction performance after measuring the wavefront on the downlink or on the launched Laser Guide Star (closed-loop simulation). Lastly, a novel concept to retrieve the tip-tilt information from a Sodium Laser Guide Star was modelled and simulated with the aim of eliminating the dependence on natural guide stars when using LGSs as a reference for wavefront sensing.

Communication links have been emulated within the Object-Oriented Matlab Adaptive Optics (OOMAO) Toolbox by taking into account their expected location and the point-ahead angle between both, in such a way that the downlink has been simulated as a source at azimuth 0″ and zenith angle 0″, and the uplink as a source launched to azimuth 0″ but zenith angle equal to the point-ahead angle in GEO and LEO satellites (4″ and 10″, respectively for simulation purposes).

All simulations and derived results are presented in following sections.

3.2 System Modelling

The OOMAO simulator is a Matlab toolbox which has been developed by Conan and Correia (2014) with the aim of simulating the behaviour of a complete AO system [1]. As an object oriented software package, it is based on class objects: atmosphere class, telescope class, source class, wavefront sensor class, deformable mirror class and imager class. Each of them needs to be set up with the proper parameters in order to be as representative of the real situation as possible; then, they are combined to simulate a complete adaptive optics system

The telescope was modelled with the Optical Ground Station (OGS) optical parameters, using both available configurations (Ritchey-Chrétien and Coudé foci) and including the central obscuration (see Table 3.1).

---

[1]The OOMAO code can be downloaded from *https://github.com/cmcorreia/LAM-Public*.

Telescope Diameter	1m
Central Obstruction	28%
Optical configuration	Ritchey-Chrétien (RC) focus
	Coudé focus
Focal Length	RC - 13.3m
	Coudé - 39.9m
Field-of-view	2.5arcmin

TABLE 3.1: Optical Ground Station (OGS) telescope optical parameters

The "ogsAtmosphere" function has been defined, within the "atmosphere class" framework, with the purpose of binding all OT atmosphere types together. The atmospheric profiles were extracted from Teide Observatory nocturnal profiles (García-Lorenzo and Fuensalida, 2011) as well as from SHABAR measurements in case of diurnal analysis (Rosa, 2016) (Figure 3.1 and Figure 3.2).

Every data set has been integrated into the simulator by concentrating the overall atmosphere distribution in only four layers; therefore, the available C_n^2 values have been used to calculate the global Fried parameter (corresponding to the atmosphere type under study) as well as the fractional Fried parameters related to each atmospheric layer. Global Fried parameter, r_0, was computed with Eq. 3.1 and fractional Fried parameters, f_{r_0}, were calculated by the procedure described in (Conan, 2013) and summarised by Eq. 3.2.

$$r_0 = (0.423k^2 \int C_n^2(h)dh)^{-3/5}, \tag{3.1}$$

where k is the wavenumber $k = 2 * \pi / \lambda$.

$$f_{r_0} = \frac{C_n^2(h)\Delta h}{\int dh C_n^2(h)}, \tag{3.2}$$

Added to the simulator functionality, it was implemented the Fresnel propagation of a Gaussian beam from the emitter plane to the first atmospheric layer and from this layer to the next one until the upper bound (at approximately 10000m in this model), plus the phase change found at each of the layers (due to the atmosphere itself); the Fresnel propagation extends from the last atmospheric layer to the receiver location at around 38000 km for the GEO case and 400 km in the LEO scenario. Talanov scale transformation (Talanov, 1970) was imposed to fix a constant ratio between the beam size and the dimensions of the discretization grid. In all simulations, the receiver was placed at the geometrical focus of the beam.

The time behaviour was taken into account by moving each phase screen perpendicular to the beam in accordance with the wind velocity profile (also extracted from the OT atmospheric profiles). Every independent realization of the propagation channel implies a movement of each atmospheric screen at its corresponding wind direction and velocity (different values of wind properties depending on the layer height in the atmospheric profile which has been taken into account).

The plenoptic wavefront sensor was introduced as an additional wavefront sensor class in the OOMAO toolbox; its physics and functionalities were coded by following the established premises in the simulator, in a way it is fully accessible and embedded in the code to be used as an additional OOMAO class. The plenoptic
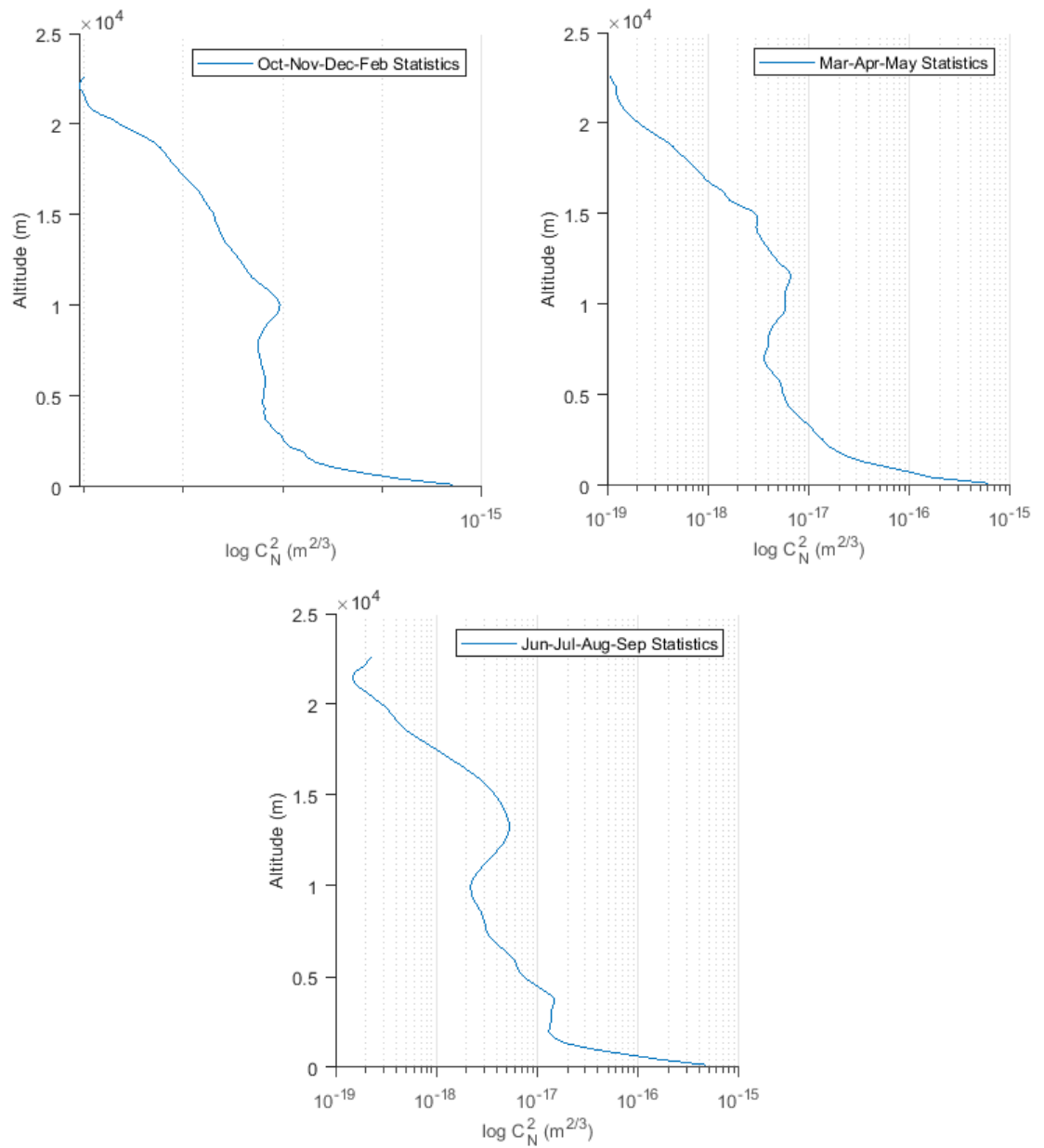
FIGURE 3.1: Average C_N^2 profiles obtained from the individual measurements at Teide Observatory (Spain) by SCIDAR instrument from 2002 November-2009 January (García-Lorenzo and Fuensalida, 2011). Statistics gathered taking into account seasonal changes.
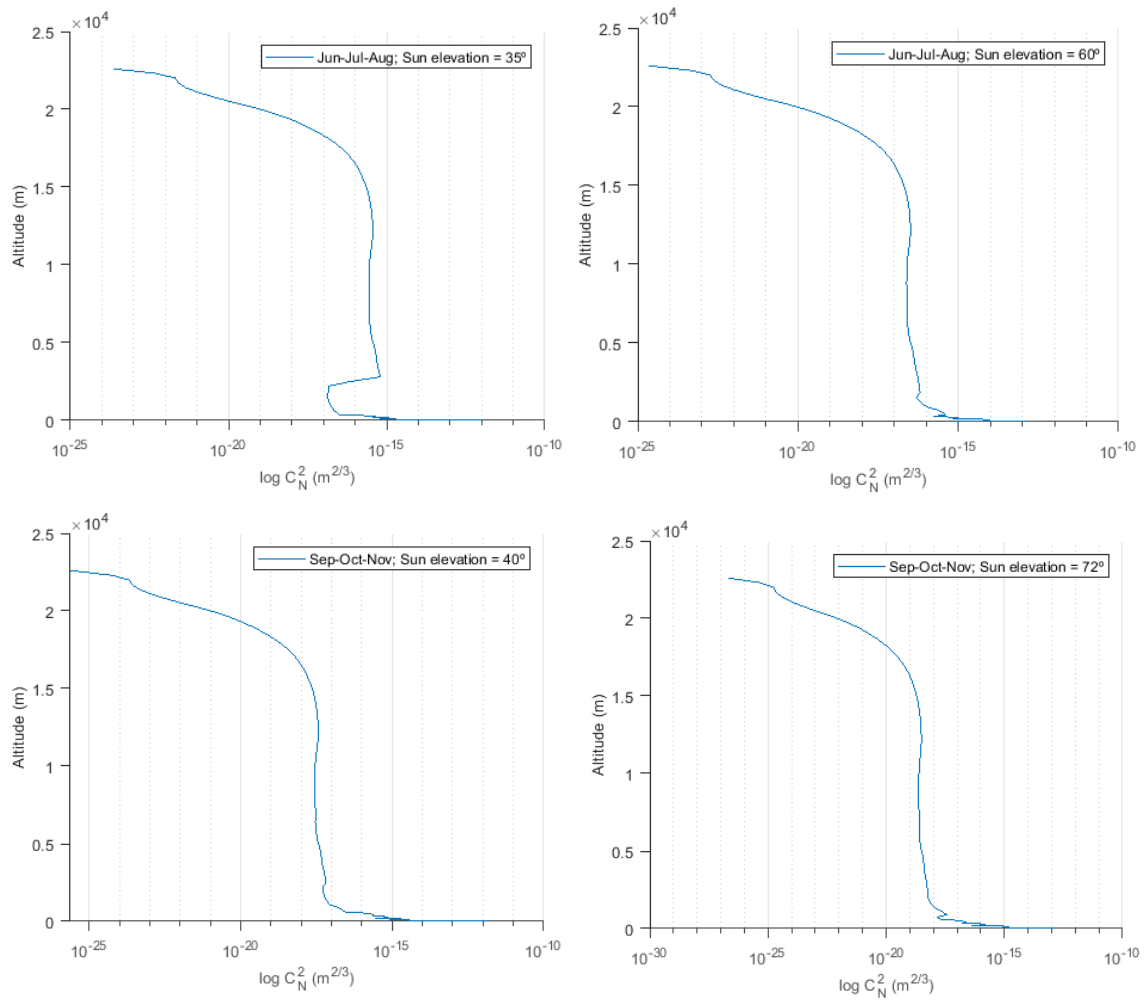
FIGURE 3.2: Average C_N^2 profiles obtained from the individual measurements at several Sun elevations by SHABBAR instrument during 2014 at Teide Observatory (Spain) (Rosa, 2016). Statistics gathered taking into account seasonal changes (data gaps between January and May).

WFS implementation into the OOMAO simulator was the outcome of a short collaboration stay at Laboratoire d'Astrophysique de Marseille (LAM), working hands-on with one of the authors.

3.2.1 Validation Metrics

The validity of the procedure and the simulation tool was proved by comparing the LEO intensity profile within the receiver plane to the simulated beam profiles gathered in C. Andrews et al. (2006). For this comparison, the beam intensity profile has been analysed using the same metrics: the W_0/r_0 ratio, where W_0 is the radius of the Gaussian beam and r_0 is the Fried parameter. Figure 3.3 shows the simulated intensity profiles which follow the same trend as the ones in C. Andrews et al. (2006) (in Figure 3.4 for comparison purposes): diffraction limit beam profile on the left, the predominant tilt when $W_0/r_0 \approx 1$ in the centre, and the beam distribution over the receiver plane when $W_0/r_0 >> 1$ on the right.

$$W_0/r_0 << 1 \qquad W_0/r_0 \approx 1 \qquad W_0/r_0 >> 1$$
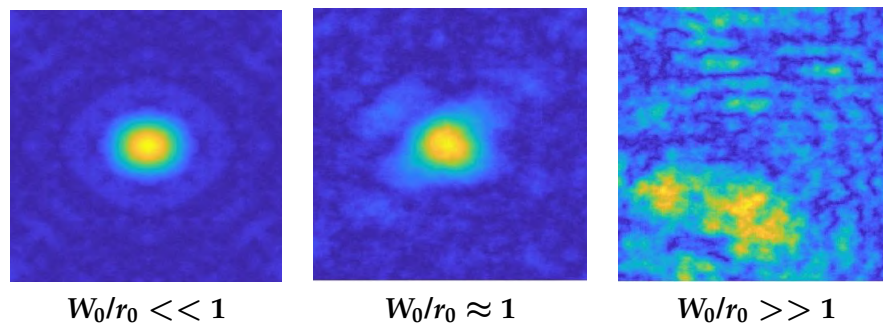
FIGURE 3.3: Uplink intensity profiles within the receiver plane at 400km. Notice the differences depending on the W_0/r_0 ratio: when this parameter is small $W_0/r_0 << 1$, the Gaussian beam shape is perfectly received; tilt effects are predominant when the ratio is close to one; and in case of strong turbulence ($W_0/r_0 >> 1$), the beam is distributed over the receiver plane.

$$W_0/r_0 << 1 \qquad W_0/r_0 = 1 \qquad W_0/r_0 >> 1$$
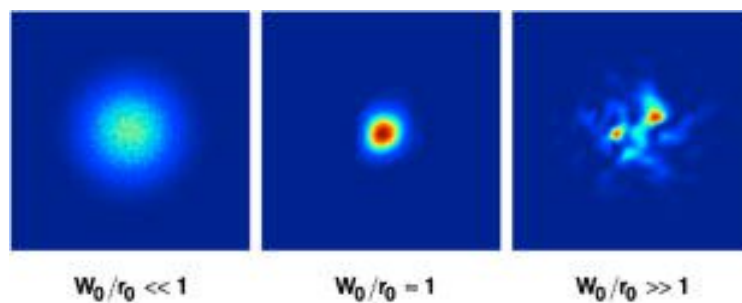
FIGURE 3.4: Beam intensity profiles, simulated based on the W_0/r_0 ratio by the wave propagation code, POPS, developed at Lincoln Laboratory. Figure extracted from (C. Andrews et al., 2006) for the method validation.

3.3   Isoplanatic Area at the OT

The analysis of the isoplanatic area at the Teide Observatory (OT) consisted of assessing whether each of the links (the uplink and the downlink, separated by the point-ahead angle) would suffer from similar atmospheric turbulence and therefore, one of them could be used as a reference source to correct the other one.

In order to achieve these conclusions, the wavefront of both sources was simulated with the available data (specific OT atmospheric profiles, telescope, sources) and checked whether each case study fulfilled the isoplanatic condition of 1rad as maximum root-mean square difference of the two wavefronts (the one suffered by the downlink and the one suffered by the uplink) (Glindemann, 2011).

Results were analysed by taking into account the main influencing variables on this study: solar time and season when the atmospherics profiles were acquired. Additionally, the inferred conclusions were evaluated under the premise of the point-ahead angle related to each orbit case.

Notice that all simulation scenarios were performed by placing the downlink at telescope zenith, and as it is well-known, this situation is the best one concerning the amount of turbulence; if the results are not satisfactory in this pointing direction, they will not be either at lower telescope elevations. The wavelengths for downlink and uplink laser were considered to be $\lambda_{down} = 1550nm$ and $\lambda_{up} = 1064nm$, respectively.

Simulation results are summarised in Fig. 3.5. The local daytime was proven to have a significant influence on the size of the isoplanatic patch: Figs. 3.5a and 3.5c (corresponding to nocturnal atmospheric measurements) show that, at the GEO point-ahead angle (4") distance, the border of the isoplanatic patch was almost reached, meaning that the uplink may be corrected by the wavefront measurement on the downlink and that correction may be good enough, although only when pointing directly to zenith, at any other elevation, the downlink signal would be outside the isoplanatic area. Teide Observatory is located at $28°17'60.00"N$ above the Equator (where the GEO satellite passes occur), hence, the OGS needs to be pointed at the corresponding angle to the satellite, and not at zenith. Furthermore, for the LEO case (10" point-ahead angle), both sources would be outside the isoplanatic area and correcting one with the incoming wavefront on the other one would introduce anisoplanatism errors; in conclusion, a Laser Guide Star, launched at the same direction as the uplink, would be the best way to measure the turbulence the uplink is exposed to.

Moreover, when dealing with diurnal links, the turbulence is much higher and concentrated at the ground layer, therefore, the isoplanatic patch becomes smaller. However, due to this strong ground layer, predictive control using the downlink wavefront information could be a possibility, which deserves further study and simulations, and opens up a future research line as, unfortunately, it cannot be covered in this thesis. Figures 3.5b and 3.5d show results of day-time simulations, pointing out the need of a LGS as a reference source for the uplink correction.

Seasonal changes were also analysed, although no big differences during the night were encountered as the OT location in the Canary Islands (Spain) has a quite stable temperature all year long. However, the difference becomes more noticeable in the case of diurnal links, as during summer, the Sun heats intensely the Earth's surface, whereas during winter, the ground does never get so hot.

The isoplanatic study conclusions remark the need of propagating a Laser Guide Star to the expected uplink location in order to perform an optimal uplink pre-compensation.
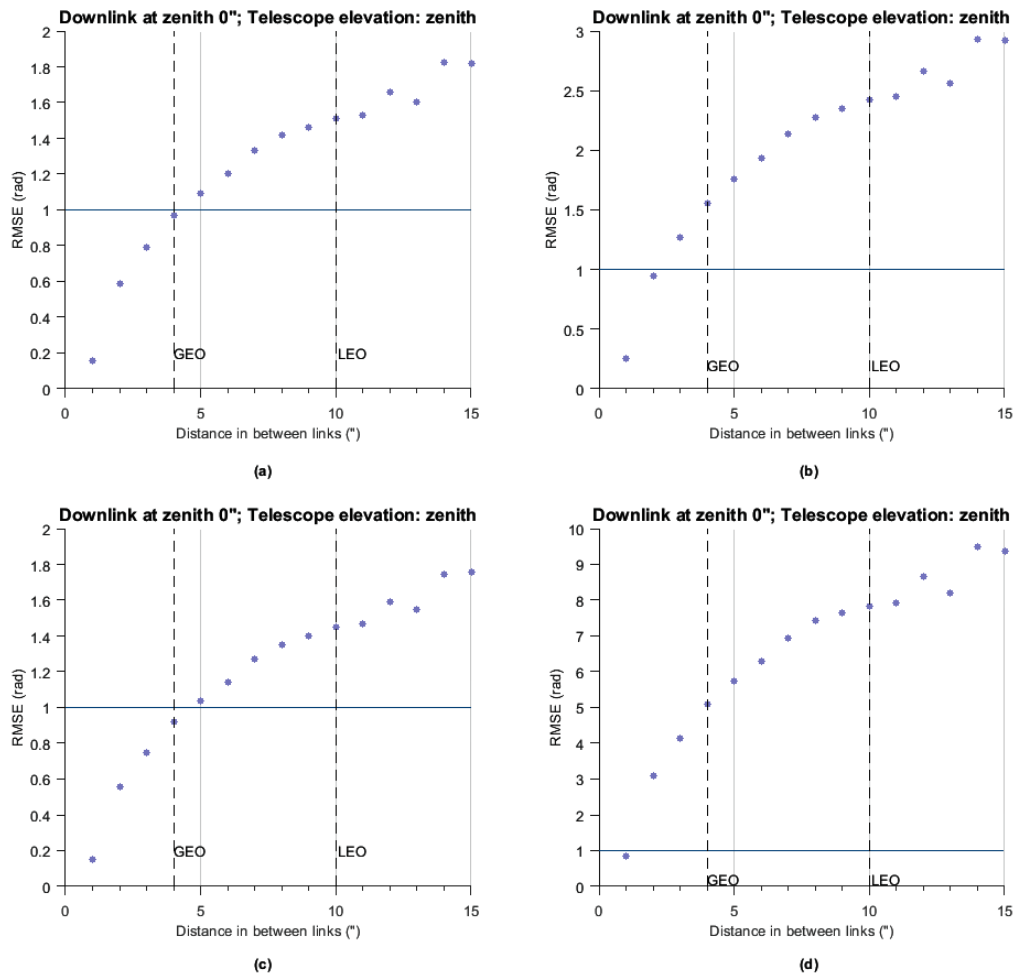
FIGURE 3.5: RMSE of the difference between phases of one downlink at telescope zenith and one uplink getting away 1″ to 15″ from zenith. Seasonal and day time variation analysis: (a) winter night profile (b) winter day profile (c) summer night profile and (d) summer day profile.

3.4   Uplink Correction Performance

An end-to-end closed-loop simulation was performed to evaluate the quality of the link corrections carried out with wavefront measurements on the downlink itself as a reference source, which will be separated from the first one by a point-ahead angle, or measuring the wavefront on a LGS launched to the uplink location. LEO satellites, with a 10″ point-ahead angle was the case under study as it was considered the worst scenario (in comparison to GEO satellites).

Regarding the performance analysis of the uplink correction, two metrics were selected: the long-term scintillation index (see Eq. 3.3) seen by a 30-centimetre receiver (treated as a point receiver for the calculations) at a given height over the Earth's surface (400km for the simulation), and the spot size of the beam at the satellite, represented by the $D\sigma$ parameter (see Eq. 3.4).

Each analysis was performed with 500 independent iterations to characterize the statistical behaviour of the propagation channel. Due to the impossibility of extracting tip-tilt data from Laser Guide Stars, both possible operation procedures (using downlink versus LGS as a reference source) consider the use of the downlink signal for the tip-tilt correction (the laser beam coming from the satellite would play two roles: the object caring the data and the guide star to measure the TT distortions). Even though, with the aim of overcoming this difficulty, a new methodology for TT retrieval was also simulated, see Section 3.5.

$$\sigma_I^2 = \frac{\langle I^2 \rangle - \langle I \rangle^2}{\langle I \rangle^2} \, , \tag{3.3}$$

$$D\sigma = \sqrt{\frac{\int_{-\infty}^{+\infty} \int_{-\infty}^{+\infty} (I(x,y)(x-\bar{x})^2 dx dy)}{\int_{-\infty}^{+\infty} \int_{-\infty}^{+\infty} I(x,y) dx dy}} \, , \tag{3.4}$$

where *I* represents the light intensity at the receiver.

Simulation parameters are listed in Table 3.5: the atmosphere model comes from OT profiles and telescope model has been built with OGS telescope optical parameters, as stated before. The Laser Guide Star model was assumed to be the European Southern Observatory's Wendelstein sodium Laser Guide Star Unit (WLGSU), whose profile and photon return were measured at Teide Observatory during 2016 (Holzlöhner et al., 2016) (Castro-Almazan, 2017) (see Figure 3.6). The AO correction was inferred by a theoretical deformable mirror with 373 useful actuators, as no optimum size for the DM was yet calculated at that point.

Atmosphere	OT atmospheric profiles (see Figure 3.1 and Figure 3.2)
Telescope	OGS Telescope optical parameters (see Table 3.1)
Uplink Source	$\lambda_{up} = 1550nm$ Zenith angle = 10″
Downlink Source	$\lambda_{down} = 1064nm$ Zenith angle = 0″
Laser Guide Star	$\lambda = 589nm$ Height = 90km Photon return flux = $7.7x10^6 photons/s/m^2$ (Holzlöhner et al., 2016) Na Layer Thickness = 20km (Castro-Almazan, 2017) Na profile (see Figure 3.6) (Castro-Almazan, 2017)
Plenoptic WFS	20x20 microlenses Sensor resolution = 300x300 pixels

Deformable Mirror	21x21 actuators (373 useful actuators)

<div align="center">TABLE 3.5: Uplink Correction Performance: Simulation Framework</div>
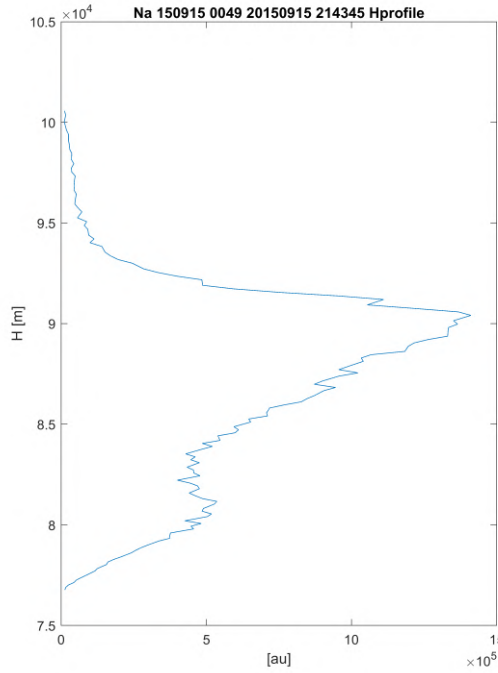
<div align="center">FIGURE 3.6: Na LGS height profiling obtained during 2016 at Teide Observatory using the LGS profiling from IAC80 telescope (Castro-Almazan, 2017).</div>

Fig. 3.7 shows the simulation results when studying the long-term scintillation index at a typical LEO height (400 km) and launching the laser from several telescope diameters (from 0.01 m to 1 m). It is pointed out how correcting the uplink by the turbulence information on its location (propagating a LGS), would reduce the scintillation index by almost two orders of magnitude in the case of a winter night atmosphere (Fig. 3.7a) and, even in a very turbulent scenario (diurnal atmosphere), the improvement is also clear with a reduction of one order of magnitude average (Fig. 3.7b). In the winter night scenario, the two first analysed Tx diameters (1 cm and 10 cm) are not big enough to make profit of the AO correction.

The analysis of the resulting spot size at the receivers altitude -400km in this case- is shown in Fig. 3.8. Measurements are shown in equivalent arcseconds seen by the telescope located at ground level. The spot size was calculated for the short-term (the measurement of the spot size at each independent realization of the propagation channel -iteration-). In case of nocturnal links (Fig. 3.8a), the improvement in the performance is represented by a reduction of 41.12% (from 2.245" down to 1.324") when using the LGS as a reference source, whereas there is almost no difference when correcting the uplink with the downlink information. However, in diurnal scenarios it is when the performance improvement becomes more noticeable, with a reduction in the spot size of almost 50% (from 4.858" with no correction, down to
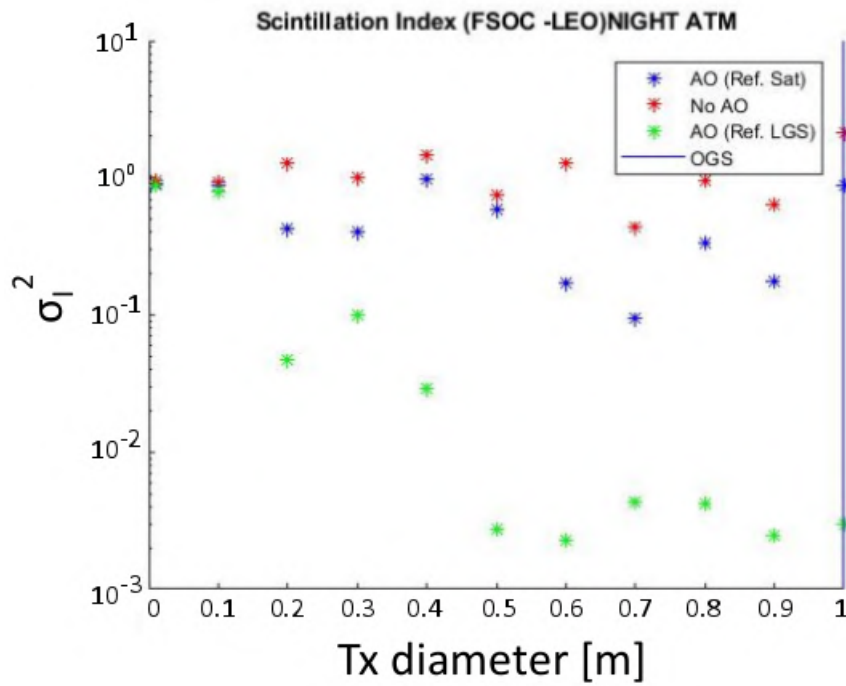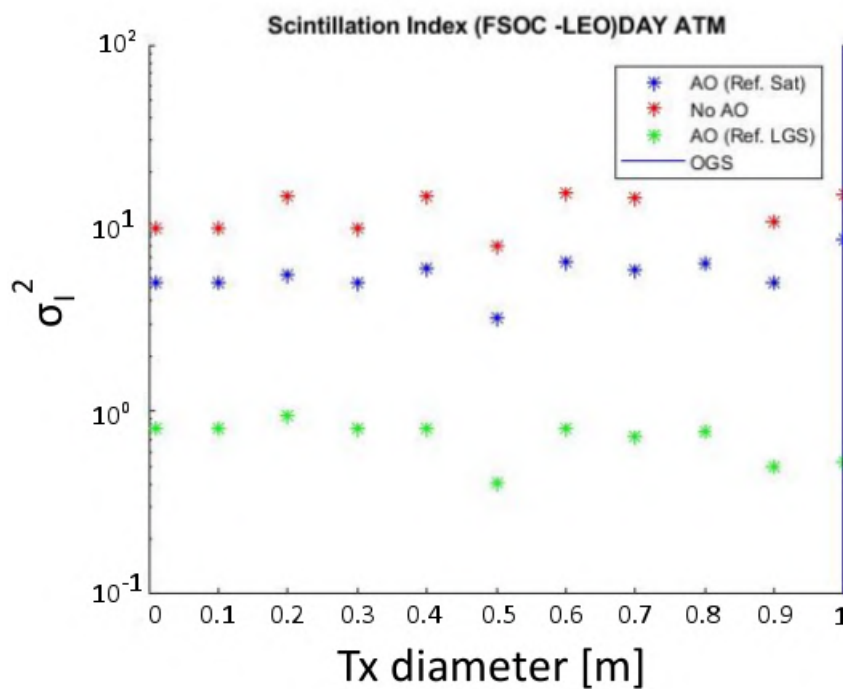
FIGURE 3.7: Uplink scintillation index with no AO correction (red), corrected by the measurements on the downlink position (blue) and by the measurements on the uplink location (green). Uplink and downlink are separated by 10″ (LEO Satellite). Day length variation analysis: (a) nocturnal atmospheric profile and (b) diurnal atmospheric profile. In the x-axis, 500 independent realizations of the atmosphere.

2.421″ when using a LGS as reference) (see Fig. 3.8b) when propagating the artificial reference to the expected uplink location and no real difference when using the downlink signal.

Previous analysis were carried out with a plenoptic wavefront sensor, although in case of using a Shack-Hartmann, the simulation output would have been similar as the spot size in the plenoptic frame did not result to be an extended object. When dealing with point sources, spreading the light among the central microlenses in the plenoptic frame in contrast to illuminating the central pixels at each sub-aperture in the SH-WFS, it is considered equivalent, as the light is distributed among a similar number of pixels.

3.5 Tip-Tilt Retrieval on Sodium Laser Guide Stars

Nowadays the ultimate limit for high-spatial resolution observations is increasingly related with the availability of a natural star bright enough to provide the tip-tilt information. This problem is especially relevant when designing an Adaptive Optics system for FSOC with a LGS as reference source.

From past experience measuring sodium layer profiles at the Teide Observatory, one could consider that the sodium layer could present anisotropies in the 1″ range, which eventually might become a low-contrast image when being illuminated by a laser beam designed with a proper width (the LGS central launch is considered in this study). Tracking such image in close loop from the launching subsystem, could be used by the receiving adaptive optics system to measure the tip-tilt as well as others components of the wavefront aberration caused by the turbulence.

Wavefront sensing of the anisotropy images ideally would need a sensor adequate for extended objects, like the plenoptic camera, using correlation-based calculations (Martínez and Ramos, 2018).

With the aim of verifying the viability of this tip-tilt measurement system, the proposed solution was simulated as a cornerstone for planning a measurement campaign at Teide Observatory in the near future, although it will not be part of the present research.

The system was modelled by considering an extended illuminated area in the Sodium layer of 1-arcminute diameter, over which the anisotropies of the Na could be tracked in order to compute the tip-tilt from the LGS itself. This extended area would be illuminated by propagating a ring-shaped beam to the Sodium, without focusing the laser at 90 km, but higher, using an axicon device to generate this shape and the entire telescope aperture for the launch (for more details about the axicon, see Chapter 4). Figure 3.9 illustrates the idea.

The ring shape in the Na layer needs to be large enough to keep the central area, and the anisotropies in it, always illuminated; in this way, the displacement of the beam due to the uplink TT would not affect this central illumination and the Sodium anisotropies would present some apparent movement as a consequence of only the downlink tip-tilt, making possible its reconstruction by the WFS.

The Sodium layer needs to be uniformly illuminated in order to properly detect the movement of the anisotropies; this uniformity would be achieved by the pre-compensation of the upwards propagated laser beam, which would reduce its scintillation, as it has been previously proven.

The simulation parameters are gathered in Table 3.8.
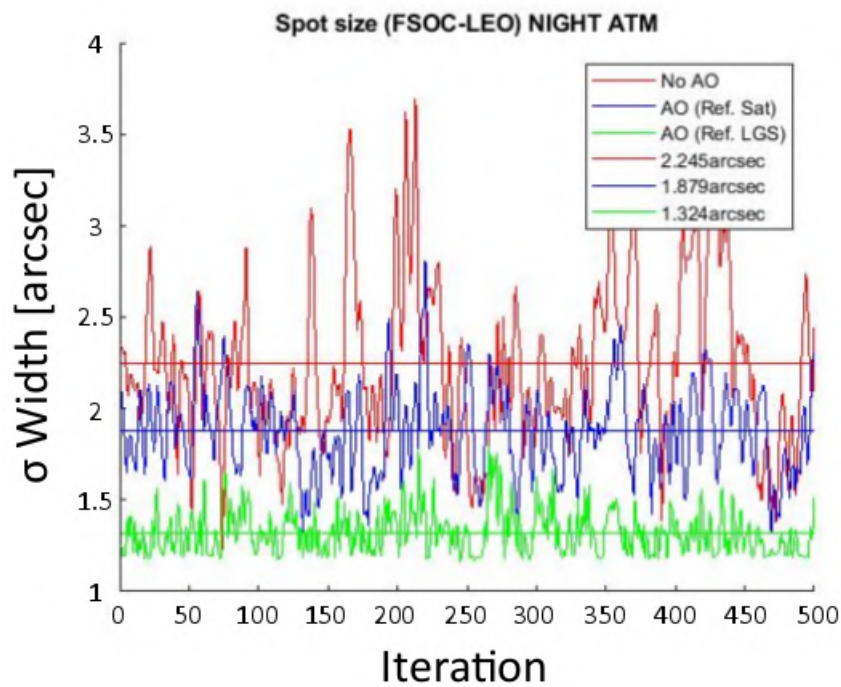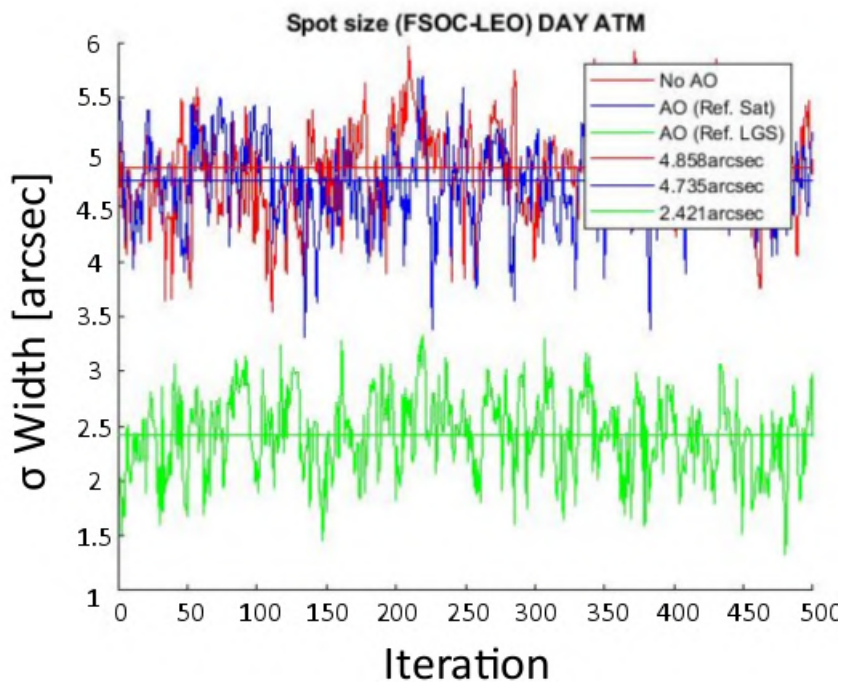
FIGURE 3.8: Uplink spot width with no AO correction (red), corrected by the measurements on the downlink position (blue) and by the measurements on the uplink location (green). In this case, uplink and downlink are separated by 10″ (LEO Satellite). Day length variation analysis: (a) nocturnal atmospheric profile and (b) diurnal atmospheric profile. In the x-axis, 500 independent realizations of the atmosphere.
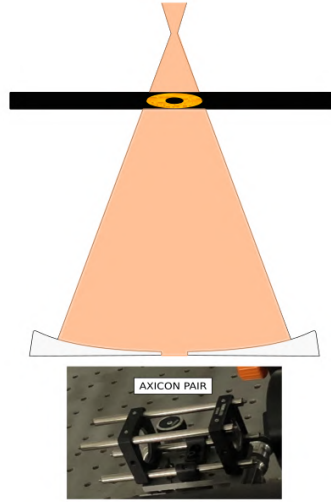
FIGURE 3.9: The axicon device could be use to generate a ring shape
in the Sodium layer.

Atmosphere	5 cm; 8 cm; 10 cm; 12cm;
	15cm (photon flux calculation); 18 cm
Telescope	OGS Telescope optical parameters (see Table 3.1)
Laser Guide Star	λ = 589nm
	Height = 90km
	Extensively illuminated = Ring shape
WFS	Plenoptic camera
	Lenslet array = 12x12
	Sensor resolution = 144x144 pixels
	Readout noise = 0.3 e^-
Operation Frequency	100 Hz

TABLE 3.8: TT retrieval from Na-layer: Simulation Framework

Simulations of the computed tip-tilt by a plenoptic wavefront sensor are presented (OOMAO Toolbox), showing the expected quality result as a function of both the photon return and the contrast of the generated extended laser guide image.

Synthetic images with five different contrast for the Na anisotropies were implemented in the simulation (Figure 3.10) with the purpose of proving the performance dependency on the contrast of the plenoptic frame. The RMS contrast of the synthetic images was calculated equivalently as in solar granulation images (see procedure described in Appendix A).

Tip and tilt coefficients were retrieved from the plenoptic images at different atmospheric cases by using the described contrast levels. Later on, the *J* similarity index between the real and the computed wavefront (Eq. 3.5) was calculated and represented for each contrast value (Figure 3.11) at each atmospheric scenario.

$$J(Real, Reconstructed) = 1 - \frac{TT_{real} - TT_{reconst}}{mean(TT_{real})} \qquad (3.5)$$
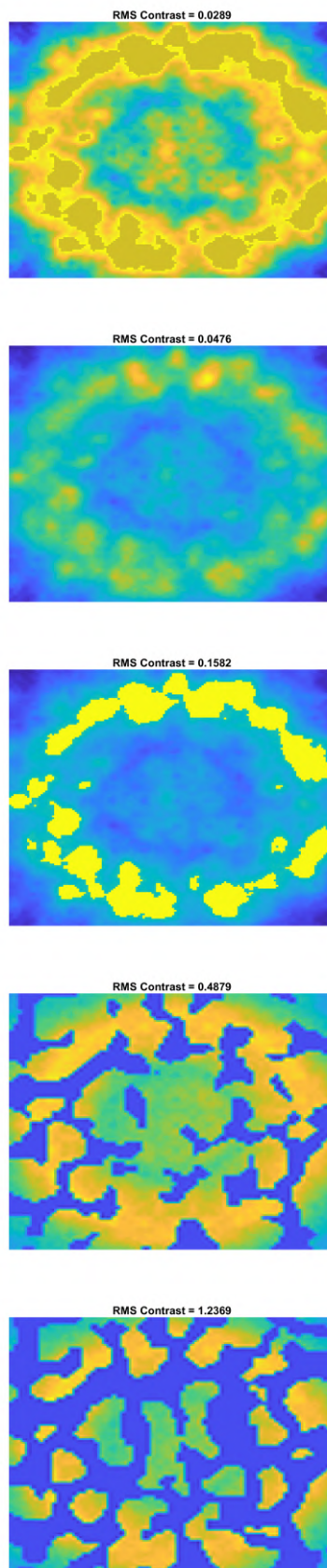
FIGURE 3.10: Synthetic images of the anisotropies in the Sodium layer, ranging from lower to larger RMS contrast.
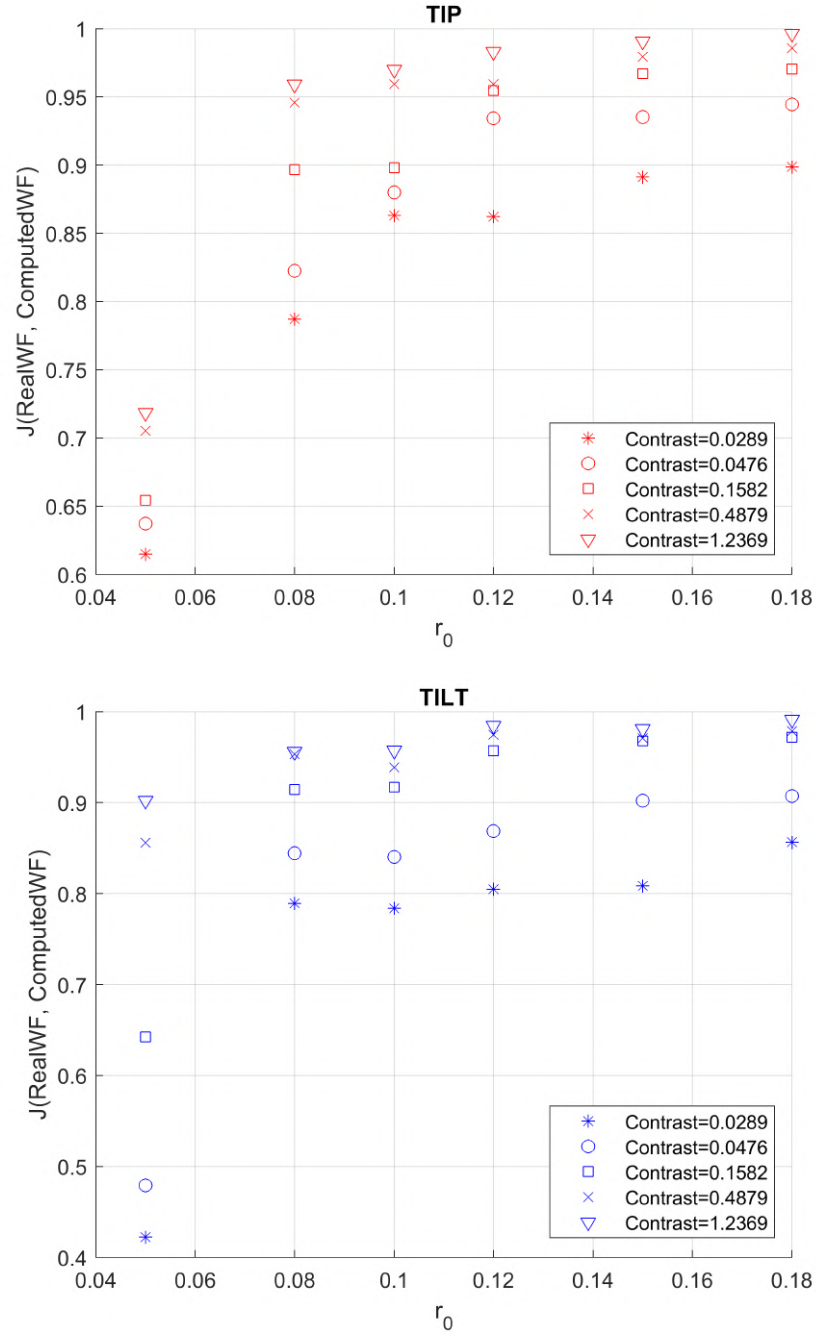
FIGURE 3.11: Similarity index between the real atmospheric tip-tilt and the estimated TT by the plenoptic WFS. Results are analysed for several atmospheric turbulence strength and RMS contrast in the Na anisotropies.
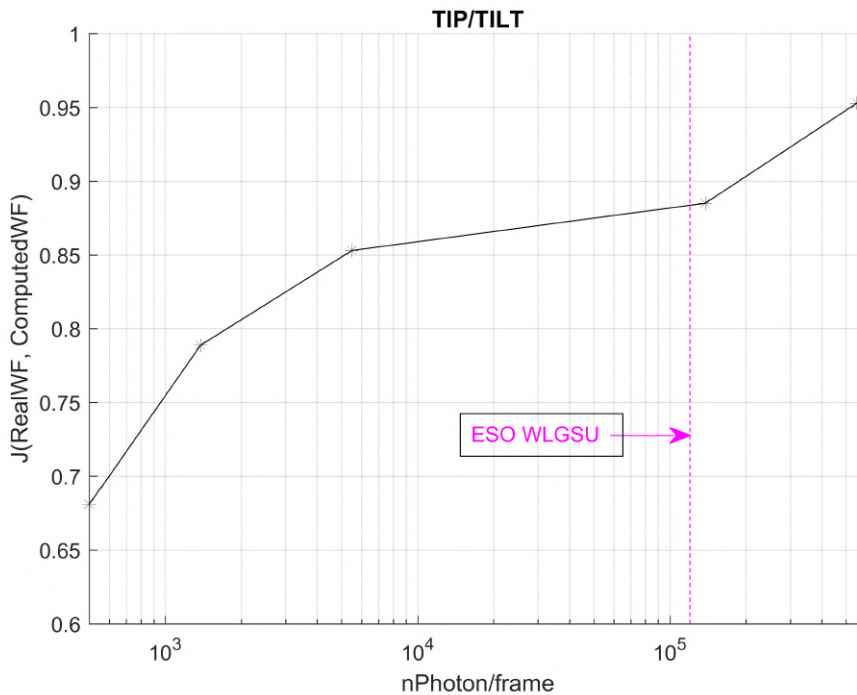
FIGURE 3.12: Similarity index between the real atmospheric tip-tilt
and the estimated TT by the plenoptic WFS and the effect of decreas-
ing the SNR in the measurements.

Additionally, the photon flux of the WFS image was gradually reduced with the
aim of detecting the minimum power necessary to illuminate 1' ring up on the Na
layer and to reconstruct properly the TT. Simulation of minimum photon flux re-
turn from the Sodium inhomogeneities were carried out only for the 15cm seeing
atmosphere and the best possible contrast in the Na anisotropies, as this result was
considered to be just a rough estimation of the required laser power.

Figure 3.12 presents the method behaviour when decreasing the Signal-to-Noise
Ratio; it shows the similarity between the real atmospheric TT, used in the simula-
tion, and the estimated one, when decreasing the photon flux per frame at 100Hz
and maintaining the readout and photon noise of the plenoptic camera. For com-
parison purposes with ESO Wendelstein LGS unit, its photon flux per frame at this
operation rate was also added to the graph (photon flux return extracted from (Hol-
zlöhner et al., 2016)).

The main limitation of the proposed method is the spatial structure of the Sodium
anisotropies: they have to be large enough and with the proper contrast to be de-
tected by the wavefront sensor; future experiments will be perform to measure the
anisotropies structure. Additionally, the stability of this structure in time needs to
be larger than the atmospheric coherence time; it can evolve in time, but slower than
the atmosphere itself.

3.6 Summary of the Simulations Outcome

Three types of computer simulations were carried out with the purpose of getting further knowledge about the wavefront correction in the uplink propagation direction and the possible solutions for the arisen operational problems.

The isoplanatic study results outline the need of propagating a Laser Guide Star to the expected uplink location in order to perform an optimal uplink precompensation, instead of using the downlink signal as a reference source for the wavefront sensing.

After accomplishing end-to-end simulation regarding the performance of an AO system pre-compensating the uplink, the influence of the point-ahead angle is remarkable in the spot size and scintillation reduction, re-validating the outcome of the isoplanatic simulation: a LGS needs to be used to measure the uplink wavefront.

The analysis of the isoplanatic patch and of the uplink correction performance are gathered in the proceedings *Simulating the performance of adaptive optics techniques on FSO communications through the atmosphere* (Martínez, Ramos, and Sodnik, 2017) and *Performance assessment of Adaptive Optics techniques on FSO communications through the atmosphere* (Martínez et al., 2017a). Additionally, a paper published in the Optical Engineering Journal presents the simulation results as well as the preliminary design of the proposed AO system (Noelia Martínez, 2018).

With the purpose of solving the Tip/Tilt retrieval problem from LGSs, currently still not verified, the third type of simulation was designed and executed: TT retrieval from the Na layer anisotropies. Results show that the TT information could be extracted from Sodium contrast images by the plenoptic sensor, although this part of the research needs to be further studied, especially whether those anisotropies eventually exist. The proposed method for the TT retrieval from the Na anisotropies is described in the proceeding *Sodium layer density anisotropies as a reference for tip-tilt measurement in laser guide stars*, publication still pending.

Chapter 4

Uplink Correction Wavefront System. Design

4.1   Introduction

The UWCS (Uplink Wavefront Corrector System) is an adaptive optics instrument whose aim is the uplink improvement of Earth-satellite communications and Laser Guide Star generation at the Optical Ground Station (OGS), by measuring and correcting the turbulence the link suffers while travelling through the atmosphere.

UWCS is divided into two development phases: UWCS I, in which the same laser would act as Laser Guide Star (wavelength, λ = 532nm) and as "simulated" communications uplink, and UWCS II, where real communications links would be corrected with an independent LGS. UWCS I is the pathfinder for the second generation and works as demonstrator of the feasibility of the uplink pre-correction.

UWCS I (Figure 4.1) was composed of a plenoptic camera as wavefront sensor, a laser acting as Laser Guide Star (WFS reference) and, at the same time, playing the role of the uplink, a deformable mirror to pre-correct the uplink, in a way the on-purpose pre-distortions on the link would counteract the atmospheric aberration while travelling through it; and a control PC to close the AO loop at the proper frequency.

Regarding UWCS II (Figure 4.2), the elements were the same with the exception of two separated lasers: one for the LGS (λ = 532nm) and another one for the optical communications (λ = 1550nm); as the purpose of the system is the improvement of the uplink performance, the DM would pre-correct the communication laser.

The design of the Uplink Wavefront Corrector System is fully described in this chapter by carefully presenting each of the subsystems of the instrument and taking into account the optimal telescope configuration to be integrated at. The chapter ends with important final considerations in the UWCS design as it is the change in the wavefront sensor type; part of the research in this thesis was the result of an ESA Express Procurement EXPRO Contract requiring the feasibility study of the plenoptic camera as WFS for Feeder links Adaptive Optics. However, time constraints would have not allowed the proper design of the UWCS full system with a plenoptic camera, but with the well-known Shack Hartmann wavefront sensor, in order to reduce the number of tasks to be performed, as it is explained at the end of the chapter.

4.2   Telescope Optical Configuration Assessment

Both Cassegrain and Coudé focus are analysed in this section in order to be further selected for the next phase experimentation. The criteria for this assessment was
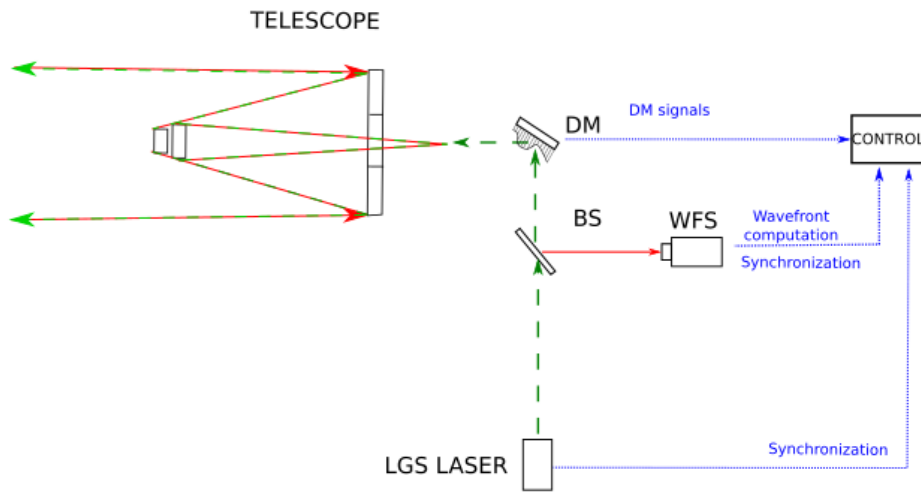
FIGURE 4.1: UWCS I Conceptual Design.
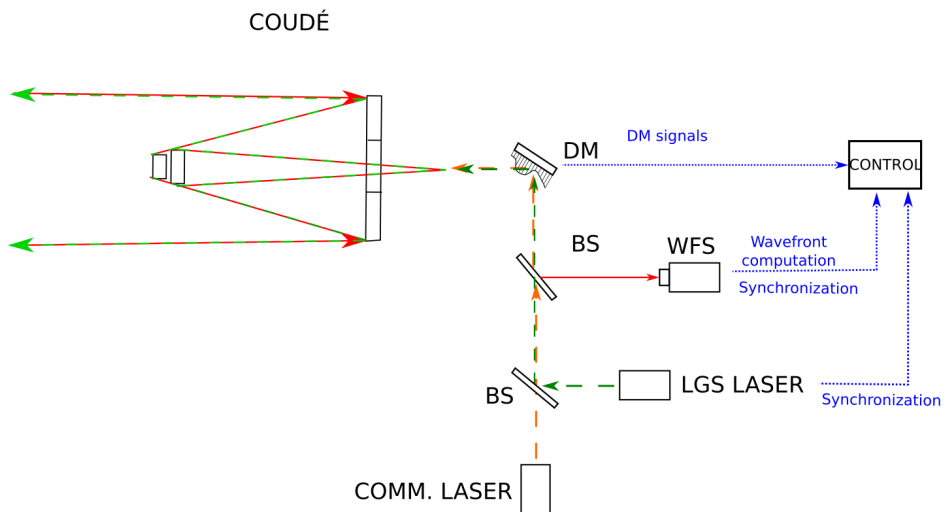
FIGURE 4.2: UWCS II Conceptual Design.

best performance versus difficulty ratio of each configuration.

4.2.1 Cassegrain Focus

The optical path of the OGS Cassegrain focus consists of two mirrors with a total focal length of 13.3m. It's shown in Figure 4.3.
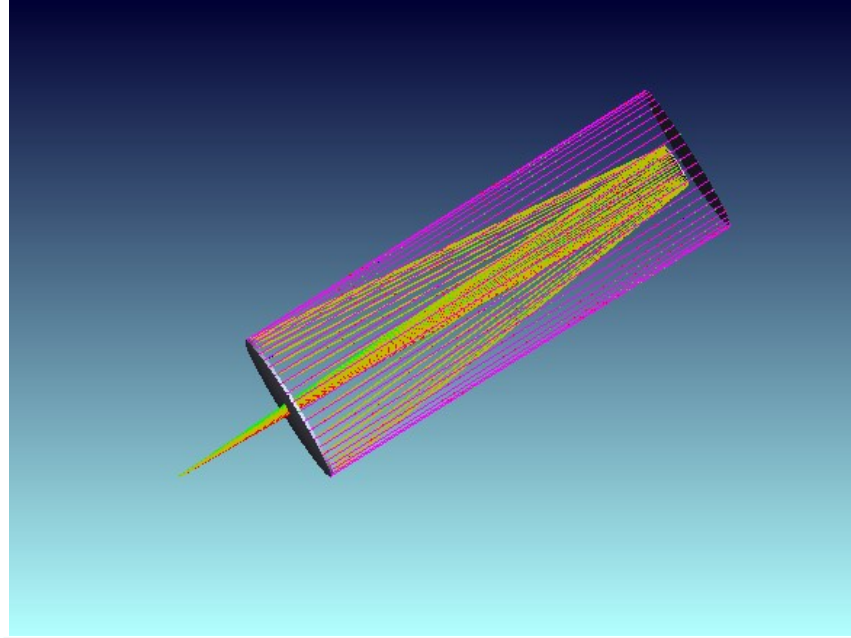
FIGURE 4.3: OGS Cassegrain focus optical layout.

A nominal optical throughput of 0.99 was assumed for both primary and secondary mirrors of the telescope. A dust factor was applied in order to account for outdoors conditions that may happen every time the dome cap is open (Table 4.1).

Optical Element	Transmission at 532nm	Dust Level (0-10)	Scatter Derated Transmission Estimate
Primary	0.99	4	**0.95**
Secondary	0.99	3	**0.96**

TABLE 4.1: Optical throughput estimation for the Cassegrain focus

The laser would travel through the primary and secondary twice (when being launched and when its return is received by the WFS), therefore the optical transmission has to be taken into account on both travels: Optical transmission for the Cassegrain focus = (0.95 x 0.96) x (0.96 x 0.95) = 0.8317.

Operating the UWCS I at the Cassegrain focus would increase the degree of complexity as it implies hanging the whole system from the telescope tube with the corresponding weight limitations, cables and cooling hoses routing and the need of a really compact design.

4.2.2 Coudé Focus

The optical path of the OGS Coudé focus consists of six mirrors with a total focal length of 38.8m. It's shown in Figure 4.4.
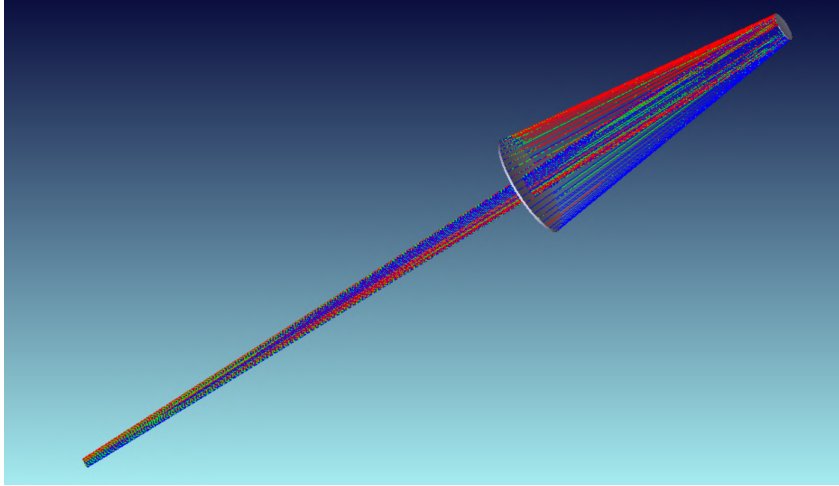
FIGURE 4.4: OGS Coudé focus optical layout.

A nominal optical throughput of 0.99 was assumed for all the mirrors in the path. A dust factor was applied in order to account for outdoors conditions that may happen every time the dome cap is open (Table 4.2).

Optical Element	Transmission at 532nm	Dust Level (0-10)	Scatter Derated Transmission Estimate
Primary	0.99	4	**0.95**
Secondary	0.99	3	**0.96**
M3	0.99	1	**0.98**
M4	0.99	0.2	**0.988**
M5	0.99	0.2	**0.988**
M6	0.99	0.2	**0.988**

TABLE 4.2: Optical throughput estimation for the Coudé focus

The laser would travel through the whole telescope path twice (when being launched and when its return is received by the WFS), therefore the optical transmission has to be taken into account on both travels: Optical transmission for the Coudé focus = (0.95 x 0.96 x 0.98 x 0.988 x 0.988) x (0.988 x 0.988 x 0.98 x 0.96 x 0.95) = 0.7611.

Even though the optical transmission for the Coudé focus would be less optimal for the LGS operation and pre-compensation, the simplicity, the lack of vibrations and the easy access when having an optical bench where the system could be located, makes the Coudé focus the best choice for the next phase experimentation.

4.3 Laser Guide Star System

Wavefront sensing needs a reference on the sky area where the atmospheric correction will be done; this reference would be artificially created in order to measure on the exact location where the communication link would take place, as it has been already explained in previous chapters.

Unfortunately, as the Sodium LGS was not available at the OT, one of the accessible lasers at the OGS would be launched to generate a Rayleigh guide star, an artificial star at 20-kilometre altitude from the Rayleigh backscattering the air molecules produce.

In order to measure the wavefront in the uplink position, the WFS shall be located on the same launching axis; and additionally, to avoid the blindness of the detector (caused by the laser light), the selected laser shall work in pseudo-pulsed operation.

4.3.1 Rayleigh Laser Guide Star

The OGS laser, which would be used as LGS, was the Coherent Verdi V18, a Diode-Pumped Solid-State laser with a CW Output of 18W at 532nm and whose technical details are summarised in Table 4.3.

Output Power	18W
Wavelength	532nm
Beam Diameter	2.25mm
Beam Divergence Angle	<0.5mrad
M^2	<1.1
Cooling Requirements	Closed-loop water cooling
Weight	8kg
Length of umbilical	3m
Laser Head Dimensions	156.06 (H) x 407.67 (L) x 137.26 (W) mm

TABLE 4.3: Coherent Verdi V18 laser technical details.

The Rayleigh Laser Guide Star would be created by combining the Verdi laser with an optical chopper.

The pulse repetition frequency was established by taking into account the maximum operating frequency of the WFS camera: the laser needed to be fired at maximum frequency of 2kHz.

4.3.2 LGS Optical Chopper

An optical chopper was used in combination with the CW Verdi laser to generate the laser pulses.

The SCITEC INSTRUMENTS 310CD optical chopper was selected for this purpose. Model 310CD is a high speed variable frequency optical chopper. The basic system consists of control unit, chopping head, a blade protector and a chemically blacked photo etched disc. This system provides operation over the frequency range 100 Hz to 120 kHz, depending on the attached disc. Its technical details are gathered in Table 4.4.

The optical chopper would be located right after the laser, which may need a beam expander to enlarge its beam diameter; there were several beam expanders available for this function, all of them in the range from 5 to 10 mm output diameter, hence, the aperture of the chopping disc cannot be smaller than 10 mm. An additional parameter needed to be considered in the optical chopper selection: the chopping velocity; due to the mechanical nature of the device, the laser beam would not be fully covered or uncovered instantaneously, but progressively with a time slope depending on the velocity itself: in order to achieve the same frequency, one chopping disc with less number of slots would moved at larger speeds. Based on the

technical specifications of the available discs and the fact that the maximum operating frequency is 2kHz (limited by the WFS), it was decided to use the 300D2 Blade, with which the maximum frequency and maximum velocity (to minimize the chopping time slope) could be achieved without surpassing the WFS operating limit.

The SCITEC INSTRUMENTS Synchroniser would handle the synchronisation between the LGS optical chopper and the WFS optical chopper (see Section 4.5).

CHOPPER CONTROLLER	
Frequency Control	Internal (10-turn potentiometer)
	External (external voltage)
Reference pick-up	IR LED and phototransistor pair
	with Schmitt trigger
CHOPPING DISCS	
Blade: 300D2	N slots = 2
	Frequency = 100-800 Hz
	Aperture Diameter = 32.0 mm
	Phase Jitter Max. = +/-0.2 °
Blade: 300D5	N slots = 5
	Frequency = 250-1850 Hz
	Aperture Diameter = 23.1 mm
	Phase Jitter Max. = +/-0.5 °
Blade: 300D10	N slots = 10
	Frequency = 500-3400 Hz
	Aperture Diameter = 13.1 mm
	Phase Jitter Max. = +/-1 °
Blade: 300D30	N slots = 30
	Frequency = 1500-9000 Hz
	Aperture Diameter = 4.8 mm
	Phase Jitter Max. = +/-3 °

TABLE 4.4: SCITEC INSTRUMENTS Optical Chopper technical details

4.3.3 LGS Launch Sub-system

The laser would be propagated through the whole telescope aperture, therefore the secondary mirror that obscures the primary mirror would introduce significant central vignetting losses.

The upwards propagation of several types of beam profiles was simulated by Fresnel propagation, without taking into account the atmospheric contribution, but only the light diffraction effects. The optical parameters of the OGS telescope were properly taken into account (Table 3.1 for further details). Table 4.5 shows the simulated beam profiles and the clipping factor the secondary mirror would introduce on them when propagating from the whole telescope aperture. The clipping factor was calculated based on the total propagated power without and with obstruction (Eq. 4.1).

$$CF = \frac{P - P_{obs}}{P} \tag{4.1}$$

Where P is the propagated power without obstruction, and P_{obs}, is propagated power through the obstruction.

Table 4.6 gathers the intensity distribution when focusing those shaped-beams at 20km height.
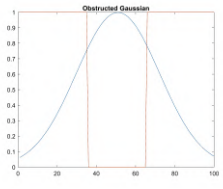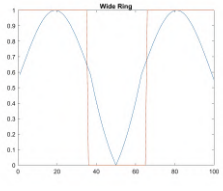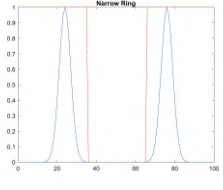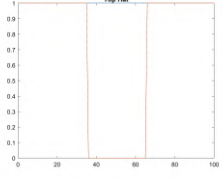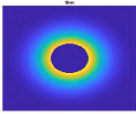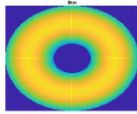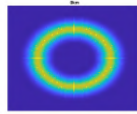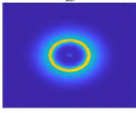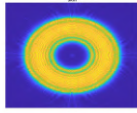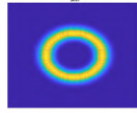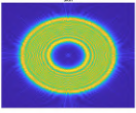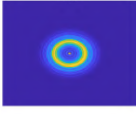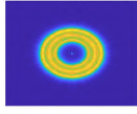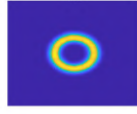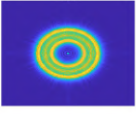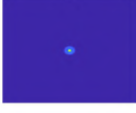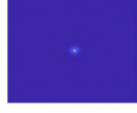
Beam Profile		Clipping Factor
Obstructed Gaussian	0.35	
Wide Ring	0.07	
Narrow Ring	0	
Top Hat	0.27	

TABLE 4.5: Simulated beam profiles and clipping factor according to the secondary mirror location.

Layer Altitude	Intensity Profiles			
	Obstructed Gaussian	**Wide Ring**	**Narrow Ring**	**Top Hat**
0km				
5 km				
10 km				
20 km				
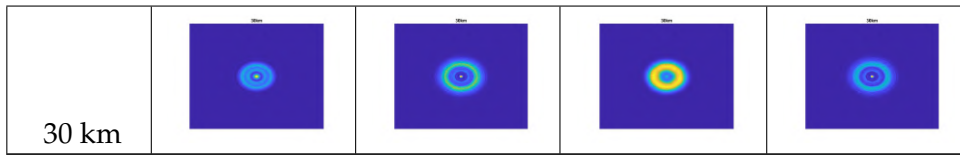
TABLE 4.6: Intensity field at several altitudes when focusing the laser
at 20km above the telescope.

The fraction of light falling on a $0.025m^2$ area at 20km over the telescope was estimated based on the laser beam profile and the Fresnel propagation of the laser to a 20-kilometre height. Results are gathered in Table 4.7. Exclusively the central area of each intensity field was analysed by selecting 50x50 px at each frame, equivalent to a $0.025m^2$ area on the sky (Figure 4.5).

Simulations point out that ring-shaped laser beams perform better when launching them through the whole telescope aperture. Hence, the laser (either FSOC or LGS laser) needed to be properly shaped before exiting from the AO system to the telescope input. An axicon-scheme was devised for efficient coupling of the laser to the obscured launching telescope.
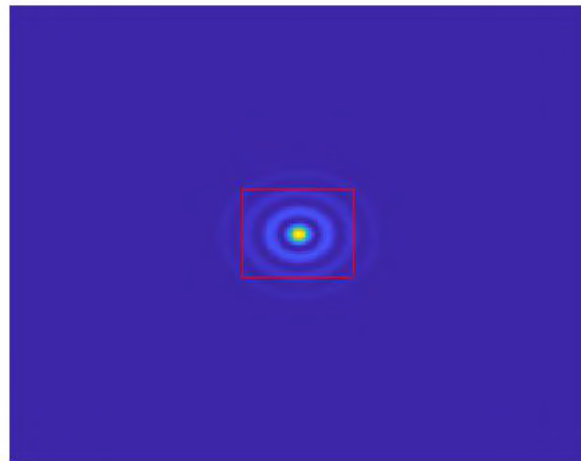
FIGURE 4.5: The area surrounded by the red square has been used to estimate the fraction of light falling in this field when propagating several beam profiles up to 20km height. It has an equivalent size of $0.025m^2$, calculated based on the pixel size.

Obstructed Gaussian	Wide Ring	Narrow Ring	Top Hat
0.8176	0.9266	0.9988	0.6641

TABLE 4.7: Fraction of light on mid-field at 20km height.

Axicons are both afocal refractive and reflective optical elements with a flat front surface and a conical rear surface. The rays near the edge of the beam entering the axicon get located at the inside edge of the annular beam when exiting. Likewise, the rays at the centre of the incident beam get located around the edge of the annular
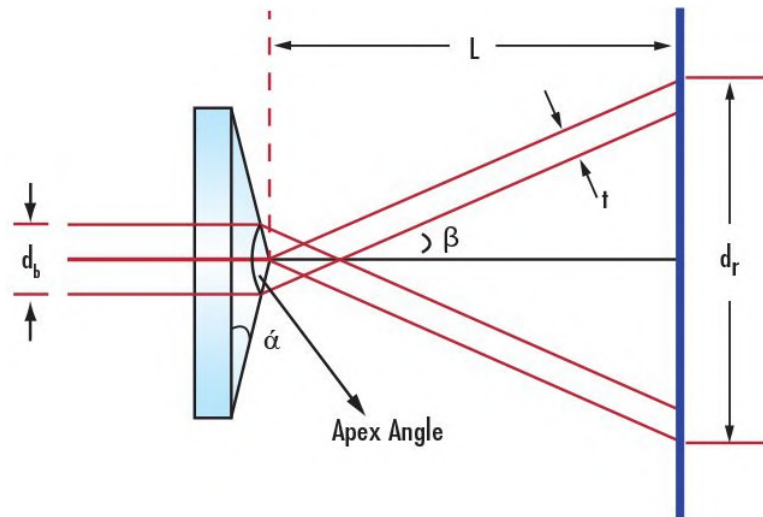
FIGURE 4.6: Definitions of thicknesses and angles in the Axicon (*Edmund Optics Tech Tools: Axicon*).

beam when exiting (*Edmund Optics Tech Tools: Axicon*). For the launching system, a refractive axicon was selected.

The axicon was designed in the way the resulting ring-shaped intensity distribution matches the ratio between the primary and secondary mirror in order to minimize coupling losses. Figure 4.6 shows the definitions of the axicon parameters to have into account when selecting the model which best fits the optical system.

The outer diameter of the ring (d_r) is defined by the physical angle of the positive axicon (α) and the distance between the last surface of the positive axicon and the first surface of the negative one (L) (see Eq. 4.2). In all the expressions below, n represents the refraction index of the axicon material. The thickness of the ring (t) only depends on the entrance diameter (d_b) (see Eq. 4.3).

$$d_r = 2L \tan(\alpha(n-1)) \tag{4.2}$$

$$t = \frac{1}{2}d_b \tag{4.3}$$

Two identical axicons would be used in the launch system, one positive and one negative, in order to create a ring shaped with a collimated input beam that keeps collimated after the second axicon.

The ratio between the secondary and the primary mirrors at the OGS which had to be matched by the axicon, was $D_{secondary}/D_{primary} = 288.912mm/1016mm = 0.28$.

With an entrance beam diameter of 10 mm and an axicon with physical angle $20°$, if the negative axicon is placed at 45 mm from the positive one (Figure 4.7a), the diameter of the output ring (d_r) will be 14.5 mm with a 5-millimetre thickness, producing a footprint on the primary mirror (Figure 4.7b) whose ratio between obscured and filled area would be 0.30. Therefore, the laser beam would not suffer from clipping losses due to the telescope central obstruction. The selected axicon was the Thorlabs AX250-A, whose technical details are gathered in Table 4.9.

(a)


```
                              Image Diagram
20/11/2018
Scale bar is 1000.0000 Millimeters.
Field position: 0.0000, 0.0000 (deg)
Efficiency:  96.997%, Total Power: 9.700E-001 Watts        UND00002.ZMX
Surface: 40                                        Configuration 1 of 2
```

(b)
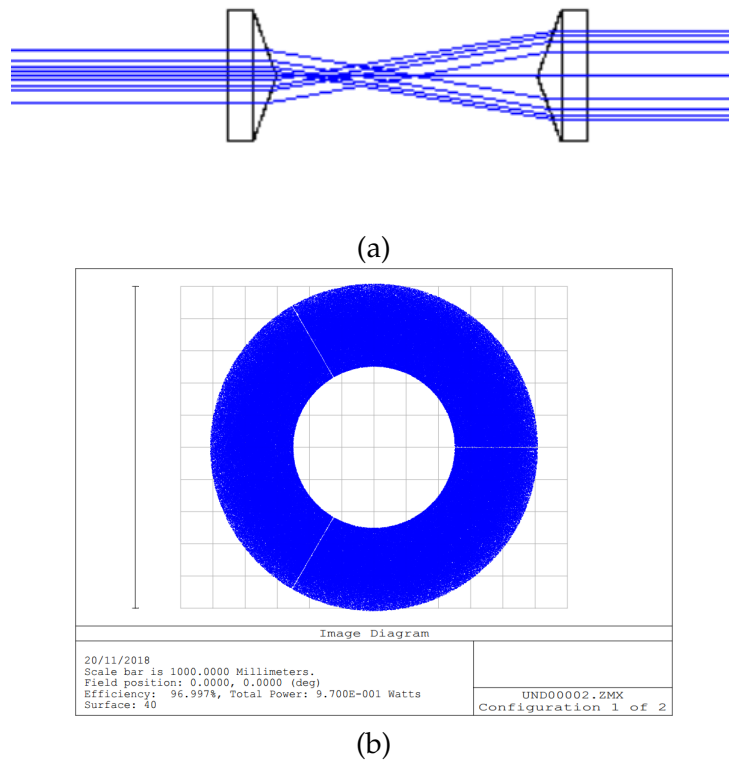
FIGURE 4.7: (a) Zemax layout of the positive and the negative axicon in the LGS launch system; (b) Footprint of the laser being launched.

THORLABS AX2520-A	
Physical Angle (α)	20.0°
Deflection Angle (β)	9.973°
Central Thickness	9.6mm
AR Coating	$350 - 700nm$
Diameter	25.4mm
Material	Fused Silica (n = 1.458)

TABLE 4.9: THORLABS AX2520-A Axicon technical details.

4.4 Wavefront Corrector System

The wavefront corrector system or Deformable Mirror (DM) is one of the main elements in any AO instrument; and some parameters need to be taken into account in order to verify the suitability of a certain DM model to perform properly within the AO system and its specifications: the number of actuators, the total actuator stroke and the absolute inter-actuator stroke:

- The highest possible spatial frequency at which the DM is able to produce useful correction depends on the number of actuators across the DM optical aperture.

- The maximum turbulent conditions to operate the DM without reaching saturation is directly sustained by the total stroke, which indicates the maximum deformation the DM can suffer.

- The absolute inter-actuator stroke indicates the maximum displacement between two adjacent actuators which is required to correct for a certain level of turbulence: the higher the turbulence, the more likely is that two adjacent actuators will have to be pushed away from each other.

The optimum DM size was determined by the relationship D/r_0, where D is the telescope diameter (1-meter in OGS scenario) and r_0 is the Fried parameter. In case of the OGS and the typical seeing values at the Teide Observatory (two selected atmospheric profiles scenarios, extracted from previous studies regarding the OT nocturnal atmospheric profiles[1], see Chapter 3)), the optimum DM size for the worst case scenario in the LGS operation ($r_0 = 0.0917m$) would be a minimum of 11x11 actuators.

In the following subsections, the required total stroke and absolute inter-actuator stroke are estimated for two atmospheric scenarios ($r_0 = 0.1744m$ and $r_0 = 0.0917m$, best and worst nocturnal profiles used in Chapter 3), in order to determine the feasibility of the available CILAS SAM97 unit as a suitable deformable mirror for the UWCS. CILAS SAM97 technical details are gathered at the end of this section (Table 4.13).

4.4.1 Stroke Calculation

The required total stroke and absolute inter-actuator stroke were calculated based on analytical expressions and numerical Monte Carlo simulations (*AOLI Deformable Mirror Stroke Calculus*).

Analytical Stroke Calculation

The mechanical stroke requested by the atmospheric aberrations was estimated based on the reflected wavefront phase excursion.

The expression which accounts for the DM reflected wavefront phase excursion (ϕ_0) that copes with 99% of the possible cases comes from the outcome of solving for ϕ_0 in Eq. 4.4.

$$P(-\phi_0 \leq \phi \leq +\phi_0) = \int_{-\phi_0}^{+\phi_0} f_\phi(\phi; D; r_0)dx = erf(\frac{\phi_0}{\sqrt{2}\sigma_\phi}) = 0.99 \qquad (4.4)$$

Whose solution is $\phi_0 = 2.576\sigma_\phi$. The dependence on D and r_0 is encoded in the value $\phi_\sigma^2 = \Delta_1$. Δ_1 is described in Noll (1976) (see Eq. 4.5), and gathers the analytical expressions for the residual wavefront phase variance upon correcting the first J Zernike polynomials. The first term is selected as the DM is thought to compensate for the total amount of aberrations; in case of having a separate TT DM, the selected term would be Δ_3 instead.

$$\Delta_1 = 1.0299\left(\frac{D}{r_0}\right)^{(5/3)} \qquad (4.5)$$

The total WF phase excursion over the entire optical aperture is therefore $2\phi_\sigma$ and Eq. 4.6 translates it into total optical path difference in the reflected wavefront (OPD^{WF}).

$$OPD^{WF} = 0.832\lambda\left(\frac{D}{r_0}\right)^{(5/6)} \qquad (4.6)$$

---

[1]Rayleigh laser operations during daytime are not realistic; although in case of using Sodium LGS daytime AO is still an open issue to be further investigated.

The same expression applies to derive the constrain on the absolute inter-actuator optical path difference in the reflected wavefront; the pupil diameter D is replaced by d, the inter-actuator distance: $d \simeq D/(n_{act} - 1)$ with n_{act} being the number of actuators along the pupil diameter (Eq. 4.7).

$$OPD_{IntAct}^{WF} = 0.832\lambda \left(\frac{d}{r_0} \right)^{(5/6)} \tag{4.7}$$

The results for the analytical stroke estimation are gathered in Table 4.10 for the two selected atmospheric scenarios and the laser wavelength ($\lambda = 532nm$).

Analytical Estimation of DM Stroke	
$r_0 = 17.44cm$	$OPD^{WF} = 1.8971\mu m$
	$OPD_{IntAct}^{WF} = 0.0705\mu m$
$r_0 = 9.17cm$	$OPD^{WF} = 3.2414\mu m$
	$OPD_{IntAct}^{WF} = 0.1204\mu m$

TABLE 4.10: Analytical estimation of the mechanical stroke requested by the atmospheric aberrations.

Stroke Calculation based on Numerical Simulations

Numerical simulations were performed with the purpose of estimating the necessary stroke, at different atmospheric conditions, and comparing it with the theoretical values. The simulations were carried out by using the Object-Oriented Matlab Adaptive Optics (OOMAO) toolbox, as in previous studies (see Chapter 3).

The actual simulation generated 10000 completely independent realizations of atmospheric turbulence corresponding to the two representative atmospheric profiles at the OT and computed the maximum difference of the wavefront on the OGS pupil at the approximate locations where the projection of the CILAS SAM97 actuators would be. The geometry of the simulation is shown in Figure 4.8.

For each independent realization of the simulated wavefront, only the values of the wavefront at the actuators locations were considered. The maximum value minus the minimum one was computed to obtain the wavefront stroke of this particular realization. This results on a total of 10000 independent total stroke values from which it was possible to derive a probability density function. Additionally, in order to estimate the actuator inter-stroke, all non-redundant non-repetitive combinations of the wavefront at any actuator position with its adjacent actuator along the x or y-axis were calculated at each one of the 10000 independent realizations of the atmosphere.

The histograms for the total stroke and absolute inter-stroke values are represented in Figure 4.9 to Figure 4.14, for both atmospheric situations ($r_0 = 9.17cm$ and $r_0 = 17.44cm$). Gaussian and log-normal fittings were attempted for all the probability distribution functions in case of total wavefront stroke and only Gaussian fitting in case of absolute interactuator wavefront stroke; the results from the fittings are gathered in Table 4.11.
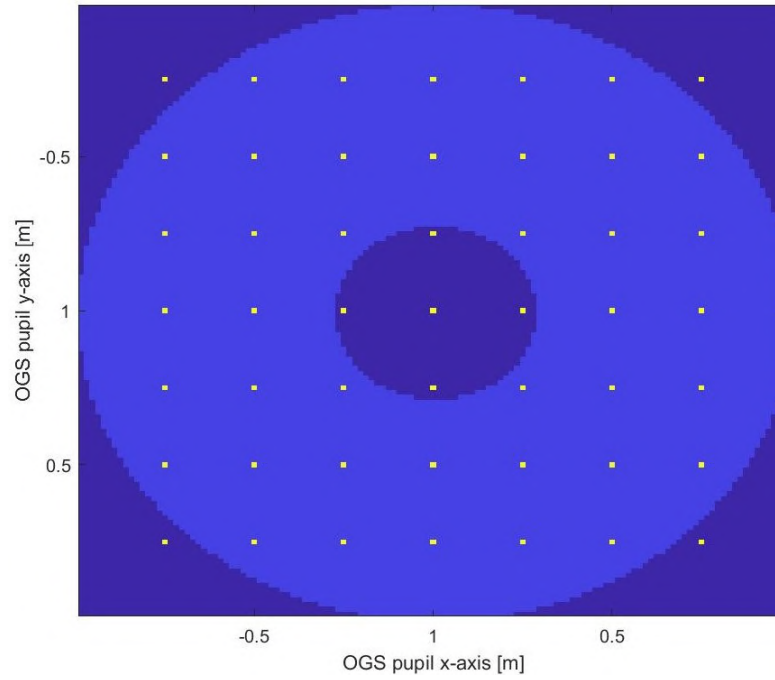
FIGURE 4.8: Arrangement of locations over the OGS entrance pupil where wavefront OPD values are measured. These locations correspond roughly to the actuators projection on the OGS Entrance pupil if a CILAS SAM97 DM were located at a pupil plane.

Numerical Estimation of DM Stroke	
$r_0 = \mathbf{17.44} cm$	
Gaussian Fitting	$OPD^{WF} = 1.6542 \mu m$ $OPD_{IntAct}^{WF} = 0.2015 \mu m$
Log-normal Fitting	$OPD^{WF} = 1.5755 \mu m$ $OPD_{IntAct}^{WF} = ^{(1)}$
$r_0 = \mathbf{9.17} cm$	
Gaussian Fitting	$OPD^{WF} = 2.7966 \mu m$ $OPD_{IntAct}^{WF} = 0.3391 \mu m$
Log-normal Fitting	$OPD^{WF} = 2.6635 \mu m$ $OPD_{IntAct}^{WF} = ^{(1)}$

[1] only fitted to Gaussian distribution

TABLE 4.11: Analytical estimation of the mechanical stroke requested by the atmospheric aberrations.
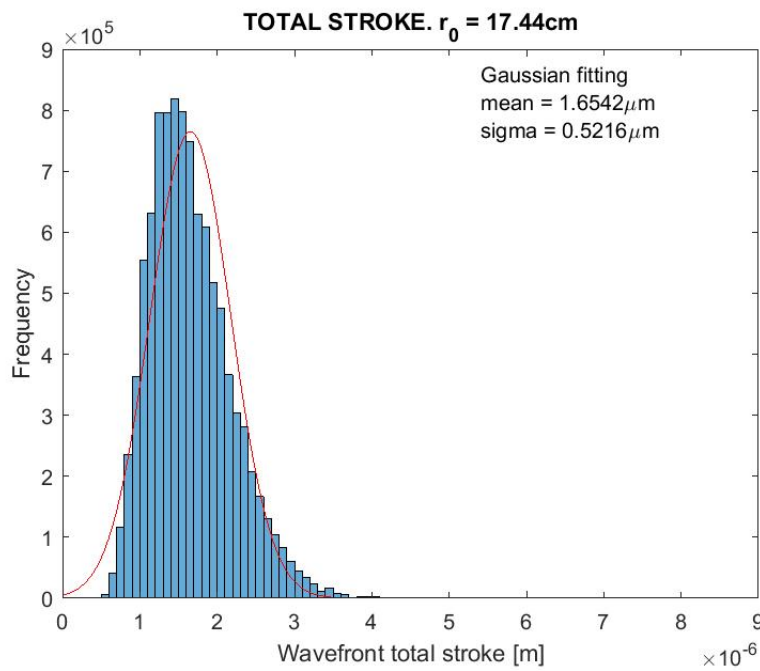
FIGURE 4.9: Histogram and corresponding Gaussian fitting of distribution of total WF stroke values for $r_0 = 17.44cm$. Notice the departure from a Gaussian PDF.
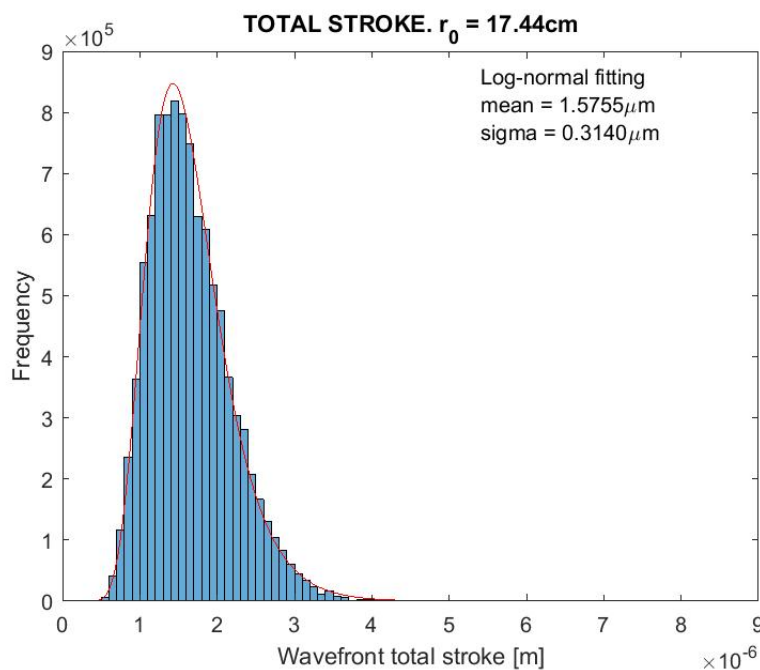
FIGURE 4.10: Histogram and corresponding Log-normal fitting of distribution of total WF stroke values for $r_0 = 17.44cm$. Notice the better fitting to a Log-normal PDF.
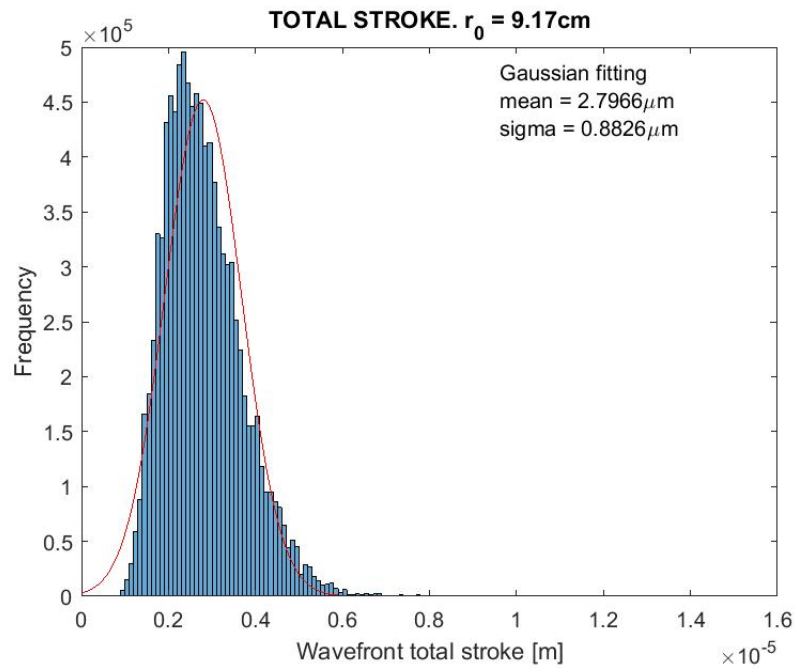
FIGURE 4.11: Histogram and corresponding Gaussian fitting of distribution of total WF stroke values for $r_0 = 9.17cm$. Notice the departure from a Gaussian PDF.
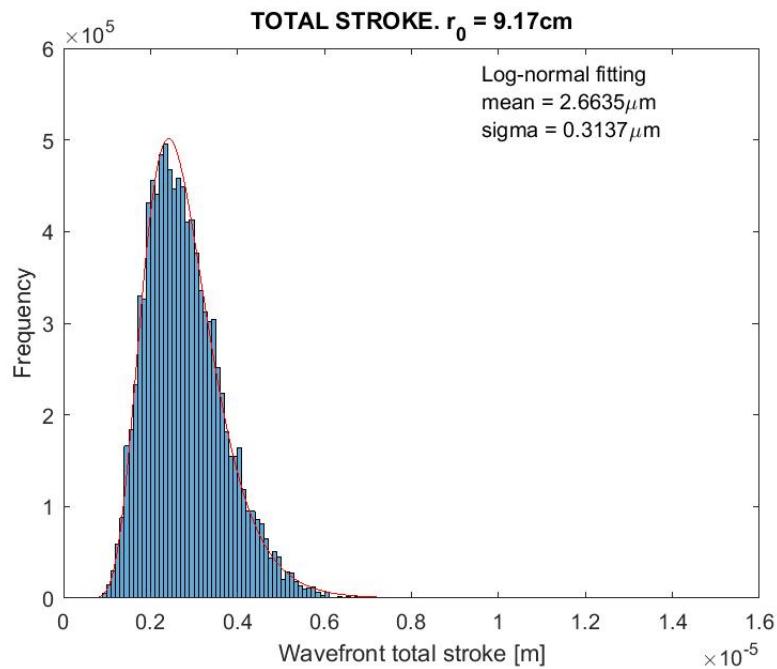
FIGURE 4.12: Histogram and corresponding Log-normal fitting of distribution of total WF stroke values for $r_0 = 9.17cm$. Notice the better fitting to a Log-normal PDF.
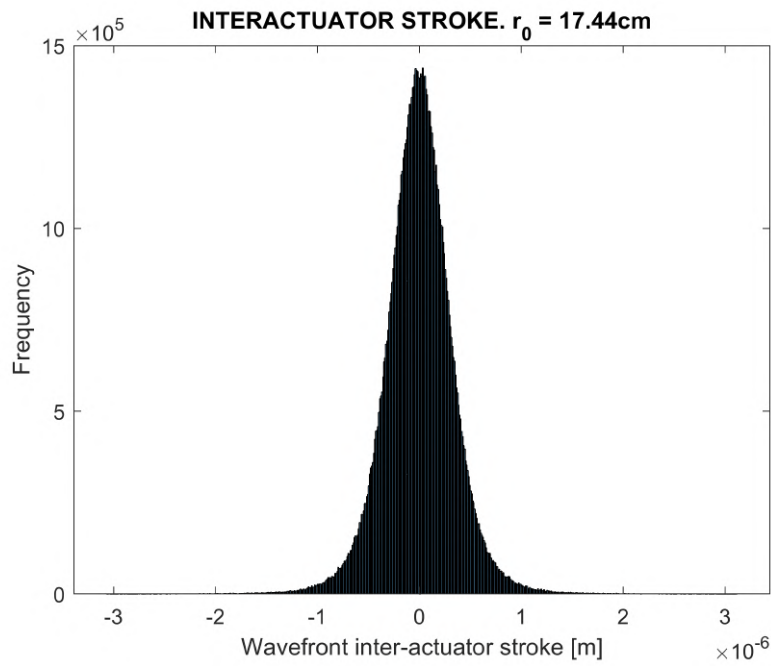
FIGURE 4.13: Histogram distribution of absolute interactuator WF stroke values for $rr_0 = 17.44cm$. Only Gaussian fit is attempted.
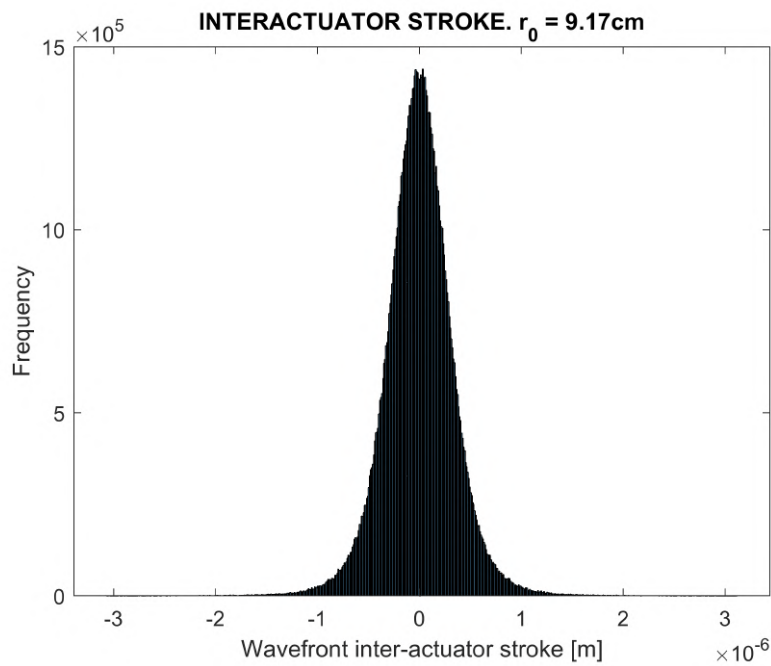
FIGURE 4.14: Histogram distribution of absolute interactuator WF stroke values for $rr_0 = 9.17cm$. Only Gaussian fit is attempted.

Results from both analytical and numerical simulations are gathered in Table 4.12 for comparison purposes; the similarity in the results obtained by both methods validate the simulation results. Log-normal fitting has been selected as the best fit for total stroke wavefront values.

Seeing Scenario	Analytical Estimation of DM Stroke	Numerical Estimation of DM Stroke
$r_0 = 17.44cm$	$OPD^{WF} = 1.8971\mu m$ $OPD^{WF}_{IntAct} = 0.0795\mu m$	$OPD^{WF} = 1.6542\mu m$ $OPD^{WF}_{IntAct} = 0.2015\mu m$
$r_0 = 9.17cm$	$OPD^{WF} = 3.2414\mu m$ $OPD^{WF}_{IntAct} = 0.1204\mu m$	$OPD^{WF} = 2.7966\mu m$ $OPD^{WF}_{IntAct} = 0.3391\mu m$

TABLE 4.12: Comparison between analytical and numerical estimations of DM total and interactuator stroke.

4.4.2 DM Selection

Table 4.13 shows the main salient features of the CILAS SAM97 deformable mirror. According to the manufacturer, the CILAS SAM97 should be able to deliver total strokes of $\pm 2\mu m$ and inter-actuator stokes of $\pm 1\mu m$. Therefore, it is a suitable candidate to pre-correct the LGS at the UWCS-I.

GEOMETRIC CONFIGURATION	
Minimum clear aperture	$98mm$
Number of active actuators	97 in $11x11$ array
Actuator spacing	$8mm$
OPERATIONAL CHARACTERISTICS	
PV Mechanical stroke (after flattening)	$> 4\mu m$
Mechanical inter-actuator stroke	$> 2\mu m$
Gaussian influence function (mechanical coupling)	$< 20\%$
Actuator hysteresis	$< 5\%$
Actuator linearity	$< 5\%$
Resonance frequency	$> 20kHz$
OPTICAL CHARACTERISTICS	
Best flat wavefront error	$< 20nm$ rms
Stroke to flatten the DM	$< 10\%$ full stroke
Surface roughness	$< 2nm$ rms

TABLE 4.13: CILAS SAM97 deformable mirror technical details.

Under the worst considered conditions in this research, the CILAS SAM97 would perform comfortably to deliver enough stroke values without incurring into saturation. The stroke budget for the correction of Non-Common Path Aberrations (NCPA) was not estimated, although it is assumed the CILAS SAM97 has large enough margins to handle them if required.

4.5 Wavefront Sensor System

The wavefront sensor would consist of a plenoptic camera built with the OCAM2S camera and a lenslet array that was customised for the specific OGS set-up. The

OCAM2S technical details are gathered in Table 4.14.

OCAM2S Camera	
QE	95% (peak)
Sensor active area	240x240 pixel
Microlenses array	Table 4.15
Frames per second	2067 fps (full frame) 3700 fps (binning 2x2)

TABLE 4.14: OCAM2S Camera Technical Details.

Several designs of microlenses arrays were custom-built to fulfil the optical requirements of both Cassegrain and Coudé focus, although only the Coudé focus configuration would be taken into account from now on. In order to avoid the blurring effects, which were introduced by the microlenses, the F number of the optical set-up shall be equal to the F number of the ensemble "camera + lenslet array" (Rodríguez Ramos, 2015).

The mathematics under the design criteria is the following: the Coudé configuration has a 38.8-meter focal length which, with a telescope diameter of 1m, results in F/38.8; the OCAM2S camera has a 240x240 pixel sensor with 24 μm/px. Depending on the number of microlenses in the lenslet array, each subaperture subtends a certain number of pixels per microlens and hence, a defined size in microns. With the purpose of minimizing the blurring, the ratio in Eq. 4.8 needed to be maintain as equal as possible.

$$\frac{D_{telescope}}{f_{telescope}} = \frac{d_{microlens}}{f_{microlens}} \tag{4.8}$$

Where f corresponds to focal length and $d_{microlens}$ to the subaperture size. All terms in meters.

Having into account this principle, the available lenslet arrays are gathered in Table 4.15. Its final selection would be performed based on the outcome of the photon return flux estimation (Section 4.6).

LENSLET ARRAYS				
Number of microlenses	12x12	16x16	20x20	24x24
Focal length	12 mm	12 mm	12 mm	12 mm
Pitch	480 μm	360 μm	290 μm	240 μm
Clear aperture	7.5 x 7.5 mm			
Substrate material	Fused Silica			

TABLE 4.15: Technical details of the available lenslet arrays for the Coudé focus. The lenslet arrays were manufactured by Power Photonic.

The OCAM2S differs from the similar model OCAM2k in its sensor type: the OCAM2S mounts one EMCCD219, a derivative of the EMCCD220 used in standard OCAM2K cameras. Each pixel has an embedded shutter system consisting of an extra drain. The shutter can be driven externally through the backside synchro connectors, or internally synchronous with the CCD frame readout. The external connector Synchro-in is used to synchronize the camera acquisition with the firing of the laser pulses.

In Burst operation mode, multiple shutter openings are issued after being triggered by the frame integration start (Synchro-in signal). This functionality allows the acquisition of several laser pulses within the same frame. The blanking period separating two pulses in this mode shall be equal to the laser idle time (time the light takes to reach the 20-km atmospheric layer). However, the electronic shutter only reduces the incoming light onto the detector by a factor of 1000, which is unfortunately not enough to deal with the extreme difference in power existing between the uplink and downlink beams.

4.5.1   WFS Optical Chopper

The UWCS was designed for shared-path operation: both laser launch and photon return follow a common optical path to a certain extent. Therefore, not only the LGS system needed an optical chopper, but also the wavefront sensor system; an optical chopper placed right before the WFS would avoid the sensor saturation when the laser is propagating and would allow the direct measurement of the Rayleigh return at the desired atmospheric height.

A second unit of the SCITEC INSTRUMENTS 310CD optical chopper was selected with the purpose of facilitating the synchronization between subsystems (described in section 4.9). The technical details of the unit are the ones described in the section 4.3.2.

4.5.2   WFS Focusing Stage

The WFS would be mounted on a linear stage with the purpose of ease the conjugation of the pupils in the optical system, as the pupil in the lenslet array needs to be conjugated to the pupil in the deformable mirror.

The NEAT 310 was selected as the focusing stage for the WFS. Its technical details are gathered in Table 4.16.

NEAT 310 Linear Stage	
Travel Range	120 mm
Drive Type	Stepper motor
Stage Type	Linear actuator
Feedback	Encoder and home switch

TABLE 4.16: NEAT 310 linear stage technical details

4.6   Rayleigh Photon Flux Return

The Rayleigh photon flux return from a Laser Guide Star depends not only on the atmosphere properties, but also on the system design. Hence, the photon flux return was estimated for the UWCS specifically in this section.

The light from the launched laser would fill the conical volume shown in Figure 4.15. The base of the cone is located at the telescope primary mirror and its tip is positioned at the focus height of the LGS (20km). Once the laser reaches this point, its beam creates a waist of certain diameter and continues up to the sky filling an inverted cone, which starts at this 20km height. The laser return signal would come from the volume comprised between the focus point plus a Δz distance which covers certain fractions of the upper and lower light cones. The scattering depth (Δz)
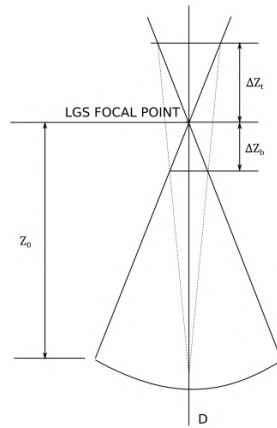
FIGURE 4.15: Schematic representation of the laser projection geometry.

was calculated for an optimal LGS return, using the expression 4.9 (Thompson and Teare, 2002).

$$\Delta z = \frac{4.88 \lambda z_0^2}{D r_0} \tag{4.9}$$

Where Δz is the scattering depth in m, λ is the laser wavelength, z_0 is the LGS focus point, D is the diameter of the launch aperture, and r_0 is the Fried parameter.

The scattering depth was calculated for two atmospheric turbulence cases, both extracted from previous simulations (see Chapter 3) and the corresponding values are gathered in Table 4.17. Only night-time atmospheric profiles were taken into account to operate the Rayleigh laser guide star.

Scattering depth (Δz)	
$r_0 = 17.44cm$	$\Delta z = 5.9km$
$r_0 = 9.17cm$	$\Delta z = 11.3km$

TABLE 4.17: Scattering depth for optimal return calculated for the study case: $D = 1m$, $\lambda = 532nm$ and $z_0 = 20km$.

The photon return due to Rayleigh backscattering in the atmosphere was estimated using the LIDAR equation (Gardner, 1989), whose expression is presented in Eq. 4.10.

$$N(z) = N_0 N_I N_{II} N_{III} N_{IV} \tag{4.10}$$

where N_0 are the laser emitted photons, N_I is the system efficiency, N_{II} describes the probability of a photon to be backscattered, N_{III} responds to the probability of that backscattered photon to be received by the telescope and N_{IV} is the laser extinction due to its propagation through the atmosphere. All terms are described in Eq. 4.11, Eq. 4.12, Eq. 4.13 and Eq. 4.14 but the last one, assumed to be despicable.

$$N_0 = \frac{P_L t}{hc / \lambda} \tag{4.11}$$

$$N_I = \eta T_A^2 \tag{4.12}$$

$$N_{II} = \sigma_R \rho(z_i) \Delta z M_{air}^{-1} N_A \tag{4.13}$$

$$N_{III} = \frac{A}{4\pi z_i^2} \tag{4.14}$$

Where P_L is the laser power (W), t is the exposure time of the WFS camera, h is the Planck's constant, c is the speed of light, λ is the laser wavelength, η is the quantum efficiency (QE) at the desired wavelength of the WFS multiplied by the system optical throughput, T_A is the atmospheric transmittance (which follows Eq. 4.15, explained below), σ_R is the Rayleigh scattering cross-section (Eq. 4.16, described below), ρ is the atmospheric density at $z_i = z + \Delta z$ and $z_{i+1} = z - \Delta z$, Δz is the scattering depth, M_{air} is the air molar mass (it would be assumed dry air), N_A is the Avogadro number, and A is the receiver telescope area.

$$T_A = 10^{-0.4\zeta A_\lambda} \tag{4.15}$$

Where ζ is the air mass, depending on the observer angle (at zenith = 1) and A_λ is the extinction coefficient. The atmospheric extinction coefficient has been monitored at Roque de los Muchachos Observatory by the Carlsberg Meridian Telescope for the last 20 years (*Atmospheric Extinction from the CMT*) at the visible band (550nm). All measurements were assumed to be valid at 532nm.

The atmospheric transmittance was estimated by selecting three different scenarios (average, high dust level and low dust level) and their related atmospheric extinction coefficient (Table 4.18). Observations were assumed to be at zenith ($\zeta = 1$).

Atmospheric Transmittance (T_A)		
Low dust level	$A_\lambda = 0.1$	$T_{ALD} = 0.9120$
Average	$A_\lambda = 0.12$	$T_{AA} = 0.8954$
High dust level	$A_\lambda = 0.5$	$T_{AHD} = 0.6310$

TABLE 4.18: Atmospheric transmittance for three different scenarios, based on measurements of the atmospheric extinction coefficient at ORM.

The Rayleigh scattering cross-section, σ_R, was calculated by taking into account the backscattered photons coming back towards the telescope aperture. It follows Eq. 4.16.

$$\sigma_R = \sigma_{RT} q(180°) 4\pi \tag{4.16}$$

$$\sigma_{RT}(x10^{-28} cm^2) = \frac{1.0455996 - 341.29061\lambda^{-2} - 0.90230850\lambda^2}{1 + 0.0027059889\lambda^{-2} - 85.968563^2} \tag{4.17}$$

The expression 4.17, extracted from (A Bodhaine et al., 1999), presents an accuracy better than 0.01% over the 250-800nm range. Units for λ in Eq. 4.17 are μm. $q(\omega)$ is the phase function $\int q(\omega) d\omega = 4\pi$, which adopts the value $q(180°) = 300/203$ (Fricke and Zahn, 1985).

Figure 4.16 shows the estimated photon flux return received through the whole telescope aperture and its dependence on the exposure time of the WFS detector. Figure 4.17 presents the results at WFS subaperture level. All calculations were performed with the parameters in Table 4.19. Larger levels of photon return are detected with worst seeing conditions due to the fact that, with stronger atmosphere, the optimal scattering depth is increased. Both graphics take into account a minimum integration time of 0.5ms (OCAM2S WFS maximum working frequency = 2kHz) and

a maximum integration time of 10ms (atmospheric coherent length). Notice that the WFS binning capabilities would increase the photon return per frame.

LGS Operation - Photon Flux Return	
Laser Power (P_L)	$18W$
Wavelength (λ)	$532nm$
QECCD at $\lambda = 532nm$	0.83
System Optical throughput	0.7611
Atmospheric Transmittance	$T_{ALD} = 0.9120$ $T_{AA} = 0.8954$ $T_{AHD} = 0.6310$
Rayleigh Scattering Cross-section	$5.1672m^2$
Scattering Depth	$\Delta z = 5.9km(r_0 = 17.44cm)$ $\Delta z = 11.3km(r_0 = 9.17cm)$
LGS Focus Height	$z = 20km$
Teide Observatory Height	$Z_{obs} = 2.390km$
Atmospheric Density[1]	$\rho(20 - 5.9km + Z_{obs}) = 0.1632kg/m^3$ $\rho(20 + 5.9km + Z_{obs}) = 0.0258kg/m^3$ $\rho(20 - 11.3km + Z_{obs}) = 0.3658kg/m^3$ $\rho(20 + 11.3km + Z_{obs}) = 0.0131kg/m^3$
Telescope Diameter	$1m$
WFS lenslet array	$12x12 subapertures$ $16x16 subapertures$ $20x20 subapertures$ $24x24 subapertures$

[1]*Extracted from International Standard Atmosphere*

TABLE 4.19: System parameters for the photon flux return estimation.

The signal-to-noise ratio (SNR) defines the ratio between the signal power and the noise power and it is an indicator of the measurement quality of an object, in this case, the laser guide star. The noise level for a typical astronomical observation consists of three components: the readout noise, a signal independent noise arising from the detector itself; the photon shot noise from the object being observed (LGS); and the shot noise in any background signal (particularly the sky background). Adding the noise terms in quadrature, the signal to noise ratio (SNR) is given by Eq. 4.18.

$$SNR = \frac{N}{\sqrt{N + S_{SKY} + S_{PHOTON} + S_{READOUT}}} \tag{4.18}$$

Where N are photons per second and the noise components are described in Eq. 4.19 to Eq. 4.22.

$$S_{SKY} = N_{20}10^{-(s-20)/2.5}scale^2binning^2 \tag{4.19}$$

$$scale = \frac{\tan^{-1}(D/f)}{D}pxSize \tag{4.20}$$

$$S_{PHOTON} = s_{CCDph}t\sqrt{F} \tag{4.21}$$

$$S_{READOUT} = s_{CCDreadout}/pxSubap \tag{4.22}$$

Where N_{20} is the observed count rate at V band and s is the sky brightness; S_{SKY} and S_{PHOTON} are expressed in photons per second and pixel, and $S_{READOUT}$ is expressed
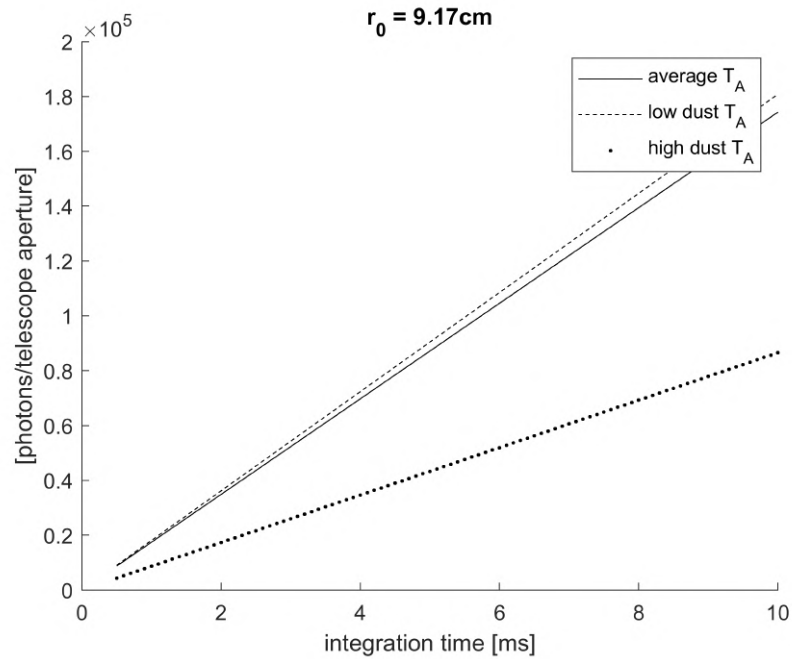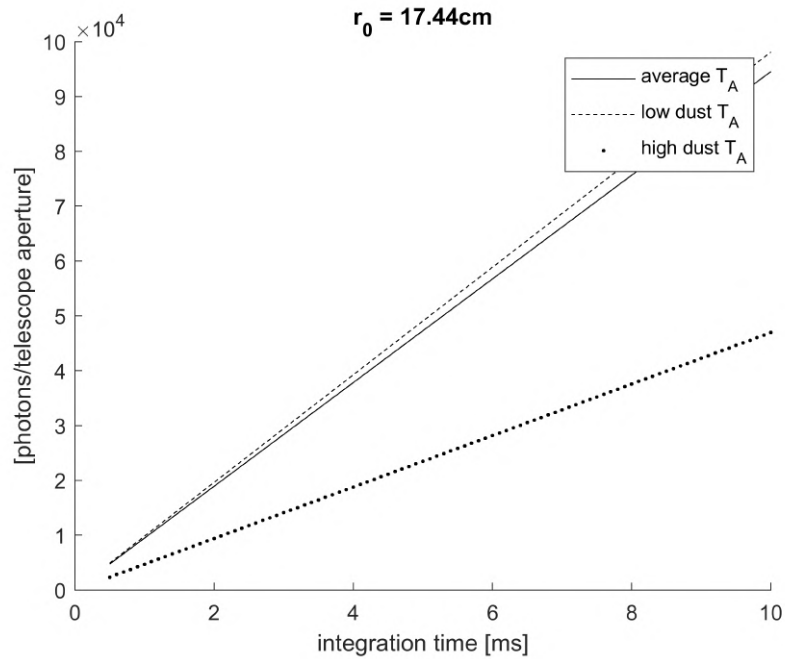
FIGURE 4.16: Estimated photon flux return received through the whole telescope aperture. Notice that with stronger atmosphere, the optimal scattering depth is increased ($\Delta z \propto 1/r_0$) and hence, the received number of photons is larger; (a) Seeing conditions: $r_0 = 17.44cm$; (b) Seeing conditions:$r_0 = 9.17cm$. Continuous line: average atmospheric transmittance; dashed line: low dust level atmospheric transmittance; pointed line: high dust level atmospheric transmittance
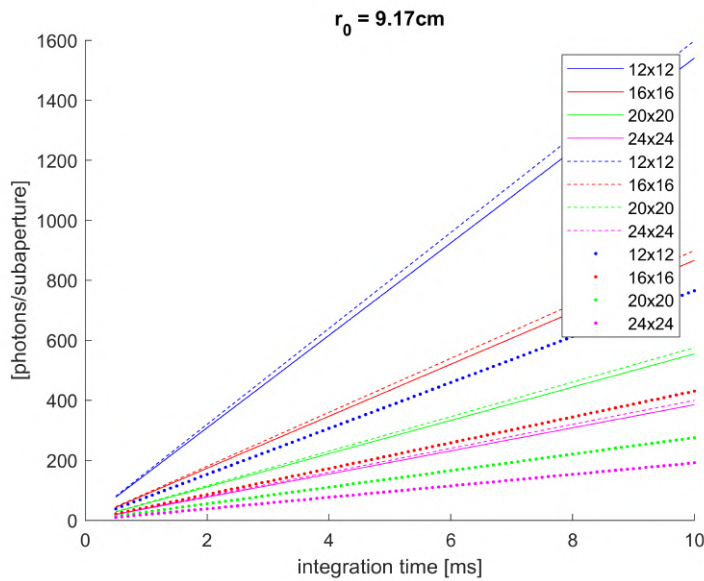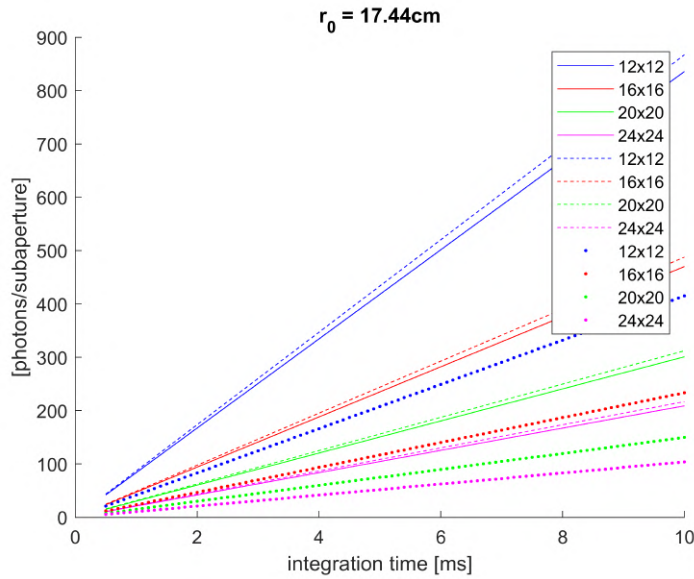
FIGURE 4.17: Estimated photon flux return received at each WFS subapertures for different lenslet array configurations. Notice that with stronger atmosphere, the optimal scattering depth is increased ($\Delta z \propto 1/r_0$) and hence, the received number of photons is larger; (a) Seeing conditions: $r_0 = 17.44cm$; (b) Seeing conditions:$r_0 = 9.17cm$. Continuous line: average atmospheric transmittance; dashed line: low dust level atmospheric transmittance; pointed line: high dust level atmospheric transmittance.

in photons per pixel. Due to the fact that the OCAM2S has an EMCCD detector, which suffers from excess noise (or multiplication noise), the *F* factor needs to be included in the computation of the photon noise; this factor quantifies the noise introduced by the electronic gain itself and it falls within the range $1.3 < F < 2$ (Denvir and Conroy, 2003). $F = 2$ was considered for the SNR computation.

There is a third error source at the CCD level of the WFS, apart from the readout and photon noise: noise derived from the production of thermal electrons in the sensor substrate. However, thermal noise (or dark current noise) can be minimised by cooling down the CCD to the point where it is negligible. The OCAM2S camera integrates a cooling system at this respect.

The zenith brightness of the night sky at the Roque de los Muchachos Observatory (ORM, La Palma) was measured on 63 nights during 1987-1996 by the ING telescope. It is a function of lunar phase, particularly at the bluer wavelengths: moonlight brightens the sky by about 1 mag (quarter moon, phase 0.5) to 4 mag (full moon) in U, B and V (*La Palma Night-Sky Brightness*). Due to lack of data at the OT, the average value of sky brightness at the ORM for the V-band measured during full moon nights was assumed to be valid at the OT as the worst case scenario of sky background contribution. A value of $s = 20.9mag/arcsec^2$ (*La Palma Night-Sky Brightness*) was considered in the calculations.

The SNR was calculated at the subaperture level based on the detected photon return flux per integration time. The parameters for the SNR calculation are gathered in Table 4.22.

LGS Operation - SNR	
N_{20} at V wavelength[1]	$1521e^-/s$
Sky brightness at V wavelength and full moon	$s = 20.9mag/arcsec^2$
Telescope Diameter	$D = 1m$
Telescope Coudé Focus Focal Length	$f = 38.8m$
OCAM2S sensor size	$240x240pixel$
OCAM2S pixel size	$24\mu m$
OCAM2S photon noise	$s_{CCDph} = 0.01e^-/px$
OCAM2S readout noise	$s_{CCDreadout} = 0.3e^-$

[1]Extracted from data of LRIS instrument at Keck Observatory

TABLE 4.22: Parameters for the Signal-to-Noise calculation

Figures 4.18 and 4.19 show the SNR results for the atmospheric scenarios taken into account in previous calculations and two binning conditions for the WFS.

In general, one can consider fairly good scenario for measurements, a SNR value above 10. Based on the results, the 12x12 lenslet array was selected to be the optimum for the UWCS I, although, it is likely that, in order to run the system at the maximum speed of the WFS (2000 fps), the sensor electronic gain needed to be applied, as the SNR was expected to be below 10 at integration times of $500\mu s$.

4.7 UWCS Final Optical Layout

The UWCS I final design is illustrated in Figure 4.20. It would be placed on an optical table with dimensions 2500 (L) x 1250 (W) x 60 (H) mm. The UWCS I has five subsystems: the laser launch system, the sensor and corrector system (WFS+DM), the injection system and the calibration system (which is illustrated in Figure 4.21).
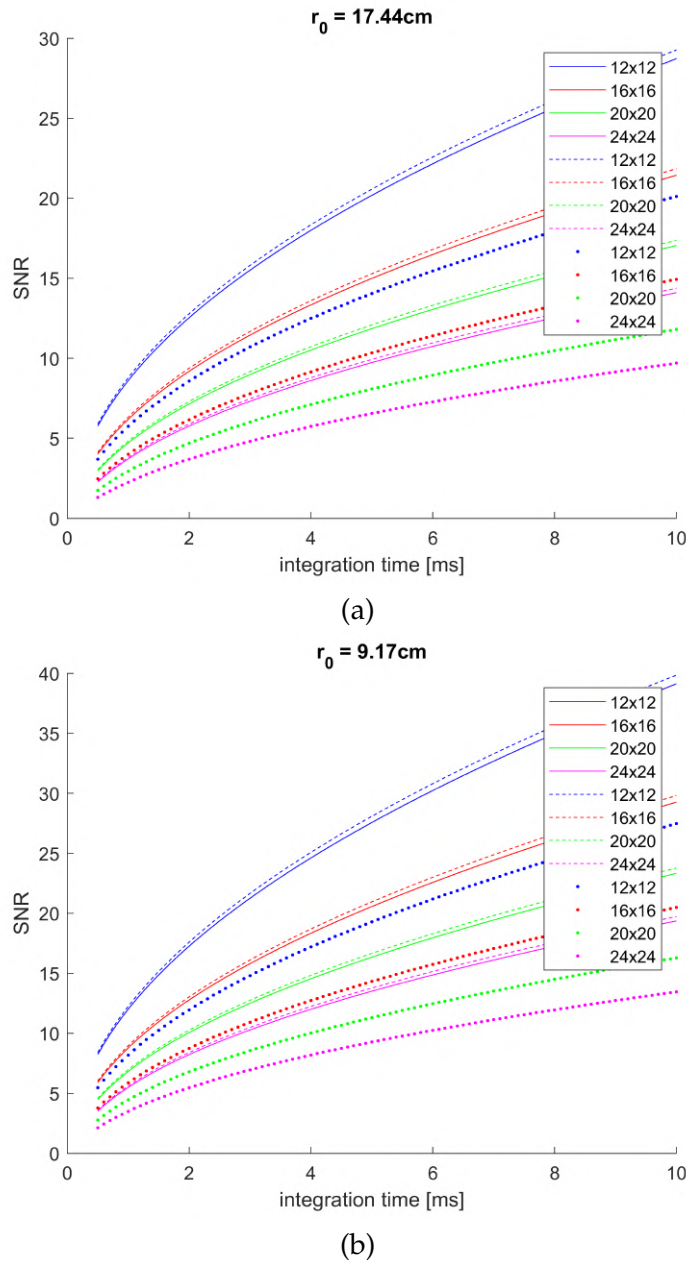
FIGURE 4.18: Signal-to-noise ratio at each WFS subapertures for different lenslet array configurations. (a) Seeing conditions: $r_0 = 17.44cm$; (b) Seeing conditions: $r_0 = 9.17cm$. Continuous line: average atmospheric transmittance; dashed line: low dust level atmospheric transmittance; pointed line: high dust level atmospheric transmittance. No binning at the CCD.
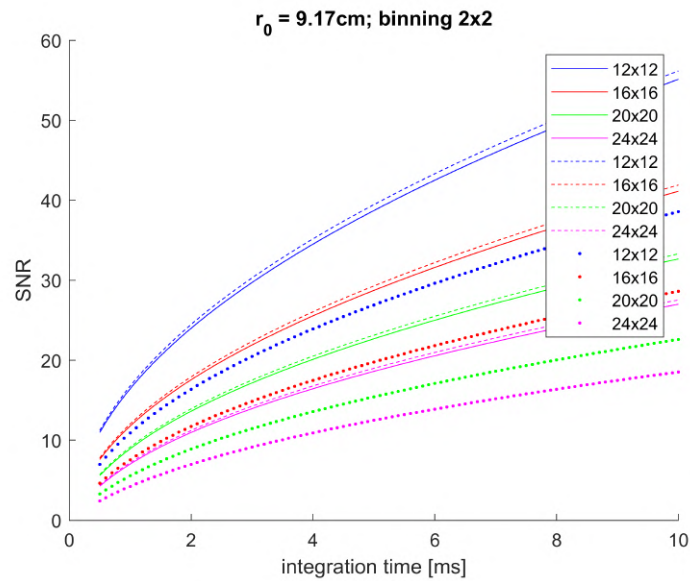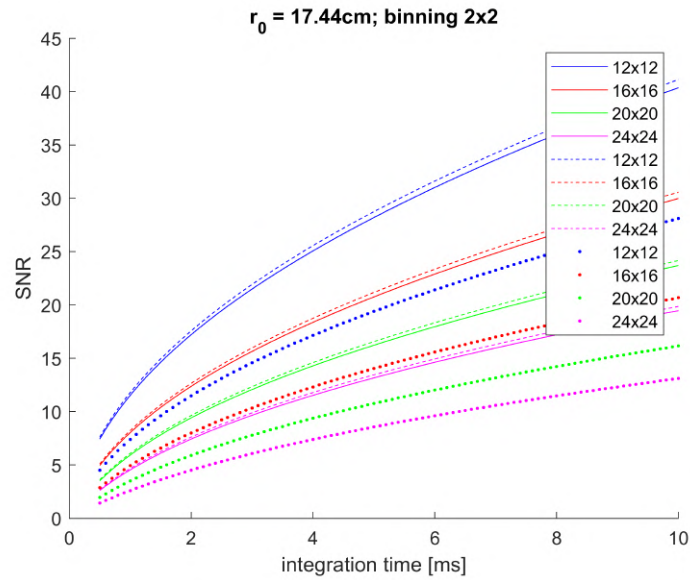
FIGURE 4.19: Signal-to-noise ratio at each WFS subapertures for different lenslet array configurations. (a) Seeing conditions: $r_0 = 17.44cm$; (b) Seeing conditions: $r_0 = 9.17cm$. Continuous line: average atmospheric transmittance; dashed line: low dust level atmospheric transmittance; pointed line: high dust level atmospheric transmittance. 2x2 binning at the CCD.
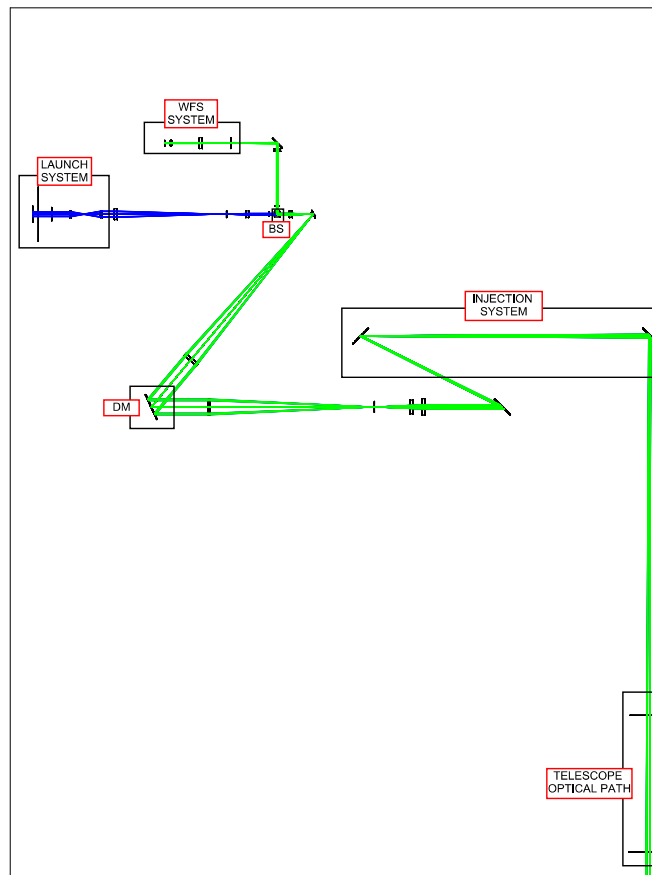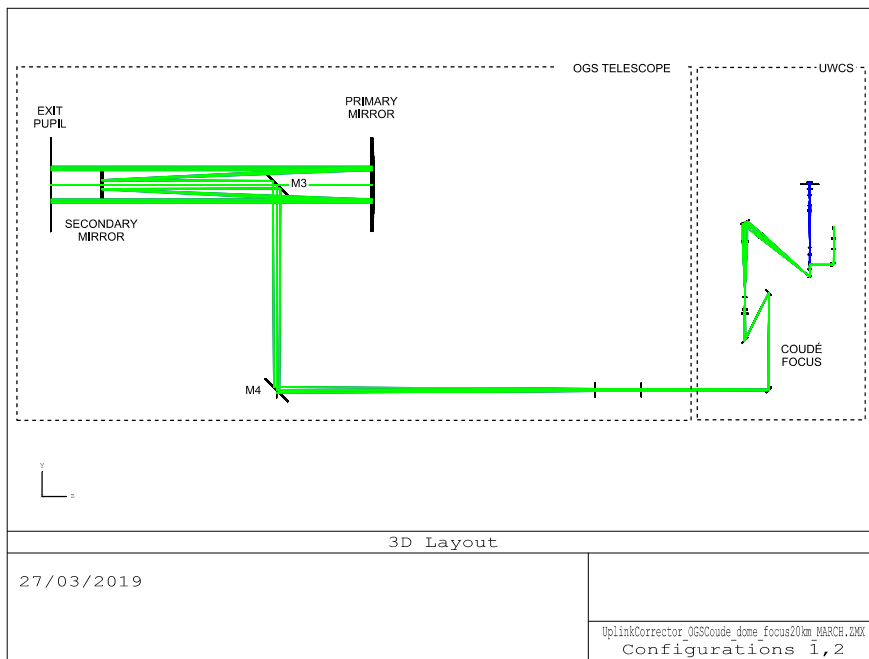
FIGURE 4.20: UWCS-I final design. Launch and return path are represented in green and blue. Full layout above; Zoom section with main elements from the laser launch system to the M6 mirror in the telescope Coudé path, below.
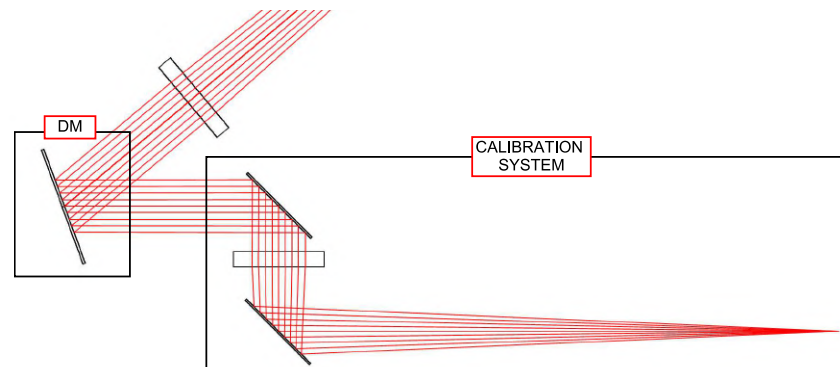
FIGURE 4.21: The calibration system leads the calibration light to the DM with a movable mirror which is introduced or removed from the optical path with the help of a mount, this one fixed to the table and positional pins, those ones fixed to the mirror.

The laser launch system and the sensor and corrector system have already been described in previous sections.

The calibration system was introduced in the design as a backup solution in case the interaction matrix between the DM and the WFS could not be computed from the LGS signal itself. It would consist of the JSDU Helium-Neon laser head and a pin-hole (which would also be part of the Simulation Test Bench, see Chapter 5), a collimating lens and a mirror pair to fold the beam onto the deformable mirror.

The injection system would lead the beam to the telescope tube by a three-mirror system in kinematic mounts which would fold the beam and change its angle until it reaches the telescope axis.

Table 4.26 gathers all the optical elements in the UWCS I.

SUBSYSTEM	ELEMENT	TYPE	FOCAL LENGTH (mm)	DIAMETER (mm)
Launch System	BE	Beam Expander	-	25
	AX+	Axicon	-	25
	AX-	Axicon	-	25
	L1	Lens	400	25
	L2	Lens	100	25
Sensor System	BS	Beam Splitter	-	25
	L3	Lens	600	25
	M1	Mirror	-	30
	L4	Lens	600	25
	LA	Lenslet Array	12	5.76
	CAM	Sensor	-	5.7
Corrector System	L5	Lens	75	25

	M2	Mirror	-	30
	L6	Lens	700	60
	DM	Deformable Mirror	-	100
	L7	Lens	600	60
	L8	Lens	200	60
	L9	Lens	700	60
Injection System	M3	Mirror	-	100
	M4	Mirror	-	100
	M5	Mirror	-	100
Calibration System	PHCalib	Pin Hole	-	5
	M1Calib	Mirror	-	30
	L1Calib	Lens	400	60
	M2Calib	Mirror	-	100

TABLE 4.26: Optical elements in the UWCS-I.

4.8 UWCS Control System

The UWCS Control System would cover software design regarding both on-line and off-line data processing; meaning by "on-line processing", all data treatment inside the Adaptive Optics loop, and by "off-line processing", necessary actions to be taken outside the control loop (i.e. plenoptic camera calibration).

The software architecture is presented in Figure 4.22. Both off-line and on-line data processing would be hosted in the Real Time Computer (RTC).
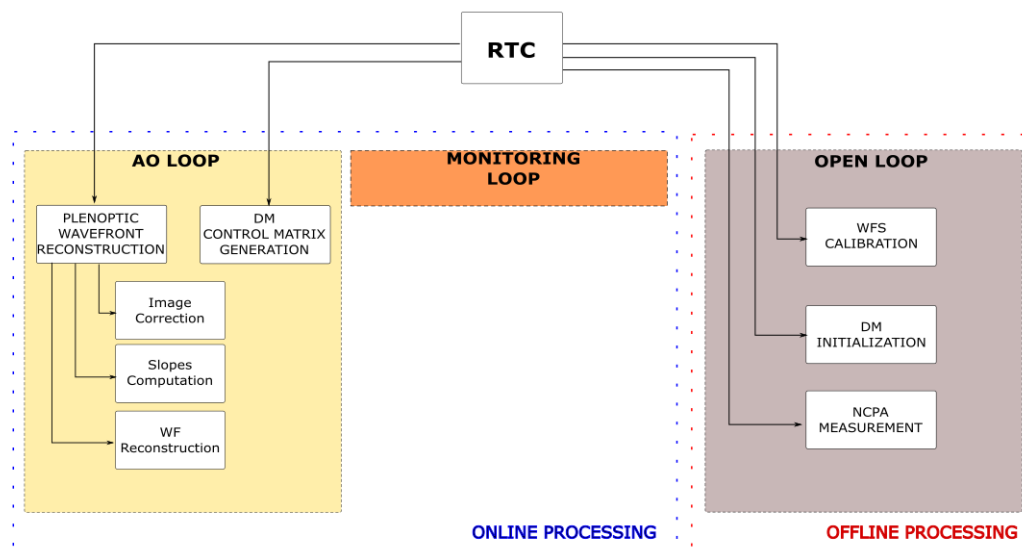
FIGURE 4.22: UWCS software architecture.

4.8.1 On-line Data Processing

The UWCS online data processing would gather all the processes to be carried out in real time inside the AO loop, as it is the treatment of acquired plenoptic images to reconstruct the incoming atmospheric wavefront and later on, the generation of DM

actuators commands. Additionally, it would also comprise the monitoring loop, at lower frequency but also real time.

Adaptive Optics Closed Loop

One general AO loop was considered in the UWCS: both tip-tilt and higher order aberrations would be corrected within it using only one deformable mirror. It would be a fast loop with a cycle rate between 150Hz and 2000Hz, depending on NGS magnitude and atmospheric conditions.

- TIP-TILT RECONSTRUCTION: Tip-tilt reconstruction would be performed by measuring the atmospheric turbulence with a NGS as a reference. As both NGS and LGS would be inside the plenoptic camera FOV, the artificial star would be the focused one whereas the natural star would be out-of-focus, as their height differs from one to the other (20-kilometre layer versus infinity).

- HIGHER ORDER MODES RECONSTRUCTION: Higher order aberrations would be reconstructed by using the Laser Guide Star as a reference. Combination of both measurements would derived into the commands for the DM actuators.

The servo control scheme is represented in Figure 4.23; $x(t)$ is the wavefront external disturbance, $m(t)$ is the AO wavefront correction and $e(t)$ is the wavefront error after AO correction. $X(s)$, $M(s)$ and $E(s)$ are their Laplace transforms. Bandwidth error budgets are not addressed.
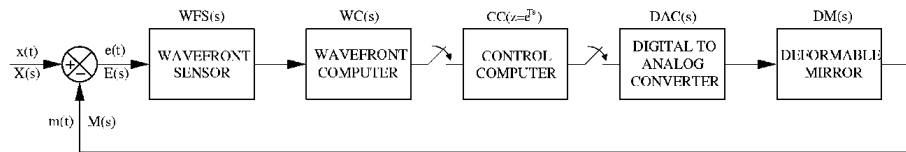
FIGURE 4.23: UWCS servo control block diagram.

Plenoptic Wavefront Reconstruction Once the image acquisition of the wavefront sensor has finished, every image shall be deeply analysed in order to extract turbulence information. The procedure is divided into three phases: image correction, slopes computation and wavefront reconstruction (Figure 4.24).
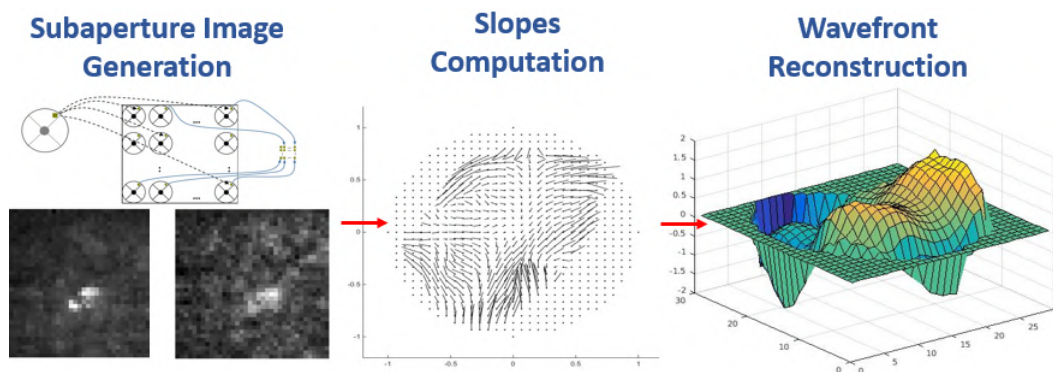
FIGURE 4.24: Plenoptic images processing.

- IMAGE CORRECTION: Every image to be used within the AO loop shall be flat-field and bias corrected.

- SLOPES COMPUTATION: The plenoptic camera allows the image synthesis of each aperture point independently and therefore, it is possible to make profit of all available techniques for the Shack-Hartmann sensor. Once the subaperture images are extracted, correlation techniques allow the estimation of the lateral displacements among them. This information would grant, after a global integration, the wavefront extraction and of course, the control matrix generation.

- WAVEFRONT RECONSTRUCTION FROM GRADIENTS: The wavefront reconstruction from gradients would be performed by following the procedure in Rodríguez Ramos (2015), which has been deeply described in Chapter 2.

DM Control Matrix Generation   Once the slopes have been computed from the plenoptic measurements and the interaction matrix of the DM is well-known (WFS/DM calibration), the control matrix would be generated by inverting this interaction matrix.

The commands vector would be obtained by multiplying the measured slopes by the control matrix. These commands ($m(t)$) would be calculated at each step of the AO loop by adding the measured slopes (σ) times the control matrix (∇) times the AO system gain to the last iteration calculated commands (Eq. 4.23).

$$m(t) = m(t-1) + gain\tau\nabla\sigma \tag{4.23}$$

Monitoring Loop

The UWCS monitoring loop would provide information about status of each subsystem. It would be configurable at a maximum frequency of 10 Hz and minimum of 1 hour and the variables to be monitored are gathered in Table 4.27.

Variable	Monitoring Frequency
WFS centroids status	10 Hz
DM actuators status	10 Hz
Wavefront error	10 Hz
Ref. Source position in the WFS frame	2 min

TABLE 4.27: UWCS variables in the monitoring loop.

4.8.2   Off-line Data Processing

The off-line data processing in UWCS covers wavefront sensor calibration (mainly plenoptic camera) and the deformable mirror initialization.

Wavefront Sensor Calibration

The UWCS wavefront sensor needs to be calibrated: some features of the plenoptic camera shall be well-known in order to reconstruct the wavefront from the acquired images.

Plenoptic calibration procedure consists of getting information regarding the positions of the multiple pupil images (from the lenslet array) and their relationship with the detector pixels. This knowledge would be extracted from some physical

parameters: the positions of the microlenses centers and consequently, the pitch in between one microlens and its neighbour, and the tilt between the pixel lines in the sensor and the microlenses within the array.

Pitch would be estimated by a two-dimensional Fourier transform of the base image, whose module will present a peak in the pitch inverse spatial frequency and which would be detected by thresholding this spatial frequency into some lower and upper bounds. Simultaneously, the inclination would also be calculated by this method and as a result of the pitch and inclination data, a grid with one microlens per square is built. Microlenses centre positions would then be obtained by computing the center of mass of the light inside each grid square.

The calibration procedure would require a bias corrected flat-field image to achieve optimum performance.

Deformable Mirror Initialization

The Deformable Mirror would need to be initialized after the UWCS is switched on as the actuators and WFS subapertures interaction matrix is a priori unknown.

The DM initialisation would need to follow a two-step procedure: mirror flattening and interaction matrix calculation. Both actions would be performed with a calibration source in the optical bench.

The mirror flattening consists of sending specific commands to the actuators in order to create the best flat surface on the DM. Several procedures for mirror flattening are described in literature, mostly based on interferometric measurements and the iterative correction until the local surface slope is reduced (Briguglio et al., 2018).

The matrix representing the response of each actuator on the WFS, called interaction matrix, would be obtained during the DM/WFS initialization by actuating each actuator individually and measuring the derived wavefront slopes.

4.9   UWCS Synchronisation System

As it has been stated in the Wavefront Sensor System description (Section 4.5), the UWCS would operate in shared launch mode, which is translated into a common optical layout among the launch and return paths and the consequent use of two optical choppers in synchronised operation for the laser propagation and the acquisition of the onwards Rayleigh return by the WFS.

A Tektronix AWG2021 Arbitrary Waveform Generator was selected as the device to carry out the synchronization, together with the SCITEC Synchroniser. The signal distribution would be the following (see Figure 4.25): the Synchroniser would control the chopping operation of the WFS optical chopper and the LGS optical chopper applying a delay in between both signals; the AWG2021 channel 1 would control the WFS plenoptic camera in order to perform the acquisition at the very exact time instant (when the laser light has reached the desired height along the atmosphere propagation path and before the laser control unit fires next pulse); at the same time, the Synchroniser feedback signal would also triggered the operation of this channel 1. Each signal is described in following sections.

The synchronization shall follow the schema in Figure 4.26. The idling in between the laser pulse and the start point of the acquisition is due to the time it takes the light to travel from the laser head to the spot where it will be imaged by the camera: for 20-kilometre altitude, idle time shall be around 67 μs x 2 (upwards and downwards propagation), $\approx$133 μs. Notice Rayleigh backscattering from the upper bound of the atmosphere (25km) would lasts around 166 μs.
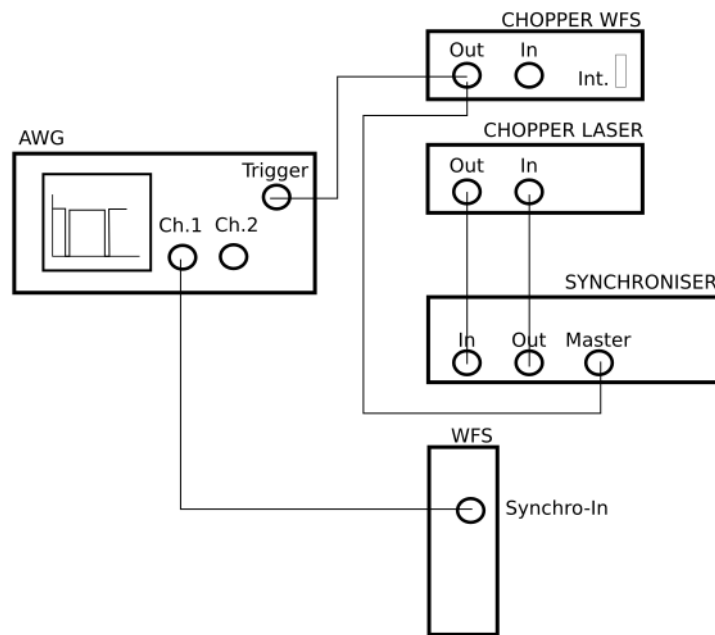
FIGURE 4.25: Signal distribution in the UWCS synchronisation.

The total exposure time of each frame shall be in the order of milliseconds (< 10ms), otherwise, no incoming wavefront could be reconstructed from the acquired images.

The maximum rate at which OCAM2S camera could work is 2 kHz, meaning CCD exposure time would be minimum 0.5ms.

4.10   Uplink Wavefront Corrector System. Final Design Considerations

The Durham Adaptive Optics Real-Time Controller (DARC) was selected as the RTC for the UWCS; DARC is a real-time control system (RTCS) for AO that was initially developed to be used with the CANARY on-sky multi-object AO technology demonstrator, due to a demand for DARC to be used with other instruments, an improved version of DARC was released to the public using an open source GNU General Public License.

Due to the research extent and time constraints, the simulation test bench and the proof-of-concept instrument would integrate a Shack-Hartmann wavefront sensor instead of a plenoptic camera, as new code implementation in DARC would be required to use this last one as a WFS within the system (slopes calculation method). The SH-WFS would be the same physical device as the plenoptic camera already described (Section 4.5, OCAM2S with 12x12 sub-aperture), except for the fact that a collimator lens would be placed right before in order to feed a collimated beam to the WFS. This was a relatively important change in the instrument design, although it was considered not relevant with regard to fulfilling the research goals: the functionality of the plenoptic camera as wavefront sensor was as well demonstrated on-sky as the uplink pre-compensation of the laser beam, even if both objectives were not
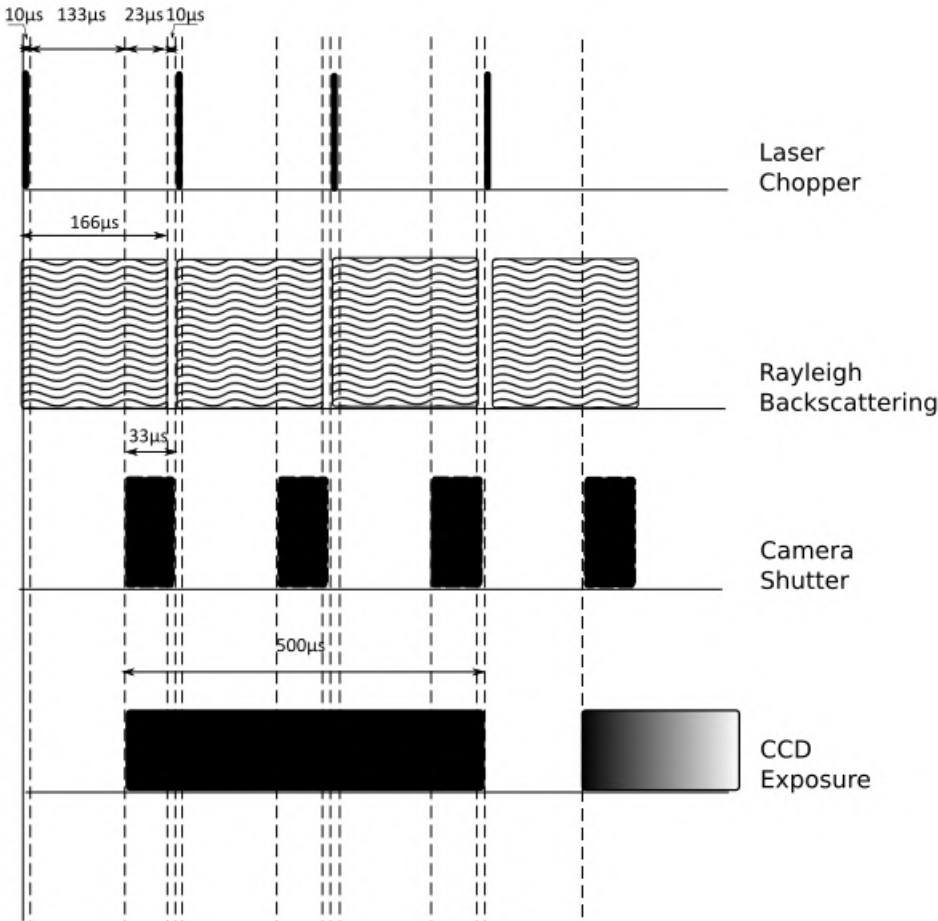
FIGURE 4.26: Synchronization schema at maximum frequency with the OCAM2S camera.

achieved in an unique experiment. Eventually, due to the non-availability of the OCAM2S during the experimentation phase, it would be replaced by an OCAM2k camera.

Chapter 5

Uplink Correction Wavefront System. Simulation Test Bench

5.1 Introduction

An uplink correction demonstrator test bench was designed and integrated at the headquarters of the Instituto de Astrofísica de Canarias with the aim of proving the feasibility of the uplink pre-correction concept for not only free-space optical communications, but also for the self-propagating path of Laser Guide Stars. It also served as a general verification of the control system and its synchronization requirements, before the sky validation.

The UWCS simulation test bench is presented and described in this chapter, as well as the subsystems characterisation and functionality tests which were performed to the possible extent in the laboratory environment, where it is not possible simulating the travelling of the light.

5.2 UWCS Test Bench

The UWCS simulation test bench consists of an Uplink Wavefront Corrector System at laboratory scale, which was designed to characterise every subsystem part of the UWCS before its integration at the OGS telescope.

The UWCS test bench was composed by the following subsystems: a laser source, the CILAS SAM97 deformable mirror, the OCAM2k and the available lenslets arrays as wavefront sensor (the OCAM2S did not arrive on time for this and next experimentation phases), and an atmospheric turbulence simulator with several phase screens ranging from weak to strong turbulence. Its optical layout is presented in Figure 5.1.

Figure 5.2 shows the simulation test bench in the IAC laboratories; the He-Ne laser hit a miniature piezo-electric (PE) tip-tilt mirror, which displaced the beam out of the light path in order to simulate the behaviour of a pulsed laser; after the PE, the beam went through a pin hole (with the aim of modelling a point-like source by creating a spherical wavefront in the beam), got reflected by a mirror and became collimated before reaching the Cilas97 deformable mirror. Once the phase was shaped by the DM, the light travelled through the optical path until a motorized phase screen, which simulated a single turbulent layer atmosphere (PS); the beam finally hit the wall (with a fluorescent painted area to emulate the star generation and the light path propagation delay) and came back again through the phase screen, the lens simulating the telescope and the two last lenses of the optical path until a 50/50 beam splitter which led the light onto the WFS camera. Details of each subsystem (source, DM, WFS and PS) are provided below.
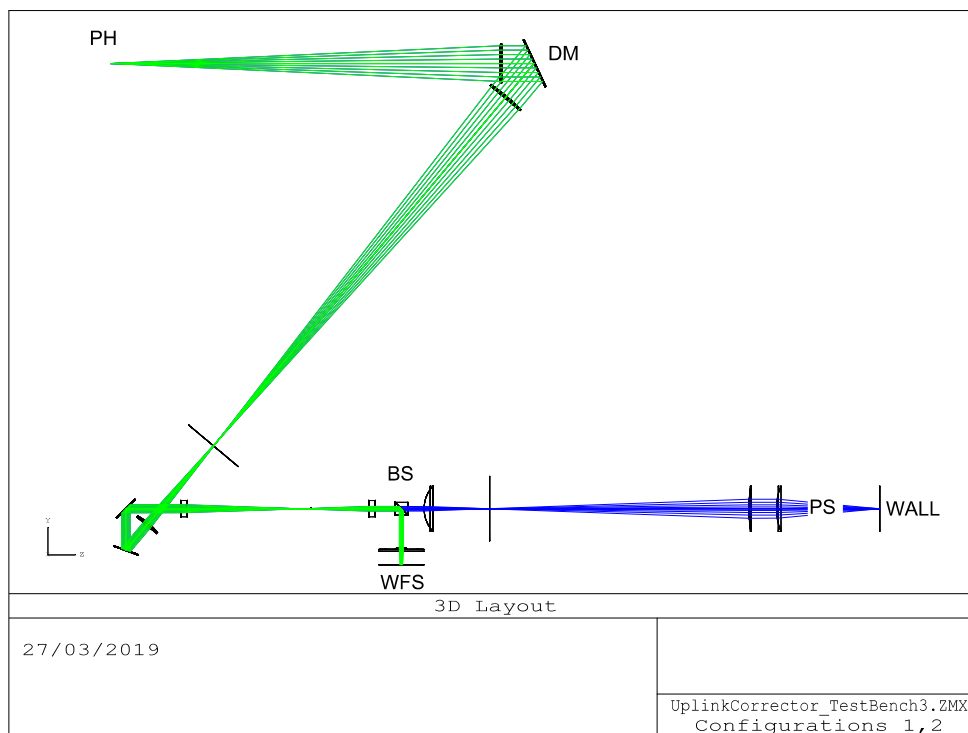
FIGURE 5.1: Optical Layout of the Uplink Corrector Test Bench.
Acronyms in the figure: PH - Pin Hole; DM - Deformable Mirror;
BS - Beam Splitter; WFS - Wavefront Sensor; PS - Phase Screen.
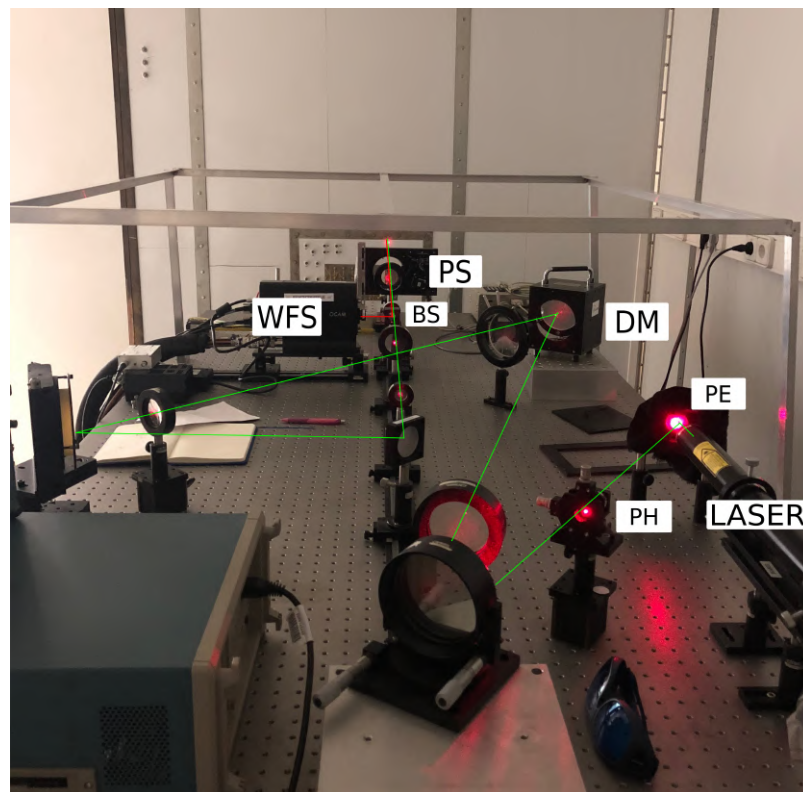
FIGURE 5.2: IAC laboratory configuration of the Uplink Correction Demonstrator Simulation Test Bench. Acronyms in the figure: PE - Piezo-Electric Tip-Tilt Mirror; PH - Pin Hole; DM - Deformable Mirror; BS - Beam Splitter; WFS - Wavefront Sensor; PS - Phase Screen.

The laser source was a JSDU Helium-Neon laser head, model 1145, of 632.8-nanometre wavelength linearly polarised with an output power of 21mW. The beam divergence is 1.15 mrad. It was launched against a S-334 piezo-electric tip-tilt mirror, which led the beam in or out the inserted pin-hole (PH) to filter out any spatial intensity variations in the laser beam. The PE tip-tilt mirror emulated the behaviour of the laser pulses; it reached 120 mrad deflection and could work up to frequencies of 1 kHz with a E-503 piezo controller system.

For the modification of the source wavefront phase, a CILAS SAM97 deformable mirror was installed in the set-up; it is based on the Stacked Array Mirror (SAM) technology. It is made of a 11x11 piezo-electric actuators (97 useful actuators) with an 8-millimetre spacing and a coated optical aperture of 100 mm diameter. The demonstrator test bench had a Shack-Hartmann as WFS in order to verify the DARC functionality without further software implementations in the Real Time Controller.

All the subsystems were verified with a two SH configuration: 24x24 sub-apertures (sub-aperture physical size 240 micron) and 12x12 sub-apertures (sub-aperture physical size 480 micron) and an Firstlight OCAM2k camera.

In order to simulate the atmosphere behaviour, several phase screens were available in the set-up. Each of the phase screens has Kolmogorov phase statistics with several r_0 values (1 mm, 3 mm and 6 mm) and beam diameter of 20 mm, which simulate seeing conditions of $r_0 = 5cm$, $15cm$ and $30cm$, respectively, at the OGS telescope. The phase screen was mounted in a Lexitek HS-100 motorized rotary stage capable of reaching the 300 rpm. The test-bench was configured for a single phase screen at the ground-layer which was located approximately at the optical conjugate of the pupil formed onto the DM and onto the WFS. The phase screen was moved out of the optical path in order to calibrate and build the interaction matrix of the WFS/DM.

The laser, pin hole and atmospheric simulator were also part of the calibration system in the UWCS during the instrument integration and testing at the OGS telescope.

5.3   Light Propagation Simulation

As it has been previously stated, the time it takes for the light to propagate from two points cannot be reproduced in the laboratory environment. However, fluorescent materials were investigated with the purpose of achieving a certain and measurable delay between the light propagation and the received signal. Unfortunately, it was not possible: either the fluorescence time was in the nanoseconds range (not feasible to detect) or in orders of magnitude of hundreds milliseconds, which would be two slow for the system, as the WFS cannot work with external synchronisation at rates lower than 100 Hz. Therefore, the fluorescence component was replaced by a flat mirror on the wall.

5.4   UWCS Subsystems Characterisation

The UWCS subsystems needed to be characterised in the laboratory regarding their configuration and response. This section describes the DM, the WFS and the Real-Time Controller setting-up and preliminary testing.

5.4.1 CILAS SAM97 Deformable Mirror

The CILAS SAM97 DM was manufactured in 2008 and re-polished in 2012, therefore some analysis had to be done in order to ensure it had not suffered any damage since then. The in-house characterization of the DM was performed with a Zygo interferometer and some issues appeared during the measurement analysis (see Figure 5.3): The CILAS SAM97 was curved on one of the axis on its edges and also seemed to have one faulty actuator. Hence, a design decision of partially actuate the DM (considering only a 55-millimetre central area) was made. Interferometry measurements point out that the curvature at the selected area was approximately 1.5λ, which was 632.8nm for Zygo interferometer, resulting in a curvature of $0.95\mu m$ in wavefront. Manufacture specifications claim a total mechanical stroke of $4\mu m$, therefore, after flattening the curved area, the remaining stroke to compensate the atmospheric aberration will be $> 3.5\mu m$, which, based on the necessary stroke estimations (see Chapter 4), was enough to achieve a good AO performance.
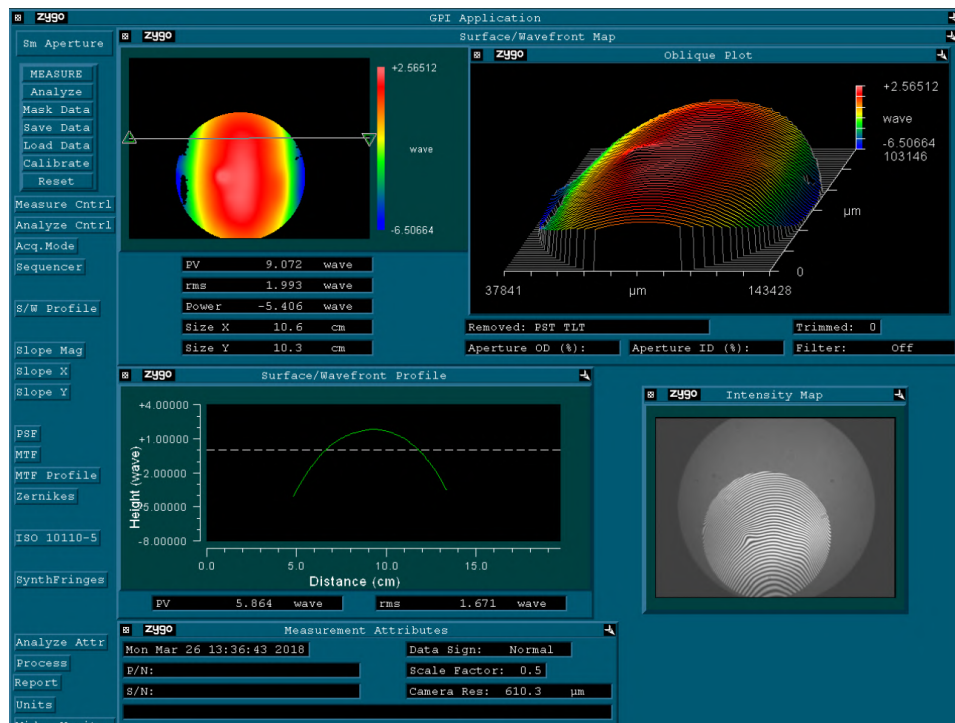
FIGURE 5.3: Characterization of the CILAS SAM97 deformable mirror with Zygo Interferometer. Notice the defects and curvature on edges.

5.4.2 Firstlight OCAM2k Shack-Hartmann Wavefront Sensor

Two features regarding the OCAM2k WFS needed to be evaluated at laboratory scales: the microlenses array alignment and the acquisition synchronisation with an external signal.

During the integration phase of the test bench, the optical alignment of the launch light path was done using the laser light itself, although the return path from the wall to the camera could not be aligned by the conventional procedure as the naked eye cannot see the light return. Therefore, an alignment procedure was established for

the return path by using an image of a star on a mobile phone screen attached to the wall in the location where the laser hit it (Figure 5.4). The microlenses array was hence verified with the Firstlight user interface (Figure 5.5).
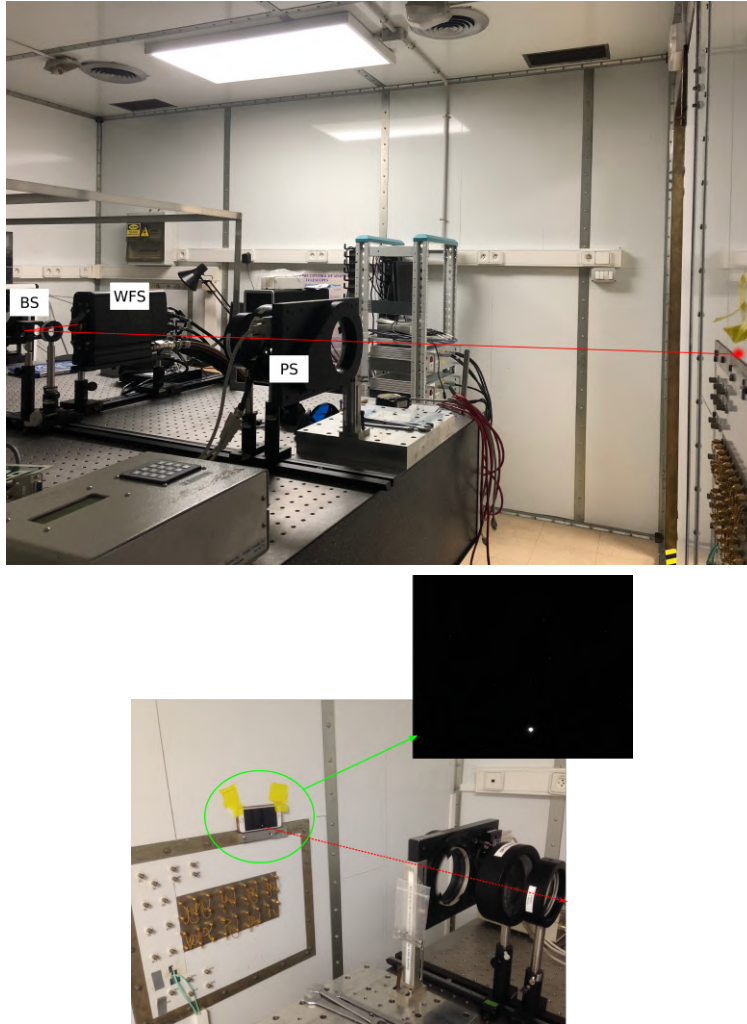
FIGURE 5.4: Alignment set-up for the optical path from the wall to
the wavefront sensor.

The laser chopping (emulated in the test bench by the piezo-electric tip-tilt mirror) and wavefront frame acquisition were synchronized with the Tektronix AWG2021 Arbitrary Waveform Generator. The distribution of channels was the following: channel 1 commanded the fast steering mirror to deviate the laser out of the optical path at the desired frequency; channel 2 fired the external trigger of the OCAM2k camera. Nevertheless, the available OCAM2k camera in the set-up had the EM-CCD220 detector, whereas EMCCD219 would be more suitable as it allows electronic shutter operation; as EMCCD220 only permits readout (and not integration) trigger, the camera is continuously integrating and therefore, acquired frames while the laser is on, shall be discarded. The synchronisation diagram to validate the control capabilities over the different devices is presented in Figure 5.6: first and second frames are not valid for wavefront estimation as the first one corresponds to the situation where the laser has not been switched on yet, and in the second frame, the laser is propagating for the first time against the wall, so no return can be recovered
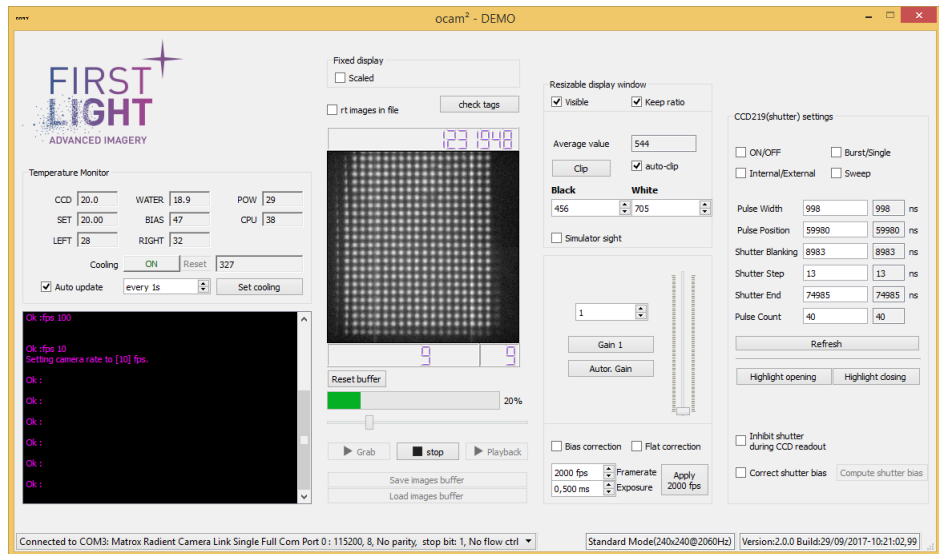
FIGURE 5.5: OCAM2k user interface showing the SH-WFS image when illuminating it with the light from the star on the mobile screen.

from the fluorescent paint yet. The third frame must be the first one in the wavefront calculation as it is the one acquired when the laser is already off and the fluorescent paint is still shining. Afterwards, next frame will be discarded and next to this one, considered. This synchronisation schema only applied to the laboratory validation; the one implemented during the telescope testing has been previously described in Chapter 4.

The WFS was mounted on a NEAT focusing stage (described in Section 4.5). The mechanical interface to attach the camera to the stage was custom-built at IAC mechanical workshop facilities (see Figure 5.7) and its integration as well as the linear stage functionalities were tested in the UWCS Simulation Test Bench by implementing a Python library to control the NEAT 310M controller.

5.4.3 WFS and Laser Optical Choppers

Unfortunately, the SCITEC INSTRUMENTS optical choppers did not arrive on time to be tested and characterised with the UWCS simulation test bench, causing harder efforts to be properly set up during the UWCS telescope integration.

5.4.4 Durham Adaptive Optics Real-Time Controller

The Durham Adaptive Optics Real-Time Controller (DARC) (Basden et al., 2010) was firstly tested by its interconnection with the Durham Adaptive Optics Simulation Platform (DASP) (Basden et al., 2018), also built by Durham University, allowing the verification of the DARC functionalities without having a physical AO system.

Afterwards, the DARC system was integrated with the UWCS simulation test bench by including in the configuration structure the libraries of the corresponding elements: DM and WFS.

Figure 5.8 shows the main DARC monitoring tools: WFS centroids positions, slopes computation and DM actuators state.

The WFS and DM integration and configuration in DARC was successfully tested with the UWCS test bech and with the final configuration of the UWCS for its integration at the OGS telescope.
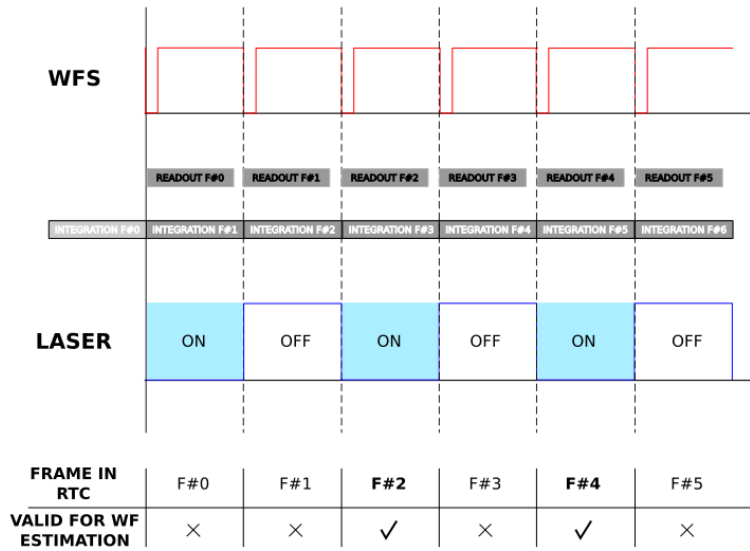
FIGURE 5.6: Synchronization signals for the WFS camera and the piezo electric electronics driven by the Tektronix AWG2021 Arbitrary Waveform Generator.
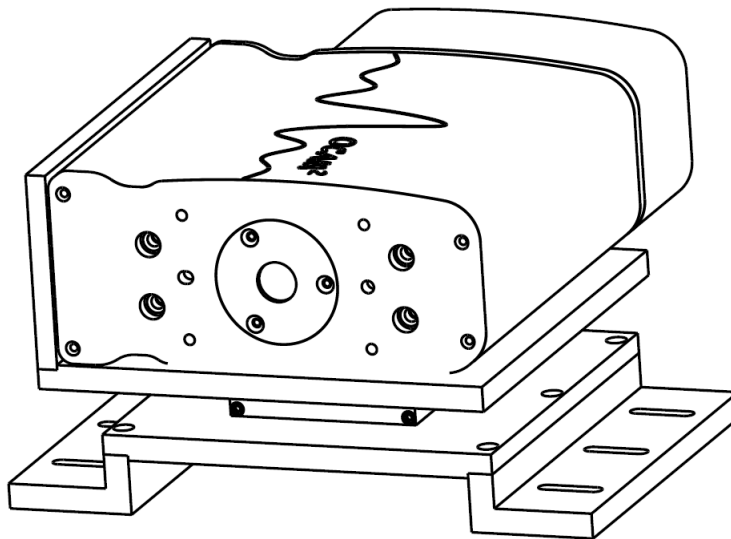
FIGURE 5.7: Custom-built mechanical interface to attach the WFS camera to the linear stage.
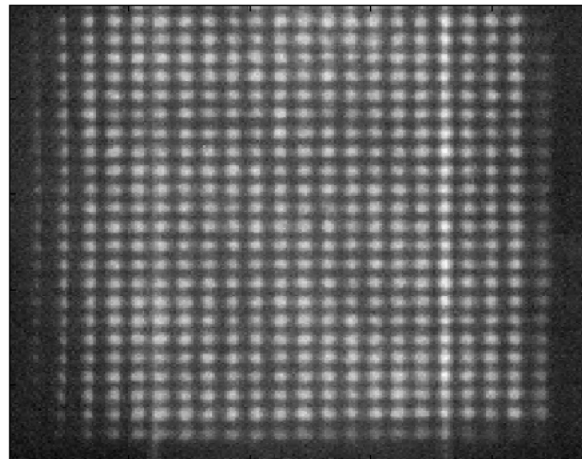
(a) WFS camera
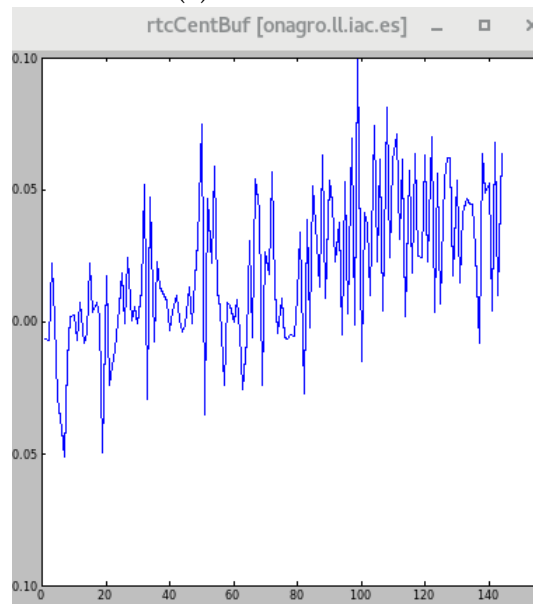
(b) WFS X/Y Slopes
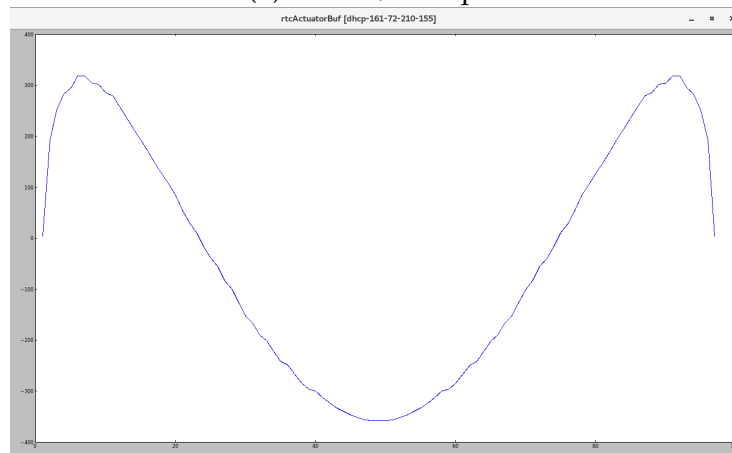
(c) DM Actuators State

FIGURE 5.8: Main monitoring graphical views in DARC.

5.5   Uplink Wavefront Corrector System. The Test Bench Outcome

The UWCS simulation test bench was designed and integrated in one of the IAC headquarters laboratories as a previous phase to transfer the system to the Optical Ground Station telescope.

All the subsystems were characterised to the possible extent, taking into account the impossibility of reproducing the light propagation in the laboratory. The CILAS SAM97 deformable mirror was measured by interferometry to verify its current state and its suitability for the UWCS; the WFS was tested in synchronised operation with an external waveform generator; and the DARC controller was integrated in the RTC computer and set-up with the final UWCS telescope configuration. Both WFS and DM operation were verified together with the Real-Time Computer, ensuring the proper communication between the units.

Due to the time invested trying to simulate the light propagation at the laboratory scale, it was not possible to accomplish further goals (close-loop operation), but the subsystem characterization; the allocated telescope time for the laser campaigns had been approved in 2017 to start in January 2019, hence, there was no more available time to analyse the UWCS performance in the laboratory.

Even though no close-loop result was derived from the laboratory phase, the UWCS simulation test bench eased and rehearsed the following integration and operation tasks during the telescope campaign.

The simulation test bench for the Uplink Wavefront Corrector System is deeply described in the proceeding *Uplink correction demonstrator: test bench and experimental results* (Martínez et al., 2018).

Chapter 6

Plenoptic WFS. On-sky Feasibility Validation

6.1 Introduction

Due to its flexibility and good behaviour with extended objects, the plenoptic camera has been proposed as a possible WFS for the Uplink Wavefront Corrector System, designed to improve the Free Space Optical communications Earth-Satellite at the OGS.

With the purpose of evaluating the feasibility of this device as sensor for the atmospheric turbulence, a test plan was suggested and followed in combination with ESO launching campaigns of a Laser Guide Star at the Teide Observatory. The goal of the testing runs was the measurement of the incoming wavefront by using natural and artificial references sensed with the plenoptic camera from the OGS.

Facilities, test plan, results and lessons learnt from one campaign to the other and from the whole verifications set to the future are described all along the present chapter.

6.2 Test Plan

With the aim of assessing the feasibility of the plenoptic camera as wavefront sensor for an AO system, a test plan was designed in collaboration with the, at that time, ongoing Laser Guide Star campaign by ESO at the Teide Observatory.

The European Southern Observatory (ESO) had been verifying their Wendelstein Laser Guide Star Unit (Bonaccini Calia et al., 2012) at the OT since January 2015 (first light) and until July 2016, time when they moved to Roque de los Muchachos Observatory in La Palma. This LGS unit (Figure 6.1) consists of a 20-watt orange beam, which, by operating at 589-nanometre wavelength, excites the sodium atoms which then re-emit the light, producing a glowing artificial star up in the 90-kilometre layer of the atmosphere.

Due to the past and current collaborations with ESO's Laser System Department, IAC applied for some observation time of the LGS simultaneously with the allocated dates at the OGS, in a way that the preliminary viability tests of the plenoptic camera as WFS at the Optical Ground Station could be performed during the laser campaigns.

The plenoptic camera would be installed in the OGS Coudé room and the telescope would be pointing at the ESO LGS. Figure 6.2 shows the distribution of the telescopes of interest at the Teide Observatory: the empty dome, where the LGS would be launched and the OGS, where the plenoptic camera is installed. The reason for this arrangement was the following: as it was a lateral laser launch with

FIGURE 6.1: First observing campaign with the "ESO Wendelstein Laser Guide Star Unit", developed by the European Southern Observatory (ESO) at the OT (January 2015). Notice the OGS on the left. Copyright Daniel López (IAC).

FIGURE 6.2: OGS Location with respect to the empty dome where the launching telescope was placed for the ESO-LGS.

respect to the plenoptic camera on-axis direction, the LGS was then an extended elongated spot; hence, the plenoptic device could take advantage of the extended shape, allowing not only the conventional wavefront reconstruction, but also its tomographic measurement.

The proposed test plan consisted of analysing the real capabilities of the plenoptic camera as wavefront sensor in an AO system to improve FSO links at the OGS: firstly, the camera integration into the Coudé room of the telescope with all its related concerns (illumination level and field-of-view); right after, the verification of its functionality as WFS with natural stars; and finally, while launching the LGS from the IAC80, its testing as WFS with artificial stars regardless of experiment time (diurnal or nocturnal measurements). All of it with the purpose of assessing its future use as WFS in a LGS-AO system to probe atmospheric turbulence on the uplink directions at the OGS while performing optical communications with GEO and LEO satellites.

6.3   Test Campaign April 2016

During ESO-LGS campaign in April 2016, it was performed a first attempt to measure the atmospheric turbulence from the OGS telescope at the OT with a plenoptic

sensor and a Laser Guide Star acting as reference source.

Unfortunately, some difficulties with the optical set-up hampered the measurements success: on one hand, the small field-of-view (20 arcsec): it was very difficult to position the Laser Guide Star from the location of the natural star at which it was pointing (minimum distance in between each other is usually around 150 arcsec); and, on the other hand, the camera needed to be replaced by another sensor with better QE in order to maximise the incoming photons.

The new proposed configuration consisted of one ANDOR camera with 1024x1024 sensor size and one microlenses array of 480 μm pitch and 20-millimetre focal length.

6.4 Test Campaign July 2016

A second attempt to test the feasibility of the plenoptic system at the OGS was carried out during the July 2016 ESO-Laser Campaign. After the lessons learned in the first run, a different optical design was followed in order to integrate the device into the Coudé configuration of the Optical Ground Station, but trying to get higher light levels. The experimental set-up of the July test run, main goals to reach and testing troubleshooting are described below.

6.4.1 Experimental Setup

The optical set-up for the July test run was designed with the aim of getting more sensitivity on the detector and dealing with the lack of illumination level at the Coudé focus. Therefore, another camera with better QE was selected as well as a slightly different lenslet array to be placed at its focal length in front on the sensor. Re-imagination lenses were removed, so the only elements on the experimental set-up (represented in Figure 6.3) were the Camera ANDOR iXon3 888 and a 28x28 microlenses array (see Table 6.1 for technical details).
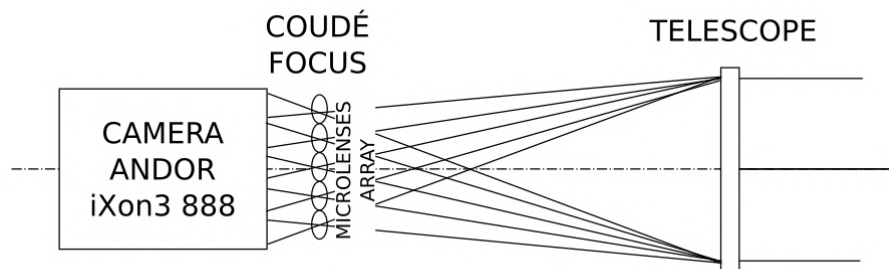
FIGURE 6.3: Optical configuration for the OGS Test Run July 2016.

ANDOR iXon3 888	
QE	Approx. 90%
Sensor active area	1024x1024 pixel
Pixel size	13 μm
Field-of-view for this optical configuration	Approx. 70 arcsec
Frame rate	8.7 - 4205 fps
Microlenses Array	
Number of microlenses	28x28
Focal Length	20.23 mm
Pitch	480 μm

TABLE 6.1: Technical Details of experimental set-up used in July run.

The chosen camera for this second verification run was the ANDOR iXon3 888 camera with 1024x1024 pixels on its detector and also better sensitivity. The microlenses array with 480-micron pitch was located at the corresponding focal length. By using this configuration, the FOV covered by the sensor was increased by a factor 3.5 (70″ in July set-up versus 20″ in April set-up), with 2 arcsec/microlens what implies at least 4 pupil samples per microlens of the measured wavefront with the LGS.

6.4.2   Test Goals

As the main goals of the first test run had not been fulfilled, same purposes were applicable to this second attempt: satisfactory integration of the plenoptic camera into the Coudé room, in such a way that the ESO-LGS could be seen in the FOV with higher intensity levels than in April run.

This second test sets should also demonstrate the capabilities of the plenoptic camera as WFS, at least with natural references and with the LGS, until the possible extent in the shared allocated time at the OGS, where three different research groups were working simultaneously.

6.4.3   Major Issues during Testing

Lessons learnt from the April campaign made possible that the July run met the expectations: the second optical set-up was the proper one in order to have fairly good light levels and a FOV big enough in the plenoptic camera.

One shall notice the difference between Figure 6.4(a) and Figure 6.4(b): both are plenoptic images with similar integration time (2s); the picture above corresponds to April campaign, and the one below to July testing. The noticeable differences verify the better suitability of the second experimental set-up.

Plenoptic images of natural stars were also acquired with shorter exposure times (1ms), those ones more realistic when dealing with turbulence measurements. However, the minimum possible integration time to image the LGS and, at the same time, keeping some light on the sensor to make it distinguishable, was 50ms. This value was too large to extract wavefront information from the data: larger exposure times makes the photographic process mask the instantaneous atmospheric phase.

The lack of intensity was due to the fact that the optical set-up was placed at the Coudé focus, with a 40-meter focal length, where the incoming light through the 1-meter telescope was drastically reduced when travelling through an optical path which needed urgent maintenance (refurbishment).
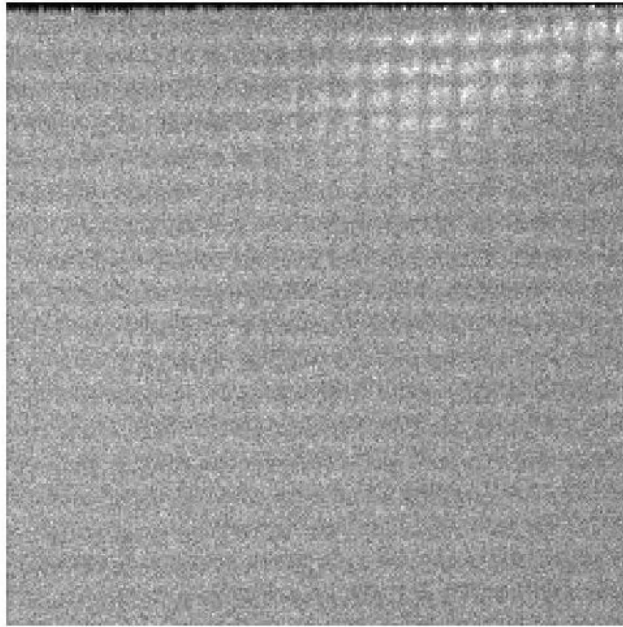
(a)
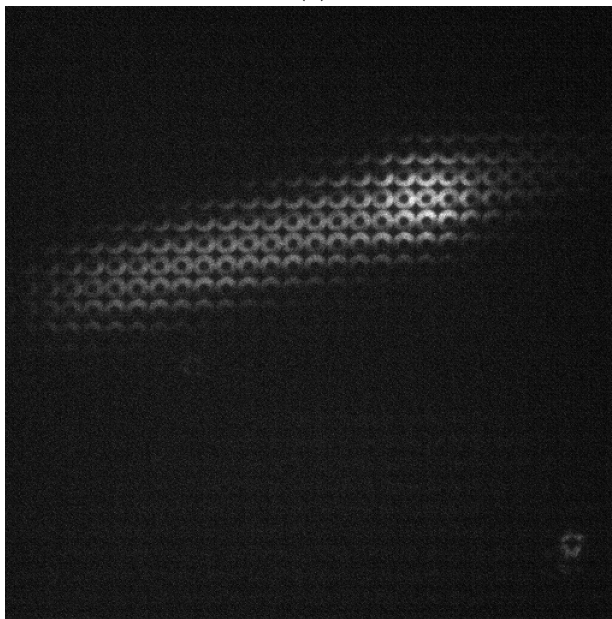
(b)

FIGURE 6.4: (a) LGS plenoptic image acquired during night April 12th 2016; (b) LGS plenoptic image acquired during night July 8th 2016.

6.5   Test Campaign Results

Results from July test run are gathered below, proving the feasibility of the plenoptic camera as a wavefront sensor.
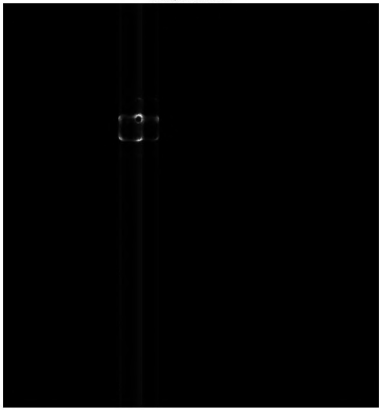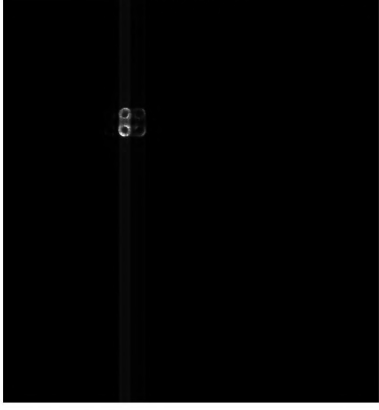
6.5.1   Focus Scan

A focus scan has been used as a mechanism to reconstruct the well-known wavefront at several focus positions and hence, denote the feasibility of the plenoptic camera as possible sensor for a future AO system at the OGS.

   A focus scan consists of changing the telescope focus position with the aim of defocus on purpose the object of interest from the best focus position, back and forth, in descending or ascending order to create a defocus aberration; Arcturus star was selected as object to point at in order to make profit of the available time slots while the LGS was not propagating.

   The telescope focus was adjusted by moving the secondary mirror, which, for the optical configuration at Coudé, was located at position -27.2 mm.

   Images were taken with an exposure time of 1ms, acquiring 200 images at each shoot. Table 6.3 gathers the average image of those 200 at each focus position. Notice Arcturus spreads across the higher number of microlenses the more defocused it is.

Focus Position	Average Image
-27.0 mm	
-27.2 mm	
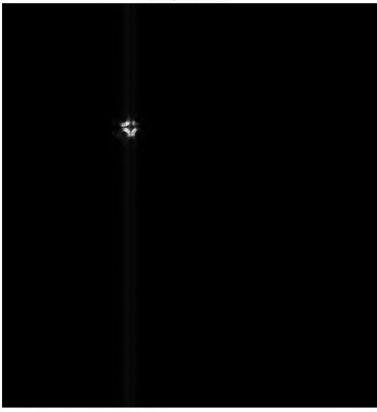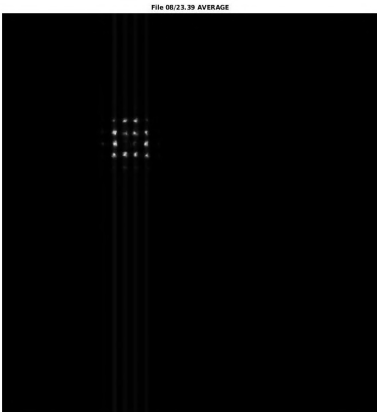
TABLE 6.3: Average image from 200 frames at each focus position.

The average wavefront of each focus position belongs to the manually introduced defocus which should be removed from the single wavefront reconstructions (from each image within the 200 set) to extract the real atmospheric turbulence.

Figure 6.5 shows the average wavefront of each focus position, denoting the further the telescope focus was moved, the bigger the defocus was.

As it has been already stated, a telescope focus of -27.2mm corresponded to the best focused position for the optical configuration with the plenoptic camera at the Coudé. However, the plenoptic image with the lowest number of illuminated microlenses seems to be the one at -27.4-millimetre focus position (Table 6.3), creating
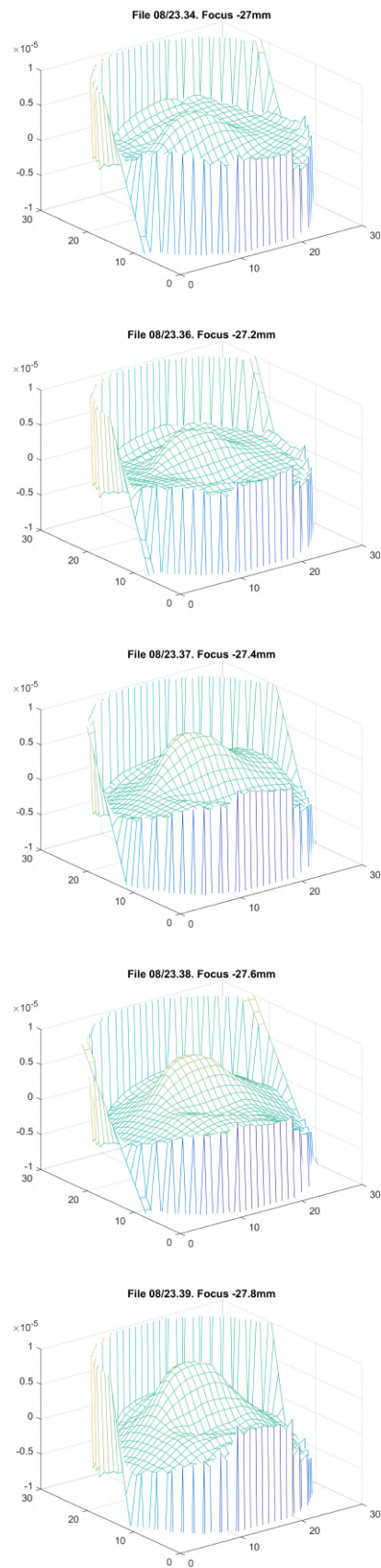
FIGURE 6.5: Average wavefront at each focus position. All units in μm.
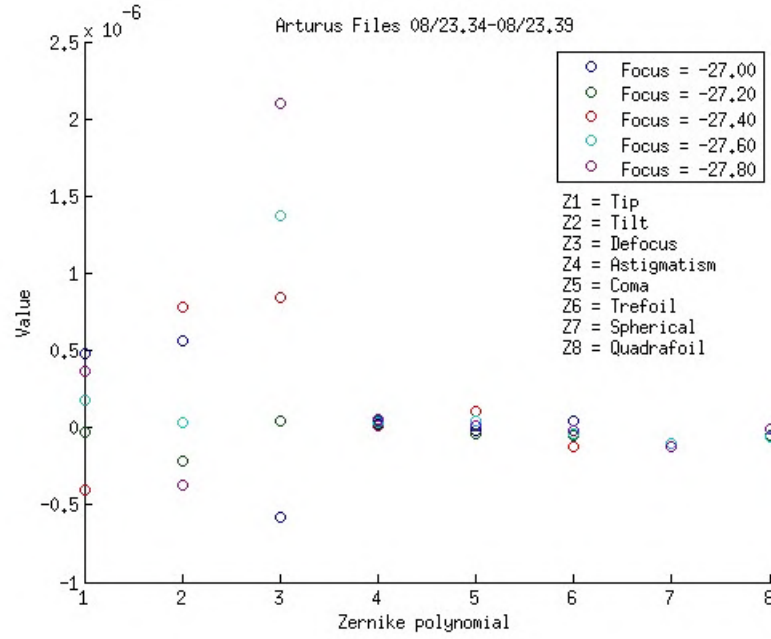
FIGURE 6.6: Zernike polynomials at each focus position.

the false perception of being the optimum focus. With the aim of verifying this inconsistency, a Zernike polynomial analysis has been performed from the single wavefront reconstructions (Figure 6.6), demonstrating that the best focused position (the one with a lower Zernike defocus polynomial) is located at -27.2mm. One should notice that higher order modes are not changing with the defocus, but a slight change in the tip and tilt, which is caused by differences in the star position due to certain drift in the telescope tracking system.

Once the average wavefront was removed from each of the single reconstructions, the atmospheric structure function was calculated from those single wavefronts. The structure function (Eq. 6.1) would demonstrate if the calculated turbulence followed Kolmogorov statistics.

$$D_\phi = < |\phi(r + \rho) - \phi(r)|^2 > \tag{6.1}$$

Where $\phi(r)$ denotes the phase and ρ, the distance in between samples.

Within the turbulence inertial range [1], the structure function behaves on the way expressed in Eq. 6.2.

$$D_\phi(\rho) = 6.88 (\frac{\rho}{r_0})^{5/3} \tag{6.2}$$

Where r_0 is the Fried parameter.

Therefore, by applying a logarithmic fit to the resulting structure, the slopes should tend to a numerical value of 5/3. However, the small size of the microlenses produces a very distinctive effect: the blurring in the wavefront reconstruction due to the fact that the phase measurements are not independent on each other. This blurring effect can be minimized by selecting small focal ratios (as it has been studied in detail in Rodríguez Ramos (2015) and described in Chapter 4), although it

---

[1]related to the interval in between the inner and the outer scale, as Hardy J. W. demonstrated in (Hardy, 1998)

will always have some residual consequences in the structure function. Rodríguez Ramos (2015) has described those effects and modelled the theoretical response of a plenoptic camera to the phase structure function by simulating the Full Width at Half Maximum (FWHM) of the PSF of one microlens with the expected slope. Hence, by calculating the FWHM of our system, it was possible to verify if the calculated structure matched the expected atmospheric behaviour.

Figure 6.7 presents the results from the slope computation of the structure function at each focus position. Mean value of the slopes is 1.882, at little further from the statistical 5/3. This difference is justified by the blurring effect, assessed below.
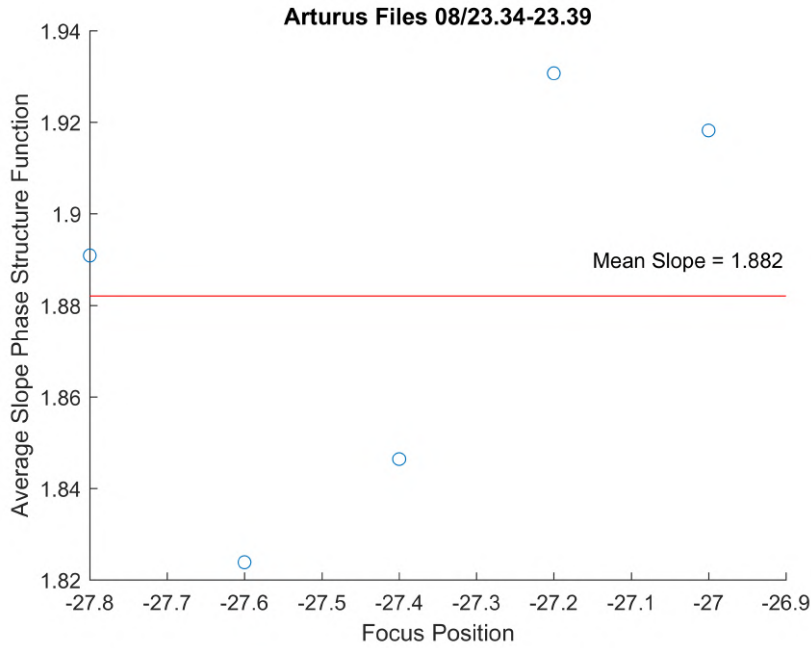
FIGURE 6.7: Slope computation of the structure function all along the focus scan.

The blurring effect was evaluated based on the microlenses manufacture details (Table 6.1). The FWHM in pixels (Eq. 6.3 and 6.4) needed to be calculated specifically for the lenslet array in the set-up, in order to compare this value to the simulated behaviour in Rodríguez Ramos (2015).

$$FWHM(\mu m) = 0.886 \frac{\lambda f}{pitch} \tag{6.3}$$

$$FWHM(px) = \frac{FWHM(\mu m) N_{samples}}{wpxSize} \tag{6.4}$$

Where f is the focal length of the lenslet array, w is the pupil width in pixel/microlens, and $pxSize$ is the pixel size in μm.

For the microlenses array described in Table 6.1, 30 central samples (out of the 36 pixels/lenslet) and 590-nanometre wavelength, the resulting FWHM in pixels is 2.0511. With this input to Figure 6.8, the expected slope would be 1.88. Hence, it was demonstrated the obtained results from the real data follow the expected statistics.
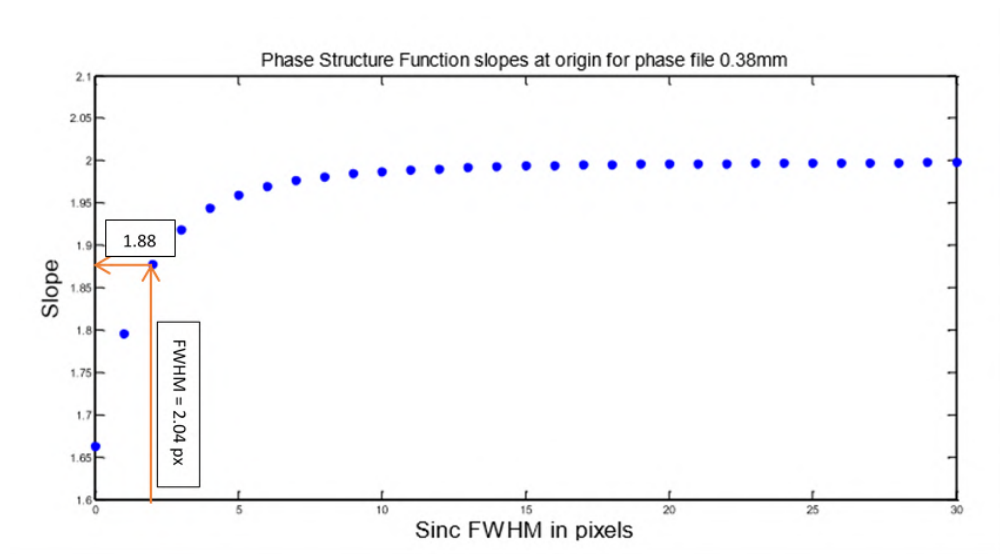
FIGURE 6.8: Theoretical slopes of the structure function in the blurring simulation (Rodríguez Ramos, 2015).

6.5.2 LGS Wavefront Reconstruction

The functionality of the plenoptic camera as wavefront sensor with Natural Guide Stars has been proven, although the proposed feasibility tests pursued richer results by making profit of the ESO-LGS campaigns. Therefore, the camera was used to sense the atmospheric turbulence from the LGS reference.

Even after applying the lessons learnt during the first campaign, it was not possible to recover the wavefront information from the acquired data. The FOV was increased almost by a factor of three, meaning the whole plume of the star was imaged by the sensor, but there was still few light coming through the Coudé optical path.

Figure 6.9 shows an example of one LGS image acquired with 50-milliseconds integration time; this one was the shortest exposure time achievable using the high electronic gain of the camera.

With the aim of verifying if this integration time would be small enough to extract turbulence information from the images, the wavefront was reconstructed and the structure function calculated; if the slope of the structure function for each LGS image matches de Kolmogorov turbulence, it will tend to the 5/3. Figure 6.10 gathers the calculated slopes all along the 200 images of the LGS; the mean slope value is 1.04, hence it was only noise what was subtracted from the acquired data, no atmospheric turbulence information seemed to be on it. Exposure times should be shorter, so it will be necessary to increase the amount of light sensed by the camera.
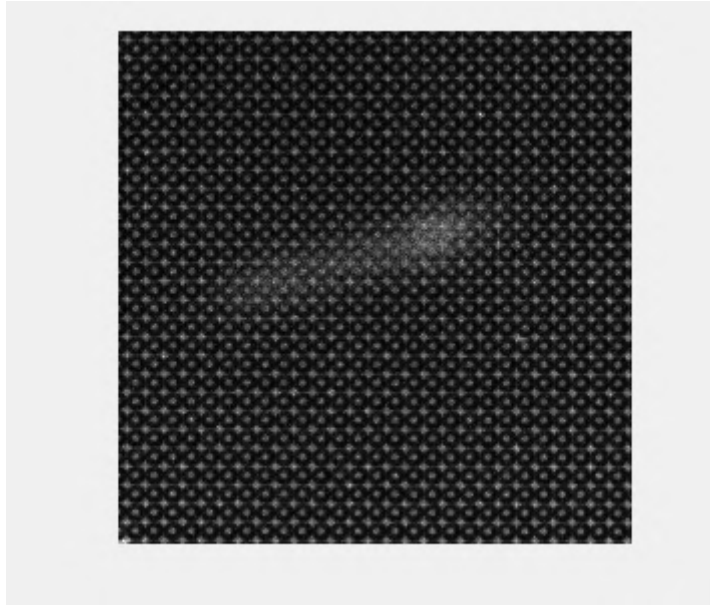
FIGURE 6.9: LGS image acquired during night April 8th 2016; exposure time = 50ms, electron multiplier gain=300 and binning 4x4.
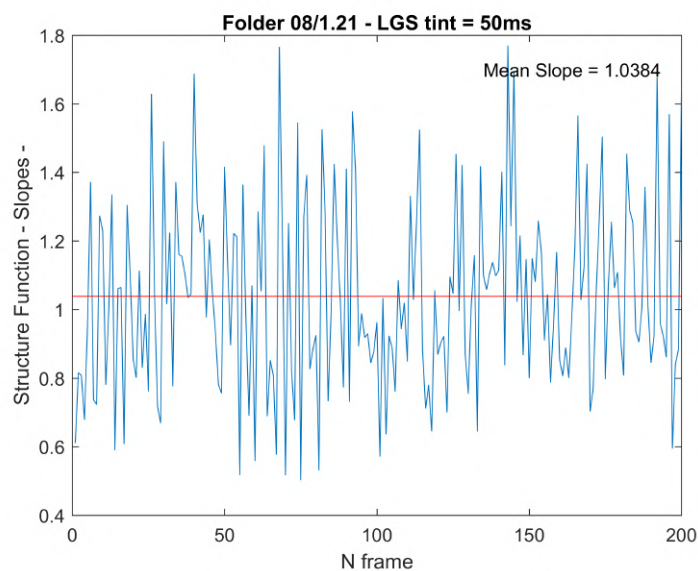
FIGURE 6.10: Slopes of the structure function all along the 200 images of the LGS.

Even though, the extracted wavefront did not present turbulence information, other optical aberrations shall be inherent to it: the LGS was probably out of focus as the artifical star it not at infinity but at the sodium layer. Therefore, the wavefront was decomposed onto several Zernike polynomials.

By recovering the Zernike modes (Figure 6.11), it is shown the strong defocus it has, proving one more time the plenoptic camera was properly working, but it needs larger light levels to acquire images with lower integration times and so atmospheric information (not averaged over large exposure times).
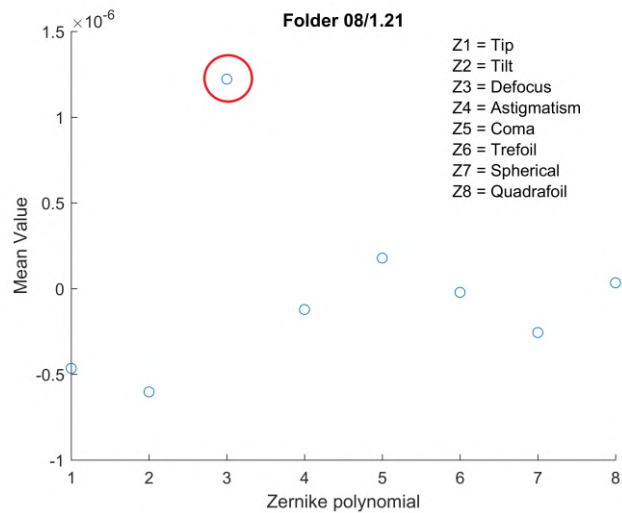
(a)
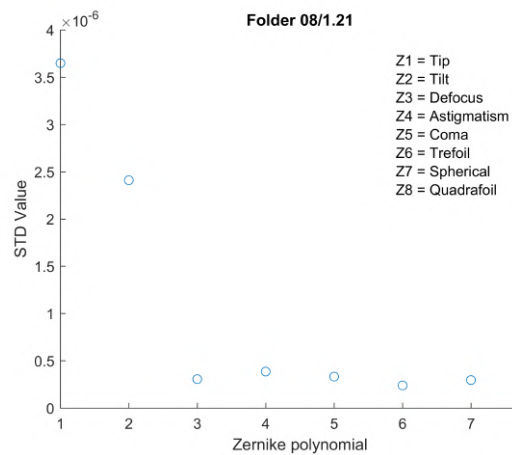
(b)

FIGURE 6.11: Zernike polynomials extracted from LGS images acquired with exposure time 50ms. (a) Mean value of some Zernike modes averaged over 200 images; strong defocus is circled in red. (b) STD value of the averaged 200 calculated Zernike modes.

6.6 Uplink Wavefront Corrector System. The On-sky Validation of the Plenoptic WFS

Besides the limitations in hardware and allocated time, the plenoptic camera has fulfilled the expectations as a WFS with natural sources. With a plenoptic sensor, it is possible to measure and extract wavefront information from natural stars, as it has been demonstrated with the performed focus scan and the comparison of the empirical results with the theoretical approaches.

The capabilities of the plenoptic camera, as a sensor with a Laser Guide Star acting as a reference, have also been tested by establishing a collaboration with ESO and its Laser System Department during the launching campaigns of April and July 2016 at the Observatory in Tenerife. However, atmospheric turbulence could not be extracted from the LGS images as the exposure time to acquire them was too large to sense instantaneous phase.

Results derived from the carried out verifications can be considered satisfactory: the lack of success in the atmospheric sensing with the LGS does not imply a malfunction of the plenoptic device as it was due to the lack of light in the Coudé room as the optical elements in the path needed to be refurbished and recoated. Maintenance tasks of the Coudé optical path started right after this campaign and have not ended yet (June 2019).

The author proposes future experiments regarding simultaneous measurements with the Shack-Hartmann wavefront sensor, the pyramid wavefront sensor and the plenoptic camera, in order to provide a more quantified comparison among wavefront sensors.

Chapter 7

Uplink Wavefront Correction System. On-sky Demonstration

7.1 Introduction

The Uplink Wavefront Correction System was designed for its integration and testing at the Optical Ground Telescope in the Teide Observatory. The UWCS on-sky demonstration was planned as a sequential execution and completion of tasks:

1. Installation of the optical bench inside the telescope dome. It comprises cables and cooling hoses routing.

2. Alignment of the optical elements of the UWCS.

3. Assembly and verification of the LGS launch system. Axicon alignment and ring-shaped Gaussian beam creation.

4. Powermeter installation on the optical bench and LGS laser power verification.

5. Setting up and verification of the synchronisation between the laser optical chopper, the WFS optical chopper and the WFS acquisition.

6. AO system calibration: interaction matrix between the WFS and the DM.

7. AO control system and closed-loop operation.

8. UWCS on-sky performance validation.

This chapter follows the structure of the consecutive tasks and goals that needed to be accomplished in order to succeed with the uplink correction demonstration.

7.2 The Optical Bench. Installation and Alignment

The UWCS optical bench was installed at the Coudé focus in the OGS dome, as the telescope Coudé room (located on the floor below) was not available due to recoating operations. Therefore, an optical table needed to be transferred from the IAC headquarters in San Cristobal de La Laguna to the telescope at the OT.

Final UWCS set-up is shown in Figure 7.1: in red the calibration system optical path (described in Section 7.6); in green solid line, the laser launch optical path, and in green dashed line, the path followed by the return light from the telescope to the WFS. The optical bench arrangements and all the UWCS elements are described in detail in Chapter 4.
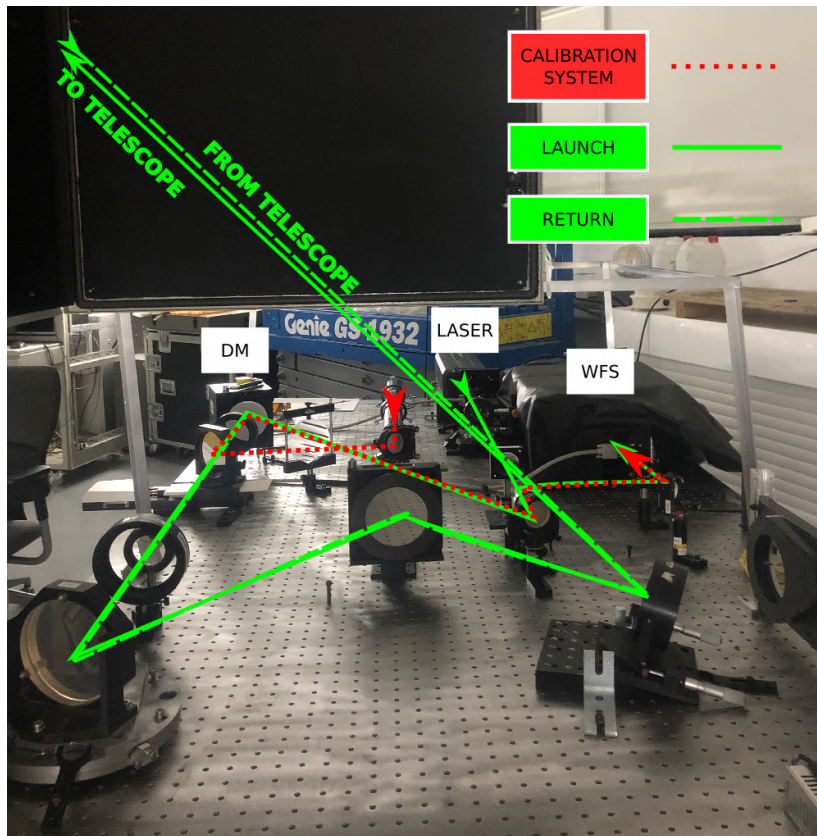
FIGURE 7.1: The light from the Verdi laser follows the solid line through the optical elements, the deformable mirror and the folded mirrors which inject the laser beam to the telescope tube; on the return path (dashed line), the light coming from the sky follows the exact same optical path until the 50/50 beam splitter which divides the beam and leads it to the WFS. In red, the calibration system described later in this chapter.
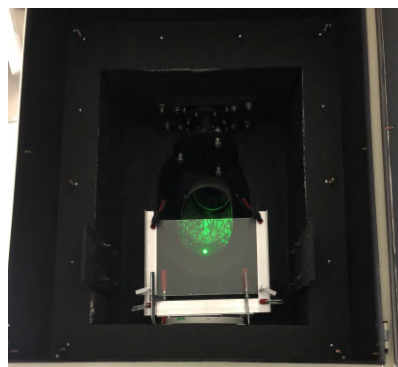
FIGURE 7.2: Alignment of the UWCS with the OGS secondary mirror by using the Verdi laser at minimum power; in the image, reflected light from the secondary mirror when hitting its center by the laser.

The UWCS was integrated on the optical table next to the south pillar of the OGS and aligned to the centre of the telescope secondary mirror by using the Verdi laser at low power (Figure 7.2).

With the purpose of acquiring the sky image as seen by the telescope, a second camera was included in the WFS system with a 50/50 beam splitter. This second camera is a JAY PULNIX TM-6740, located right before the microlenses plane (Figure 7.3). This modification did not imply any alteration in the UWCS optical design except for an additional BS.
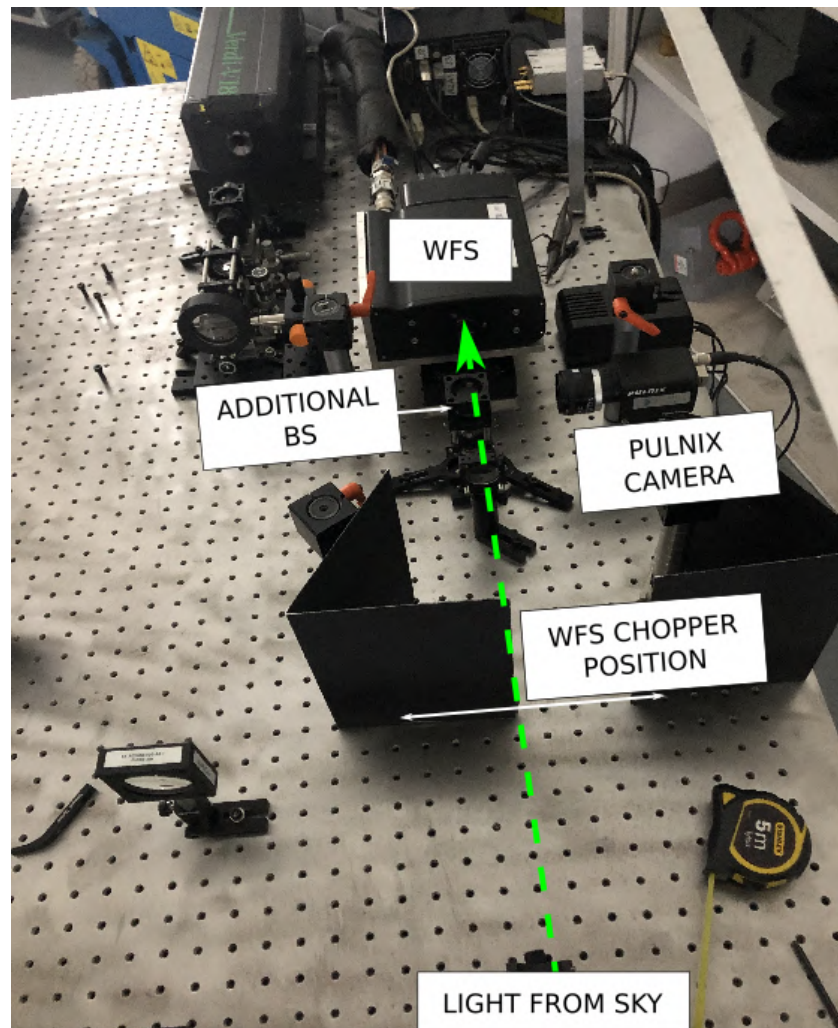
FIGURE 7.3: An additional Jay Pulnix camera is introduced in the WFS system to allow sky images acquisition.

7.3 LGS Launch System. Ring-shaped Beam Creation

As it has been stated in Chapter 4, the LGS was planned to be launched by creating a ring shape in the laser beam with the purpose of avoiding the secondary mirror losses. Therefore, the laser beam needed to be expanded from a collimated 3-millimetre diameter (approximately) to a collimated 10-millimetre output beam by the Edmund Optics x3 MT Fixed beam expander; once the laser had the proper

size, was lead to the axicon pair which produced a ring of 15-millimetre diameter (Figure 7.4). For more details about the axicon design, refer to Chapter 4.
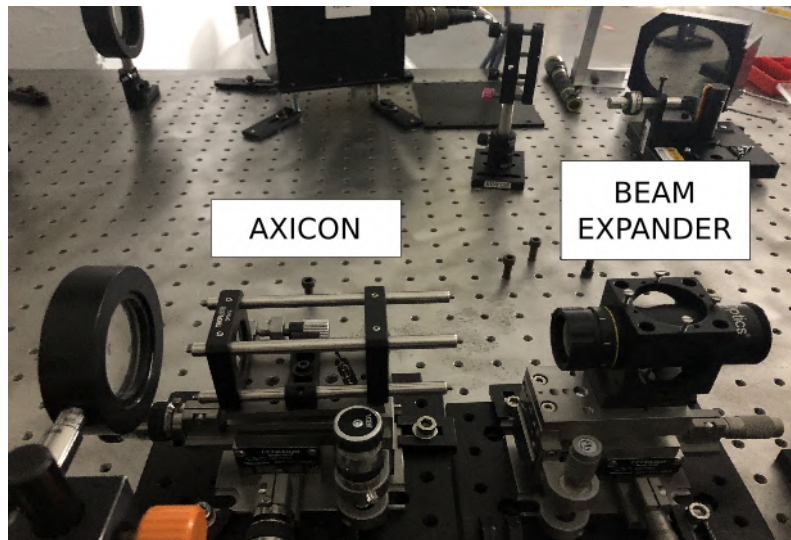
FIGURE 7.4: The LGS Launch System is composed by the optical elements which allow the ring-shaped beam creation: the beam expander and the axicon pair.

The laser ring was propagated throughout the optical set-up to the telescope tube and ultimately, to the sky. Figure 7.5 presents the ring generation during the UWCS alignment phase on the lens right after the axicon and on the OGS dome. It was extremely important the fine alignment of the axicon pair with other optical elements in the set-up; any tilt would have introduced artifacts in the beam shape, causing a mismatch in the obscured/illuminated ratio and hence, clipping losses due to the secondary mirror. This fine alignment was reached by mounting the axicon in a multi-axis platform with a tip/tilt stage (Newport ULTRAlign for precision fiber optic alignment), whose crossed roller bearings ensured $< 100\mu rad$ of angular deviation in any axis. This devices allowed the position adjustment of the axicon pair in all the necessary degrees of freedom.

7.4   Laser Power and Optical Throughput Analysis

The Edmund Optics Premier Powermeter, and a volume absorber sensor with detecting capacity up to 30W, were used to measure the Verdi laser power and its absorption by the optical surfaces all along the launch path.

The sensor was placed at several points in the set-up, analysing the remaining power after the absorption of the different optical elements (Figure 7.6).

Measurements were acquired for 5 minutes at a rate of 10 samples/s; the acquisition began at the time instant when the laser was turned on and it started warming up, until it reached the stable state. Figure 7.7 shows the totality of the measurements and a zoom section of the last 1000 samples; the results show how the laser power oscillated $\pm$ 100 mW when it was considered to be stable. This intensity oscillation will introduce uncertainties when analysing the UWCS performance (see Section 7.8).

It is remarkable that the ensemble beam expander-axicon pair-lens absorbs around a 10%, less than the losses that the secondary mirror obstruction would cause when
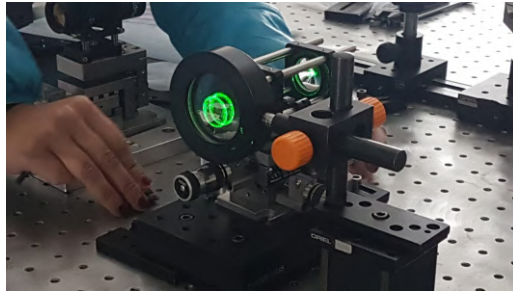
FIGURE 7.5: Above, the ring-shaped generation with the axicon during alignment tasks; below, the laser ring at the OGS dome.
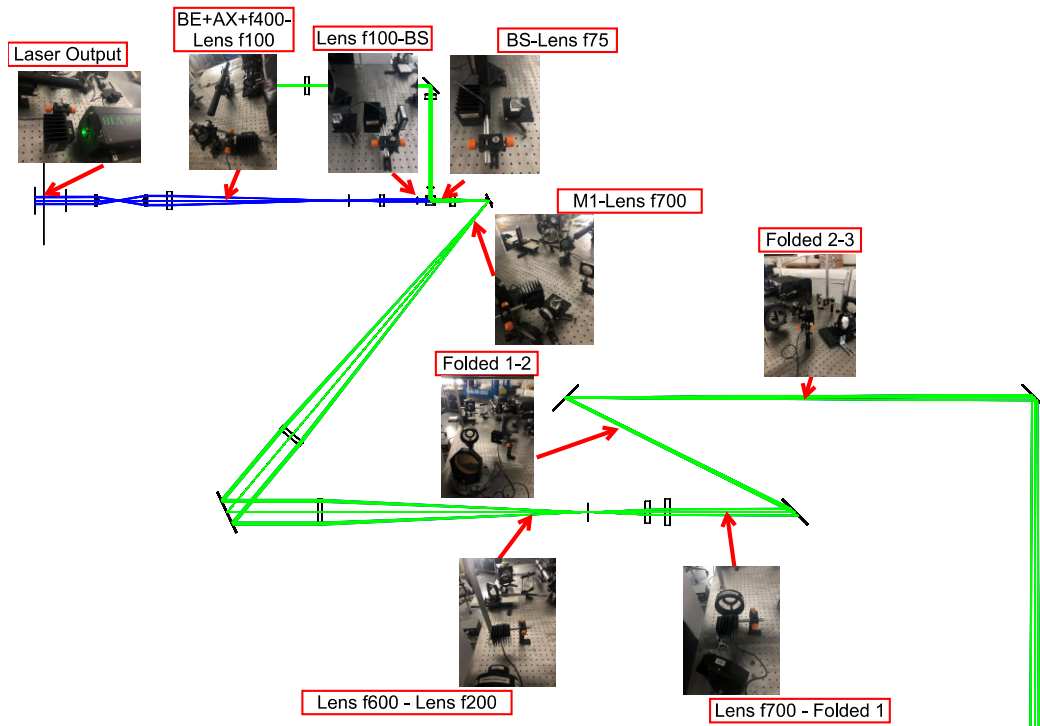
FIGURE 7.6: The powermeter is placed at several locations in the
launch optical path to measure the laser power after being absorbed
by the different optical surfaces.

launching a Gaussian beam through the whole telescope aperture (Clipping factor
described in Chapter 4).

The lenses and mirrors in the set-up had not an optimum response at the laser
wavelength (532 nm), as not all of them had been acquired purposely for the UWCS,
but already available within the IAC optical material sets.
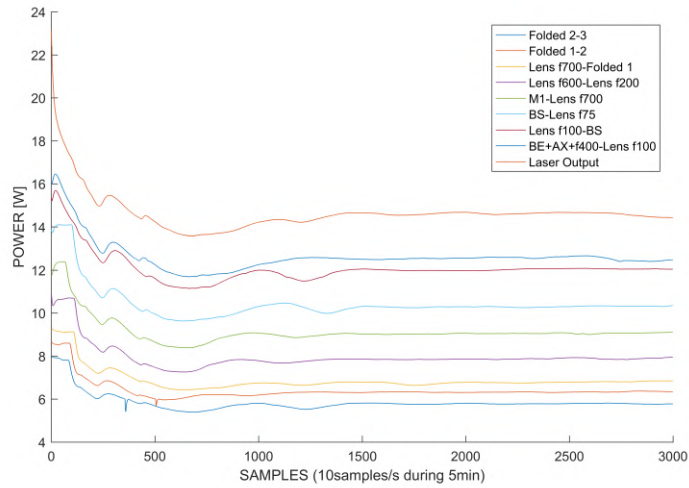
(a)
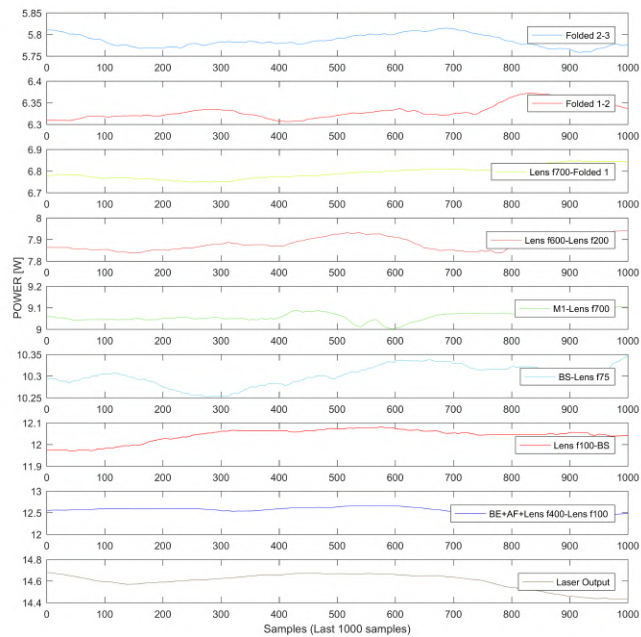
(b)

FIGURE 7.7: Laser power measurements at locations in Figure 7.6. (a) 30000 samples starting when switching on the laser; (b) Zoom section of the last 1000 samples when the laser is considered to be stable, although there is a noticeable intensity variation.

7.5   Laser/WFS Chopping Operation in Synchronisation Mode

The main function of the optical choppers in the UWCS was allowing the shared-path operation: the WFS chopper needed to operate in synchronised mode with the laser chopper in order to avoid the blindness of the camera detector when launching the laser. Both optical choppers (Laser and WFS in Figure 7.8) were integrated in the optical bench by taking into account the beam size at the chopper position: the smaller the beam diameter, the faster it would be chopped. Hence, the optical choppers needed to be located one at the laser output where the beam had minimally suffered from divergence, and the other one, at the focus position immediately before the WFS (Figure 7.9).
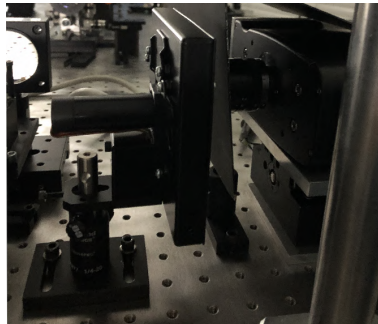
(a)
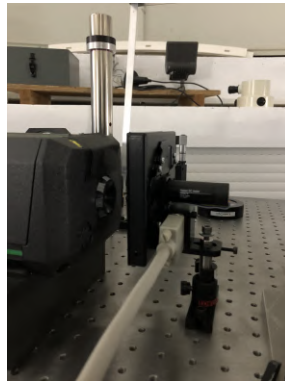
(b)

FIGURE 7.8: SCITEC INSTRUMENTS 310CD Installation; (a) Wavefront Sensor Optical Chopper; (b) Laser Optical Chopper

Chopping discs for the LGS and for the WFS did not have the same design but an equal number of slots: the SCITEC INSTRUMENTS Blade 300D2 (2 slots) was integrated in the laser chopper; and a custom-manufactured 2-slot blade needed to be used in the WFS chopper (see Figure 7.10) as the obscuring aperture, which blocked the incoming light to the camera, shall be larger than the open slot.

As it has been stated in Chapter 4, the idling time between the laser pulse and the camera acquisition shall be around 133 μs, which implies a very precise and stable synchronisation schema.

Due to a slight difference in weight of the custom-built disc, the maximum allowed chopping speed by the SCITEC INSTRUMENTS synchroniser was 300 Hz in order to ensure this sharp synchronisation.
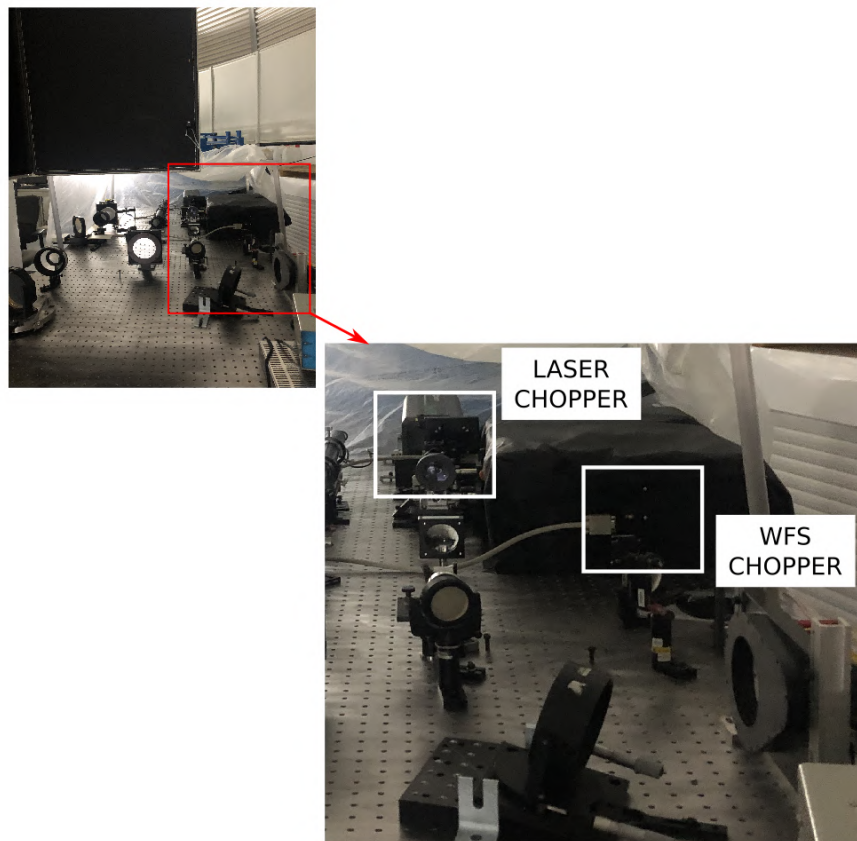
FIGURE 7.9: Positions of the optical choppers in the UWCS set-up: the laser chopper is located at the laser output to minimise the beam divergence effect; the WFS chopper is placed at the immediately preceding focus.
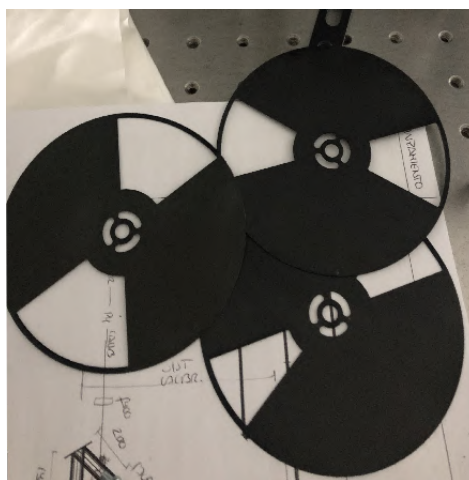
FIGURE 7.10: Several designs of chopping discs have been custom-manufactured at IAC mechanical workshop facilities with the purpose of obscuring the WFS for larger periods than the ones with open aperture.

However, due to the mechanical nature of the optical choppers and the limited chopping speed, neither the laser beam nor the return light from the Rayleigh backscattering were chopped abruptly in time, but in several microseconds, causing delays in the reception which were translated into a reduction on the received backscattered return. Figure 7.11 represents this fact: combining all the signals (the Rayleigh return produced by the laser emission, whose direction depends on the laser chopping frequency, and the WFS chopping, which will only allow the sensing at the desired atmospheric height where the laser is being focused) at 300 Hz, only between a 10% and 20% (depending on the focusing height) of the Rayleigh return was acquired by the WFS.
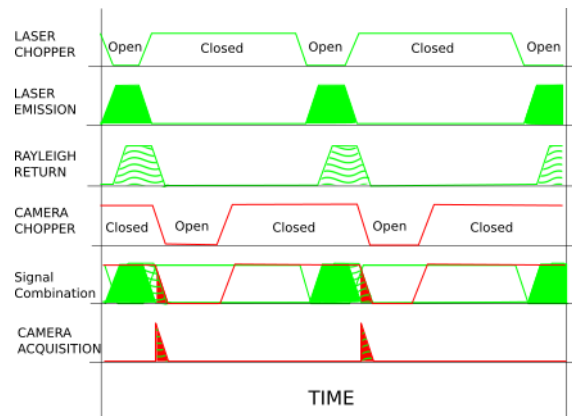
FIGURE 7.11: The slopes in the opening or closing of the laser and WFS aperture cause a reduction on the Rayleight return from the sky that the WFS is capable of sensing.

Figure 7.12 shows the negligible Rayleigh return which was detected by the camera without the lenslet array (which would distribute even more the light); this return appears to be out-of-focus as the synchronisation schema was designed to capture the light from a specific height in the atmosphere, which does not correspond to the one in the image, due to oscillations between the synchronisation signals.

FIGURE 7.12: Out-of-focus Rayleigh backscattered light, acquired by the WFS camera without the lenslet array, pointing Arcturus with the telescope in low elevation position.

7.6 AO System Calibration

The calibration system was installed in the UWCS with the purpose of calculating the interaction matrix between the slopes computation in the WFS and the DM actuation.

Figure 7.13 shows the UWCS calibration system. An additional element was introduced in the system apart from the ones described in Chapter 4: the linear stage to mount the last folded mirror of the system. Technical details of the PI linear stage are not relevant as its only function was injecting the calibration laser beam onto the DM: home position was used for normal UWCS on-sky operation and the limit switch position, for the calibration mode.
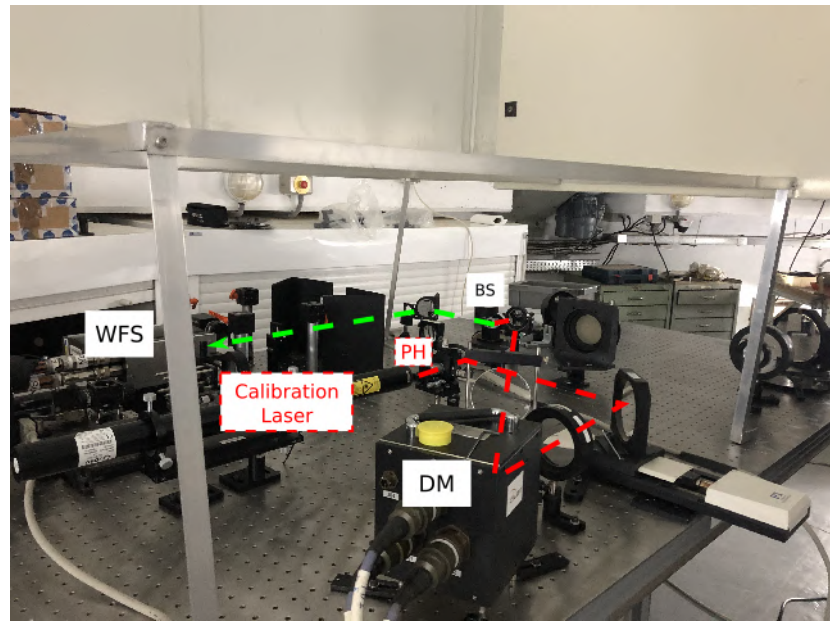
FIGURE 7.13: UWCS Calibration System. The optical path follows
the red dashed line.

Prior to the interaction matrix computation, the DM needed to be initialized to its best flat configuration. However, the conventional mirror flattening technique could not be applied due to the non-availability of the interferometer at the telescope. Hence the wavefront sensor was directly illuminated by a reference fibre source ensuring uniform and parallel illumination of the lenslet array (Figure 7.14). The WFS centroids were computed and saved; later on, the deformable mirror should be actuated in the way, the calibration light travelling through the DM to the WFS, registered the same centroids positions as in the reference light case. This actuator configuration was considered the best flat shape of the DM.

The estimated DM best flat was tested with the calibration system as it is presented in Figure 7.15: the curved shape of the DM, measured by the interferometer during laboratory characterisation (Chapter 5), was clearly noticeable in the WFS frame before the mirror flattening (even though, only a central 55-millimetre area of the DM was illuminated by the calibration laser as it is the area affected by the LGS itself, based on design decisions); after the flattening (Figure 7.15(b)), the curvature effect was less present, although there were some defects on the outer part due to mirror irregularities in this area.
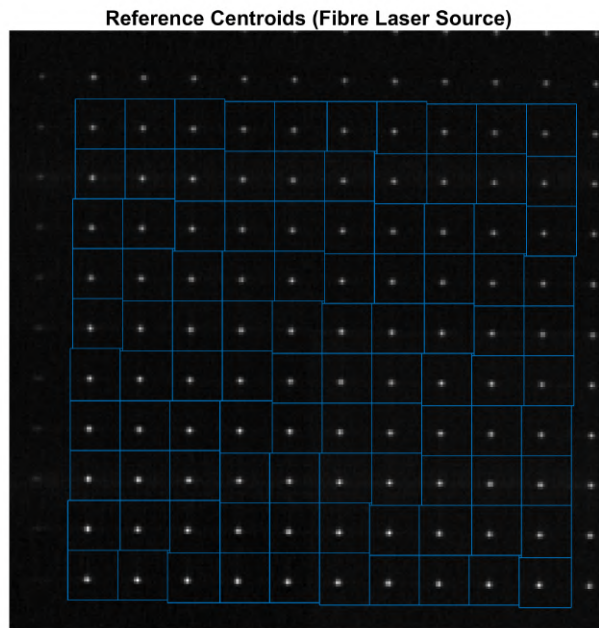
FIGURE 7.14: Reference illumination of the lenslet array to compute
the best mirror flat configuration.

Both wavefront sensor and deformable mirror use a certain software mask for their proper operation; this mask was manually defined by taking into account only the influence area of the DM on the laser (the illuminated central area) as well as the number of microlenses in the WFS receiving light from the calibration system or from the sky.

Furthermore, bias and flatfield images (Figure 7.16) were necessary in order to improve the performance of the WFS camera; the bias image was captured with the WFS chopper closed and the wavefront sensor system enclosed under a black cover, ensuring minimum illumination, and the flatfield was acquired with the telescope dome open during twilight.

After the initialisation phase, the system was ready to measure the interaction matrix. The WFS/DM interaction matrix was computed by inverting the poking matrix, the one relating the actuation and the WFS slope, after applying some voltage separately to each of the DM actuators.

LASER CALIB; NO FLAT DM

(a)

LASER CALIB; FLAT DM
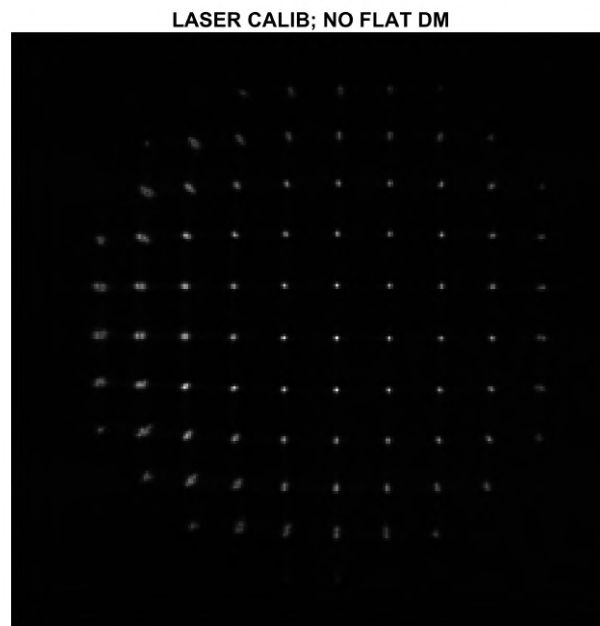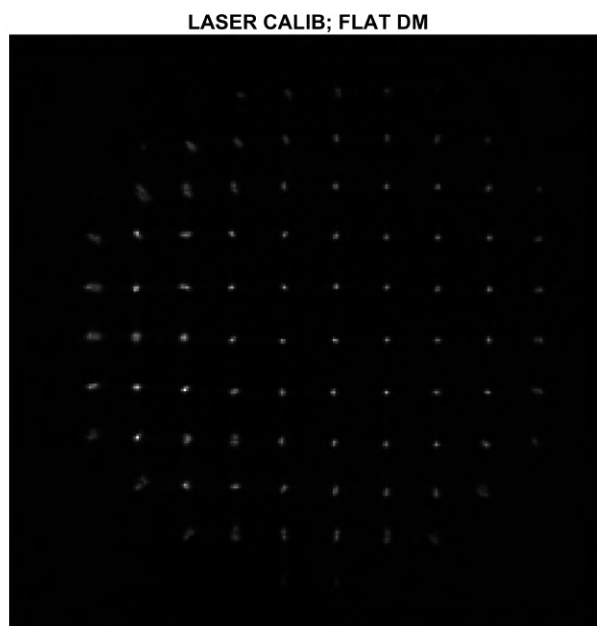
(b)

FIGURE 7.15: WFS frame with calibration source illumination (a) before DM flattening and (b) after DM flattening. Notice that the WFS is not uniformly illuminated due to a misalignment in the set-up.
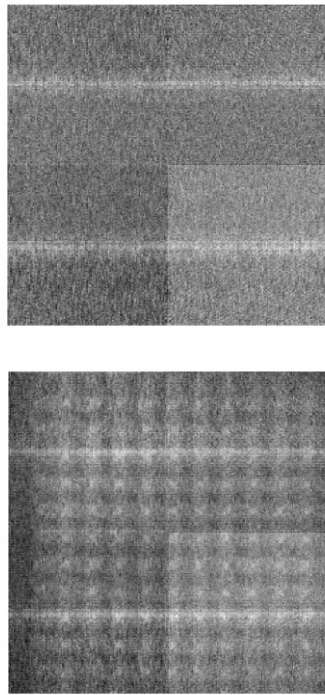
FIGURE 7.16: Bias and flat images for the WFS operation.

7.7   AO Control System and Closed-Loop Operation

The UWCS Control System was also installed at the dome, next to the south pillar of the telescope as the CameraLink cables for the WFS frame grabber have a maximum length of 10m. Figure 7.17 presents the electronics cabinet with the DM control modules, the NI PXI to send the corresponding actuation to the mirror electronics, and the RTC computer, which contained the DARC controller.

Initially, the UWCS design was thought to use the Rayleigh return from the launched Laser Guide Star as the reference source for the wavefront sensing and therefore, the close loop operation. However, based on the insignificant Rayleigh return captured by the camera without the microlenses array, the decision of using a Natural Guide Star instead to close the AO loop, had to be made in order to guarantee the experiment success.

Theoretical results indicated that the expected Rayleigh return would be such that the SNR would be high enough for the measurement (Chapter 4). Nevertheless, the calculations did not take into account the already described chopping problem and another encountered difficulty: some residual light entering the wavefront sensor when operating the laser at maximum power. After carefully analysing the UWCS set-up, the cause was found out to be a fluorescence light coming from the beam splitter, which lasted around 3ms. Figure 7.18 shows the fluorescence source and its effect on the WFS frame. As a consequence, the camera could not be operated with the electronic gain necessary to detect the Rayleigh return, and, hence, the natural guide star became the most suitable solution.

FIGURE 7.17: UWCS Control System: from left to right, electronics cabinet with CILAS control modules on top (junction box and two signal amplifiers), National Instruments PXI-E and Ethernet switch below, and RTC PC.
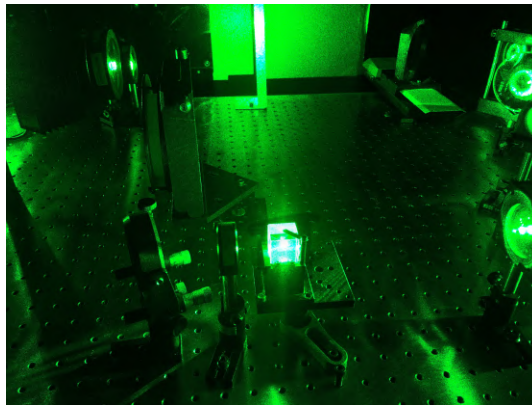
(a)
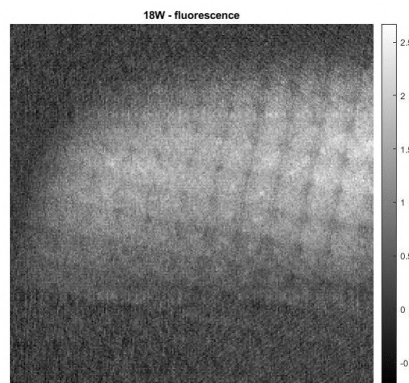
(b)

FIGURE 7.18: Fluorescence coming from the beam splitter is detected by the WFS; (a) Beam splitter illuminated by the Verdi laser; (b) Detected fluorescence on the WFS frame at 300 Hz.

Regarding the AO loop, the closed-loop parameters needed to be properly configured for both the WFS and the control loop itself. The DARC controller offers the possibility of defining a threshold value in the photon flux per sub-aperture with the aim of avoiding miscalculations due to poor illumination at the WFS lenslet array. This threshold, as well as the number of brightest pixels (per sub-aperture) which were taken into account in the centroids estimation, needed to be set up based on the light level captured by the WFS.

The reference centroids, imposed as the true value with refer to which the wavefront error was minimised, were computed by averaging the NGS centroids positions over 1000 frames at 150Hz rate. The use of the calibration reference centroids was also tested, although the optimum operation was achieved by the averaging the star movement.

Regarding the AO control loop, two main parameters needed to be established: the gain and the decay factor (this factor is included in the control algorithm in order to progressively ignore the unseen modes which are not properly measured by the WFS, i.e. waffle mode). Both were first fixed at preliminary values to produce very slight changes in the system: gain close to 0 and decay factor close to 1; these values needed to be tuned in a very gradual way to avoid the system to become unstable.

7.8 On-sky Performance Validation

The OGS has a 20 cm finder telescope, attached and aligned to the main telescope. This finder telescope was used to get a large field-of-view image to ease the localization and spot size analysis of the LGS launched through the 1 meter telescope focus. An ANDOR iXon3 888 with 1024x1024 pixels was attached to the finder telescope as scoring camera. Figure 7.19 shows the location of the scoring camera in the telescope.
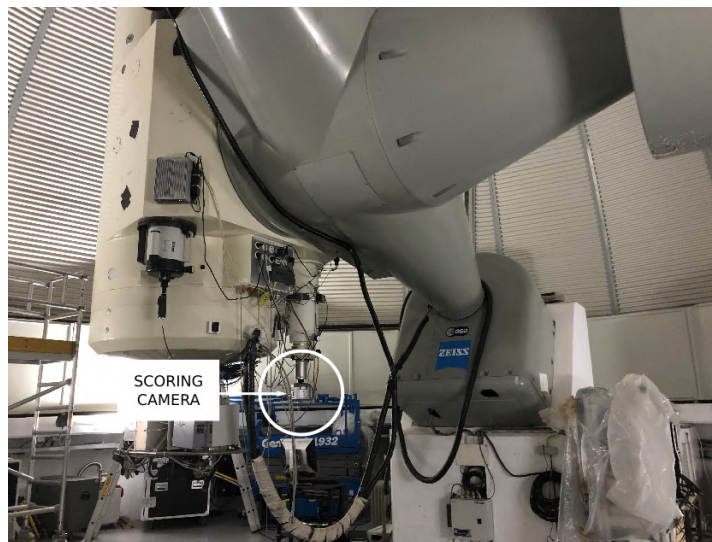
FIGURE 7.19: Scoring camera installation in the finder telescope.

Figure 7.20 presents the detected laser light by the scoring camera during a cloudy night; as the clouds were located at heights of around 8 km, the laser did not come to focus and the propagated ring was backscattered by the clouds.
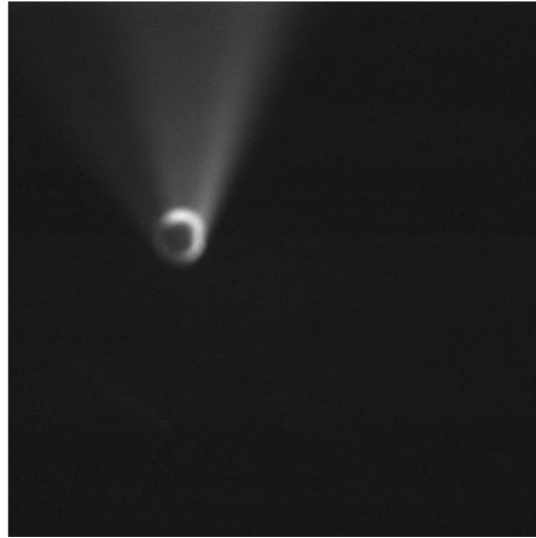
FIGURE 7.20: Image of the laser ring acquired during a cloudy night; the laser light is scattered by the clouds before reaching the focus point altitude. The ring is not uniformly illuminated due to a still ongoing alignment phase at that point of the experimentation campaign.

The AO control loop was closed with Arcturus (mV=-0.05) as Natural Guide Star, as explained above, and the wavefront correction in the laser uplink was evaluated by analysing the detected light in the scoring camera. Figure 7.21 shows two long exposure frames (integration time 500 ms) from the ANDOR camera, before and after closing the loop, demonstrating the successful pre-compensation of the LGS upwards propagated path, whose plume gets brighter at its focus position when closing the AO loop.

The ANDOR images of the laser beam have been analysed by selecting a region of the plume and within it, 5 columns in the image to study the intensity profile shape (Figure 7.22).

The beam profiles along the selected lines in the laser plume are represented in Figure 7.23; the top graph corresponds to the least focused positions in the LGS plume (first red line on the left in Figure 7.22), and the bottom graph to the most focused one (last red line on the left in Figure 7.22).

The analysis has been repeated for a case in which the AO loop was closed without the prior DM flattening (Figure 7.24), with the purpose of studying the effect of ignoring the best flat configuration of the deformable mirror.

OPEN LOOP

CLOSE LOOP
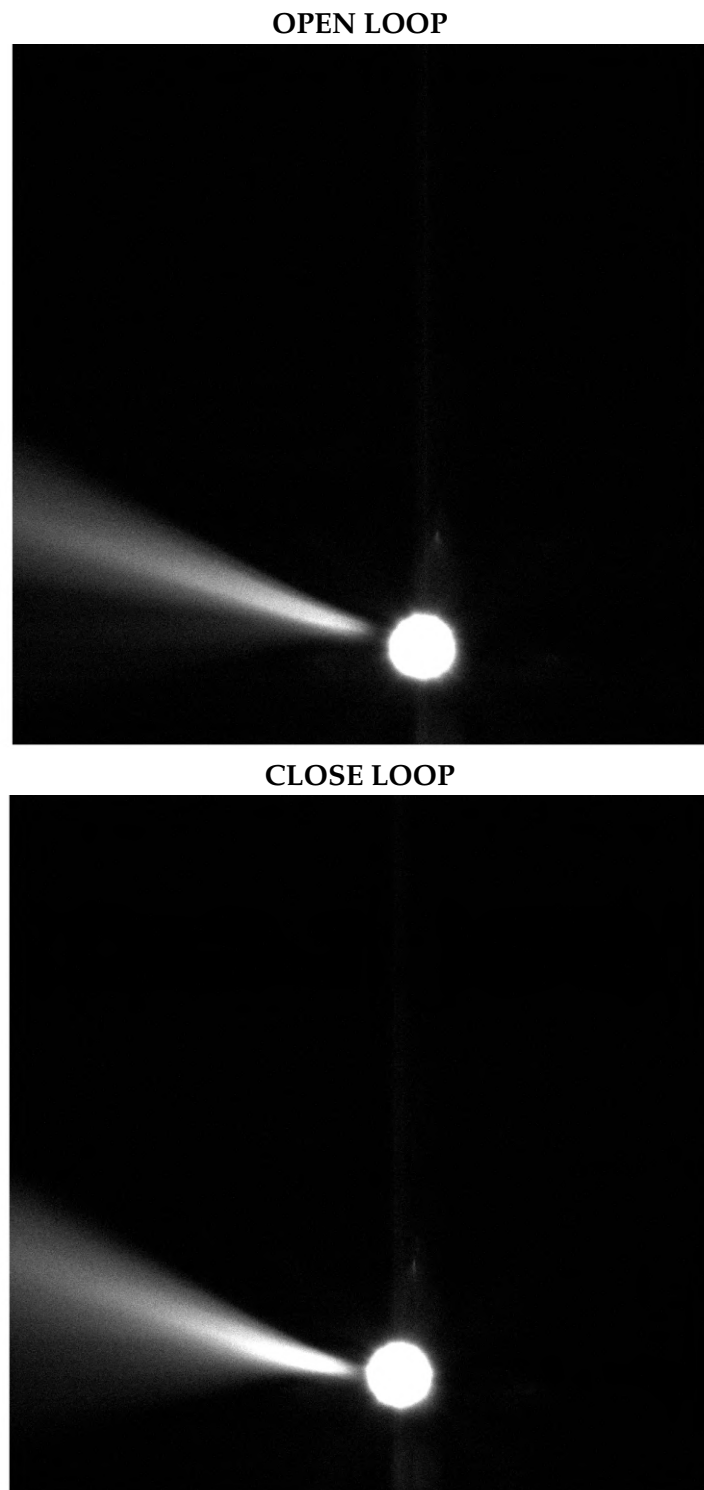
FIGURE 7.21: Scoring camera images of the laser plume before and after closing the AO loop with Arcturus as NGS, also in the image. Notice the increase in brightness when the laser wavefront is being pre-compensated.
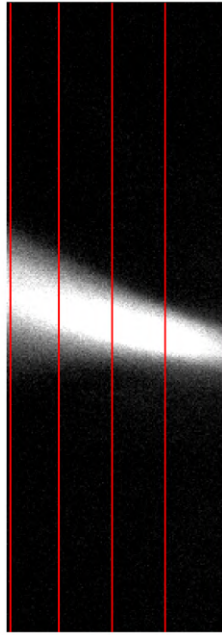
FIGURE 7.22: Selected region of the plume; the light distribution along the red lines has been selected for further analysis.

When closing the loop with the optimal parameters and after initialising and calibrating the system properly, an increase of 22% in the laser intensity is achieved at the most focused position; and the beam profile becomes narrower with a 25% decrease in the FWHM (Figure 7.25(a)); whereas, without performing the DM flattening (Figure 7.25(b)), the light gain is around 20%, but the FWHM only diminishes by a 9%. This result indicates that the FWHM in open loop is mostly due to the atmospheric aberrations, as the DM flattening only becomes noticeable when applying the wavefront correction, in which case, the optimum performance of the AO system is achieved when the deformable mirror has been previously flattened. In both scenarios, the beam shifts one respect to the other (when closing the loop), although without flattening the DM, this shift is much more noticeable (the number of pixels of the shift is double in this last case, with respect to the scenario where the proper DM flattening was performed).

By accessing the QR code in Figure 7.26, one can see the closing of the AO loop on the laser beam, having Arcturus as NGS. Each frame in the video is acquired with an integration time of 30 ms by the scoring camera. Notice the intensity oscillation in the laser beam, present in both open and closed loop operation. It is uncertain if this intensity oscillation is due to the non-fully corrected atmospheric wavefront or to the laser itself, whose power was measured and proved to be non-stable.
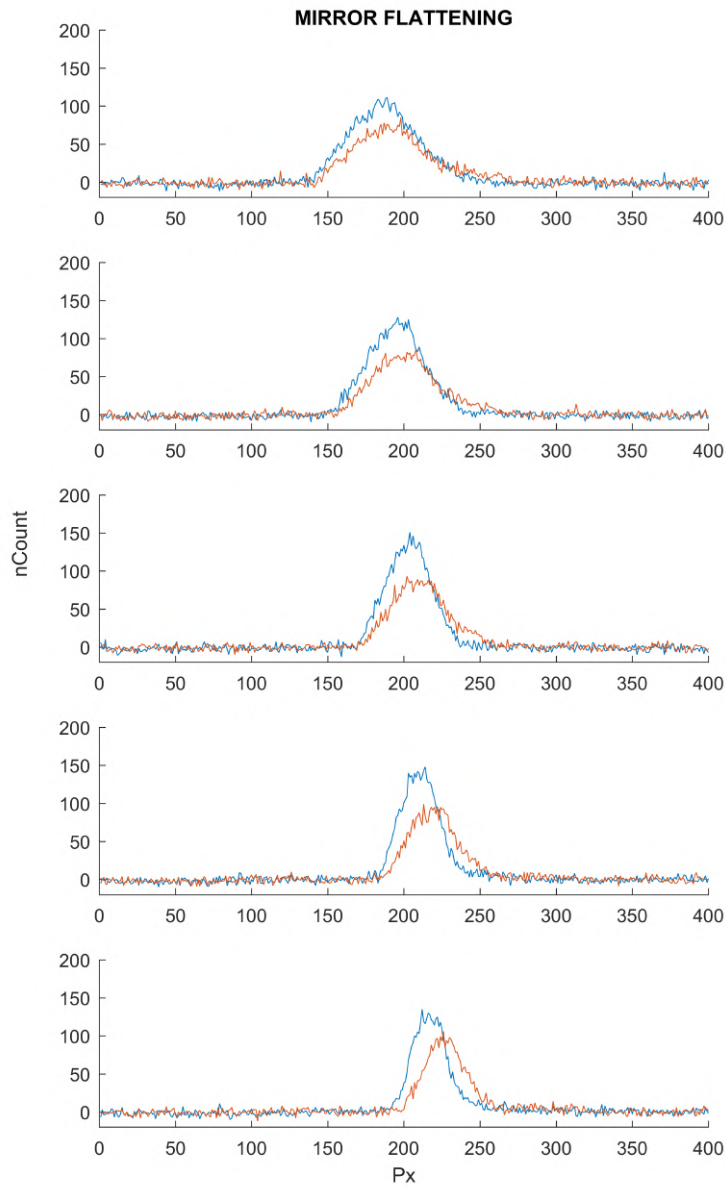
FIGURE 7.23: From top to bottom light distribution corresponding to the selected lines in the laser plume (red lines from left to right in Figure 7.22); in red open-loop operation, in blue, close-loop operation.
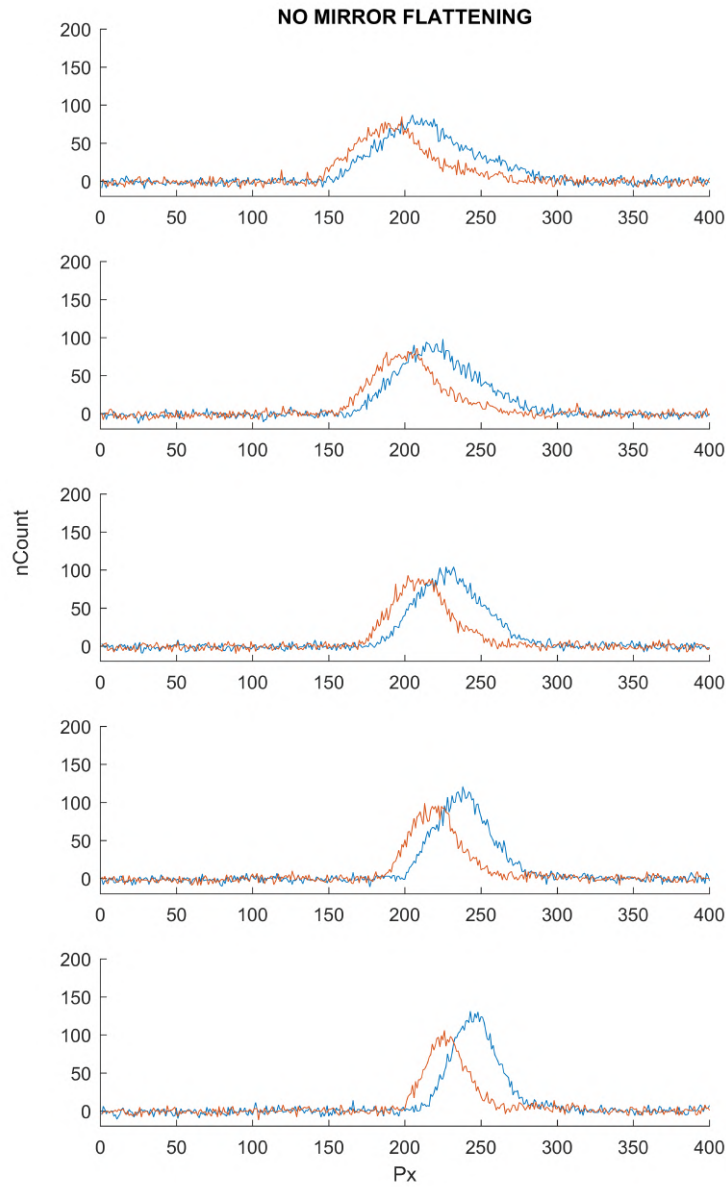
FIGURE 7.24: From top to bottom light distribution corresponding to the selected lines in the laser plume (red lines from left to right in Figure 7.22); in red open-loop operation, in blue, close-loop operation without performing the DM flattening.

(a)

(b)
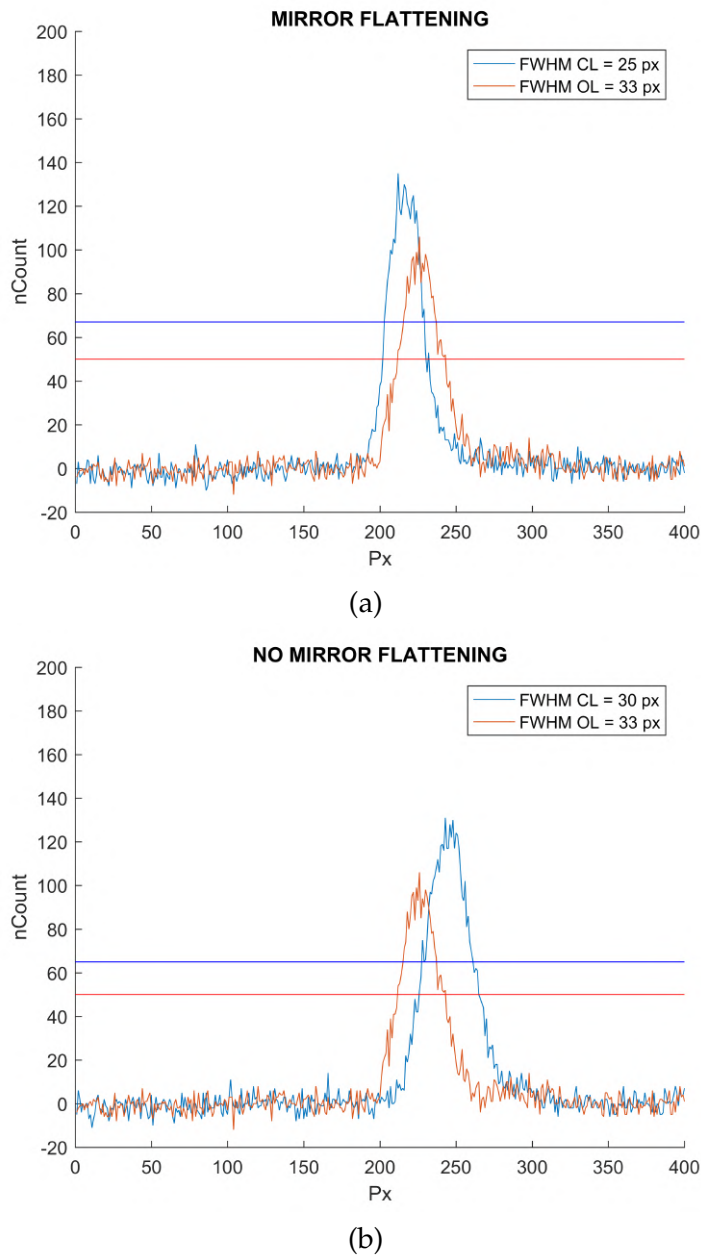
FIGURE 7.25: Laser intensity distribution corresponding to the most focused point the laser plume (last red line in Figure 7.22); in red open-loop operation, in blue, close-loop operation with (a) and without (b) performing the DM flattening.

7.9. Uplink Wavefront Corrector System. Conclusions from the on-sky demonstration

119

FIGURE 7.26: Video acquired by the scoring camera at 30 fps, showing the closing of the AO loop and the enhancement of the laser plume brightness.

7.9 Uplink Wavefront Corrector System. Conclusions from the on-sky demonstration

The UWCS was successfully integrated in the OGS telescope by installing an optical bench inside the dome and aligning the optical set-up with the telescope axis. The Rayleigh Laser Guide Star was propagated using the whole primary mirror; the axicon launch system allowed the avoidance of the central obscuration due to the secondary mirror and hence, the clipping losses in the laser beam. No previous record of propagating a laser with this ring-shape generator has been found, therefore it is considered a novel approach in laser launch systems, which has been completely accomplished in the UWCS. The axicon absorption in terms of laser power was measured and proved to be less than the clipping losses for a Gaussian beam.

Due to the limitations associated to the mechanical nature of the optical choppers and an unexpected fluorescence coming from the beam splitter, it was not possible to use the Rayleigh return from the LGS as the reference for the wavefront sensor. However, the Adaptive Optics loop was successfully closed with a Natural Guide Star, demonstrating the uplink pre-compensation of the laser beam.

The UWCS validation on-sky was presented at the *XIII Annual Workshop on Laser Technology and Systems for Adaptive Optics* in June 2019. Part of the results are gathered in the proceeding *Uplink Wavefront Corrector System: On-sky performance validation*, publication still pending. A paper for the Optics Express journal is currently in preparation with all the on-sky experimentation results.

Chapter 8

Conclusions

The conclusions of the research performed in this thesis are summarised in this chapter.

- The isoplanatic study results outline the need of propagating a Laser Guide Star to the expected uplink location in order to perform an optimal uplink pre-compensation, instead of using the downlink signal as a reference source for the wavefront sensing. The investigation of using the downlink signal as a guide star with a predictive controller to estimate the wavefront in the uplink position, is proposed for future analysis.

- After accomplishing end-to-end simulation regarding the performance of an AO system pre-compensating the uplink, the influence of the point-ahead angle is remarkable in the spot size and scintillation reduction, re-validating the outcome of the isoplanatic simulation: a LGS needs to be used to measure the uplink wavefront.

- The analysis of the isoplanatic patch and of the uplink correction performance are gathered in the proceedings *Simulating the performance of adaptive optics techniques on FSO communications through the atmosphere* (Martínez, Ramos, and Sodnik, 2017) and *Performance assessment of Adaptive Optics techniques on FSO communications through the atmosphere* (Martínez et al., 2017a). Additionally, a paper published in the Optical Engineering Journal presents the simulation results as well as a preliminary design of the proposed AO system (Noelia Martínez, 2018).

- With the purpose of solving the Tip/Tilt retrieval problem from LGSs, currently still not verified, the third type of simulation was designed and executed: TT retrieval from the Na layer anisotropies. Results show that TT information could be extracted from Sodium contrast images by the plenoptic sensor, although this part of the research needs to be further studied.

- The proposed method for the TT retrieval from the Na anisotropies is described in the proceeding *Sodium layer density anisotropies as a reference for tip-tilt measurement in laser guide stars*, publication still pending.

- The Uplink Wavefront Corrector System has been designed for its integration at the Coudé focus of the OGS telescope. The main elements composing the

system were: a 18W Verdi laser as LGS, the axicon optical device to generate the ring shape, 12x12 sub-aperture Shack-Hartmann WFS and the CILAS SAM97 deformable mirror with 97 actuators in a 11x11 grid.

- The simulation test bench for the Uplink Wavefront Corrector System is deeply described in the proceeding *Uplink correction demonstrator: test bench and experimental results* (Martínez et al., 2018).

- The capabilities of the plenoptic camera, as a wavefront sensor with a Laser Guide Star acting as a reference, have also been tested by establishing a collaboration with ESO and its Laser System Department during the launching campaigns of April and July 2016 at the Observatory in Tenerife. Results derived from the carried out verifications demonstrated the capabilities of the plenoptic camera as wavefront sensor to the possible extent. The laser campaign was carried out right before the maintenance of the optical path towards the Coudé room, whose lenses and mirror needed refurbishment, therefore the optical throughput was not enough to sense the LGS at low integration times and hence, only the defocus of the LGS was successfully retrieved. Experiments regarding simultaneous measurements with the Shack-Hartmann wavefront sensor, the pyramid wavefront sensor and the plenoptic camera, are proposed as future tasks, in order to provide a more quantified comparison among wavefront sensors.

- The UWCS Rayleigh Laser Guide Star was propagated using the whole OGS aperture; the axicon launch system allowed the avoidance of the central obscuration due to the secondary mirror and hence, the clipping losses in the laser beam. No previous record of propagating a laser with this ring-shape generator has been found, therefore it is considered a novel approach in laser launch systems, which has been completely accomplished in the UWCS. The axicon absorption in terms of laser power was measured and proved to be less than the clipping losses for a Gaussian beam.

- The uplink pre-compensation of the laser beam has been successfully demonstrated in the UWCS proof-of-concept instrument, achieving brightness increases of 20% in the laser plume.

- The UWCS validation on-sky was presented at the *XIII Annual Workshop on Laser Technology and Systems for Adaptive Optics* in June 2019. Part of the results are gathered in the proceeding *Uplink Wavefront Corrector System: On-sky performance validation*, publication still pending. A paper for the Optics Express journal is currently in preparation with all the on-sky experimentation results.

Appendix A

Plenopic Wavefront Sensor for Solar Adaptive Optics

A.1 Introduction

Day-time Adaptive Optics deals with different challenges in comparison to night-time AO: worse day-time seeing, observations at visible wavelengths and the low-contrast extended objects the wavefront sensor shall work with (like solar granulation) (Rimmele, 2000). Therefore, researching about wavefront sensors novel concepts could be fundamental in this field of expertise. Moreover, the Sun is an ideal object for the development of Multi Conjugate Adaptive Optics (MCAO) since solar structure provides multiple "guide stars" in any desired configuration.

This chapter demonstrates the suitability of the plenoptic wavefront sensor not only for conventional solar adaptive optics but also for MCAO systems.
It is organised into the following sections: the on-sky feasibility test at the VTT solar telescope with the achieved results and conclusions, and the performance simulation of a solar MCAO system with the plenoptic camera as a single WFS.

A.2 Plenoptic Solar WFS: on-sky feasibility test

During November 2015, several tests with a plenoptic camera were performed at the VTT solar telescope (see Table A.1), located at the Teide Observatory (Canary Islands, Spain) with the aim of measuring atmospheric aberrations with solar images as reference.

A.2.1 Experimental Set-up

The plenoptic WFS consisted of a Pulnix TM6200 camera plus a microlenses array at the lenslet focal length (25mm) from the camera detector (Table A.2), which was installed at the telescope focus. Additionally, a 589.5-nanometre filter (Sodium wavelength) was used to avoid sensor over-exposure. Schematics of the experimental set-up is represented in Figure A.1. Due to the Sun elevation at this time of the year and the telescope design itself, the VTT pupil was not fully illuminated (Figure A.2).

Telescope Diameter	70cm
Focal Length	46m
AO system	36x36 SH at 70Hz

TABLE A.1: Vacuum Tower Telescope (VTT) optical parameters
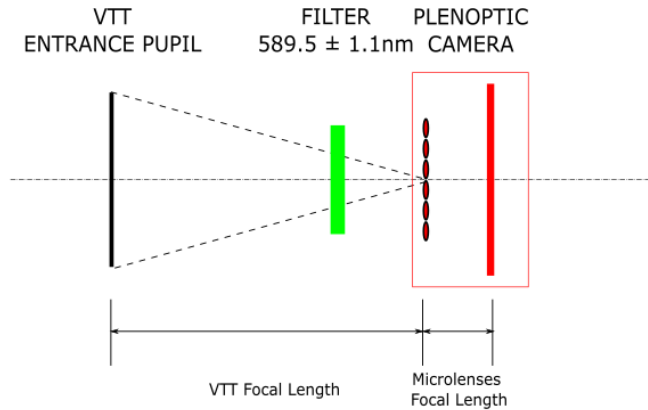
FIGURE A.1: Schematics of the experimental set-up installed at the VTT Solar Telescope during November 2015 test runs.

FIGURE A.2: VTT partially illuminated pupil during November 2015 test runs due to the sun elevation at that time of the year.

Camera Model	Pulnix TM6200
Sensor Size	2048x2048 pixel
Microlenses Array	$400\mu m$ pitch and 25mm focal length

TABLE A.2: Plenoptic Camera optical parameters

Several acquisition runs were performed in order to characterise the plenoptic camera as a wavefront sensor for solar AO: bias and flat field images were first captured to ease the device calibration procedure; sun spots were imaged with and without the adaptive optics system present in the telescope, and additionally, solar images with some optical aberrations added on purpose were also obtained with the aim of outlining the capabilities of the plenoptic camera to detect them.

A.2.2 Results

Results of November 2015 testing campaign at the VTT solar telescope are presented in this section.

Artificial aberrations were introduced on purpose into the optical path by changing the shape of the deformable mirror (present in the current VTT AO system, called KAOS with a 36x26 sub-aperture Shack Hartmann and a 35 electrodes bimorph deformable mirror). The added aberrations have been studied by imaging sunspots through the telescope (Figure A.3 shows an example of a sunspot acquired by the plenoptic sensor).

Several optical aberrations have been introduced into the system and deeply analysed: defocus, trefoil and spherical aberration.
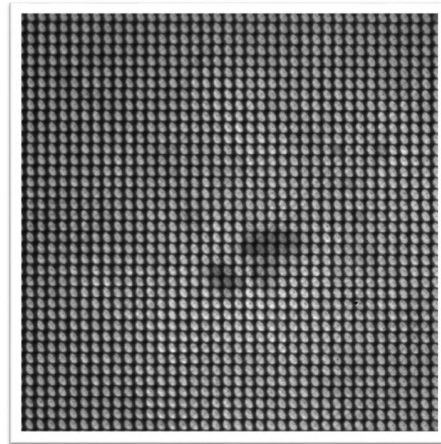
FIGURE A.3: Plenoptic image of a sunspot acquired through the VTT solar telescope.

Firstly, defocus was introduced by changing the DM shape, which was altered by commanding the AO control system to reproduce a defocus mode with arbitrary units; Figure A.4 shows the reconstruction of several degrees of defocus aberration after being sensed by the plenoptic camera. In Figure A.5, one can observe the linearity between the introduced defocus and the measured mode, demonstrating the proper functioning of the plenoptic wavefront sensor.

After the focus analysis, the trefoil aberration was created by applying the corresponding shape to the DM; reconstruction of trefoil is shown in Figure A.6. Due to the partially illuminated pupil, only the trefoil peaks can be seen on the left side.

The spherical aberration could not be evaluated due to technical problems in the AO system which were discovered afterwards during the image processing phase.

In all the wavefront reconstruction cases, in order to see only the artificial aberration of interest, 100 images have been averaged to suppress the atmospheric effect.

Besides the partially illuminated pupil, algorithms for plenoptic images processing have successfully reconstructed manually introduced aberrations, demonstrating the capability of this device as wavefront sensor for solar Adaptive Optics systems.

Due to the poor atmospheric seeing during the test campaign, it was not possible to compute the wavefront from the solar granulation but from the captured sunspot. This fact implies no tomographic reconstruction could be performed from the plenoptic solar images, as the entire frame needs to be divided into several sub-images with contrast good enough to extract turbulence information from each of them. Next section will assess via simulations the functionality of the plenoptic camera as tomographic wavefront sensor to be considered a possible candidate for the MCAO systems in solar telescopes. Further testing regarding on-sky tomographic reconstruction will follow in the future.
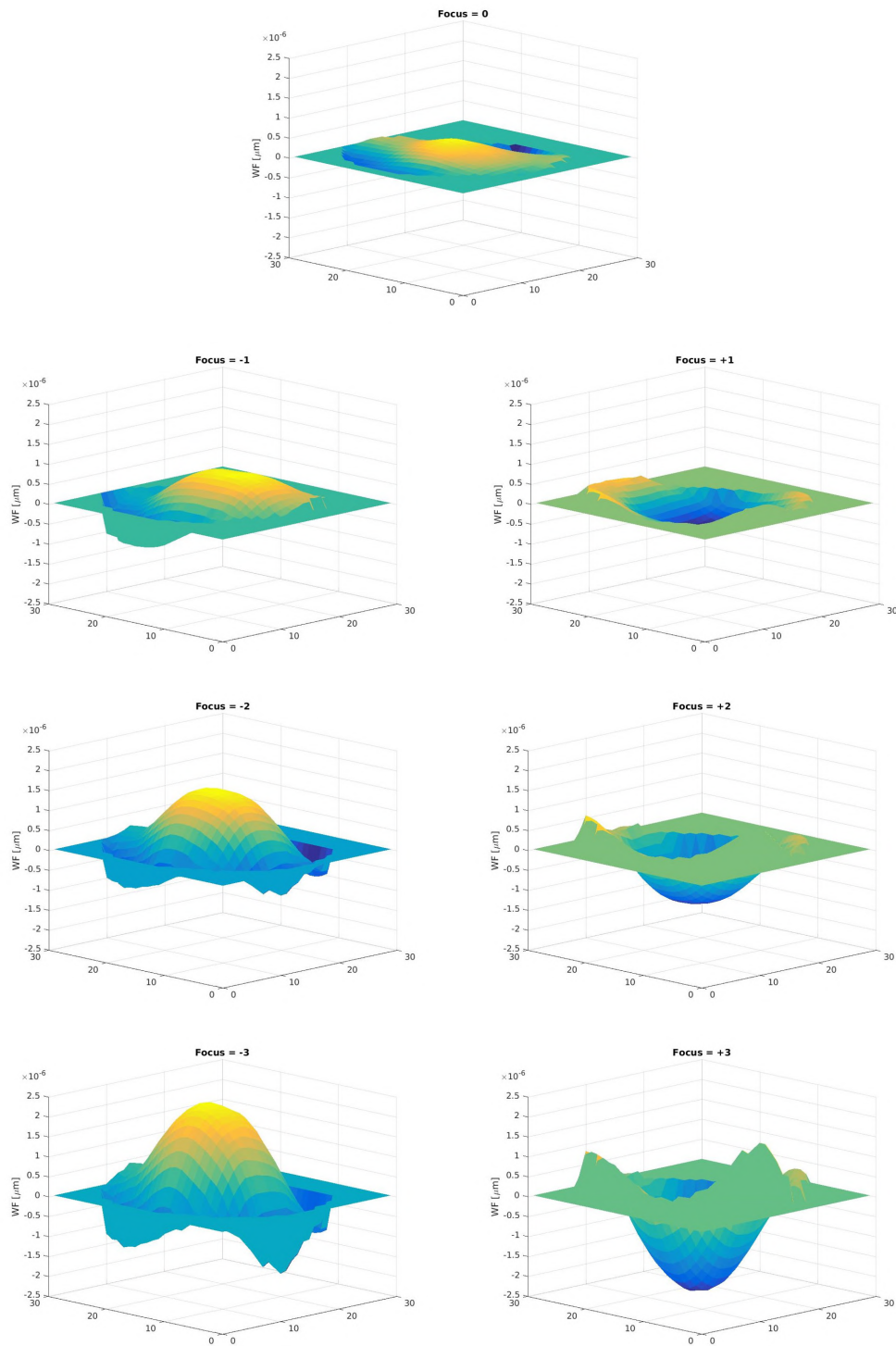
FIGURE A.4: Defocus aberration created by changing the telescope focus and reconstructed from the plenoptic images.
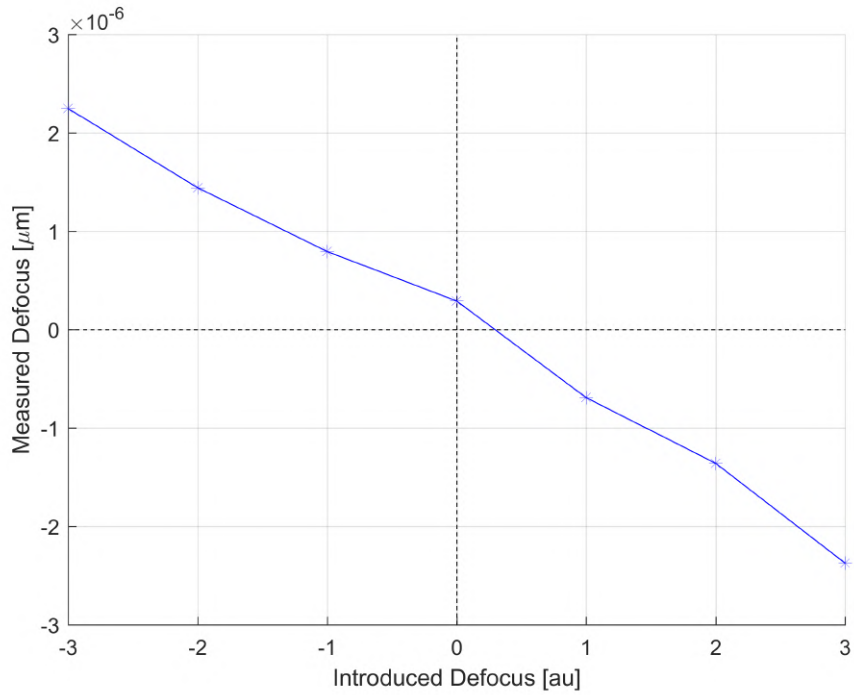
FIGURE A.5: Linearity plot between the introduced defocus and the measured mode.

(a)   (b)
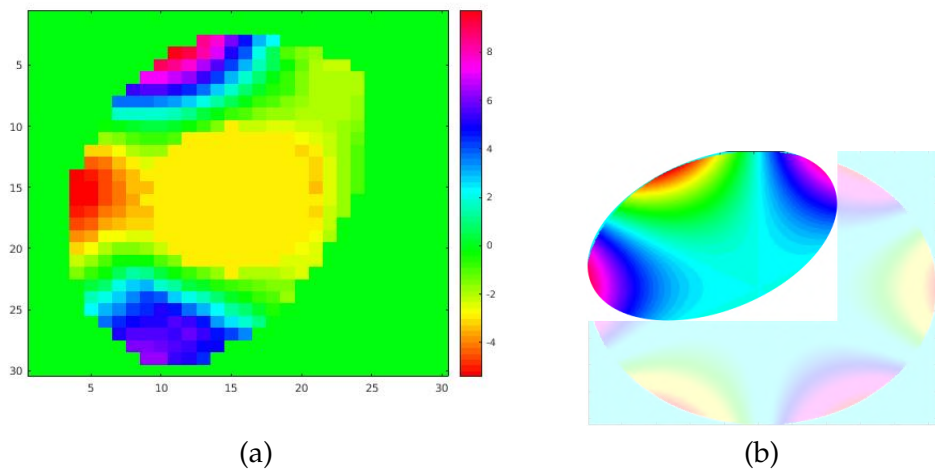
FIGURE A.6: (a) Trefoil aberration created by changing the shape of the DM in the VTT AO system and reconstructed from the plenoptic images; (b) Trefoil Zernike Representation and the area corresponding to the partial pupil.

A.3   Solar Atmospheric Tomography

Atmospheric tomography is based on the estimation of the atmosphere volumetric information above the telescope; the plenoptic camera gathers light data from as many viewpoints as pixels inside each microlens within the array, creating as many sub-aperture images as those viewpoints establish (see Chapter 2, Section 2.5 for sub-aperture image generation). When the atmospheric turbulence is not concentrated at the pupil plane, but distributed over a volume above this plane (which from now on, will be discretized on a finite number of layers), each of these viewpoints will not be affected by the same turbulence (the light rays will have travelled through different areas of atmospheric turbulence). Therefore, atmosphere volumetric information will be available within the plenoptic image and can be extracted by subdividing it into a *n-number* of lines of sight.

Current procedures to solve atmospheric tomography are based on what is called the *3-step approach*, which consists of splitting up the problem into three independent sub-problems: first, the estimation of the incoming wavefront from the WFS measurements, second, the reconstruction of the discretized atmosphere from the incoming wavefront, and finally, the fitting of this reconstruction onto the available deformable mirrors of the system (Ramlau, Saxenhuber, and Yudytskiy, 2014). This paper describes the implementation of the two first; no fitting has been carried out, but instead, a direct subtraction of the reconstructed phase from the simulated one layer by layer, resembling the optimal situation where perfect conjugated mirrors to each turbulence layer are available.

Figure A.7 represents the tomography problem when using a plenoptic camera as a single WFS in the system. The plenoptic CCD image will be the result of the Sun light travelling from different directions down to the telescope, so the plenoptic image shall be divided into smaller fields where the wavefront slopes will be calculated (Figure A.8) by a cross-correlation algorithm as, for solar adaptive optics, the image behind each lenslet is extended. The more the image is sub-divided, the more guide sources will be considered in the computation (the reconstruction may be better), but the less number of pixels will be available to estimate the slopes; therefore, a trade-off shall be established. After the cropping and the gradients computation processes, directional vectors, which relate slopes/sub-image to guide source, shall be determined with the aim of reconstructing the discretized atmosphere. This last step is performed by solving the tomography problem equation $\phi = A\theta$ via Kaczmarz algorithm (Rosensteiner and Ramlau, 2013).

A.3.1   MCAO Simulations. Procedures and Results

End-to-end simulations have been performed with the Object-Oriented Matlab Adaptive Optics (OOMAO) Toolbox (Conan and Correia, 2014) in order to prove the feasibility of using one plenoptic camera as a wavefront sensor in a solar MCAO system, opposite to several wide-field Shack-Hartmann.

The OOMAO simulator has already been described in previous sectios (see Chapter 3).

Regarding the atmosphere class, same diurnal atmospheric profiles as in Chapter 3 (extracted from Rosa (2016)) have been included into the simulations. More specifically, an average profile corresponding to measurements at Sun elevations larger than 45 degrees has been used (Figure A.9), after considering it the worst case scenario where almost a 90% of the turbulence is concentrated at the first kilometres of
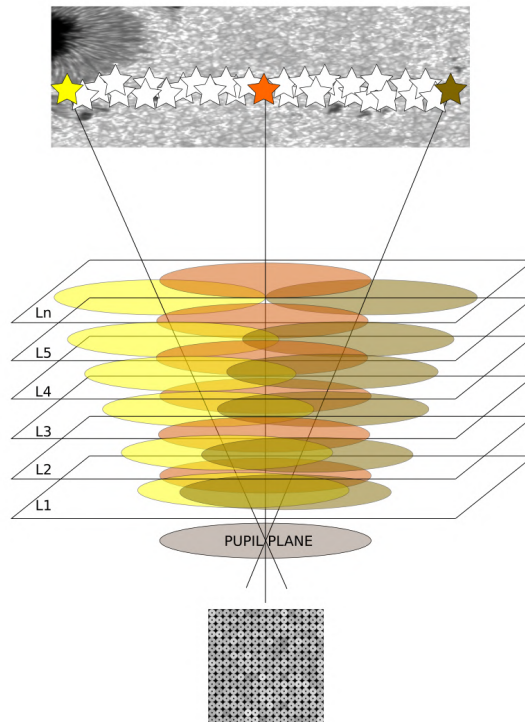
FIGURE A.7: Atmospheric tomography problem formulation with a single sensor: the plenoptic image will comprehend wavefront information from several viewpoints allowing the estimation of the atmosphere volume above the telescope.
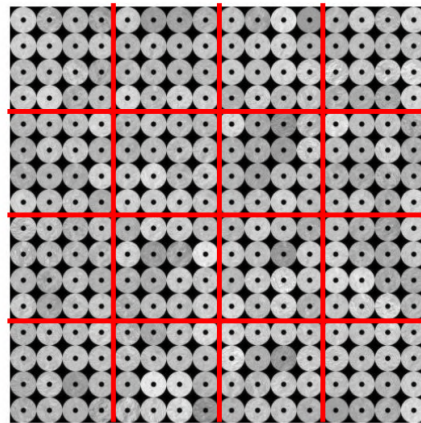
FIGURE A.8: Plenoptic simulated image with solar granulation. The plenoptic image shall be divided into as many sub-images as number of guide sources in the tomographic reconstruction process. As a consequence, the number of pixels to calculate the correlations per sub-image will be reduced. The red squares represent the guide sources.
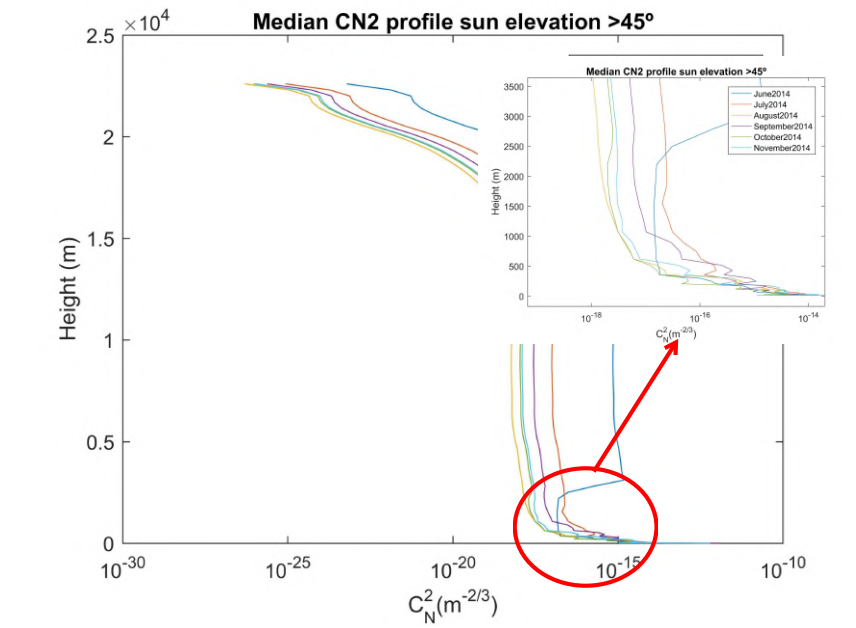
FIGURE A.9: Average $C_N^2(h)$ profile obtained from the individual measurements at Sun elevations larger than 45° derived from generalized SHABAR observations during 2014 at Teide Observatory (Rosa, 2016).

the atmosphere.

Concerning the telescope, it has been modelled by taking into account the EST telescope design parameters (Sánchez-Capuchino et al., 2010): a 4-meter diameter and a 20% central obscuration due to the 800-millimetre secondary mirror.

A plenoptic wavefront sensor has been designed for this configuration, consisting of a 32x32 microlenses array and 32 pixel per lenslet, resulting in a 1024x1024 pixel CCD image. This sensor in a f/50 set-up could cover a field-of-view of 1 arcminute (with, i.e., a 15-micron pixel size).

As it has been already mentioned, no deformable mirror projection has been considered, except for the pupil plane, where a DM has been introduced in the simulation conjugated at 0km above the telescope (33x33 actuators) and only the fitting error from this one is taken into account; for the other eleven atmospheric layers, it has been done a direct subtraction of the reconstructed phase (calculated from the tomography process) from the atmospheric layer phase.

The simulation framework is summarised in Table A.5.

Atmosphere		Telescope		Plenoptic WFS	
r_0	≈ 2.8cm	Diameter	4m	Microlenses array	32x32 lenslets
Layers	12	Central obscuration	20%	Resolution	1024x1024 px

TABLE A.5: Simulation Framework

No solar source simulation procedure is currently available in the OOMAO tool, therefore the Hinode's high resolution view of solar granulation (Studio, 2007) has been used by cropping one area and creating a synthetic reference image (Figure A.10) for the WFS. The extracted 1024x1024 pixel section was selected under the premises just solar granulation appears on the image (higher contrast sunspots would be a less challenging reference image to estimate the incoming wavefront). This reference image propagated through the microlenses array will become the CCD plenoptic image.

(a)   (b)
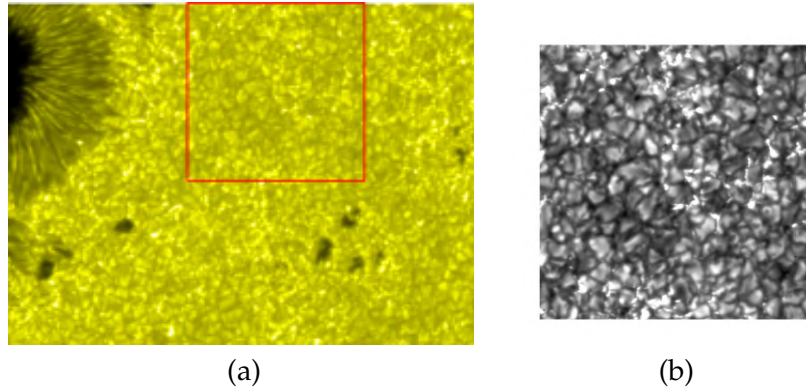
FIGURE A.10: (a) Hinode's high resolution view of solar granulation Studio, 2007 and (b) selected area (corresponding to red square in (a)) to create the synthetic solar reference image for the WFS.

Validation metrics to assess the performance of the simulated MCAO system have been chosen by assuming the Strehl ratio (usually used in nocturnal AO to quantify the quality of the final image) cannot be computed from solar extended images. Therefore a parameter called $rms_{contrast}$ is established as the performance metrics. The $rms_{contrast}$ is defined as the squared root of the variance of the normalized observed brightness fluctuations (Roudier and Muller, 1986) (Eq. A.1).

$$rms^2_{contrast} = \frac{\sum_{i=1}^{N}(I - \bar{I})^2}{N\bar{I}^2},\tag{A.1}$$

where $\bar{I}$ is the mean intensity of the observed image and N is the number of pixels in it. This parameter depends not only on the image content, but also on the instrument PSF: the contrast of the image will be low if there is a substantial stray light contribution, no matter how well the AO system is performing (I. Montilla, 2016). However for simulation purposes, it is possible to obtain the "original image" with no atmospheric effect and therefore, compare the $rms_{contrast}$ of this first one with the $rms_{contrast}$ of the resulting image after applying the MCAO correction, allowing a direct measurement of the image quality improvement.

Once the solar AO framework has been established, the simulation procedure is as follows:

- Synthetic solar granulation image propagation through the atmosphere onto the plenoptic WFS and $rms_{contrast}$ quantification.

- Plenoptic image cropping to create plenoptic sub-images depending on the considered guide source.

- Slopes per plenoptic sub-image estimation.

- Tomography computation (12 atmospheric layers).

- Fitting of the reconstructed phase at pupil plane onto the 33x33 DM conjugated at 0km (*layer*#0).

- Subtraction of the reconstructed phase at layer n from the atmospheric phase at layer n (starting from *layer*#1) ("ideal" MCAO).

- Synthetic solar granulation image propagation through the atmosphere onto the plenoptic WFS and $rms_{contrast}$ quantification.

By following this method, simulation outcomes demonstrate the potential of the plenoptic camera to act as a single WFS in a solar MCAO system. Figure A.11 shows the improvement on the image quality after applying the tomographic reconstruction: whereas the original image presents a $rms_{contrast}$ of 5.83, with the diurnal atmospheric influence, the 4-meter telescope would not see a contrast larger than 0.56. However, after performing an "ideal" MCAO correction the $rms_{contrast}$ would increase up to 3.36. For comparison purposes, an SCAO correction was simulated with the same parameters as in the MCAO case; the MCAO performance recovers a 58% of the original $rms_{contrast}$, whereas when applying the SCAO correction, it is only recovered a 22% of the original $rms_{contrast}$.

Additionally, within the simulation environment, it is possible to compare in terms of RMS difference, the real phase in each of the atmospheric layers and the reconstructed phase result of using the tomography method with the plenoptic sensor. Table A.8 summarizes this information. The RMS difference between the phases is shown in wavelength units. The good performance of the plenoptic camera for solar AO is demonstrated once again with a mean value of 0.1988λ in RMS difference between the real and the reconstructed phase.

#LAYER	LAYER ALTITUDE (m)	RMS DIFF (λ)
0	0	0.1921
1	500	0.1857
2	1000	0.2356
3	2000	0.2119
4	3000	0.1593
5	4000	0.2567
6	5000	0.2245
7	6000	0.2555
8	7000	0.1958
9	8000	0.1150
10	9000	0.2150
11	10000	0.1386

TABLE A.8: RMS Difference Real-Reconstructed phase.
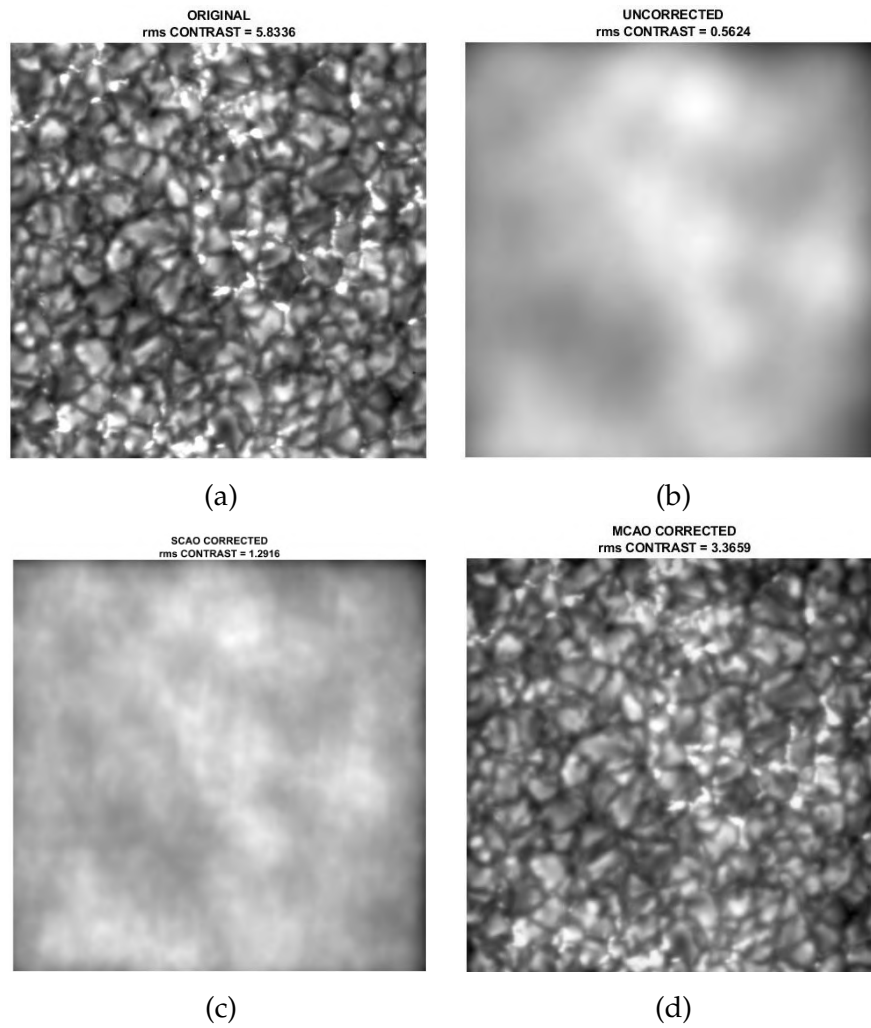
FIGURE A.11: (a) Simulated 1-arcmin science image with no atmosphere; (b) After propagating through a diurnal atmosphere ($r_0 = 2.8cm$); (c) After SCAO correction; (d) After ideal MCAO correction.

A.4　Plenoptic WFS for Solar AO. Conclusions

Wavefront retrieval from solar images using the plenoptic camera has been demonstrated after its integration at the VTT Solar Telescope, proving the feasibility of this sensor for solar AO; telescope experiment and results were published in the proceeding *The Plenoptic Camera as Wavefront Sensor for the VTT Solar Telescope* (Martínez et al., 2017b).

A MCAO solar system has been simulated by the integration of the plenoptic camera as WFS, and the simulation outcome seems to be very promising; future work could imply the integration of this novel sensor in a MCAO simulation test bench for the European Solar Telescope, with the purpose of further investigating its potential at laboratory scale. The plenoptic camera for MCAO wavefront sensor was presented in the *Durham Workshop Week 2018* and gathered in the proceeding *Solar MCAO with a single sensor: simulating tomographic reconstruction with the plenoptic camera* (Martínez and Ramos, 2018).

Appendix B

Australian Adaptive Optics Demonstrator

From September to December 2018, the author was collaborating with the Australian National University, in Canberra (Australia), involved in integration tasks for the ANU/EOS Adaptive Optics Demonstrator. This collaboration stay was built with the objective of sharing the know-how to successfully achieved the uplink correction, as the Australian Adaptive Optics Demonstrator also involved the precompensation of a laser beam for space debris manoeuvre.

B.1   ANU/EOS Adaptive Optics Demonstrator

The Adaptive Optics Demonstrator (AOD) is a joint project of the Australian National University (ANU) and the EOS Space Systems, conducted under the framework of the Cooperative Research Centre for Space Environment Management (SERC)[1], with the aim of equipping the EOS laser space debris tracking station at ANU Mt Stromlo Observatory, Canberra (Australia), with Sodium Laser Guide Star Adaptive Optics.
The AOD project comprises two AO benches, an adaptive optics system for debris tracking and pushing (AOTP) and another one for satellite imaging (AOI); both system profit from the Laser Guide Star Facility (LGSF), described in detail in Section B.2.

B.1.1   AO for Tracking and Pushing (AOTP)

In more than 60 years of space activities, about 5400 launches (excluding failures) have resulted in more than 8100 tonnes of space objects in Earth orbit. As the latest figures provided by ESA's Space Debris Office at ESOC, Darmstadt (Germany) point out, the number of debris objects estimated by statistical models to be in orbit are around 29000 objects larger than 10 cm, 750000 objects from 1 cm to 10 cm and 166 million objects from 1 mm to 1 cm (ESA's Space Debris Office, 2018).
As a consequence of the rising debris object count, the probability of catastrophic collisions will also grow progressively; doubling the number of objects will increase the collision risk by approximately four times. As the debris population grows, more collisions will occur. This self-sustained process, which is particularly critical for the LEO region, is known as the 'Kessler syndrome'. It must be avoided by

---

[1]SERC is a collaboration between government agencies, universities and space industry professionals from Australia, USA and Japan
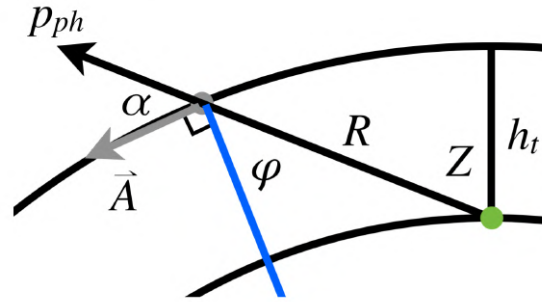
FIGURE B.1: Schematics of the photon pressure technique (Bennet et al., 2015)

the timely application of mitigation and remediation measures on an international scale. SERC operates research programs for space object and environmental characterization, tracking, collision prediction, as well as optical techniques for space debris mitigation.

The Adaptive Optics Tracking and Pushing (AOTP) system is being developed as a demonstrator to prove the concept of ground-based orbital debris manoeuvring via photon pressure from a high power (HP) 1064 nm 10 kW laser (Bennet et al., 2012).
The laser induced photon pressure technique consists of illuminating a debris target and causing a momentum transfer, which can have a component along the targets orbital velocity and therefore, will imply a perturbation in its orbit overall several passes. This technique entails four force components : three of them as a result of photon momentum conservation (photon pressure) and a fourth induced by temperature gradients in the surface of the illuminated object. The first and most significant force component is parallel to the incoming laser beam and caused by the momentum of all incoming photons (p_{ph}). Specular and diffuse photon reflection add two additional forces, as well as thermally emitted photons due to temperature gradients on the surface. However, most objects over 600 km are assumed to be tumbling fast, cancelling the three latter effects for most cases (Stupl et al., 2014). The p_{ph} momentum will depend on h/λ, where h is Planck's constant and λ is the wavelength of the light. It will be transferred in the direction the laser beam is reflecting from the target and therefore, it can have an effect on the targets orbital velocity ($\vec{A}$) (Figure B.1) (Bennet et al., 2015). This is yet to be demonstrated because even with the advances in HP lasers, the Earth atmosphere still diffracts the laser beam rendering the photon density at the target too low. An AO system to pre-compensate the laser upwards propagation is needed.
The AOTP (Zovaro et al., 2016) consists of a 1064 nm 10 kW CW laser by IPG Photonics and an AO system to pre-correct its uplink with the purpose of increasing the laser flux on the debris target. The AO correction system uses a sodium LGS to measure high order aberrations and the sunlight reflection from the target for TT measurements. The atmospheric wavefront is measured by a Shack-Hartmann WFS (OCAM2 E2V CCD220 deterctor with 19x19 lenslet array) and corrected by a cooled DM with TT stage (20x20 actuators over a 205 mm aperture). The AO system works at 1.5 kHz loop with a slower TT control (500 Hz).

B.1.2 AO for Satellite Imaging (AOI)

Satellite imaging, as any other sky observation, is limited by the resolving power of the telescope aperture and the Earth atmosphere. When applying AO techniques, a 1.8-meter telescopes can resolve objects around 40-50 cm in size with wavelengths between 800 nm and 1000 nm for a satellite at 800 km, which, without AO would, only resolve objects of 6 m in size, with 1.5″ seeing (Bennet et al., 2015).

Resolving small features of satellites can provide new information on satellite orientation or debris tumbling which can be used to further refine orbital parameters and predictions. It would also allow the characterisation of the state of debris objects and may play an important role in space environment management by providing more information on what is currently in orbit, including providing good candidates for engagements with the AOTP system (Bennet et al., 2015).

Adaptive Optics systems for satellite imaging share some of the design challenges with the AOTP due to the similar operation requirements of non-sidereal tracking. The AOI has been designed to characterize objects in LEO orbits and assist in orbit determination for GEO satellites by imaging them and determining their angular position regarding the stars in the Gaia catalogue. It consists of an AO system with both NGS and LGS modes, a SH-WFS (OCAM2k camera and a 16x16 lenslet array) working at 2 kHz and one optics assembly on a motorized linear stage for the wide-field acquisition mode (Grosse et al., 2017).

B.2 AOD LGS Facility

The AOD Laser Guide Star Facility (LGSF) (D'Orgeville et al., 2014) provides sodium LGS operation mode to the Adaptive Optics Demonstrator for the EOS 1.8 m telescope at Mt Stromlo Observatory. It has different functional requirements than the ones typically applied to LGS facilities for astronomical applications: the fact that, in order to track space debris, the LGS must be pointed ahead of the telescope optical axis along the debris trajectory.

The LGSF hosts two laser prototypes: the Guide Star Laser Prototype (GSLP) built by EOS Space Systems (together with the laser enclosure), and the Guide Star OPSL Prototype, built by the partnership between ANU, the Australian Astronomical Observatory (AAO), the University of New South Wales (UNSW), the Giant Magellan Telescope Organization and SERC participants EOS Space Systems and Lockheed Martin Space Systems.

The GSLP consists of a CW laser system including $1.34 \mu m$ and $1.05 \mu m$ oscillators and amplifier chains, and direct-sum frequency mixing of the two spectral lines, with an average output power of 30W.

The Guide Star OPSL Prototype is an Optically Pumped Semiconductor Laser, built by a semiconductor gain structure (gain chip) which consists of a GaAs substrate, a Distributed Bragg Reflector grown on top of it, a periodic quantum well gain region and a diamond heat spreader bonded onto it (d'Orgeville and Fetzer, 2016).

Both lasers will be mounted on three CFRP CarbonVision breadboards, kinematically attached to a steel frame. The assembly will be bolted to the right side fork tine of the EOS 1.8 m telescope.

Figure B.2 shows the schematic of the AOD LGS facility. The Beam Expander Unit (BEU) will be fed either by the GSLP or the OPSL prototype.
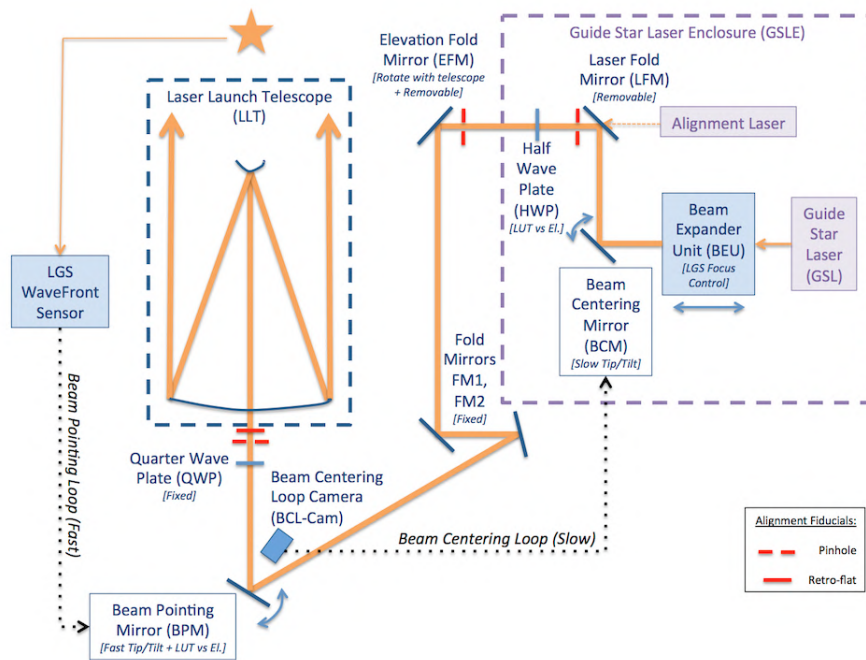
FIGURE B.2: AOD Laser Guide Star Facility schematic (D'Orgeville et al., 2014)

B.2.1 Beam Transfer Optics

The Beam Transfer Optics (BTO) is an optics ensemble whose functionality is relaying the LGS laser beam to the Laser Launch Telescope (LLT). All its subsystems and elements are described below following the beam path as in Figure B.2.

First, the beam width needs to be enlarged by the Beam Expander Unit (BEU) from a 2.8-millimetre diameter (provided by the GSLP/OPSL prototypes) to a diameter of 10 mm. The BEU is provided also with a linear stage to enable the focus adjustment of the LGS on sky. Afterwards, the beam travels until the Beam Centering Mirror (BCM) which keeps the laser beam centered on the Beam Pointing Mirror (at the LLT downstream, see Section B.2.2).The BCM subsystem receives feedback information from the Beam Centering Loop (see Section B.3.3). From the BCM unit, the laser is fed by the Laser Fold Mirror (LFM) onto the telescope elevation axis after going through the Half Wave Plate (HWP), which maintains a fixed linear polarization in the beam by rotating with the telescope elevation. Once in the telescope elevation axis, the laser beam is folded onto the LLT by the Elevation Fold Mirror (EFM) subsystem. All the elements of the BTO but the Elevation Fold Mirror are located inside the Guide Star Laser Enclosure.

Figure B.3 shows the blocks diagram of the Beam Transfer Optics.

B.2.2 Laser Launch Telescope

The Laser Launch Telescope (LLT) performs an off-axis launch of the LGS beam in the EOS telescope. The off-axis launch was a design decision based on several technical constraints like the small size of the EOS telescope secondary mirror, the high
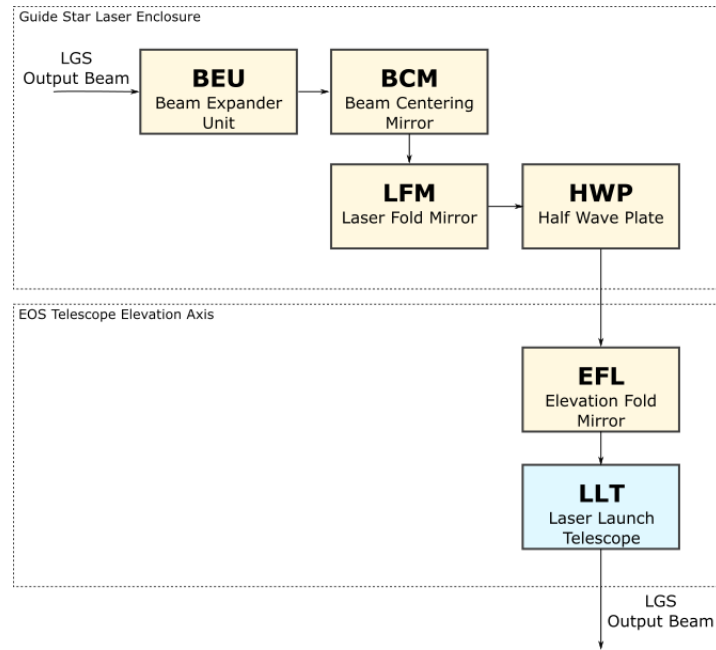
FIGURE B.3: Beam Transfer Optics blocks diagram in yellow

noise levels that a shared aperture with the AOTP HP laser would cause, and a former design for an off-axis launch telescope which could be feasibly adapted for the LGSF.

The laser beam enters the LLT from the BTO Elevation Fold Mirror; it first encounters the Fold Mirror 1 (FM1) and Fold Mirror 2 (FM2). Afterwards, a Quarter Wave Plate (QWP) transforms the beam linear polarization into circular polarization, and leads the beam into the LLT input divergence lens, which provides a x20 magnification ratio to the exit lens. The laser beam travels then towards the Beam Pointing Mirror (BPM), providing beam steering capability over the LLT FOV. The beam position on the BPM is imaged by the BCM-Cam, the camera which supplies feedback information to the BCM (BTO subsystem). After being reflected by the BPM, the laser travels to two fold mirrors (one first 6″ mirror and second 9″ mirror) and finally, to the 330-millimetre LLT exit lens.

The LLT, as well as the Elevation Fold Mirror (BTO), are located at te EOS telescope elevation axis. Figure B.4 shows the blocks diagram of the Laser Launch Telescope.

B.3 Assembly, Integration and Verification of the AOD LGS Facility at Stromlo Observatory

The AOD LGS Facility has been assembled in the Optical Laboratory at the Advanced Instrumentation and Technology Centre (AITC) to be later integrated in the 1.8m telescope by EOS at Mt Stromlo Observatory, by locating some subsystems inside an enclosure next to the telescope and some others in the telescope elevation axis itself. Figure B.5 shows the Guide Star Laser Enclosure, fully assembled at the AITC facilities.
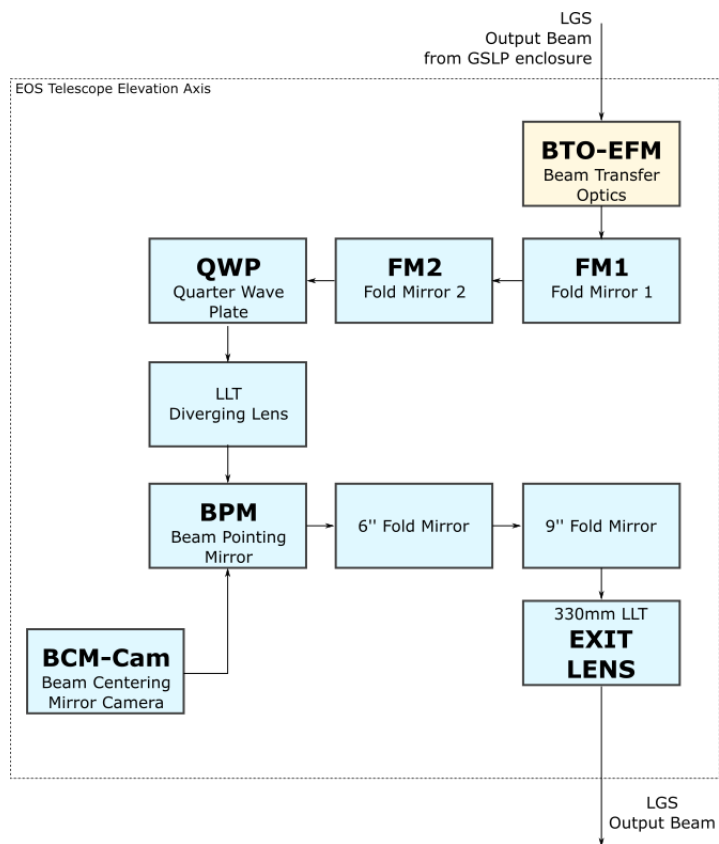
FIGURE B.4: Laser Launch Telescope blocks diagram in blue

FIGURE B.5: Guide Star Laser Enclosure. The Beam Transfer Optics will be mounted on the middle bench, whereas the upper and lower breadboards are assigned to the GSLP and the OPSL subsystems.

B.3.1 Assembly stage of the Beam Transfer Optics

The LGSF Beam Transfer Optics (BTO), comprising the Beam Expander Unit, the Beam Centering Mirror, the Laser Fold Mirror, the Half Wave Plate and the Elevation Fold, has been built and assembled as the first step to the AIV of the AOD LGSF. Figure B.6 shows an early stage of the BTO assembly process. All the BTO elements, except for the last one, are integrated to a base plate (Figure B.7) which will be located inside the LGS enclosure, allowing the fully assembly and almost complete alignment of this subsystem within the laboratory clean environment.

Beam Expander Unit Alignment

The BEU has a total of three lenses to expand the beam size; the third lens also acts as a focus compensator. The Zemax design of the BEU with its optical properties is shown in Figure B.8. First two lenses are mounted on the BEU tube and the third one on a separate flexural mount attached to the Newport M-461-X-M linear stage with the Newport Conex NSA12 motorized actuator (Figure B.9).

The BEU assembly has been aligned after completing three different steps: Barrel alignment with Point Source Microscope (PSM), Barrel + third lens alignment with alignment laser and BEU final alignment with alignment telescope. The full procedure is described below.

BEU alignment with the Point Source Microscope   The Point Source Microscope (PSM) is an instrument for locating the centers of curvature of optical surfaces

FIGURE B.6: The BTO subsystem has been assembled and aligned in the Optical Laboratory at the AITC.

FIGURE B.7: BTO base plate which allows the attachment and independent alignment of the BEU, BCM, LFM and HWP units.

```
SURFACE DATA SUMMARY:

Surf      Type        Radius      Thickness              Glass     Diameter       Conic   Comment
 OBJ STANDARD        Infinity           10                                0           0 Laser EXIT
 STO STANDARD         -14.486            4              C79-80         4.48           0 Lens 1
   2 STANDARD        Infinity        63.62                             4.89           0
   3 STANDARD        Infinity            6              C79-80        14.01           0 Lens 2
   4 STANDARD         -98.163        14.94                            14.57           0
   5 STANDARD        Infinity            6              C79-80        15.71           0 Lens 3
   6 STANDARD         -98.163            5                               16           0
 IMA STANDARD        Infinity                                            16           0 BEU EXIT
```
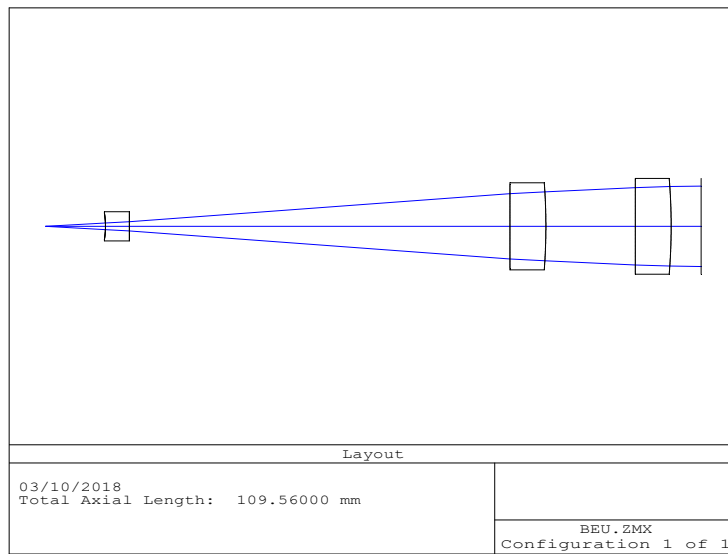

FIGURE B.8: BEU Zemax optical design.
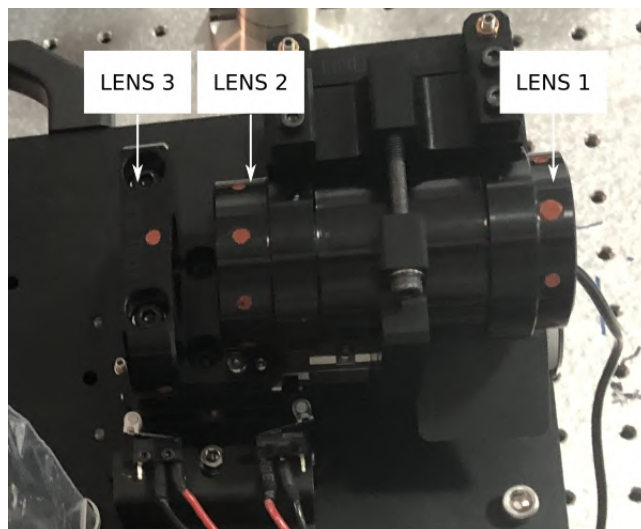
FIGURE B.9: Lens 1 and lens 2 of the BEU are mounted on the BEU tube (left), whereas lens 3 is mounted on a separate flexural mount (right) to act as a focus compensator.
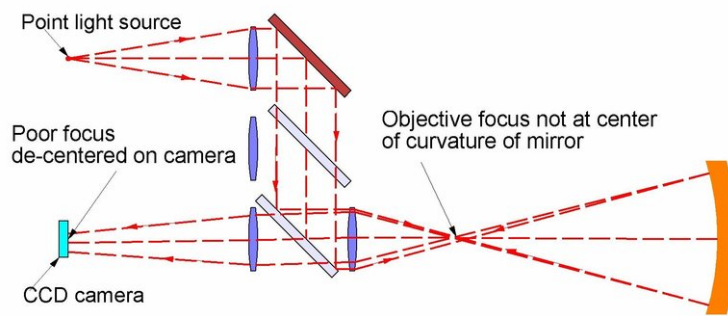
FIGURE B.10: PSM working principle: if the objective focus is not at
the centre of curvature, the image on the CCD will be poor-focused
and decentred (Parks and Kuhn, 2005)

to micron accuracy for alignment of optical elements. The PSM is a reflected illu-
mination microscope with an illumination point source created by a fibre pigtailed
laser diode that is conjugated to the microscope object surface. When focused on an
optical surface, the PSM produces a retro-reflected spot which is relayed back to the
CCD detector; therefore, if the PSM objective focus is not coincident with the centre
of curvature of the optical element, the return image will neither be centred nor well
focused (Parks and Kuhn, 2005). The displacement of the image formed by each op-
tical surface in the system will lead to the determination of the misalignment of the
optical surface itself. Figure B.10 presents the PSM working principle.

The PSM has been used to aligned the first two lenses in the BEU barrel.The
alignment set-up is shown in Figure B.11. It consists of a rotary table where the tube
is located, a dial test indicator to minimize decenter and tilt of both the rotary table
itself and the barrel, and a vacuum injector to locate each lens at its nominal position.
The PSM needs to be moved up and down with respect to the lens under study in
order to find out where the corresponding surface is reflecting back. Each lens has a
front and a rear surface, which will produce corresponding return images at the PSM
CCD detector, those return images will move in a circular pattern when moving the
rotary table underneath, causing a run-out of the image which will be measured in
millimetres by the PSM software. Each return image is obtained after focusing the
PSM objective to the virtual points created by the lens itself. Zemax analysis have
been previously performed with the aim of knowing the distances at which the PSM
shall be located with respect to the optical assembly and the equivalence between the
measured run-out in the PSM software and the tilt or decenter aberration causing
such run-out. The alignment configurations, extracted from Zemax analysis, are
gathered in Table B.1. Each layout represents the corresponding PSM position in
order to retrieve the return image of each surface in the assembly.
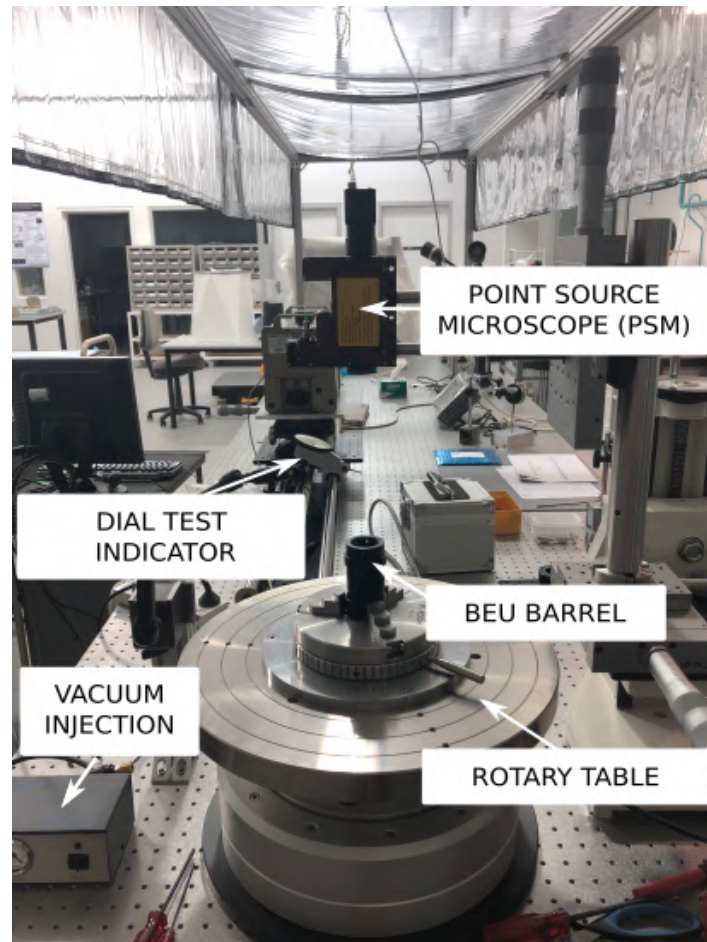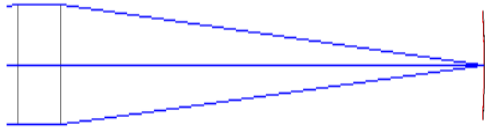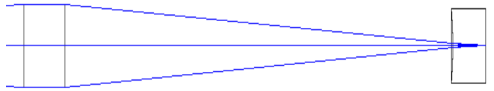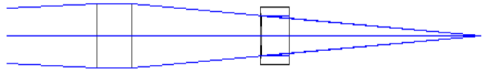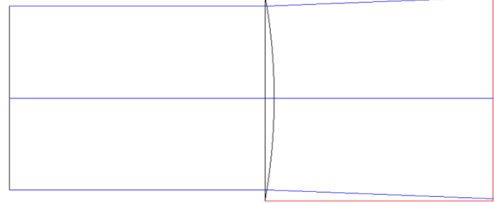
FIGURE B.11: Alignment set-up with the Point Source Microscope. the BEU barrel is located on the rotary table beneath the PSM.

Surface Type	Alignment configuration
Lens 1 - Surface 1 - CatsEye	
Lens 1 - Surface 2 - CatsEye	
Lens 1 - Surface 1	
Lens 1 - Surface 2	
Lens 1 - Surface 1 - Reverse	
Lens 1 - Surface 2 - Reverse	
Lens 1 - Surface 2 - Collimated	

Lens 2 - Surface 1 - CatsEye Reverse	
Lens 2 - Surface 1 - Reverse	
Lens 2 - Surface 2 - Reverse	
Lens 1+2 - Surface 1	
Lens 1+2 - Surface 2	
Lens 2+1 - Surface 1	
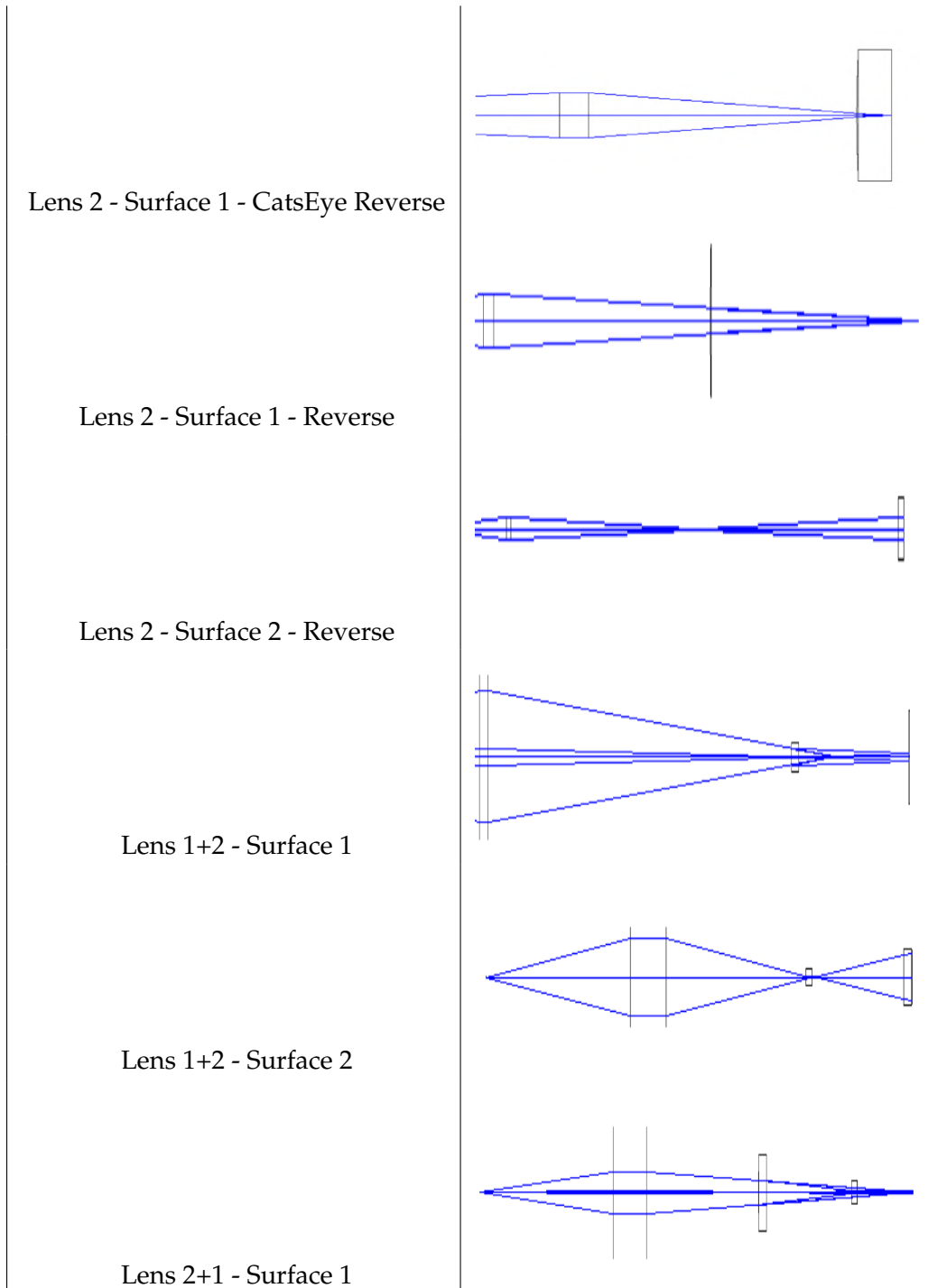
TABLE B.1: PSM alignment configurations extracted from Zemax
analysis of the PSM + L1+L2 assembly.

After repeating the procedure iteratively (adjusting the corresponding lens and measuring the image run-out), both lenses L1 and L2 fulfil tilt and decenter tolerances.

BEU alignment with alignment laser   The BEU lenses inside the barrel need to be aligned with the third lens, the one located on the focus stage. This alignment is carried out by coarse positioning of the focusing lens using an alignment laser. The
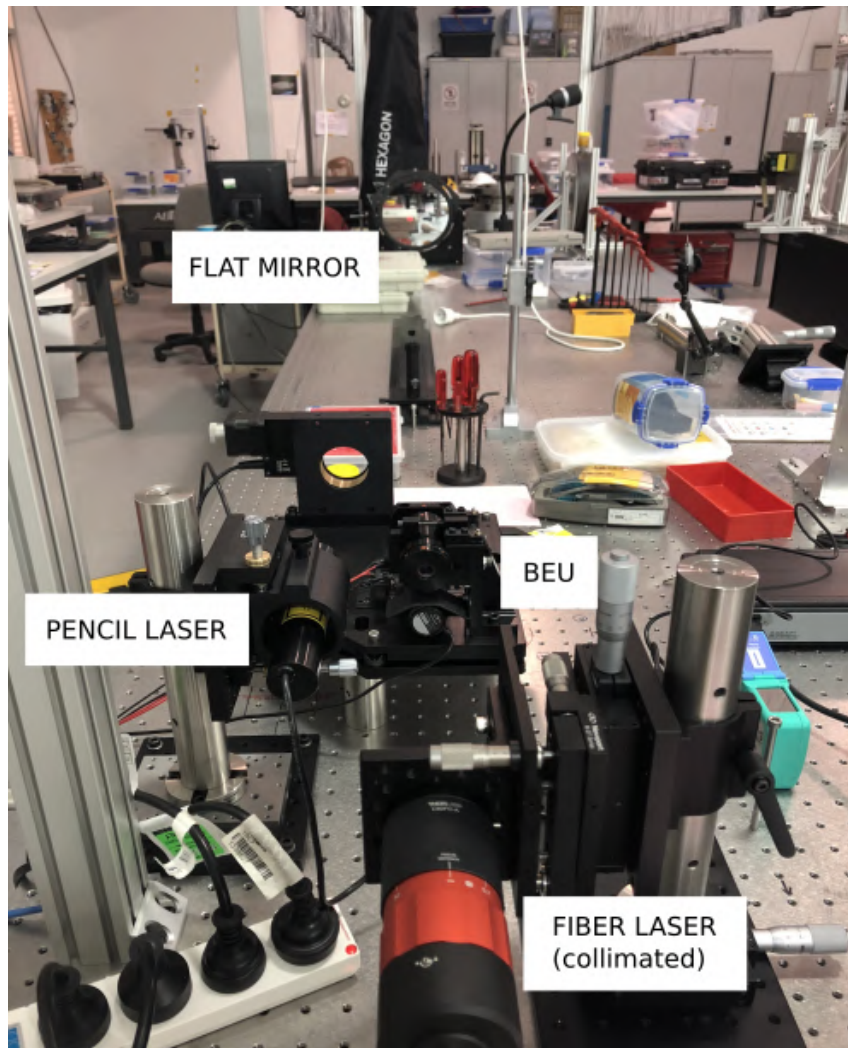
FIGURE B.12: Alignment set-up with the alignment laser.

set-up is presented in Figure B.12.

Both pencil laser and fibre-fed lasers are aligned to the big flat mirror by first, establishing the mechanical axis reference to the pencil laser and afterwards, squaring the fibre-fed laser to this reference.
Once both pencil laser and fibre-fed laser are squared to the big flat mirror, the BEU base plate is placed on the optical axis. The push-pull adjustments in the BEU are used to get the proper return. The linear stage is moved back and forth to check the angle variation produced by big flat mirror return. This angle variation must fulfil BEU tolerances, although this goal is unlikely to be achieved before third and last step on the alignment procedure (BEU alignment with Alignment Telescope).

The minimum displacement of the beam that it has been achieved is comprised between 1mm and 2mm and the maximum displacement at 2.6m –distance laser source to BEU- should be $288.5\mu m$, calculated from Zemax model, for the BEU alignment to be within tolerances. Fine L1+L2+L3 alignment is described in next Section.
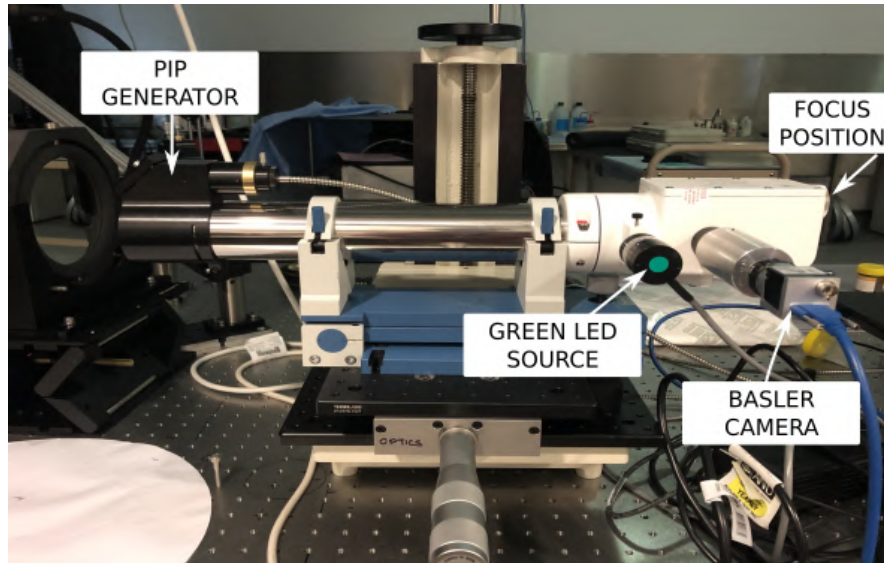
FIGURE B.13: Alignment telescope and its elements.

BEU alignment with alignment telescope   The third lenses of the BEU have been coarsely aligned by using an alignment laser and a reference flat, although an alignment telescope needs to be utilized in order for the assembly to fulfil the tolerances specified during the design phase.

Alignment telescopes serve to establish an accurate line of sight to targets at different distances and determine the deviation of the targets with respect to the reference line. Figure B.13 presents the alignment telescope, which has been integrated in the set-up: an illumination point source created by a fibre pigtailed laser diode (PIP generator) is attached to the front part of the alignment scope; it is built into an anodized aluminium housing, with a first fold mirror to lead the light into the alignment utile and second small fold mirror inside the housing to allow two degrees of tilt adjustment and rotation. A second light source (green LED) is assembled to the rear part in order to illuminate the target inside the alignment telescope; this target is necessary to determine the displacement of the pips during the alignment process (described below). Right after the green LED source, the instrument includes a penta prism, which is used to deviate the straight line through exactly 90 degrees and measure squareness; this feature allows the integration of a Basler ACE A1920-40um (1920x1200 px and pixel size 5.86 μm) camera, which will acquire the pip returns from the lenses surfaces. Finally, the alignment device incorporates a focus knob to adjust the telescope focus in order to image each of the lenses surfaces.

The alignment telescope is included into the laboratory set-up by using the same flat mirror as in previous adjustments (Figure B.14).

By changing the focus position of the Alignment Telescope, the pip returns from the different lenses inside the BEU appear on the screen. The Zemax files help to guess which pip relates to which surface on the lenses (see Table B.2).
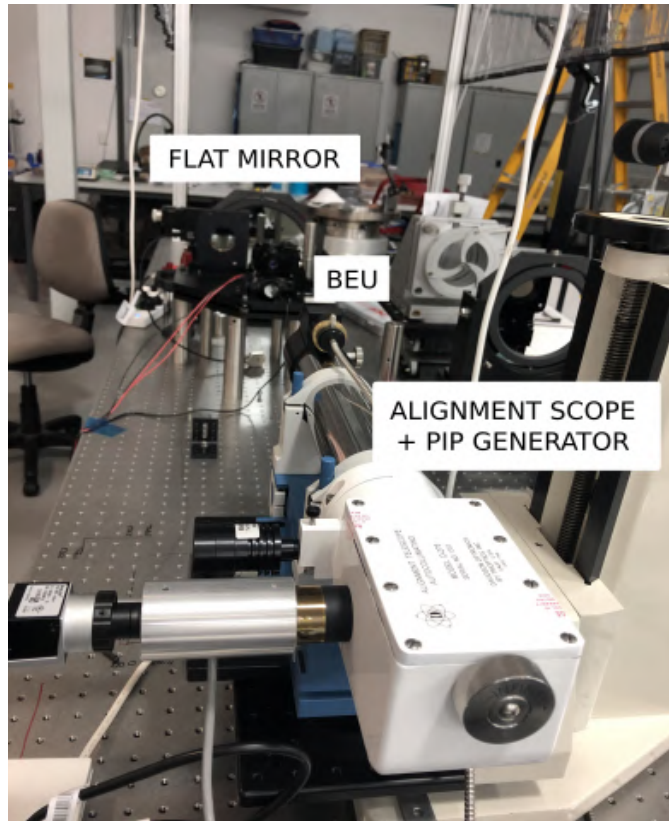
FIGURE B.14: Alignment set-up with alignment telescope.

Surface Type	Alignment configuration
Lens 1 - Surface 1	
Lens 1 - Surface 2	
Lens 1+2 - Surface 1	

Lens 1+2 - Surface 2

Lens 1+2+3 - Surface 1

Lens 1+2+3 - Surface 2
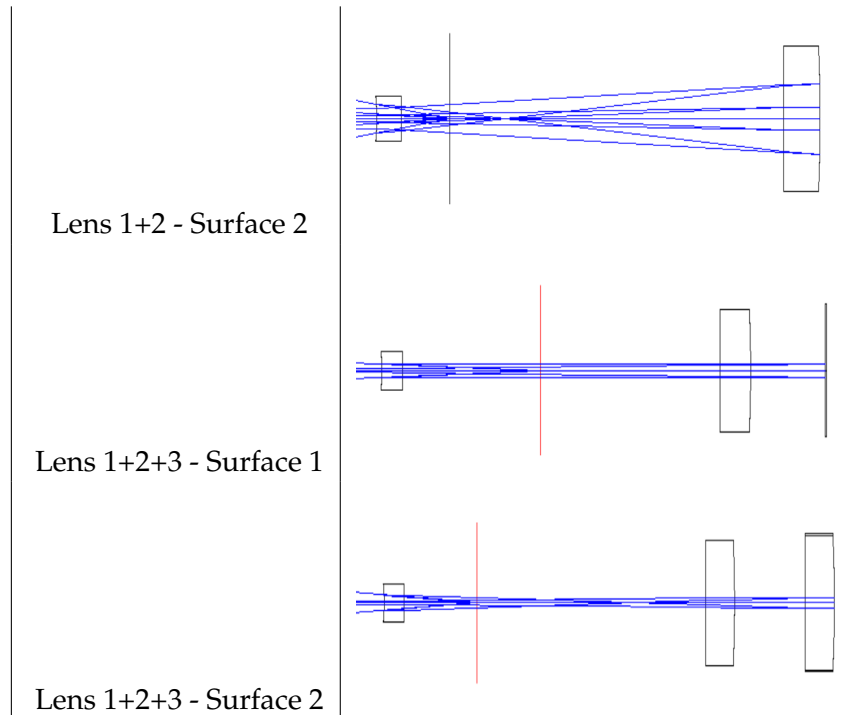
TABLE B.2: Zemax analysis of the ALIGNMENT SCOPE + L1+L2+L3 assembly

All possible degrees of freedom in the BEU need to be adjusted until all the pips are located at the centre of the cross hair in the screen, meaning that the system is properly aligned. Final adjustments are done with the flat mirror return: the alignment telescope focus is changed to get this return visible on the screen; the focusing stage is moved back and forth to detect the displacement of the pip return. Final adjustments are performed on the lenses until the difference in position between pips, measured at several locations of the linear stage, is minimized.

These differences in position between pips are measured in pixels on the CCD and the magnification of alignment telescopes typically varies as a function of object distance, therefore a scale calibration needs to be done in order to get knowledge about the equivalent mm; this value and the known distance at which the device is focusing, are used in the calculation of the decentre angle, which is responsible for the pips movement and hence, shall be comprised within the tolerance range. Scale calibration shows that 1 CCD pixel is equivalent to 0.0113mm at a distance of 1250mm from the alignment scope, where the BEU is located.

Tolerances for the BEU assembly are 10′ Tilt and 100μm Decenter, which will cause an image motion of 0.474mm and -3.890mm respectively at 1250mm. After the alignment procedure is completed, the image motion is just 0.2820mm and 0.1695mm: BEU assembly fulfils tolerances.

Beam Centering Mirror Assembly

After exiting the Beam Expander Unit, the LGS beam travels towards the Beam Centering Mirror (BCM), whose function is keeping the laser centered on the upcoming elements of the LGSF.

The BCM consists of an OIM102-3 Fast Steering Mirror Mount (Figure B.16), a mechanical base, to position the mount at the nominal beam height over the base plate, and the elliptical mirror, custom manufactured, whose details are gathered in Table B.3 and Figure B.15.

Surface Data	SURFACE 1	SURFACE 2
ROC [mm]	Plano	Fine Grind
Center Thickness [mm]	6.0 +-0.25	
Material	Corning HPFS 7980	
Wedge [deg]	Reference Surface <0.0833	
Outer diameter [mm]	71.84 x 50.8 +-0.15 (elliptical)	
Clear aperture [mm]	61 x 43 +-0.15 (elliptical)	
Weight [kg]	0.042	

TABLE B.3: BCM Elliptical mirror optical details
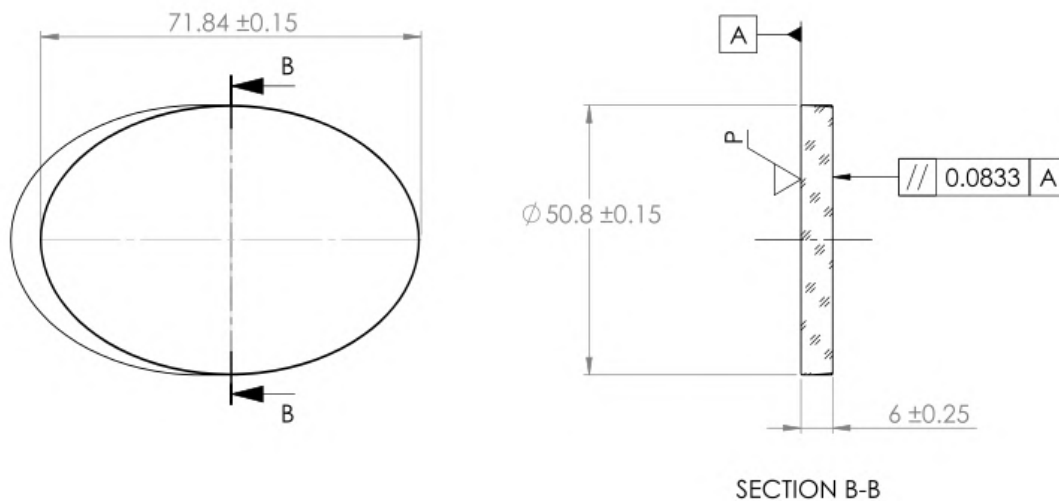
FIGURE B.15: Elliptical Mirror for the BCM unit.

The elliptical mirror is attached to the steering mount by pad mounting using Momentive RTV88 as bonding agent. The required total bonding area and bondline thickness are calculated based on expression B.1 (Yoder and Vukobratovich, 2015) and expression B.2 (Herbert, 2006).

$$Q_{min} = \frac{Wa_G f_s}{J} \tag{B.1}$$

where W is the mirror weight, a_G is the expected acceleration it will suffer, f_s is the safety factor and J is the adhesive tensile strength.

$$h_{Bayar} = \frac{d_o(\alpha_c - \alpha_o)}{2\left(\frac{1+v_b}{1-v_b}\alpha_b - \alpha_c\right)} \tag{B.2}$$

where d_o is the mirror diameter, and α_n the thermal coefficients for the cell or mount (α_c), for the optics (α_o), and for the bonding material (α_b), and v_b is the bonding material Poisson number.

FIGURE B.16: OIM102-3 Fast Steering Mirror Mount for the BCM
unit.

Bonding calculations have been performed by having into account the maximum frequency at which the steering mount will operate (500 Hz) and hence, the acceleration the mirror pads need to handle. Corresponding results for a triangular pattern of three equal circular bonds are gathered in Table B.4.

Number of bonds	Safety Factor	Required bond diameter	Bondline Thickness
3	2	3.36 mm	0.78 mm
3	5	5.31 mm	0.78 mm

TABLE B.4: BCM Elliptical mirror optical details

As the mirror is equally designed for both BCM and BPM units, calculations are applicable also to this last one and both mirrors have been bonded with the same procedure. Figure B.17 shows the bonding curing.
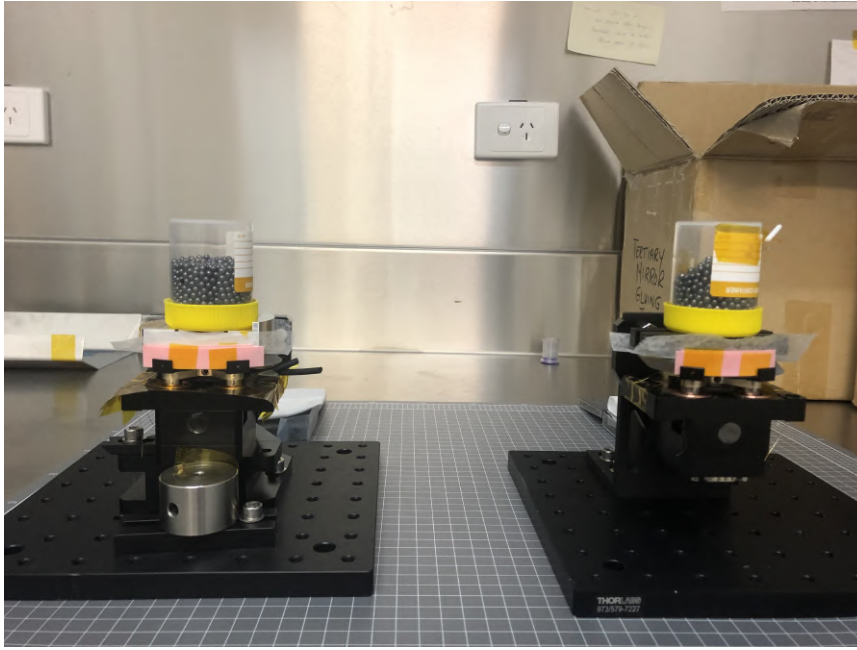
FIGURE B.17: Bonding curing process of elliptical mirrors for BCM and BPM units. Both mirrors rest under a recipient of bearing balls to secure the contact between the mirror rear surface, the adhesive and the mount.

Laser Fold Mirror Assembly

The Laser Fold Mirror (LFM) is mounted on a BKL-4 Newport kinematic base, which allows easy removal of the LFM, essential to have direct access to the elevation axis during the alignment process of the LGSF in the EOS telescope.
The LFM assembly is shown in Figure B.18; the 2" broadband dielectric mirror is attached to the kinematic mount through a retaining ring.

Half Wave Plate Assembly

The Half Wave Plate (HWP) is mounted in a remotely controlled Thorlabs rotator stage. The Union Optic WPF-2238-589-M50.8 half wave plate is hold to the stage through a retaining ring.

Elevation Fold Mirror Assembly

The Elevation Fold Mirror (EFM) mount is fully customized and designed at AITC, due to the space constraints on this subsystem location into the telescope structure. The mechanical interface holds the 2-inch dielectric mirror and a reticle target for alignment purposes (Figure B.19).
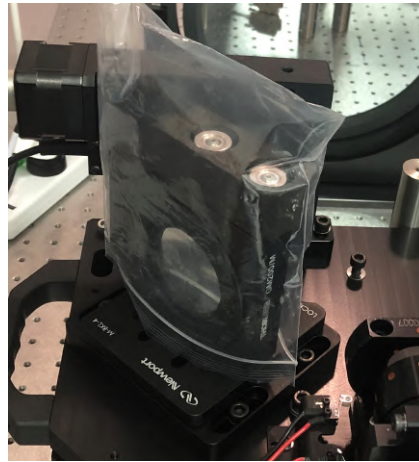
FIGURE B.18: Laser Fold Mirror assembly.
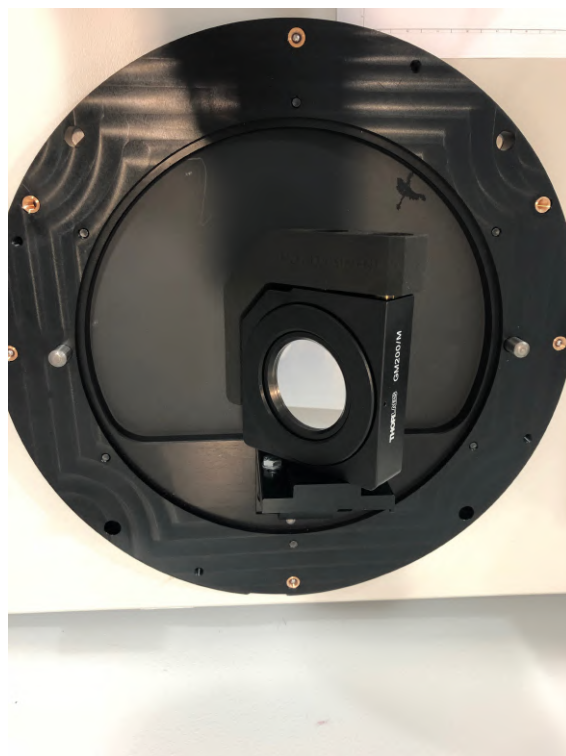
FIGURE B.19: Elevation Fold assembly. The reticle target is located
behind the mirror.

B.3.2 Assembly Stage of the Laser Launch Telescope

The Laser Launch Telescope consists of an afocal reflective on-axis beam expander to magnify the laser beam by 20. The spacing between the primary and secondary mirror is constrained to 475mm. The LLT optical design is presented in Figure B.20.

Surf:Type		Comment	Radius	Thickness	Glass	Semi-Diameter	Conic
OBJ	Standard		Infinity	Infinity		Infinity	0.000
1	Standard	FSM	Infinity	100.000		11.814	0.000
2*	Standard	PM vertex	Infinity	475.000		11.150	0.000
*	Standard	Sec Mir	50.000	-474.998 V	MIRROR	11.500 U	-1.000
4*	Zernike S..	Prim Mir	1000.000	475.000	MIRROR	170.000 U	-1.000
5*	Standard	Obscuration	Infinity	20.000		163.471	0.000
6*	Standard	Spider	Infinity	70.000		163.478	0.000
IMA	Standard		Infinity	–		163.501	0.000

FIGURE B.20: LLT optical design

The LLT primary mirror is mounted kinematically on three equally-spaced triangular trusses. It is assumed that most of the primary mirror surface irregularity tolerance can be allocated to gravity distortion; this surface irregularity has been modelled as astigmatism by taking into account the maximum tolerance for the primary mirror surface (150 nm P-V) in the Zemax software. The effect of this aberration onto the upwards propagated beam is further analysed via Fresnel propagation in Matlab by adding a 9th order Zernike with its corresponding coefficient (extracted from Zemax) as it is represented in Figure B.21.

(a)   (b)
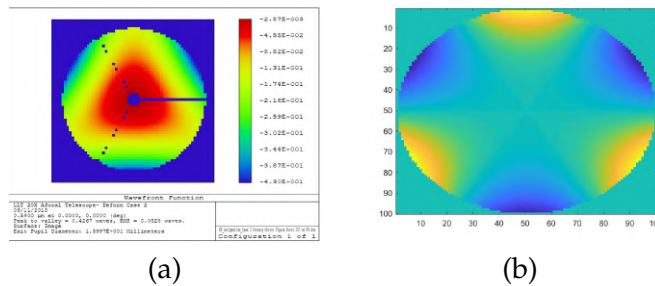
FIGURE B.21: (a) Zemax wavefront map of the LLT with astigmatism aberration in the primary; (b) Astigmatism Zernike taken into account in the Matlab propagation simulation.

Results from the upwards propagation simulation of the beam after existing a LLT with an aberrated primary is shown in Figure B.22. The intensity field at 90km

above Earth surface of the laser beam is affected in much lower order of magnitude than the atmospheric effect over the beam propagation, therefore it is considered negligible.

(a)

(b)

FIGURE B.22: (a) Intensity fields at the Na layer (90km) of a Gaussian beam launched from the LLT without any aberration (left) and with the astigmatism in the primary mirror (right); (b) Cross-section of the intensity profile of a Gaussian beam launched from the LLT without any aberration (left) and with the astigmatism in the primary mirror (right). All units in pixels.

The LLT is assembled in the Optical Laboratory of the AITC facilities; the gluing process of the primary mirror to the LLT mount might cause slight misalignments between the primary and the secondary, which need to be fully characterised before its integration at the telescope. Figure B.23 shows the custom-built structure for the LLT characterization and alignment at the Stromlo Observatory facilities.

Additionally, the effect of this possible misalignment is also analysed via Matlab Fresnel propagation by modelling the aberration of the primary mirror with both the previously studied astigmatism and a second decenter aberration between primary and secondary mirrors. Zemax model of the resulting aberration and its Matlab implementation are shown in Figure B.24.

Results from the upwards propagation simulation of the beam after existing a LLT with an aberrated primary and a 0.1mm decentre between primary and secondary is shown in Figure B.25. This study case shows slight variations in the beam shape at 90km height, which will derive mostly in pointing error: when considering a 0.1mm decentre in the secondary with respect to the primary, the centre of the beam will be displaced by less than 10px, 0.078arcsec, at the Na layer.

Laboratory characterization of the LLT will show the exact value of misalignment if any; the 0.1mm value that has been taken into account in the simulation exceeds

FIGURE B.23: The LLT is mounted on the shown structure for alignment purposes.

(a)   (b)
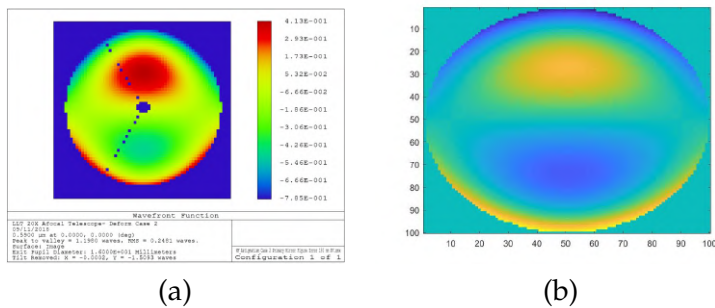
FIGURE B.24: (a) Zemax wavefront map of the LLT with astigmatism aberration in the primary and Y-decentre of 0.1mm in the secondary mirror; (b) Coma Zernike taken into account in the Matlab propagation simulation.

(a)

(b)

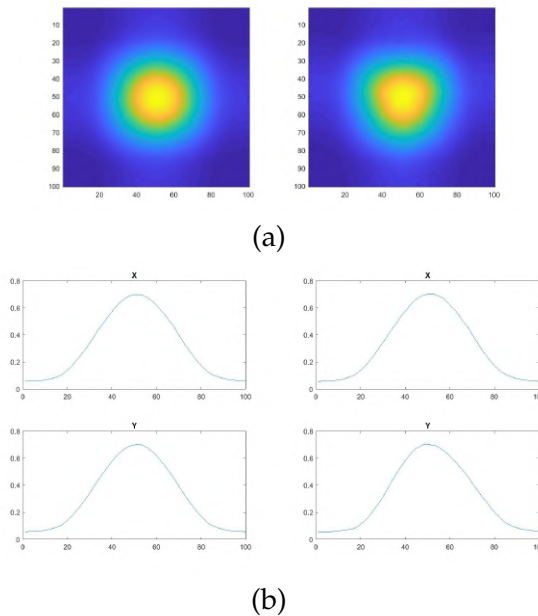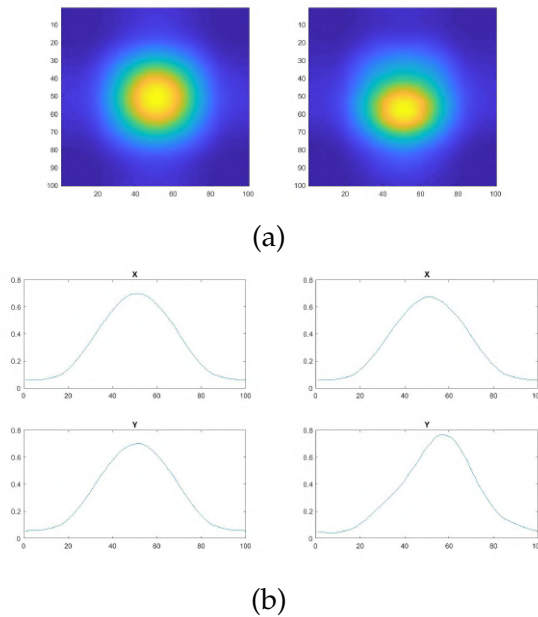FIGURE B.25: (a) Intensity fields at the Na layer (90km) of a Gaussian beam launched from the LLT without any aberration (left) and with the resulting aberration from the 0.1mm decentre + astigmatism in the primary (right); (b) Cross-section of the intensity profile of a Gaussian beam launched from the LLT without any aberration (left) and with the resulting aberration from the 0.1mm decentre + astigmatism in the primary (right). All units in pixels.

by far the expected real value.

B.3.3 LGS Facility Control System

The AOD LGS facility has a control system based in an x86 architecture PC running a Linux OS. As part of this larger adaptive optics control system, there are four active optical elements in the beam transfer path which are controlled by a Beckhoff Ethercat architecture; this control architecture allows bringing together electromechanical components from different vendors.

The Beckhoff Ethercat architecture (Figure B.26) is a modular I/O system consisting of electronic terminal blocks and an Ethercat coupler providing Ethercat protocol down to the individual terminals. These terminals are available for all common digital and analogue signal types, offering different connection options for optimum adaptation to the respective application. The LGSF Beckhoff architecture gathers two EL7031 modules, providing suitable connections for stepper motors (BEU and HWP mechanisms) and two El4132 modules with two analogue outputs each, which allow the proper control of fast steering mounts (BCM and BPM mechanisms).

BTO Mechanisms

These four active elements in the beam transfer path of the AOD LGSF are the following: the Beam Expander Unit linear stage for control of the LGS focus; the Beam
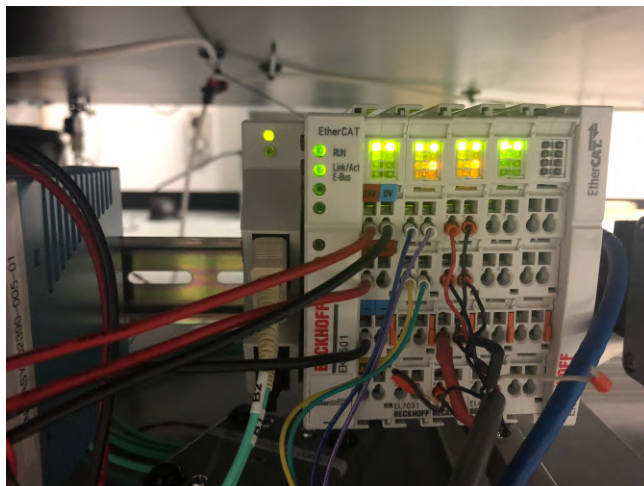
FIGURE B.26: The LGSF control system is mastered by a Beckhoff
Ethercat architecture.

Centering Mirror to keep the laser alignment through the BTO and the Beam Point-
ing Mirror to steer the LGS off-axis and maintain the point-ahead angle with the
target; and the rotary stage of the Half Wave Plate to provide linear polarization in
the laser beam.

BEU focus stage   As it has been previously described, the BEU third lens is
mounted on a linear stage to provide focusing capability. The linear stage is a New-
port Conex NSA12, whose main technical details are gathered in Table B.9.

Travel Range	11 mm
Drive Type	Micro Step Drive Stepper
Stage Type	NSA12 Linear Actuator
Minimum Incremental Motion	$0.20 \mu m$
Feedback	Open loop, no encoder
Interface connector	DB9 male

TABLE B.9: Newport Conex NSA12 technical details

The stepper motor in the linear stage is driven by the outputs of the EL7031
Beckhoff module, an EtherCat terminal intended for the direct connection of 2-phase
stepper motors, with two inputs for limit switches.
Two limit switches have been installed in the BEU unit to avoid an excess translation
movement of the linear stage and to ease the homing sequence. The limit switches
are two OMRON D2F-01FL2, SPDT-NO/NC Roller Lever Microswitch.The inputs
need to transition high when the limit is reached; therefore, the COM pin of each
limit switch is wired to the 24V Ethercat pin in the EL7031 module and the NO pins
of both switches are connected to the inputs I1 and I2 of the EL7031 module. I1 will
act as the home switch and I2 as the range end limit switch. Figure B.27 shows the
limit switches installation.
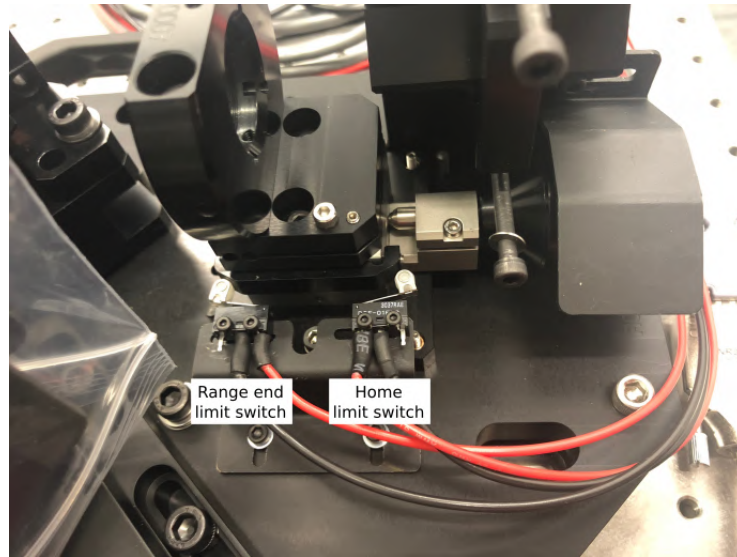
FIGURE B.27: Installation and wiring of the limit switches in the BEU unit.

The stage position will be configured based on the anticipated distance to the Sodium layer.

BCM and BPM steering mount   Both BCM and BPM units need the same mechanism type: a voice-coil actuated platform serving as tip-tilt mechanism. The BCM fast steering mount keeps the laser beam centered on the upstream components of the system; and the BPM mechanism maintains the point-ahead angle between the target and the LGS along its trajectory. Both fast steering mounts are Optics In Motion OIM102-3 units, whose main technical details are gathered in Table B.10.

Travel Range	+/- 1.5° mechanical (+/- 3° optical)
Drive Type	Voice-coil actuated platforms
Feedback	Position feedback input local or external
Interface connector	DB25 male

TABLE B.10: OIM102-3 technical details

The BCM and BPM mechanisms are controlled via analogue voltages in the +/-10V range, provided by two EL4132 Beckhoff modules. The two analogue outputs of each module provide the proper voltage to the mirror controller, a remote enclosure connected to the steering mount via a 6-ft cable; each output is related to X-axis movement and Y-axis movement, respectively. An amplifier board (Figure B.28) is necessary to properly interface both the Ethercat module and the OIM controller; the PCB needs one power supply of +/-15V and another one of 5V, which are provided by the OIM controller once the board is connected to it. The X and Y gains relating the analogue output voltages and the input signal to the mirror controller for X and Y movements, need to be configured depending on the application (BCM and BPM).

The mirror controller implements positioning servo-control with configurable proportional, integral and derivative gains. The low-frequency feedback loop is based on position error information in the BCM case, whereas the BPM works in open loop with a signal derived from the target trajectory and telescope axis.
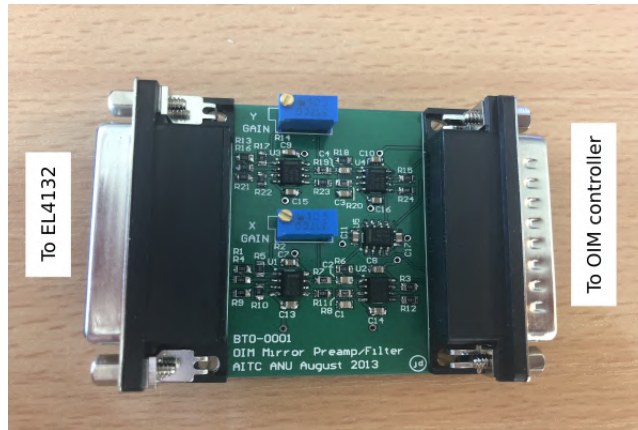
FIGURE B.28: Amplifier board to interface EL4132 module and the
OIM102-3 mirror controller.

HWP rotation stage   The HWP needs to be mounted on a rotation stage to ensure the unit polarization capabilities. The rotation stage is a Thorlabs NR360S Motorized Rotation Stage, whose main technical details are gathered in Table B.11.

Travel Range	360° continuous rotation
Drive Mechanism	Worm Drive 2-phase stepper motor
Step Angle	$1.8°/sec$
Speed Range	$50°/sec$
Limit Switches	Mechanical, normally open
Interface connector	DB15 female

TABLE B.11: Thorlabs NR360S Motorized Rotation Stage technical
details

The stepper motor in the rotation stage is driven by the Beckhoff module EL7031, same as in the BEU focus mechanism, an EtherCat module for the direct connection of 2-phase stepper motors, with two inputs for limit switches.

The Thorlabs NR360S Motorized Rotation Stage incorporates a limit switch, whose ground is connected to the motor body. This limit switch remains closed (to ground) during normal operation, and it opens when the limit position is reached, between $177°$ and $180°$. It should be approached from the counter clockwise direction to open at the 180-degree mark. Due to this fact, in order to get an input into the corresponding Ethercat pin, a pull-up resistor has been soldered to the limit switch input wire and connected to the 24V of the Ethercat terminal. The resistor was selected to get a voltage above the activation threshold of 3.5V, resulting in a 3.8kΩ resistor (which provides a voltage of 5.5V, measured in the input signal (I1) when the motor reaches the limit switch position).

The AOD installation and commissioning phase at the 1.8-meter telescope is scheduled for the end of 2019.

B.4 Author Contribution to the ANU/EOS Adaptive Optics Demonstrator

The author has lead the integration and alignment of the Beam Transfer Optics of the Laser Guide Star Facility, as well as participated into the assembly tasks of the Laser Launch Telescope. Another part of the accomplished tasks was the design of the electrical interface among the mechanisms and the verification of their functionality with the Beckhoff controller.

Based on the stay outcome, the author will publish a proceeding as a co-author in the 17th IAA SYMPOSIUM ON SPACE DEBRIS: Mitigation - Tools, Techniques and Challenges in October 2019, whose title is *Debris collision mitigation from the ground using Laser Guide Star Adaptive Optics at Mount Stromlo Observatory: results from the first artificial star ever created in Australian skies*.

Bibliography

A Bodhaine, Barry et al. (Feb. 1999). "On Rayleigh Optical Depth Calculations". In: *Journal of Atmospheric and Oceanic Technology - J ATMOS OCEAN TECHNOL* 16. DOI: 10.1175/1520-0426(1999)016<1854:ORODC>2.0.CO;2.

Abou-Rjeily, Chadi and Ahmad Slim (Apr. 2011). "Cooperative Diversity for Free-Space Optical Communications: Transceiver Design and Performance Analysis". In: *Communications, IEEE Transactions on* 59, pp. 658 –663. DOI: 10.1109/TCOMM.2011.121410.100032.

Adelson, Edward H. and James R. Bergen (1991). "The Plenoptic Function and the Elements of Early Vision". In: *Computational Models of Visual Processing*. MIT Press, pp. 3–20.

Andrews, Larry. C and Ronald L. Phillips (2005). *Laser Beam Propagation through Random Media*.

Atmospheric Extinction from the CMT. https://www.ast.cam.ac.uk/ioa/research/cmt/camc_extinction.html. Accessed: 2018-10-04.

Babcock, H.W. (1953). "The Possibility of Compensating Astronomical Seeing". In: *pasp* 65.386, p. 229. DOI: 10.1086/126606.

Bahcall, J.N. and R.M. Soneira (1981). "The distribution of stars to V = 16th magnitude near the north galactic pole - Normalization, clustering properties, and counts in various bands". In: *apj* 246, pp. 122–135. DOI: 10.1086/158905.

Basden, A.G. et al. (2018). "The Durham Adaptive Optics Simulation Platform (DASP): Current status". In: *SoftwareX* 7, pp. 63 –69. ISSN: 2352-7110. DOI: https://doi.org/10.1016/j.softx.2018.02.005. URL: http://www.sciencedirect.com/science/article/pii/S2352711018300232.

Basden, Alastair et al. (2010). "Durham adaptive optics real-time controller". In: *Appl. Opt.* 49.32, pp. 6354–6363. DOI: 10.1364/AO.49.006354. URL: http://ao.osa.org/abstract.cfm?URI=ao-49-32-6354.

Béchet, Clémentine et al. (2014). "Beam shaping for laser-based adaptive optics in astronomy". In: *Optics Express* 22.11, p. 12994. DOI: 10.1364/OE.22.012994.

Bennet, F. et al. (2015). "Adaptive Optics for Satellite Imaging and Space Debris Ranging". In: *Advanced Maui Optical and Space Surveillance Technologies Conference*, p. 2.

Bennet, Francis et al. (2012). *Adaptive optics for laser space debris removal*. DOI: 10.1117/12.925773. URL: https://doi.org/10.1117/12.925773.

Berent, J and PL Dragotti (2007). "Plenoptic Manifolds: Exploiting Structure and Coherence in Multi-View Images". In: *IEEE Signal Processing Magazine* 24, pp. 34–44.

Bonaccini Calia, D et al. (Sept. 2012). "The ESO transportable LGS Unit for measurements of the LGS photon return and other experiments". In: *Proc SPIE*. DOI: 10.1117/12.926898.

Briguglio, Runa et al. (Dec. 2018). "Optical calibration and performance of the adaptive secondary mirror at the Magellan telescope". In: *Scientific Reports* 8. DOI: 10.1038/s41598-018-29171-6.

C. Andrews, Larry et al. (July 2006). "Strehl ratio and scintillation theory for uplink Gaussian-beam waves: Beam wander effects". In: *Optical Engineering - OPT ENG Vol 45*.

Cao, Jingtai et al. (June 2017). "Performance analysis of a coherent free space optical communication system based on experiment". In: *Optics Express Vol. 25*, p. 15299.

Castro-Almazan J. Alonso, A. Bonaccini Calia D. Centrone M. Lombardi G. Montilla I. Muñoz-Tuñon C. Reyes M. (2017). *Na LGS height profiles at Teide Observatory, Canary Islands*. DOI: 10.26698/AO4ELT5.0183.

Clare, R. and R. Lane (2005). "Wave-front sensing from subdivision of the focal plane with a lenslet array". In: *J. Opt. Soc. Am.* A 22, pp. 117–125.

Cole, M. and K. Kiasaleh (2004). "Signal intensity estimators for free-space optical communications through turbulent atmosphere". In: *IEEE Photonics Technology Letters* 16.10, pp. 2395–2397. ISSN: 1041-1135. DOI: 10.1109/LPT.2004.833924.

Conan, R. (2013). *Object-Oriented Matlab Adaptive Optics. User Guide*.

Conan, R. and C. Correia (2014). *Object-oriented Matlab adaptive optics toolbox*. DOI: 10.1117/12.2054470.

Correia, Carlos M. et al. (2015). "Spatio-angular minimum-variance tomographic controller for multi-object adaptive-optics systems". In: *Appl. Opt.* 54.17, pp. 5281–5290. DOI: 10.1364/AO.54.005281. URL: http://ao.osa.org/abstract.cfm?URI=ao-54-17-5281.

Denvir, Donal J. and Emer Conroy (2003). *Electron-multiplying CCD: the new ICCD*. DOI: 10.1117/12.457779. URL: https://doi.org/10.1117/12.457779.

D'Orgeville, Celine et al. (2014). *A sodium laser guide star facility for the ANU/EOS space debris tracking adaptive optics demonstrator*. DOI: 10.1117/12.2055050. URL: https://doi.org/10.1117/12.2055050.

d'Orgeville, Céline and Gregory J. Fetzer (2016). *Four generations of sodium guide star lasers for adaptive optics in astronomy and space situational awareness*. DOI: 10.1117/12.2234298. URL: https://doi.org/10.1117/12.2234298.

Edmund Optics Tech Tools: Axicon. https://www.edmundoptics.com/resources/tech-tools/axicon/. Accessed: 2018-11-01.

ESA's Space Debris Office (2018). *Space Debris by the numbers*. URL: https://www.esa.int/Our_Activities/Operations/Space_Debris/Space_debris_by_the_numbers (visited on 09/21/2018).

Escarate, Pedro et al. (Apr. 2017). "Model Predictive Control for Laser Beam Shaping". In: *IEEE Latin America Transactions* 15, pp. 626–631. DOI: 10.1109/TLA.2017.7896347.

Femenía, Bruno. *AOLI Deformable Mirror Stroke Calculus*.

Feng, F., I. H. White, and T. D. Wilkinson (2014). "Aberration Correction for Free Space Optical Communications Using Rectangular Zernike Modal Wavefront Sensing". In: *Journal of Lightwave Technology* 32.6, pp. 1239–1245. ISSN: 0733-8724. DOI: 10.1109/JLT.2014.2301634.

Feng, Feng, I. H. White, and Timothy D. Wilkinson (2013). "Holographic wavefront sensing and correction for free space optical communications". In: *Asia Communications and Photonics Conference 2013*. Optical Society of America, AW4E.2. DOI: 10.1364/ACPC.2013.AW4E.2. URL: http://www.osapublishing.org/abstract.cfm?URI=ACPC-2013-AW4E.2.

Flicker, Ralf and Francois Rigaut (Jan. 2002). "Tilt anisoplanatism and PSF retrieval in LGS MCAO using a predictive controller". In:

Fricke, K.H. and U von Zahn (May 1985). "Mesopause temperature derived from probing the hyperfine structure of the D2 resonance line of sodium by lidar". In:

Journal of Atmospheric and Terrestrial Physics 47, pp. 499–512. DOI: 10.1016/0021-9169(85)90116-3.

García-Lorenzo, B. and J. J. Fuensalida (2011). "Statistical structure of the atmospheric optical turbulence at Teide Observatory from recalibrated generalized SCIDAR data". In: *Monthly Notices of the Royal Astronomical Society* 410.2, pp. 934–945. ISSN: 1365-2966. DOI: 10.1111/j.1365-2966.2010.17492.x. URL: http://dx.doi.org/10.1111/j.1365-2966.2010.17492.x.

Gardner, Chester (Apr. 1989). "Sodium resonance fluorescence lidar applications in atmospheric science and astronomy". In: *Proceedings of the IEEE* 77, pp. 408 –418. DOI: 10.1109/5.24127.

Gershun, A. (1939). "The Light Field". In: *Journal of Mathematics and Physics* 18.1-4, pp. 51–151. DOI: 10.1002/sapm193918151. eprint: https://onlinelibrary.wiley.com/doi/pdf/10.1002/sapm193918151. URL: https://onlinelibrary.wiley.com/doi/abs/10.1002/sapm193918151.

Glindemann, A. (2011). *Principles of Stellar Interferometry*. Springer. ISBN: 978-3-642-15028-9.

Goodman J. W., Gustafson S. C. (1996). *Introduction to Fourier Optics*.

Gortler, Steven J. et al. (1996). "The Lumigraph". In: *Proceedings of the 23rd Annual Conference on Computer Graphics and Interactive Techniques*. SIGGRAPH '96. New York, NY, USA: ACM, pp. 43–54. ISBN: 0-89791-746-4. DOI: 10.1145/237170.237200. URL: http://doi.acm.org/10.1145/237170.237200.

Grosse, Doris et al. (2017). "Adaptive Optics for Satellite Imaging and Earth based Space Debris Manoeuvres". In: *7th European Conference on Space Debris, Darmstadt, Germany*, p. 6.

Guesalaga, Andres et al. (2012). *Improving stability, robustness, and performance of laser systems*. DOI: 10.1117/12.924908. URL: https://doi.org/10.1117/12.924908.

Guo, Hong et al. (June 2010). "Influence of beam wander on uplink of ground-to-satellite laser communication and optimization for transmitter beam radius". In: *Optics letters* 35, pp. 1977–9. DOI: 10.1364/OL.35.001977.

Hardy, J. W. (1998). *Adaptive Optics for Astronomical Telescopes*. Oxford University Press. ISBN: 9780195090192.

Hemmati, H. (2006). *Deep space optical communications*. Wiley. ISBN: 978-0-470-04002-7.

Herbert, James Joseph (2006). "Techniques for deriving optimal bondlines for athermal bonded mounts". In: *SPIE Optics + Photonics*.

Holzlöhner, R. et al. (2016). *Comparison between observation and simulation of sodium LGS return flux with a 20W CW laser on Tenerife*. DOI: 10.1117/12.2233072. URL: https://doi.org/10.1117/12.2233072.

I. Montilla J. Marino, A. Asensio Ramos M. Collados L. Montoya M. Tallon (2016). *Solar adaptive optics: specificities, lessons learned, and open alternatives*. DOI: 10.1117/12.2233652. URL: https://doi.org/10.1117/12.2233652.

J. M. Rodríguez-Ramos B. Femenía Castellá, F. Pérez Nava S. Fumero (2008). *Wavefront and distance measurement using the CAFADIS camera*. DOI: 10.1117/12.789380. URL: https://doi.org/10.1117/12.789380.

Jasmine, S., S. Robinson, and K. Malaisamy (2015). "Investigation on free space optical communication for various atmospheric conditions". In: *2015 2nd International Conference on Electronics and Communication Systems (ICECS)*, pp. 1030–1034. DOI: 10.1109/ECS.2015.7124736.

Kanev, F. Y. and V. P. Lukin (1991). "Amplitude phase beam control with the help of a two-mirror adaptive system". In: DOI: Atmos.Opt.4,878-881.

Kaushal, H. and G. Kaddoum (2017). "Optical Communication in Space: Challenges and Mitigation Techniques". In: *IEEE Communications Surveys Tutorials* 19.1, pp. 57–96. ISSN: 1553-877X. DOI: 10.1109/COMST.2016.2603518.

Ko, Jonathan and Christopher C. Davis (2017). "Comparison of the plenoptic sensor and the Shack Hartmann sensor". In: *Appl. Opt.* 56.13, pp. 3689–3698. DOI: 10.1364/AO.56.003689. URL: http://ao.osa.org/abstract.cfm?URI=ao-56-13-3689.

Koishi, Y. et al. (2011). "Research and development of 40Gbps optical free space communication from satellite/airplane". In: *2011 International Conference on Space Optical Systems and Applications (ICSOS)*, pp. 88–92. DOI: 10.1109/ICSOS.2011.5783717.

La Palma Night-Sky Brightness. http://www.ing.iac.es/Astronomy/observing/conditions/skybr/skybr.html. Accessed: 2018-10-04.

Levoy, M. and P. Hanrahan (1996). "Light Field Rendering". In: *Proc. ACM SIGGRAPH '96*. DOI: 10.1145/237170.237199.

Lüke, J. P. (2014). *Recuperación de la geometría de una escena a partir de imágenes plenópticas aplicando técnicas locales*. Phd Thesis. Universidad de La Laguna.

Luna, Ricardo et al. (Oct. 2009). "Experimental Demonstration of a Hybrid Link for Mitigating Atmospheric Turbulence Effects in Free-Space Optical Communication". In: *Photonics Technology Letters, IEEE* 21, pp. 1196 –1198. DOI: 10.1109/LPT.2009.2024214.

Martínez, Noelia and Luis Fernando Rodríguez Ramos (2018). *Solar MCAO with a single sensor: simulating tomographic reconstruction with the plenoptic camera*. DOI: 10.1117/12.2310087. URL: https://doi.org/10.1117/12.2310087.

Martínez, Noelia, Luis Fernando Rodríguez Ramos, and Zoran Sodnik (2017). *Simulating the performance of adaptive optics techniques on FSO communications through the atmosphere*. DOI: 10.1117/12.2273692. URL: https://doi.org/10.1117/12.2273692.

Martínez, Noelia et al. (2017a). "Performance assessment of Adaptive Optics techniques on FSO communications through the atmosphere". In: DOI: 10.26698/AO4ELT5.0143.

Martínez, Noelia et al. (2017b). "The Plenoptic Camera as Wavefront Sensor for the VTT Solar Telescope". In: DOI: 10.26698/AO4ELT5.0154.

Martínez, Noelia et al. (2018). *Uplink correction demonstrator: test bench and experimental results*. DOI: 10.1117/12.2310088. URL: https://doi.org/10.1117/12.2310088.

Montilla, I et al. (July 2010). "Multiconjugate adaptive optics with plenoptic cameras and the Fourier Transform Reconstructor". In: *Proc SPIE* 7736. DOI: 10.1117/12.857100.

Nader M. Namazi Harris Rayvon Burris, Charles Conner G. Charmaine Gilbreath (2006). "Synchronization and detection of binary data in free-space optical communication systems using Haar wavelet transformation". In: *Optical Engineering* 45, pp. 45 –45 –13. DOI: 10.1117/1.2162029. URL: https://doi.org/10.1117/1.2162029.

Noelia Martínez Luis Fernando Rodríguez Ramos, Zoran Sodnik (2018). "Toward the uplink correction: application of adaptive optics techniques on free-space optical communications through the atmosphere". In: *Optical Engineering* 57, pp. 1 –11 –11. DOI: 10.1117/1.OE.57.7.076106. URL: https://doi.org/10.1117/1.OE.57.7.076106.

Noll, Robert J. (1976). "Zernike polynomials and atmospheric turbulence∗". In: *J. Opt. Soc. Am.* 66.3, pp. 207–211. DOI: 10.1364/JOSA.66.000207. URL: http://www.osapublishing.org/abstract.cfm?URI=josa-66-3-207.

Parenti, Ronald R. (1992). "Adaptive Optics for Astronomy". In: *The Lincoln Laboratory Journal* 5.1, pp. 93–114.

Parks, Robert E. and William P. Kuhn (2005). *Optical alignment using the Point Source Microscope*. DOI: 10.1117/12.618165. URL: https://doi.org/10.1117/12.618165.

Petit, Cyril et al. (2009). "Linear quadratic Gaussian control for adaptive optics and multiconjugate adaptive optics: experimental and numerical analysis". In: *J. Opt. Soc. Am. A* 26.6, pp. 1307–1325. DOI: 10.1364/JOSAA.26.001307. URL: http://josaa.osa.org/abstract.cfm?URI=josaa-26-6-1307.

Ragazzoni, Roberto (Feb. 1996). "Pupil plane wavefront sensing with an oscillating prism". In: *Journal of Modern Optics - J MOD OPTIC* 43, pp. 289–293. DOI: 10.1080/095003496156165.

Raj, A. A. B., J. A. V. Selvi, and S. Raghavan (2010). "Terrestrial free space line of sight optical communication (TFSLSOC) using adaptive control steering system with laser beam Tracking, Aligning and Positioning (ATP)". In: *Wireless Communication and Sensor Computing, 2010. ICWCSC 2010. International Conference on*, pp. 1–5. DOI: 10.1109/ICWCSC.2010.5415900.

Raj, A. A. B., J. A. V. Selvi, and S. Raghavan (2010). "Terrestrial free space line of sight optical communication (TFSLSOC) using adaptive control steering system with laser beam Tracking, Aligning and Positioning (ATP)". In: *2010 International Conference on Wireless Communication and Sensor Computing (ICWCSC)*, pp. 1–5.

Ramlau, R., D. Saxenhuber, and M. Yudytskiy (2014). *Iterative reconstruction methods in atmospheric tomography: FEWHA, Kaczmarz and Gradient-based algorithm*. DOI: 10.1117/12.2057379. URL: https://doi.org/10.1117/12.2057379.

Rimmele, Thomas R. (2000). *Solar adaptive optics*. DOI: 10.1117/12.390301. URL: http://dx.doi.org/10.1117/12.390301.

Roddier, François and Claude Roddier (1991). "Wavefront reconstruction using iterative Fourier transforms". In: *Appl. Opt.* 30.11, pp. 1325–1327. DOI: 10.1364/AO.30.001325. URL: http://ao.osa.org/abstract.cfm?URI=ao-30-11-1325.

Rodríguez-Ramos, J. et al. (2010). "The CAFADIS camera: a new tomographic wavefront sensor for Adaptive Optics". In: *1st AO4ELT conference*. Vol. 05011.

Rodríguez Ramos, L. F. (2015). *Utilización de la cámara plenóptica como sensor de frente de onda para Óptica Adaptiva en Astrofísica*.

Rodriguez Ramos, Luis Fernando et al. (Aug. 2009). "The plenoptic camera as a wavefront sensor for the European Solar Telescope (EST)". In: *Proc SPIE* 7439. DOI: 10.1117/12.828578.

Rodriguez Ramos, Luis Fernando et al. (July 2012). "Concepts, laboratory and telescope test results of the Plenoptic Camera as a wavefront sensor". In: *Proc. SPIE* 8447, pp. 45–. DOI: 10.1117/12.925327.

Rosa L. Montoya, M. Collados I. Montilla N. Vega Reyes J. Marco de la (2016). *Daytime turbulence profiling for EST and its impact in the solar MCAO system design*. DOI: 10.1117/12.2229471. URL: https://doi.org/10.1117/12.2229471.

Rosensteiner, Matthias and Ronny Ramlau (2013). "Kaczmarz algorithm for multiconjugated adaptive optics with laser guide stars". In: *J. Opt. Soc. Am. A* 30.8, pp. 1680–1686. DOI: 10.1364/JOSAA.30.001680. URL: http://josaa.osa.org/abstract.cfm?URI=josaa-30-8-1680.

Roudier, Th. and R. Muller (1986). "Structure of the solar granulation". In: *Solar Physics* 107.1, pp. 11–26. ISSN: 1573-093X. DOI: 10.1007/BF00155337. URL: https://doi.org/10.1007/BF00155337.

S. Shaik, K (Apr. 1988). "Atmospheric Propagation Effects Relevant to Optical Communications". In: *Telecommunications and Data Acquisition Progress Report*, pp. 180–200.

Sánchez-Capuchino, Jorge et al. (June 2010). "Current Concept For The 4-m European Solar Telescope (EST) Optical Design". In:

Stewart McKechnie, T (Jan. 2015). *General Theory of Light Propagation and Imaging Through the Atmosphere*. Vol. 196, pp. 1–624.

Studio, NASA/Goddard Space Flight Center Scientific Visualization (2007). *Hinode's High-resolution view of solar granulation*. URL: http://svs.gsfc.nasa.gov/3412.

Stupl, Jan et al. (2014). "LightForce Photon-Pressure Collision Avoidance: Updated Efficiency Analysis Utilizing a Highly Parallel Simulation Approach". In: *Advanced Maui Optical and Space Surveillance Technologies Conference*, p. 16.

Talanov, V.I. (1970). "Focusing of Light in Cubic Media". In: *Soviet Journal of Experimental and Theoretical Physics Letters* 11, p. 199.

Thompson, Laird A. and Scott Teare (Sept. 2002). "Rayleigh Laser Guide Star Systems: Application to the University of Illinois Seeing Improvement System". In: *Publications of The Astronomical Society of The Pacific - PUBL ASTRON SOC PAC* 114, pp. 1029–1042. DOI: 10.1086/342043.

Thorlabs. *Shack-Hartmann Wavefront Sensors*. URL: https://www.thorlabs.com/newgrouppage9.cfm?objectgroup_id=5287.

Toyoshima, Morio, Hideki Takenaka, and Yoshihisa Takayama (2011). "Atmospheric turbulence-induced fading channel model for space-to-ground laser communications links". In: *Opt. Express* 19.17, pp. 15965–15975. DOI: 10.1364/OE.19.015965. URL: http://www.opticsexpress.org/abstract.cfm?URI=oe-19-17-15965.

Tyson, R. K. (1991). *Principles of Adaptive Optics*. DOI: ISBN9780127059006.

Tyson, R. K. (2000). *Adaptive Optics Engineering Handbook*. DOI: ISBN0-8247-8275-5.

Williams W. Dan, Collins Michael Boroson Don M. Lesh James Biswas Abihijit Orr Richard Schuchman-Leonard Sands O. Scott (2007). "RF and Optical Communications: A Comparison of High Data Rate Returns From Deep Space in the 2020 Timeframe". In: DOI: 20070017310. URL: https://ntrs.nasa.gov/search.jsp?R=20070017310.

Wilson, K et al. (Feb. 2004). "Daytime adaptive optics for deep space communications". In: 117.

Wu, Chensheng et al. (2018). "Phase and amplitude beam shaping with two deformable mirrors implementing input plane and Fourier plane phase modifications". In: *Appl. Opt.* 57.9, pp. 2337–2345. DOI: 10.1364/AO.57.002337. URL: http://ao.osa.org/abstract.cfm?URI=ao-57-9-2337.

Yoder, Paul and Daniel Vukobratovich (2015). *Opto-Mechanical Systems Design, Volume 1. Design and Analysis of Opto-Mechanical Assemblies*. CRC Press. ISBN: 9781315215068.

Zepp, Andreas (2013). *Characterization of the holographic wavefront sensor for free-space optical communications*. DOI: 10.1117/12.2028999. URL: https://doi.org/10.1117/12.2028999.

Zhu, X. and J. M. Kahn (2002). "Free-space optical communication through atmospheric turbulence channels". In: *IEEE Transactions on Communications* 50.8, pp. 1293–1300. ISSN: 0090-6778. DOI: 10.1109/TCOMM.2002.800829.

Zhu, X. and J. M. Kahn (2003). "Markov chain model in maximum-likelihood sequence detection for free-space optical communication through atmospheric turbulence channels". In: *IEEE Transactions on Communications* 51.3, pp. 509–516. ISSN: 0090-6778.

Zovaro, A. et al. (2016). "Harnessing Adaptive Optics for Space Debris Collision Mitigation". In: *Advanced Maui Optical and Space Surveillance Technologies Conference*, p. 127.